# Planetary Geological Science and Aerospace Systems Engineering Applications of Thermal Infrared Remote Sensing for Earth, Mars, and the Outer Bodies

by

Michael Veto

A Dissertation Presented in Partial Fulfillment
of the Requirements for the Degree
Doctor of Philosophy

Approved June 2018 by the
Graduate Supervisory Committee:

Philip Christensen, Chair
Erik Asphaug
James Bell III
Amanda Clarke
Steven Ruff
Srikanth Saripalli
Jim Tyburczy, proxy

ARIZONA STATE UNIVERSITY

August 2018

ABSTRACT

Many planetary science missions study thermophysical properties of surfaces using infrared spectrometers and infrared cameras. Thermal inertia is a frequently derived thermophysical property that quantifies the ability for heat to exchange through planetary surfaces.

To conceptualize thermal inertia, the diffusion equation analogies are extended using a general effusivity term: the square root of a product of conductivity and capacity terms. A hypothetical thermal inductance was investigated for diurnal planetary heating. The hyperbolic heat diffusion equation was solved to derive an augmented thermal inertia. The hypothetical thermal inductance was modeled with negligible effect on Mars.

Extending spectral performance of infrared cameras was desired for colder bodies in the outer solar system where peak infrared emission is at longer wavelengths. The far-infrared response of an infrared microbolometer array with a retrofitted diamond window was determined using an *OSIRIS-REx*—OTES interferometer. An instrument response function of the diamond interferometer-microbolometer system shows extended peak performance from 15 μm out to 20 μm and 40% performance to at least 30 μm. The results are folded into E-THEMIS for the NASA flagship mission: *Europa Clipper*.

Infrared camera systems are desired for the expanding smallsat community that can inherit risk and relax performance requirements. The Thermal-camera for Exploration, Science, and Imaging Spacecraft (THESIS) was developed for the *Prox-1* microsat mission. THESIS, incorporating *2001 Mars Odyssey*—THEMIS experience, consists of an infrared camera, a visible camera, and an instrument computer. THESIS was planned to provide images for demonstrating autonomous proximity operations

between two spacecraft, verifying deployment of the Planetary Society's *LightSail-B*, and conducting remote sensing of Earth. *Prox-1*—THESIS was selected as the finalist for the competed University Nanosatellite Program-7 and was awarded a launch on the maiden commercial SpaceX *Falcon Heavy*. THESIS captures 8-12 μm IR images with 100 mm optics and RGB color images with 25 mm optics. The instrument computer was capable of instrument commanding, automatic data processing, image storage, and telemetry recording. The completed THESIS has a mass of 2.04 kg, a combined volume of 3U, and uses 7W of power. THESIS was designed, fabricated, integrated, and tested in ASU's 100K clean lab.

DEDICATION

for my mother, Julie; my brothers, Chris and Bobby; and my future family

in memory of my father,

John Veto

who taught me math, how to build things, and how to help others

ACKNOWLEDGMENTS

GENERAL

I thank my friends, there are far too many to name, for fun and encouragement, the Moeur building as a professional family, my committee members for guidance, all of my teachers and staff in the Chandler Unified School District and Arizona State University for incremental contributions to my development, and the Arizona and Federal taxpayers for 26 years of a wholly public education.

CHAPTER 2 & 3

This chapter was inspired from a post-qualification exam suggestion. Chris Mount provided a candid review of the thermal effusivity manuscript. Inspiration for the project was provided in-part by the lectures of the Mattia De' Michieli Vitturi, Amanda Clarke, Jim Clark, and Phil Christensen.

CHAPTER 4

The long-far wavelength camera development could not have been accomplished without the support of Dan Pelham, Bill O'Donnell, Stillman Chase, Saadat Anwar, Steve Ruff, Ian Kubik, Tara Fisher, and Ashley Toland. This project was funded by my advisor through a competed grant of the National Aeronautics and Space Administration (NASA) for the Planetary Instrument Definition and Development Program (PIDDP) (#NNX12AJ17G). I appreciate that Phil Christensen trusted me to undertake this endeavor that played a small part to help develop a NASA flagship instrument to search for life on Europa.

CHAPTER 5

The Air Force Research Lab (AFRL) provided the competitive opportunity for students to design and implement a mission through the University Nanosat Program (UNP). The *Odyssey*-THEMIS project office provided a spacecraft-instrument

collaborative example and experienced mentors from which this student project draws. The School of Earth and Space Exploration provided space in the 100K clean room to work on this project. The OTES Engineering Team has been invaluable for mentorship: Greg Mehall, Saadat Anwar, Bill O'Donnell, Dan Pelham, Rob Woodword, Ian Kubik, and Mark Miner. Tara Fisher, Ashley Toland, and Heather Valentine have been helpful for administrative support. Sri Saripalli provided engineering advice with parallel efforts. Experience with *MER*-Pancam, Jim Bell, and team folded into the image and telemetry schemes for THESIS. Andy Ryan provided his experience and lab for a preliminary TVAC test. Sean Marshall provided analysis in the early concept stages of selecting the optics. Amber Keske lent experience and completed the final analysis of the resolution of the imagers and the visible camera performance; she was essential for showing that edge-detection algorithms can solve the blur created when images were out of focus.

Dave Spencer was the principal investigator of *Prox-1* that chose to work with ASU. Without him, this project would have never been started. Dave also provided significant mission and systems engineering education to me throughout this project. The dozens of students at Georgia Tech provided an opportunity to collaborate on *Prox-1* and its predecessor *R*$^3$. I hope to work with them in my future career.

My advisor Phil Christensen provided this opportunity to propose an instrument system as an undergraduate Honor's thesis that matured, through graduate school, into an instrument system that was delivered, integrated onto a spacecraft, and almost launched. All of this work was subsequent to my first class in college in which Phil tasked the class to design a payload to capture images from sky while in parallel capturing images from THEMIS in orbit around Mars to explore the surface of another planet—twelve years ago. Phil also provided invaluable life mentorship, inspiration, friendship, and is a positive influence and role model for how to be both a gentleman and a scientist.

TABLE OF CONTENTS

Page

CHAPTER Page

CHAPTER Page

CHAPTER Page

APPENDIX

CHAPTER Page

LIST OF TABLES

Table Page

Table Page

LIST OF FIGURES

Figure Page

Figure Page

Figure Page

Figure Page

Figure Page

Figure Page

Figure Page

Figure Page

Figure Page

Figure Page

Figure Page

Figure Page

Figure Page

Figure Page

Figure Page

Figure Page

Figure Page

Figure Page

Figure Page

Figure Page

Figure Page

Figure Page

Figure Page

Figure Page

# LIST OF SYMBOLS

These are included within each individual chapter.

# PREFACE

Space exploration is accomplished through a synthesis of intelligent and motivated people working together to create sophisticated machines and instruments capable of producing data that is distilled into discoveries, refined characterizations, databases, maps, and new hypothesis. The people that make this happen tend to define themselves as scientists, engineers, mathematicians, and technicians. Each of these fields is specialized in different skill sets, modes of thinking, goals, allowable precision and accuracy, spatial scales, time scales, schedules, end-products, expectations, and metrics of success. In the absence of a cross-disciplinary, collaborative environment, it can be difficult for people of one STEM-class to understand or work with people in a different STEM-class. The School of Earth and Space Exploration at Arizona State University provides an environment for all STEM-class people to interact on complex projects. This encourages a mutual understanding of one another and provides an opportunity to accomplish great projects. This PhD experience was devised for a recently graduated bachelor of engineering student to work, to travel, to live, and to learn with planetary scientists. It was an effort to learn how scientists think and to become a scientist in some fraction. I claim that this goal was achieved. Four projects are included in this defense and two projects are either addendums or will be completed in the future.

The first project was the result of a post-qualification exam suggestion: derive thermal inertia from first principles. I attempted to explain this through analogy as the easiest method. The second chapter was a self-initiated curiosity that expands upon the thermal inertia derivation. Aerospace Engineers are often taught circuits through analogy to mechanical systems. Extending the analogy to heat transfer, the mathematics seems more consistent to describe thermal inertia or thermal inductance as a stand-alone term—independent of the conductive and capacitive terms.

The third project was carried out after of my advisor Phil Christensen was awarded a Planetary Instrument Definition and Development Program (PIDDP) proposal to investigate the performance of diamond windows on microbolometer arrays. This project grew into a rewarding experience of characterizing the performance of a long-far infrared diamond-windowed imaging spectrometer. This new technology development folds into the development of the E-THEMIS infrared camera for the *Europa Clipper*—a NASA flagship mission.

The fourth project continues the work of a Technology Readiness Level -4 (TRL-4) infrared instrument system concept that was the subject of my undergraduate honor's thesis advised by Phil Christensen. The infrared instrument concept was part of a proposal with Professor Dave Spencer and his students at the Georgia Institute of Technology. In parallel to the PhD program, this work continued on the side as a bonus project: the THermal-camera for Science, Exploration, and Imaging Spacecraft (THESIS) for the *Prox-1* microsat mission. Subsequent to my PhD oral exam, this project was selected at the winner of the 7$^{th}$ University Nanosatellite Program competition and awarded a berth on the maiden, commercial Space X *Falcon Heavy*. THESIS was designed and integrated into a TRL-5 completed instrument system that was bolted onto a spacecraft and ready for environmental testing. In order to deliver an instrument system capable of meeting the mission design (Level 2 requirements) and the full mission success criteria (Level 1 requirements) within the allocated schedule, cost, and risk, THESIS grew in scope of this dissertation from a side-project to the flagship chapter. All of the threshold requirements were completed and the instrument was delivered. Baseline requirements to complete environmental testing and radiometric testing prior to delivery were descoped, so the mission would not be cancelled as a result of a failure to deliver threshold instruments. Nevertheless, the mission, as a whole, was

cancelled, because the entire team did not complete full integration on-schedule. In the space missions, everyone must complete their jobs or nobody will succeed.

There were two projects originally proposed for my oral exam that were not fully completed as chapters for this dissertation. The first science project proposed for this to study cold craters in Utopia Planetia on Mars using THEMIS. Data is still being collected for this project, and I hope that I will have time to return to this project at some point in the future as side-project of my future career. The second project involved completing a sensitivity analysis of a terrestrial explosive volcanology model to Mars in order to determine how the various parameters at Mars may affect the resulting explosive plumes. Much of this analysis was completed, however the application of the results to learning something new about Mars is outstanding work. Although these chapter provided an opportunity to study interesting scientific questions about the geology of Mars, their completion was descoped from my PhD to allocate resources for completing the PIDDP and THESIS projects and to postpone the due diligence necessary for producing sound findings worthy of publication. Stay tuned. These will come, in time.

In the end, I realize that each PhD, or even a career, is a mission. There are performance requirements, and there is some cost threshold, schedule for completion deadline, and personal risk to manage. It is up to each of us to determine our objectives, success criteria, and performance requirements achievable within our available resources. Oftentimes, there are many things we scientists want to do and thus we over commit, but as Dad used to say there are wants and needs. There are baselines and thresholds. Learning how to tactfully descope to what's good enough is an art unto itself.

A motto at Orbital was that you can't launch until you equate your flight hardware in paperwork mass. THESIS was 2.04kg/4.5lbs. If 100 piece of a paper equals a pound, then somewhere ~450 pages was about right.

# CHAPTER 1

# INTRODUCTION

Thermal inertia is a parameter used for studying the surfaces of planetary bodies. For science, this parameter is used to elucidate the geologic history of a planetary field site, to investigate active geologic processes, and to infer the presence of volatiles. For engineering, thermal inertia maps are used to constrain landing sites and to guide the planning of rover traverses. Thermal inertia is defined as the square root of the product of thermal conductivity, density, and specific heat; it has the SI units of joules per meter squared per kelvin per root second and is the ability of a material to exchange heat. Thermal inertia is recognized as thermal effusivity within other fields of science and industry. For example, the clothing industry measures the thermal effusivity different materials and the pharmaceutical industry measures the thermal effusivity of mixed drugs and vitamins. It is likely that the thermal effusivity, or the thermal inertia as it is known in planetary science, has been measured for much of the clothes and vitamins that planetary scientists have worn and consumed! Thus an awareness of the vast industrial use of thermal effusivity provides an opportunity for new innovations. Perhaps these other industries have produced literature on how fluids affect the thermal effusivity of materials with pore spaces as an example.

Thermal inertia is a bit of an esoteric property that is not well-known beyond the scientists studying it. Because it is not a property found in most physics textbooks, many students are left without a basic introduction in their high school or early university physics course. In Chapter 2, analogies are provided to equivalent systems using diffusion equations that are commonly taught in elementary physics courses; the square root of thermal conductivity and heat capacity is similar to the square root of electrical conductivity and capacitance. The systems of equivalence framework was extended to

propose similar effusivities that are mathematically equivalent to thermal inertia/thermal effusivity. A general effusivity equation and a general effusion equation are proposed.

Expanding upon the systems of equivalence analogies, the obvious question arises: What is the corresponding thermal inductance? For Chapter 3, Thermal inductance was incorporated into an expanded, relativistic thermal effusivity to expand the mathematical representation of the observed thermal inertia of a surface. By analogy, a corresponding inductive term in heat transfer may be analogous to mass (i.e. in the mass-spring-damper system) and inductance (i.e. in the inductor-resistor-capacitor circuit). Many papers have been published in heat transfer journals that describe this thermal inductance. The thermal inductance was related to a relaxation time coefficient that was added to Fourier's empirical law to produce the theoretical Cattaneo and Vernotte equation and added to the heat diffusion equation to produce the hyperbolic heat diffusion equation. In most applications, the thermal inductance was undetectable. Maxwell noted 150 years ago that this term could be ignored. Today however, some researchers have claimed to measure thermal inductance in specific experimental apparatuses that involve cooled helium with some reported success e.g. (Ackerman et al. 1966) While the parabolic heat equation was sufficient for most heat transfer problems, the hyperbolic heat equation may be more accurate under specific situations involving high frequency pulsed heat excitation and length scales where heat transfer cannot be assumed to instantaneously permeate through the control area. This phenomenon is sometimes referred to as relativistic for its implications that even heat has a finite speed limit that cannot exceed the speed of light. Here, this hyperbolic heat diffusion equation was solved for a relativistic thermal effusivity. A simple model was applied using planetary surface properties to test the applicability of relativistic thermal effusivity. No

reasonable application was found for terrestrial planets in our solar system; though it was possible to speculate. The framework of system equivalence was further extended to include the thermal inductance term.

While the preceding chapters propose to extend a mathematical framework out of *Curiosity*, chapter 4 provides measured data to extend the performance of infrared cameras arrays out of *Necessity*. Objects that are colder than Mars require infrared cameras that are sensitive in the far infrared wavelengths, because their emission is centered at greater wavelengths. Furthermore, mineral absorption lines greater than 12μm are desirable to be measured. While this would enhance the detection of many minerals that are currently mapped, it would make detection of salt minerals possible that currently do not have absorption features in the longwave infrared. At present, these minerals are inferred in infrared cameras from featureless infrared spectra (Osterloo et al., 2008). To fill this need, the long-far wavelength performance of a diamond-retrofitted-640x480-uncooled microbolometer array was characterized. A CVD diamond window was designed and integrated onto a 640x480 microbolometer array. Two experimental methods were performed in order to ascertain an instrument response function. First, a series of gold THz filters were equipped into two filter wheels to determine the spectral response at discrete wavelength bands. A long-pass cut-off filter was procured to block observed out-of-band leakage. As a result, blackbody radiance appears to be detected up to ~45 μm. A second experiment was performed by integrating the microbolometer array, with retrofitted diamond window, onto the qualification unit of the OSIRIS-REx Thermal Emission Spectrometer (OTES) interferometer. This was the first known time that a diamond interferometer-microbolometer array has captured images of infrared interferograms. A wavenumber instrument response function (IRF) was produced in a series of tests. Upgrading the interferometer from the OTES

qualification unit to the OTES engineering unit increases the performance of the instrument system. The final IRF shows that the peak response was extended to ~500 $cm^{-1}$/~20 μm. The response then begins to decrease to ~25% at ~285 $cm^{-1}$/~35 μm. Thermal instability of the detector was a likely source of error that inhibits the confident analysis of the IRF beyond 35 μm. The enhanced performance of diamond microbolometer arrays will likely enable infrared cameras to image the surface of cold bodies and to capture multi-point spectral images of minerals that were previously unidentifiable, and the results are folded into the development of E-THEMIS for the *Europa Clipper*.

While E-THEMIS supports the NASA flagship-class civil science community, the small student-led spacecraft support the developing newspace community. Chapter 6 describes The Thermal-camera for Exploration, Science, and Imaging Spacecraft (THESIS)—an instrument system consisting of an infrared camera, a visible camera, and an instrument computer that was designed for the *Prox-1* microsatellite mission. *Prox*-1 was selected for the Air Force Research Laboratory's (AFRL) University Nanosatillte Program (UNP). The goal of the mission was to demonstrate proximity operations around *LightSail-B* using image-based vectors for closed-loop attitude control. The four goals of THESIS are to provide visible and infrared images that 1) verify *LightSail-B* deployment of solar sails, 2) provide images for proximity operations, 3) conduct Earth remote sensing, and 4) raise the TRL of small satellite technology for future planetary science small sat missions. Several innovations were completed to create and deliver an instrument subsystem.

Chapter 6 draws synthesis, concludes, and proposes future work.

CHAPTER 2

# THERMAL EFFUSIVITY: THE PARABOLIC THERMAL INERTIA

*"If you can't explain it simply, you don't understand it well enough" – Einstein.*

## INTRODUCTION AND BACKGROUND

In planetary science, the thermal inertia of a surface material characterizes its ability to exchange heat. In the literature, thermal inertia was sometimes refered to as the resistance of a material to change temperature; however, this definition describes the observational effect of the physical process. Both definitions, the first describing the physical process and the second describing the observational effect, are used. To first order, thermal inertia is a constant thermophysical property of a material and is defined as the square root of the produce of thermal conductivity, $k$; specific heat, c; and density, ρ. This is mathematically expressed with respective terms as $(k\rho c)^{1/2}$. Thermal inertia has the SI units of joules per square meter per kelvin per root second ($J\ m^{-2}\ K^{-1}\ s^{-1/2}$). Thermal conductivity, density, and specific heat require in-situ measurements, but these thermophysical properties are collectively inferred from orbital remote sensing. More specifically, the thermal inertia of a surface is modeled from remotely measured diurnal temperature changes. The thermal inertia of a material has far reaching scientific implications for study of the Moon, e.g. (Wesselink, 1948); the Earth, e.g.(Price, 1977); Mars e.g. (Kieffer et al., 1977); and other small bodies.

Many of the initial studies of thermal inertia were results of observations of lunar eclipses. During the lunar eclipse of June 14, 1927, Pettit and Nicholson [1930] collected temperature data of the lunar disc and calculations of the thermal inertia of the Moon agreed with Epstein [1929] from a previous eclipse (P. S. Epstein, 1929; Pettit &

Nicholson, 1930). Wesselink [1948] derived $(kc)^{1/2}$, using $c$ as the volumetric-heat capacity. The term $(kc)^{1/2}$ multiplied with the square root of the frequency of the forcing function yields $(kc)^{1/2}(\omega)^{1/2}$ with SI units of (J $m^{-2}$ $K^{-1}$ $s^{-1}$)—which may be easier to conceptualize. In order to explain the observed values of $(kc)^{1/2}$, Wesselink predicted the Moon was covered in a powder with a maximum grain size of 0.3 mm and invoked the claim of Petit and Nicholson that the Moon was void of an atmosphere. For the moon, these observations were later modeled numerically with periodic step functions e.g. (J. C. Jaeger, 1953). These investigations continue with modern spacecraft orbital observations (Paige et al., 2009).

The early lunar observations were complemented with terrestrial observations. The term $(kc)^{1/2}$, divided by a square root of 2, has been referred to as the diurnal soil conduction coefficient for studies of the Earth (Lönnqvist, 1962). Lönnqvist used terrestrial data to create a slightly more sophisticated analytical model that accounted for the asymmetry of the diurnal surface temperature (Franssila, 1936). Effects from radiative and evaporative cooling were incorporated and the solution of the heat equation was modified to a Fourier series of four harmonics derived from the corresponding harmonics for solar insolation (Franssila, 1936; Lönnqvist, 1962). Although the derivation shown later in this paper only uses the dominate first harmonic, the previous sources should be referenced to understand the details of the true asymmetry. With these models, further studies could be conducted using spacecraft data.

As infrared imagery became available on geosynchronous spacecraft, thermal inertia maps of the Earth, focusing on the arid regions of the American southwest, were produced to infer soil moisture (Price, 1977). Although Price [1977] uses the term thermal inertia, he explicitly cites Sellers [1965] for using the term “thermal property” (Sellers, 1965).

Thermal inertia has been studied in great detail on Mars. This began with the early planetary science investigations of Mariner 6 and 7 (Neugebauer, Münch, Kieffer, Chase, & Miner, 1971), Mariner 9 (Kieffer, Chase, Miner, Münch, & Neugebauer, 1973), Mars-2 and Mars-3 (Moroz & Ksanfomaliti, 1972), Mars-5 (Ksanfomaliti & Moroz, 1975), Viking (Kieffer et al., 1977), Mars-5 Phobos-2 (Kuzmin, Borozdin, & Selivanov, 1991; Selivanov et al., 1989), Mars-5, Mars Global Surveyor e.g. (Christensen et al., 2001; Jakosky et al., 2000; Mellon, Jakosky, Kieffer, & Christensen, 2000), and Mars Express (Audouard et al., 2014)). Today, the temperature of Mars was mapped down to 100 m resolution with the Thermal Emission Imaging System (THEMIS), and thermal inertia images are derived (Christensen et al., 2004; Edwards et al., 2011; Fergason, Christensen, & Kieffer, 2006a; Kieffer, 2013).

The observations show that a surface material with a higher thermal inertia was observed to have a lower diurnal temperature change. This results from a higher value for any the constituent parameters of thermal inertia: $k$, heat is conducted efficiently to underlying material; $\rho$, there is a greater density of matter to share the heat; and/or $c$, the molecular structure of the material has many degrees of freedom to store thermal energy. Conversely, a material with a low thermal inertia has a larger diurnal temperature change. It was therefore possible to infer particle size, to identify outcrops of bedrock and indurated materials, and to estimate ice content, because these geologic properties affect, in various ways, the constituent bulk factors of thermal inertia (Neugebauer et al., 1971; Nowicki & Christensen, 2007). For Mars, materials with very low thermal inertia are typically associated with unconsolidated dust e.g. (Piqueux & Christensen, 2009a). As the particle size of the material increases, the thermal inertia increases (Jakosky, 1986; Presley & Christensen, 1997b). A low thermal inertia material is sand. Higher thermal inertia materials consist of more consolidated materials

(Piqueux & Christensen, 2009b; Presley & Christensen, 1997a). In increasing order from moderate to high thermal inertia are indurated particulate material or duricrust, rocks, bedrock, and ice.

In addition to learning about the surface geology, knowledge of surface materials has many engineering implications such as choosing clear, safe landing sites and planning safe rover traverses (Fergason et al., 2006b; Golombek et al., 2005; 2012; Hamilton, Vasavada, & Sebastián, 2014). Thermal inertia maps will likely influence the landing site selection for the Mars 2020 rover.

For more reference, a thorough chapter of applications on Mars using thermal inertia can be found in the chapter *The thermal inertia of the surface of Mars* by M.T. Mellon, R.L. Fergason, and N.E. Putzig in the book *The Martian Surface: Composition, Mineralogy, and Physical Properties* edited by Jim Bell III.

## NEED, GOAL, AND OBJECTIVES

This chapter responds to a need to produce a simplified primer on the mathematics of thermal inertia. The goal was to provide readers with sufficient background to understand the fundamentals of thermal inertia and to persuade readers that thermal effusivity was a better term to define the mathematical root of a product of terms. This was pursued via accomplishing the following four objectives.

First, the mathematical derivation of thermal inertia was reproduced from first principles. The derivation of the periodic flow of heat in a semi-infinite solid was traced back at least a century. Ingersoll and Zobel [1913] present a solution with historical contexts. Other texts on heat conduction have been published and used e.g. (Houstoun, 1912; Jakob, 1967; Schneider, 1955) and the most commonly cited derivation in the planetary science literature comes from (Carslaw & Jaeger, 1959). These texts do not

explicitly define the term that was now known as thermal inertia, although it was readily recognized in their final solution.

Second, thermal effusivity was described. In other realms of science and industry, thermal inertia was often referred to as thermal effusivity. It was suggested in this work that the term thermal effusivity may be more consistent to use in planetary science, because 1) thermal effusivity was used in other fields, 2) thermal effusivity was similar to its sibling term—thermal diffusivity, and 3) the general inertia term was perhaps reserved for a different theoretical thermophysical property: the subject of the following chapter presents an alternative thermal inertia.

Third, the framework of equivalent system analogies was extended to propose that the corresponding effusivity similarly describes the ability of a potential variable to change within its respective diffusion scenario undergoing its respective periodic boundary condition.

Fourth, a general effusivity equation and a general effusion equation are proposed to synthesize the analogies.

**VARIABLES**

A area, albedo, integration constant

B damping coefficient, integration constant

C integration constant, electrical capacitance

D diffusivity

F heat flux from radiative atmosphere, Force

I thermal inertia, electrical current

J diffusion flux, current density

K hydraulic conductivity, general conductivity

L latent heat

M mass

P period, momentum

Q heat, charge

R electrical resistance

S solar insolation, specific storage, compliance

U internal energy, integration parameter

V volume, voltage

X integration by parts parameter

Y integration by parts parameter

a hydraulic viscosity

c specific heat capacity

d capacitive distance

h hydraulic head

i imaginary number, incidence angle

k thermal conductivity, spring constant

m mass

q time varying heat

r density

t time

u instantaneous internal energy

v specific volume, velocity

x displacement 1st Dimension

y displacement 2nd Dimension

z displacement 3rd Dimension, depth

$\Gamma$ general capacitance

K general conductivity

$\Phi$ heat flux, hydraulic discharge flux

$\nabla$ spatial gradient

$\Delta$ change

$\alpha$ thermal diffusivity

$\beta$ thermal skin depth

$\gamma$ integration constant

$\delta$ thermal skin depth alternate

$\epsilon$ emissivity

$\kappa$ hydraulic permeability

$\mu$ viscosity

$\nu$ kinematic viscosity

$\rho$ density

$\sigma$ Steven-Boltzman constant, electrical resistivity

$\varsigma$ general effusivity

$\tau$ shear stress

$\theta$ instantaneous temperature

$\phi$ phase angle, concentration

$\zeta$ damping coefficient

$\phi$ general amplitude for effusivity equation

$\omega$ angular frequency

## OBJECTIVE 1: DERIVE THERMAL INERTIA

### Approach Overview

The subsequent section derives thermal inertia from first principles building on previous works on heat conduction (Carslaw & Jaeger, 1959; 1986; L. R. Ingersoll & Zobel, 1913; Schneider, 1955). The roadmap is shown in *Figure 1*.

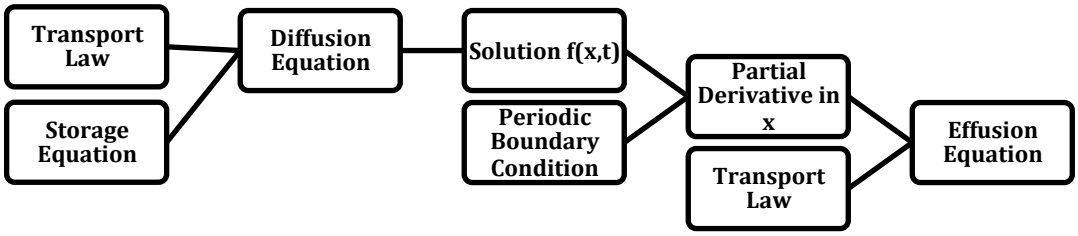


*Figure 1.* Flowchart for deriving a periodic flux equation. Starting with the diffusion equation, thermal inertia was found by 1) solving the heat equation for temperature as a function of both time and position for an instantaneous equation, 2) applying the periodic forcing function as a boundary condition, 3) taking the derivative with respect to position, and 4) substituting the result into Fourier's law in order to find a function for the instantaneous heat. Thermal inertia was recognized in this equation. Additionally, this function was then integrated with respect to time for half of the diurnal time period in order to determine the total positive heat transfer into the system.

The problem was defined using the following assumptions illustrated in *Figure 2*.

1. Consider a homogenous semi-infinite solid (e.g. planetary surface of ~10 thermal skin depths). A skin depth was the point at which the diurnal wave was attenuated to $1/e$ or ≈37%. Ten skin depths essentially attenuates the amplitude to zero.
2. At x=0, there was an interface to a free-surface (e.g. boundary of surface with atmosphere).
3. A steady, periodic forcing function applies heat to the solid at the free-surface. (e.g. the diurnal heat flux from the sun, here assumed to not change with season)
4. The system has been oscillating long enough such that there are no effects from the start up (e.g. although the system was changing throughout the day, each day will yield the same result).

**Surface boundary condition: periodic forcing function**

The boundary condition was a steady, periodic forcing function that describes the temperature at the surface. Assuming that the surface temperature can be represented by simple harmonic function, equation ( 1 ) was defined as the instantaneous temperature $\theta_i$ was equal to a cosine function of the diurnal frequency $\omega$ and time $t$, multiplied by the amplitude of the temperature change at the surface $\theta_{0_i}$, plus the average temperature at the surface $\bar{\theta}_i$. At any point along $x$, the temperature will oscillate with a decayed amplitude $\theta_x$ out of phase by some amount time $\Delta t$. The temperature was noted as $\theta$.

$$\theta_i = \theta_{0_i} \cos(\omega t) + \bar{\theta}_i \quad (1)$$

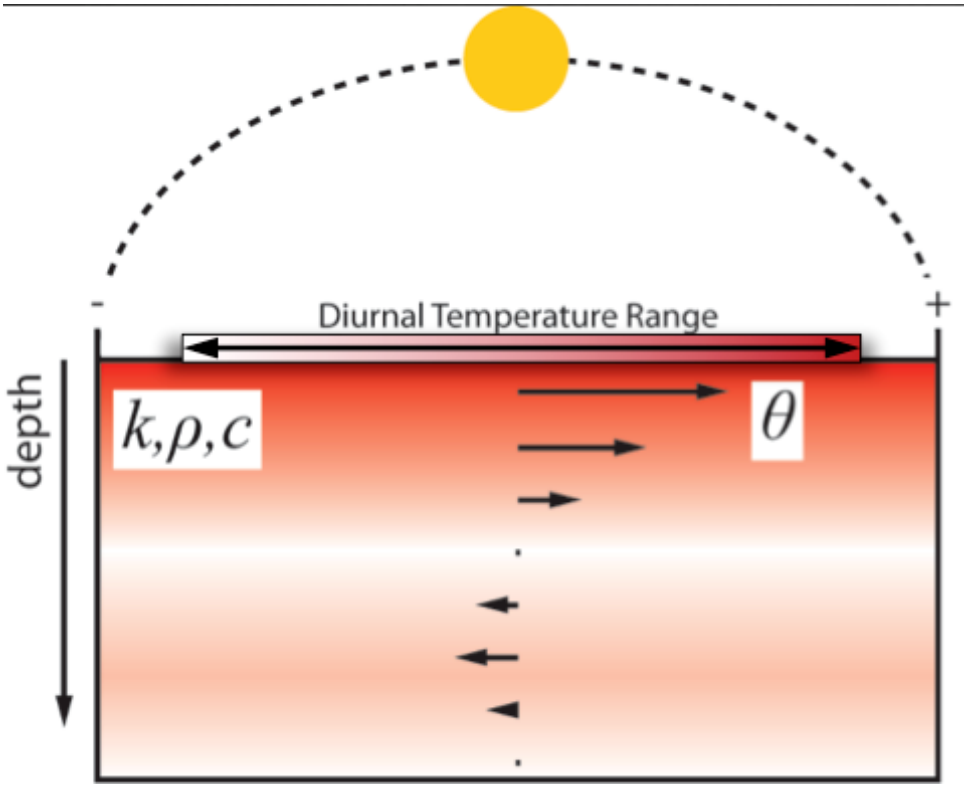


*Figure 2*. Cartoon of diurnal planetary surface heating. Solar insolation heats the surface to a higher temperature θ. The semi-infinite subsurface was characterized by k, ρ, c. A temperature wave descends through the surface with decreasing amplitude. A "cold wave" has a lower temperature that was transmitting down into the subsurface from the previous night. Eventually, the amplitude of the wave becomes zero and the subsurface at that depth reaches the average steady-state temperature.

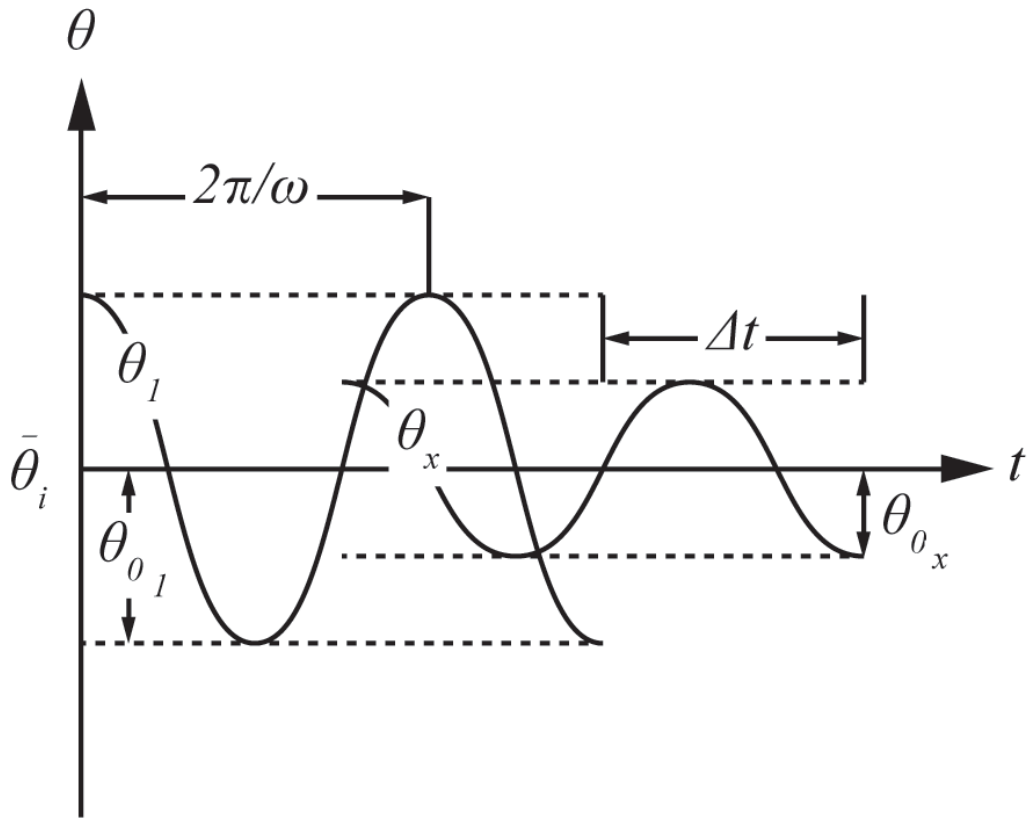


*Figure 3*. The periodic forcing function and a periodic temperature at a depth x as a function of time t. At the surface, $\boldsymbol{\theta_1}$, the amplitude of the wave has the greatest amplitude. A wave at some depth $\boldsymbol{\theta_x}$, has a smaller amplitude and was offset in phase with a lag time of $\boldsymbol{\Delta t}$. The average surface temperature was $\boldsymbol{\overline{\theta}_i}$. This was reproduced and modified from (Schneider, 1955).

## Governing equations

**Fourier's law.** The derivation begins with the theory of heat conduction described by Jean Baptiste Joseph Fourier who developed the mathematical theory of heat conduction from the somewhat unclear publications of experimental physicists Lambert, Biot, and others (as noted by (L. R. Ingersoll & Zobel, 1913)). His work culminated in the classical work *Theorie analytique de la Chaleur*. Here Fourier described that a quantity of heat $dQ$ conducted in the x-direction per quantity of time $dt$ was the product of the conducting area $A$ normal to the flow path, the temperature gradient $d\theta$ across the interval $dx$, and the thermal conductivity inherent to the material, $k$. This was the Fourier heat conduction equation in its transient form equation ( 2 ). The second law of thermodynamics supports a temperature gradient of decreasing temperature in the direction of heat flow, hence the negative sign. While this equation alone was sufficient to model heat flow for a steady state example, the change in internal energy within the volume must be considered for a transient case in the following section.

$$\frac{dQ}{dt} = -kA\frac{\partial\theta}{\partial x} \qquad (2)$$

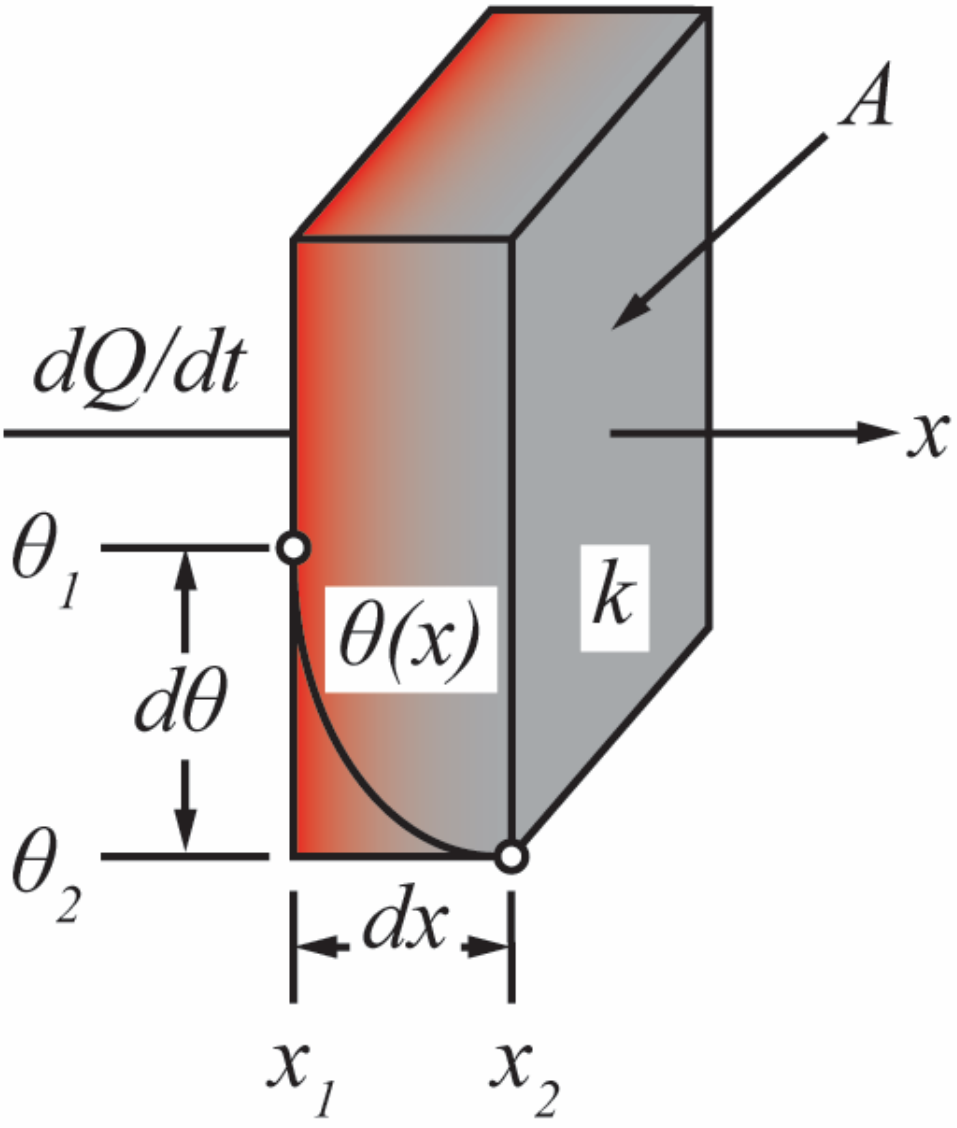


*Figure 4.* A graphical representation of Fourier heat conduction. As some amount of heat Q enters a surface with area A, the temperature θ was increased. The temperature gradient decreases to a reference temperature across some unit length. This was reproduced and modified from (Schneider, 1955).

**Heat capacity.** The heat capacity must be considered when the system was transient. The heat flowing into the system will not be equal to the heat flowing out of the system. Heat flowing into the unit volume raises the internal energy of the unit cell. In accordance with energy conservation equation ( 3 ), the difference in heat flow through the system was equal to the internal energy deposited plus any heat generated (Schneider, 1955). While there was a small amount heat generated in geologic materials via radioactive decay, here it was assumed that this was insignificant. Since there was no significant heat generated within a given material under investigation, $dQ_g$ goes to zero.

The quantity of internal energy change $dU$ was thus equal to the product of specific heat of the material, the mass, the rate of temperature change, and a quantity of time as postulated by *Joseph Black* in the late 1700's and shown in equation ( 4 ). This equation was integrated to become ( 5 ). The specific heat was the amount of heat required to raise a unit mass by a unit temperature.

If the boundary conditions are constant, then the change in internal energy will eventually become zero as the unit volume reaches equilibrium. For transient boundary conditions, such as that of a periodic forcing function, the internal energy of the unit volume will always be changing, because the temperature was changing at a varying rate.

$$dQ_{in} + dQ_g = dQ_{out} + dU \tag{3}$$

$$dU = cm\frac{\partial \theta}{\partial t}dt \tag{4}$$

$$U = cm\Delta\theta \rightarrow c = \frac{U}{m\Delta\theta} \tag{5}$$

**The heat diffusion equation.** The heat diffusion equation that describes the transient flow of heat through a conducting solid in one dimension was now derived. It was a combination of Fourier's law, equation ( 2 ); energy conservation, equation ( 3 );

and the heat capacity equation, ( 4 ). Following the derivation from (Schneider, 1955), a rectangular prism of volume $V = dxdydz$ was considered, with heat flowing into and out of the system (see *Figure 5*). To satisfy the conservation of energy, three elements are defined: the heat into the system, the change in internal energy, and the heat out of the system. The heat into the system was defined as $dQ_{in}$. For the x-direction, this was further specified as $dQ_x$ equation ( 6 ).

$$dQ_{in} = dQ_x \tag{6}$$

The addition of heat was found using Fourier's law, where heat flowing into the x-direction through an area defined by $dydz$ for a uniform material of constant conductivity $k$. This results in equation ( 7 ). The gradient was a partial derivative, because $\theta$ can also be a function of $y$ and $z$.

$$dQ_x = -dydz\left(k\frac{\partial\theta_x}{\partial x}\right)dt \tag{7}$$

The heat out of the system was defined as $dQ_{x+dx}$, but this must be defined in terms of $dQ_x$. To do this, a Taylor series expansion of the function $Q(x)$ was used with the first two terms of equation ( 8 ). Substituting equation ( 7 ) into equation ( 8 ), yields equation ( 9 ). Finally the increase of internal energy was rewritten substituting density and volume for mass.

$$dQ_{out} = dQ_{x+dx} = dQ_x + \frac{\partial Q_x}{\partial x}dx \tag{8}$$

$$dQ_{x+dx} = -dydzk\left[\left(\frac{\partial\theta_x}{\partial x}\right) + \frac{\partial}{\partial x}\left(\frac{\partial\theta_x}{\partial x}\right)dx\right]dt \tag{9}$$

$$dU = c\rho dxdydz\frac{\partial\theta}{\partial t}dt \tag{10}$$

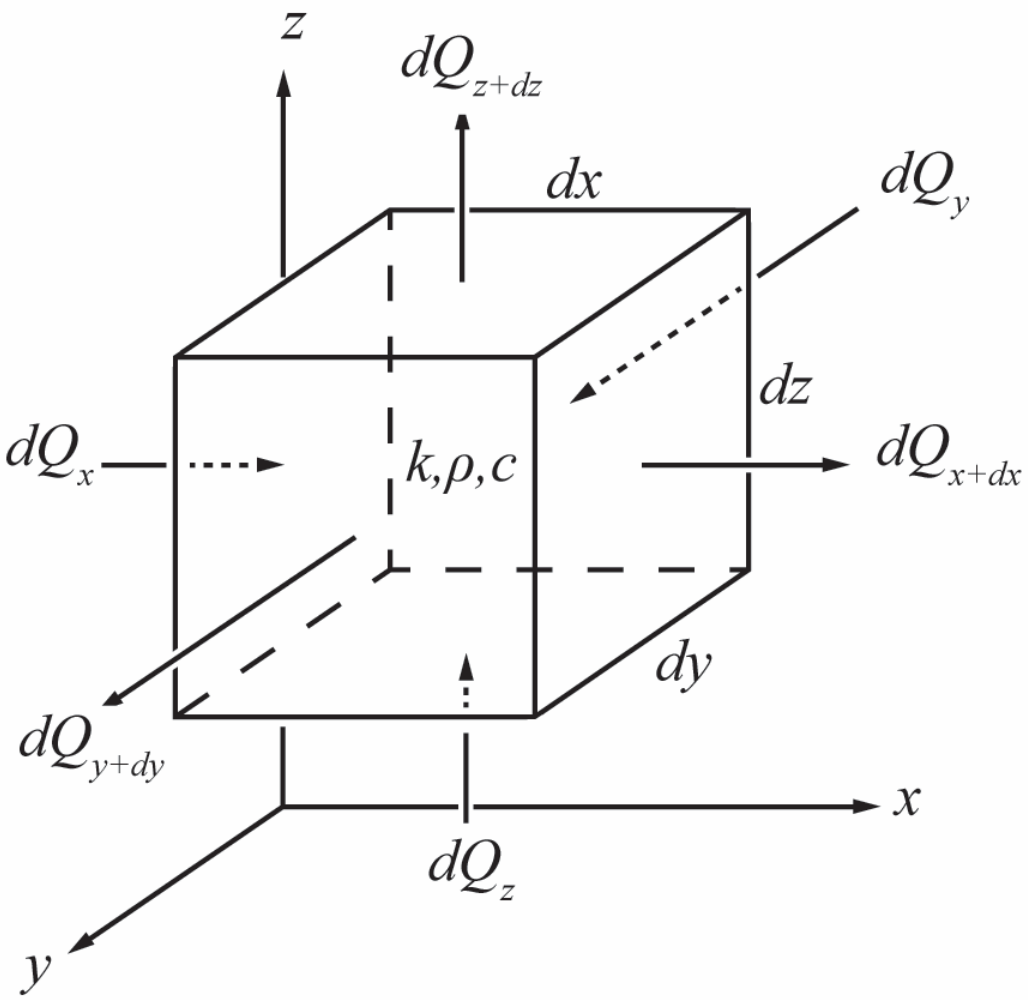


*Figure 5*. A unit cell representation of three dimensional heat flux with heat capacity. This was reproduced and modified from (Schneider, 1955).

These equations are combined to yield the total energy conservation equation ( 11 ). This was simplified to equation ( 12 ). The fundamental equation governing transfer of heat through a medium was the heat equation ( 13 ).

( 11 )

$$-dydz\left(k\frac{\partial\theta_x}{\partial x}\right)dt$$

$$= -dydzk\left[\left(\frac{\partial\theta_x}{\partial x}\right)+\frac{\partial}{\partial x}\left(\frac{\partial\theta_x}{\partial x}\right)dx\right]dt + c\rho dxdydz\frac{\partial\theta}{\partial t}dt$$

( 12 )

$$k\frac{\partial}{\partial x}\left(\frac{\partial\theta_x}{\partial x}\right) = c\rho\frac{\partial\theta}{\partial t}$$

( 13 )

$$\frac{\partial^2\theta_x}{\partial x^2} = \frac{c\rho}{k}\frac{\partial\theta}{\partial t}$$

**Thermal diffusivity.** The thermal diffusivity was defined in ( 14 ). It was a ratio of the ability of a material to conduct heat compared to the ability of a material to store heat and effectively quantifies the ability of a system to reach equilibrium. Using this definition, the heat diffusion can be rewritten.

( 14 )

$$\alpha \equiv \frac{k}{\rho c}\left[\frac{m^2}{s}\right]$$

Here the three fundamental terms found in thermal inertia are present. These three terms are as follows.

k: thermal conductivity [J $m^{-1}$ $K^{-1}$ $s^{-1}$]

ρ: density [kg $m^{-3}$]

c: thermal capacity [J $kg^{-1}$ $K^{-1}$]

Single dimension heat equation:

( 15 )

$$\frac{\partial^2\theta_x}{\partial x^2} = \frac{1}{\alpha}\frac{\partial\theta}{\partial t}$$

Three dimensional heat equation for an isotropic medium:

$$\frac{\partial^2\theta}{\partial x^2}+\frac{\partial^2\theta}{\partial y^2}+\frac{\partial^2\theta}{\partial z^2}=\frac{1}{\alpha}\frac{\partial\theta}{\partial t} \quad (16)$$

**Solving the problem**

**Solution to the heat equation.** A solution to the heat equation was presented. This was required to quantify the temperature at the surface as a function of time. Fortunately, the heat equation, as the prototypical parabolic partial differential equation, has a relatively straightforward solution. Using the separation of variables method, a function for *U(x,t)* was developed as product of two functions: the function *X* as a function of *x* and the function *Y* as a function of t. Next, ( 17 was combined with the heat equation (( 15)—where $\theta$ becomes *U*. The resulting equation (( 18) was rearranged to combine like terms.

Separation of Variables Method:

$$U(x,t)=X(x)Y(t) \quad (17)$$

Combining ( 15 ) and ( 17 ):

$$\frac{\partial^2 X(x)Y(t)}{\partial x^2}=\frac{1}{\alpha}\frac{\partial X(x)Y(t)}{\partial t} \quad (18)$$

Like terms are then combined, and these sides of the equation are set equal to a constant for integration $\gamma$ .

$$\frac{\alpha}{X(x)}\frac{\partial^2 X(x)}{\partial x^2}=\frac{1}{Y(t)}\frac{\partial Y(t)}{\partial t}=\gamma \quad (19)$$

The solutions for Y(t) and X(x) are now solved. The solution to Y(t) was one of the most basic and well-known of ordinary differential equations. Its solution was the general exponential function with amplitude $Y_o$, rate $\gamma$, and time t. The +/- in the

general solution implies that the function represents either decay or growth—this will later become a negative and represent a decay function.

Solving for Y(t):

$$\frac{1}{Y(t)}\frac{\partial Y(t)}{\partial t} = \gamma \tag{20}$$

$$\frac{\partial Y(t)}{\partial t} = \gamma * Y(t)$$

Solution for Y(t):

$$Y(t) = Y_0 e^{\pm \gamma t} \tag{21}$$

The solution for X(x) was also a well known differential equation that describes simple harmonic motion. The solution was shown in equation ( 24 ), where it can be written as either the sum of a cosine and a sine term or as an exponential.

Solving for X(x):

$$\frac{\alpha}{X(x)}\frac{\partial^2 X(x)}{\partial x^2} = \gamma \tag{22}$$

$$\frac{\partial^2 X(x)}{\partial x^2} - \frac{\gamma}{\alpha}X(x) = 0 \tag{23}$$

Solution for X(x):

$$X(x) = A\cos\left(\sqrt{\frac{\gamma}{\alpha}}x\right) \pm Bi\sin\left(\sqrt{\frac{\gamma}{\alpha}}x\right) = X_0 e^{\pm i\sqrt{\frac{\gamma}{\alpha}}x} \tag{24}$$

Now that both of these components have been solved, equations ( 21 ) and ( 24 ), simplified in exponential form i.e. ( 31 ), are combined into equation ( 17 ), which becomes equation ( 25 ).

( 25 )

$$U(x,t) = X_0 e^{\pm i\sqrt{\frac{\gamma}{\alpha}}x} Y_0 e^{\pm\alpha\gamma t} = Z_0 e^{\pm\gamma t \pm\sqrt{\frac{\gamma}{\alpha}}x}$$

Next *iω was* substituted for the integration constant γ.

( 26 )

$$\gamma \equiv \pm i\omega$$

( 27 )

$$U(x,t) = Z_0 e^{\pm i\omega t \pm\sqrt{\frac{i\omega}{\alpha}}x}$$

Equation ( 28 ) was used as an identity and ( 27 ) was rewritten in the form of equation ( 29 ). The imaginary terms are then brought together in ( 30 ).

( 28 )

$$i = \frac{1}{2}(i+1)^2$$

( 29 )

$$U(x,t) = C_0 e^{\pm i\omega t \pm (i+1)\sqrt{\frac{\omega}{2\alpha}}x}$$

( 30 )

$$U(x,t) = C_0 e^{\pm\sqrt{\frac{\omega}{2\alpha}}x \pm i\left(\omega t \pm\sqrt{\frac{\omega}{2\alpha}}x\right)}$$

The trigonometric identity of equation ( 31 ) was applied to produce ( 32 ).

( 31 )

$$e^{i\omega} = \cos(\omega) \pm i\sin(\omega)$$

( 32 )

$$U(x,t) = C_0 e^{\pm\sqrt{\frac{\omega}{2\alpha}}x}\left[\cos\left(\omega t \pm\sqrt{\frac{\omega}{2\alpha}}x\right) \pm i sin\left(\omega t \pm\sqrt{\frac{\omega}{2\alpha}}x\right)\right]$$

Because U(0,0) must be real, the sine component was eliminated—otherwise U(0,0) would be imaginary. In addition the operator in the cosine must have the same sign as before the radical. This leads to the following two set of solutions.

$$U(x,t) = C_0 e^{\sqrt{\frac{\omega}{2\alpha}}x}\left[\cos\left(\omega t + \sqrt{\frac{\omega}{2\alpha}}x\right)\right] \quad (33)$$

$$U(x,t) = C_0 e^{-\sqrt{\frac{\omega}{2\alpha}}x}\left[\cos\left(\omega t - \sqrt{\frac{\omega}{2\alpha}}x\right)\right] \quad (34)$$

Of these two equations, ( 33 ) increases exponentially with depth, whereas ( 34 ) decreases exponentially with depth. Because it was known that the temperature will decay to some average temperature with depth for a semi-infinite solid, equation ( 34 ) was selected. Furthermore, the constant $C_o$ can be replaced with the amplitude of the temperature of the forcing function wave at the surface $\theta_{0_1}$. Finally, the temperature $\theta$ must be referenced to absolute zero rather than the decay temperature, so the decaying wave solution *U(x,t)* was added with the average reference temperature $\bar{\theta}$ using ( 35 ).

Temperature Reference:

$$\theta(x,t) = U(x,t) + \bar{\theta} \quad (35)$$

Spatial-Temporal Temperature Profile:

$$\theta(x,t) = \theta_{0_1} e^{-\sqrt{\frac{\omega}{2\alpha}}x}\left[\cos\left(\omega t - \sqrt{\frac{\omega}{2\alpha}}x\right)\right] + \bar{\theta} \quad (36)$$

**Thermal skin depth.** It should be mentioned here that the thermal skin depth—the distance at which the heat decays to $e^{-1}$ or ≈ 37% of the maximum value—can be recognized in equation ( 36 ). It was the inverse of the term in the previous equation $\sqrt{\frac{\omega}{2\alpha}}$. More specifically, when *x* was equal to $\sqrt{\frac{2\alpha}{\omega}}$, then the exponent of *e* will be equal to negative one. The definition of skin depth was equation ( 37 ). Note that P was the period equal to 1 over frequency (f).

$$\delta \equiv \sqrt{\frac{2\alpha}{\omega}} = \sqrt{\frac{k}{\rho c} \cdot \frac{P}{\pi}} \quad (37)$$

**Heat flux through the surface.** Using the equation for temperature as a function of depth and time equation ( 36 ), an equation for the temperature gradient was found. Taking the derivative of equation ( 36 ) with respect to depth yields equation ( 38 ).

$$\frac{\partial \theta}{\partial x}(x,t) = \theta_{0_1}\left\{-\sqrt{\frac{\omega}{2\alpha}}e^{-\sqrt{\frac{\omega}{2\alpha}}x} * \left[\cos\left(\omega t - \sqrt{\frac{\omega}{2\alpha}}x\right)\right] + \left[\sqrt{\frac{\omega}{2\alpha}}\sin\left(\omega t - \sqrt{\frac{\omega}{2\alpha}}x\right) * e^{-\sqrt{\frac{\omega}{2\alpha}}x}\right]\right\} \quad (38)$$

The surface, $x$=$0$, was applied as a boundary condition to determine the thermal gradient at the surface.

$$\frac{\partial \theta}{\partial x}(0,t) = \theta_{0_1}\sqrt{\frac{\omega}{2\alpha}}[\sin(\omega t) - \cos(\omega t)] \quad (39)$$

Using a trigonometric identity ( 40), equation ( 39 ) was reduced to equation ( 41 ).

$$\cos(\omega t) - \sin(\omega t) = \sqrt{2}(\cos\left(\omega t + \frac{\pi}{4}\right) \quad (40)$$

$$\frac{\partial \theta}{\partial x}(0,t) = -\theta_{0_1}\sqrt{\frac{\omega}{\alpha}}(\cos\left(\omega t + \frac{\pi}{4}\right) \quad [\mathrm{K} \cdot \mathrm{m}^{-1}] \quad (41)$$

The temperature gradient at the surface was then applied to Fourier's law ( 2 ) was reproduced as ( 42). A small q was used for the notation, because it was varying in time.

$$\left(\frac{dq}{dt}\right)_{x=0} = -kA\frac{\partial\theta}{\partial x} \quad [\mathrm{J\cdot s^{-1}\ or\ W}] \tag{42}$$

$$\left(\frac{dq}{dt}\right)_{x=0} = kA\theta_{0_1}\sqrt{\frac{\omega}{\alpha}}\cos\left(\omega t + \frac{\pi}{4}\right) \quad [\mathrm{J\cdot s^{-1}\ or\ W}] \tag{43}$$

It can also be rewritten with a heat flux term.

$$\frac{dq}{dt\cdot A} = \phi_q = k\theta_{0_1}\sqrt{\frac{\omega}{\alpha}}\cos\left(\omega t + \frac{\pi}{4}\right) \quad [\mathrm{J\cdot s^{-1}\cdot m^{-2}\ or\ W\cdot m^{-2}}] \tag{44}$$

**Recognizing thermal inertia**

With an equation for heat flux at the surface (i.e. the energy with respect to time through a unit area) a few more rearrangements are made to develop the equation for the thermal inertia. Dividing out the amplitude of the temperature change in equation ( 44 ) yields equation ( 45 ).

$$\frac{(dq)_{x=0}}{dt\cdot A\cdot\theta_{0_1}} = \frac{\Phi_q}{\theta_{0_1}} = k\sqrt{\frac{\omega}{\alpha}}\cos\left(\omega t + \frac{\pi}{4}\right) \quad [\mathrm{J\cdot s^{-1}\cdot m^{-2}\cdot K^{-1}\ or\ W\cdot m^{2}\cdot K^{-1}}] \tag{45}$$

The thermophysical properties associated with thermal diffusivity are substituted.

$$\frac{dq}{dt\cdot A\cdot\theta_{0_1}} = \frac{\Phi_q}{\theta_{0_1}} = k\sqrt{\frac{\rho c\omega}{k}}\cos\left(\omega t + \frac{\pi}{4}\right) \quad [\mathrm{J\cdot s^{-1}\cdot m^{-2}\cdot K^{-1}}] \tag{46}$$

The thermal conductivity term outside of the radical was squared and brought inside of the radical.

$$\frac{dq}{dt \cdot A \cdot \theta_{0_1}} = \frac{\Phi_q}{\theta_{0_1}} = \sqrt{k\rho c}\,\sqrt{\omega}\cos\left(\omega t + \frac{\pi}{4}\right) \quad [\mathrm{J \cdot s^{-1} \cdot m^{-2} \cdot K^{-1}}] \tag{47}$$

$$\Phi_q = \theta_{0_1}\sqrt{k\rho c}\,\sqrt{\omega}\cos\left(\omega t + \frac{\pi}{4}\right) \quad [\mathrm{J \cdot s^{-1} \cdot m^{-2}}] \tag{48}$$

Equation ( 47 ) shows that the thermal energy [J] per unit area [m²] per unit temperature [K] per unit time [s], was equal to the square root of the thermal conductivity, $k$; the density, $\rho$; and the specific heat, $c$, multiplied by the square root of the frequency [$\omega$] and an oscillating cosine term with a phase shift of $\pi/4$. Thermal inertia was clearly seen as the first of three factors influencing the heat flux per unit temperature, and the inverse-root-second was a result of a multiplicative root of angular frequency term that was not considered part of the thermal inertia. Although frequency was not a thermophysical property of the material undergoing a temperature change, it does affect the temperature. For planetary science applications, the frequency of the planet's rotation was separated from thermal inertia, so that geologic materials can be compared across planets. As a further result of denying the rotation of a planet as an inherent surface property, the cosine term was not a surface property.

Adding the temperature amplitude back to the right side of the equation yields an equation for the periodic heat flux at the surface as a function of temperature in equation ( 48 ). This was an important equation that should be kept in mind as the most simplified equation to explain surface heat flux using a single harmonic forcing function. This was defined here as the effusion equation—not found elsewhere in the literature.

Taking this a step further, the *dt* term can be moved to the right side of the equation to integrate over half of the time period to find the total positive amount of energy entering and leaving the surface.

$$\frac{dq}{A} = \theta_{0_1}\sqrt{k\rho c}\,\sqrt{\omega}\cos\left(\omega t + \frac{\pi}{4}\right)\cdot dt \quad [\mathrm{J}\cdot\mathrm{m}^{-2}] \tag{49}$$

$$\int \frac{dq}{A} = \int_{-\frac{3\pi}{4\omega}}^{\frac{\pi}{4\omega}} \theta_{0_1}\sqrt{k\rho c}\,\sqrt{\omega}\cos\left(\omega t + \frac{\pi}{4}\right)\cdot \mathrm{dt} \quad [\mathrm{J}\cdot\mathrm{m}^{-2}] \tag{50}$$

$$\frac{Q_{total\_input}}{A} = \theta_{0_1}\sqrt{k\rho c}\sqrt{\omega}\cdot\left(\frac{2}{\omega}\right) \quad [\mathrm{J}\cdot\mathrm{m}^{-2}] \tag{51}$$

$$\frac{Q_{total\_input}}{A} = 2\cdot\theta_{0_1}\cdot\sqrt{k\rho c}\cdot\omega^{-1/2} \quad [\mathrm{J}\cdot\mathrm{m}^{-2}] \tag{52}$$

Assuming that the total heat input was equal to the total heat output (Schneider, 1955), the total cumulative heat transfer per unit area—input and output—is twice the input. In order to find the total absolute value of heat flowing into and out of the surface, equation ( 52 ) was multiplied by two. Also, the period was substituted for frequency as the length of a day or sol was more suitable than the rotational frequency for planetary science.

$$\frac{Q_{total}}{A} = 4\cdot\theta_{0_1}\cdot\sqrt{k\rho c}\cdot\sqrt{\frac{P}{2\pi}} \quad [\mathrm{J}\cdot\mathrm{m}^{-2}] \tag{53}$$

The above equation simplifies to the following.

$$\frac{Q_{total}}{A} = \theta_{0_1}\cdot\sqrt{k\rho c}\cdot\sqrt{\frac{8P}{\pi}} \quad [\mathrm{J}\cdot\mathrm{m}^{-2}] \tag{54}$$

Thus an equation for the total amount of heat per unit area per semi-period—the heat flux density—into and out of the surface was produced. Equation ( 54 ) was essentially composed of three factors: the amplitude of the temperature change, the thermal inertia, and the diurnal period. Where the thermal inertia was essentially a constant thermophysical property of a surface material, the period was essentially a

constant parameter of a planet's rotation, and the total integrated daily heat density ignoring solar longitude ($L_s$) was essentially a constant output from the Sun, then the amplitude of the temperature change was the dependent variable. In reality the model was more complicated. There are temperature induced variations to the thermal inertia of a material (Piqueux & Christensen, 2011), the rotation speed of planets vary on large timescales, and the solar input varies throughout the year. When the solar insolation changes across $L_s$, so too does the temperature amplitude. More complex models use higher order harmonics in order explain the asymmetry of the temperature curve at the surface i.e. (Lönnqvist, 1962). Nonetheless, for the most basic model thermal inertia can be defined in terms of the other variables as in equation ( 55 ). This shows that for the simple model described here, with a constant period and constant heat flux density, the thermal inertia was inversely proportional to the temperature amplitude.

$$\sqrt{k\rho c} = \frac{Q_{total}}{\theta_{0_1} \cdot A \cdot \sqrt{8P/\pi}} \quad [\mathrm{J \cdot m^{-2} \cdot K^{-1} \cdot s^{-1/2}}] \tag{55}$$

**Defining thermal balance on Mars**

The previously described scenario considers a steady, periodic forcing function applied to semi-infinite, homogenous surface. The case for a planetary surface was a bit more complex. The instantaneous thermal balance presented in equation ( 56 ) was well-described in the literature and presented in a number of sources e.g. (Kieffer, 2013; Mellon et al., 2000). On the left hand side was the heat lost from the surface via radiation, where $\epsilon$ was the bolometric emissivity, $\sigma$ was the Stefan-Boltzmann constant, and *T was* the temperature of the surface raised to the forth power. The right hand side consists of four terms of heat added to the surface. The first term was the solar input $S_m$, which was scaled by the albedo and the cosine of the incident angle. The second term represents the downwelling emission from the atmosphere $F_{IR}$ that was absorbed by the

surface. The third term was the latent heat of sublimation. Finally, the forth term was the heat conducted in and out of the surface.

Heat balance equation:

$$\epsilon\sigma T_s^4 = (1-A)S_m\cos(i) + F_{IR} + L\frac{\partial m}{\partial t} + k\left.\frac{\partial T}{\partial z}\right|_{z=0} \quad (56)$$

Heat loss through radiation:

$$\Phi_R = \epsilon\sigma T_S^4 \quad (57)$$

Heat input from the sun, where A was albedo:

$$\Phi_{Sun} = (1-\mathrm{A})\mathrm{S_m}\cos(\mathrm{i}) \quad (58)$$

Heat input from the radiating atmosphere:

$$\Phi_{IR} = F_{IR} \quad (59)$$

Heat input from sublimation of condensable materials:

$$\Phi_L = L\frac{\partial m}{\partial t} \quad (60)$$

Heat input from the subsurface:

$$\Phi_K = k\frac{\partial T}{\partial z} \quad (61)$$

The full equation ( 56 ) was rewritten using a non-dimensionalized value for $z$ and the skin depth (defined here as $\beta$, but called $\delta$ in ( 37 ) ) to produce ( 64 ).

$$\left.\frac{\partial T}{\partial z}\right|_{z=0} = \frac{1}{\beta}\left.\frac{\partial T}{\partial z'}\right|_{z=0} \quad (62)$$

$$\epsilon\sigma T_s^4 = (1-A)S_m\cos(i) + F_{IR} + L\frac{\partial m}{\partial t} + k\frac{1}{\beta}\left.\frac{\partial T}{\partial z'}\right|_{z=0} \quad (63)$$

$$\sigma T_s^4 = (1-A)S_m\cos(i) + F_{IR} + L\frac{\partial m}{\partial t} + \sqrt{k\rho c}\sqrt{\frac{\pi}{P}}\left.\frac{\partial T}{\partial z'}\right|_{z=0} \quad (64)$$

## OBJECTIVE 2: DESCRIBE THERMAL EFFUSIVITY

Whereas the planetary science community refers to the previously described thermophysical property as thermal inertia, much of the greater scientific community refers to this property as thermal effusivity. As an example, the C-therm TCi Thermal Conductivity Analyzer was a contact instrument used to directly measure the thermal effusivity of a material in contact using the modified transient plane source method conforming to ASTM D7984. Dr. Nancy Mathis developed this tool for her PhD dissertation in Chemical Engineering and created a company that distributes the product.

A comparison of effusivity versus diffusivity for several materials was reproduced in *Figure 6* and tabulated in the Appendix from Clemens J.M. Lasance in the magazine *Electronics Cooling*. Nov.1 2007. For most materials, the effusivity was dominated by the thermal conductivity, the effusivity scales to the square root of thermal conductivity, and the diffusivity scales linearly with thermal conductivity (see *Figure 6*).

There are three reasons why the planetary science community should consider switching to using the term thermal effusivity over thermal inertia. First, as previously mentioned, other fields of science and industry already use this term. It was consistent to adopt this term similarly to how all scientist and engineers have a common term for mass, velocity, thermal conductivity, thermal diffusivity, etc. Second, there was some

parallelism in comparing diffusivity, as the ratio of the conductivity and capacity, to effusivity, as the square of the product of the conductivity and capacity. Equation ( 48 ) was proposed here to be called the thermal effusion equation. Finally, the term inertia was reserved for mass in Newtonian mechanics and was related to inductance in the electrical analogy. Mass was not the product of the spring and dashpot coefficients; mass was a unique parameter of matter. Inductors are not composed of resistors and capacitors; inductors are unique electrical components. Therefore, it more consistent, as will be shown in the following section, to reserve the thermal inertia term for a different unique parameter as opposed to a bulk product of the thermophysical properties.

Thermal diffusivity: the ability for a material to reach thermal equilibrium.

$$\alpha \equiv \frac{k}{\rho c} \left[\frac{m^2}{s}\right]$$

Thermal effusivity: the ability for a material to exchange heat.

$$e \equiv \sqrt{k\rho c} \left[\frac{J}{m^2 \cdot K \cdot s^{0.5}}\right]$$

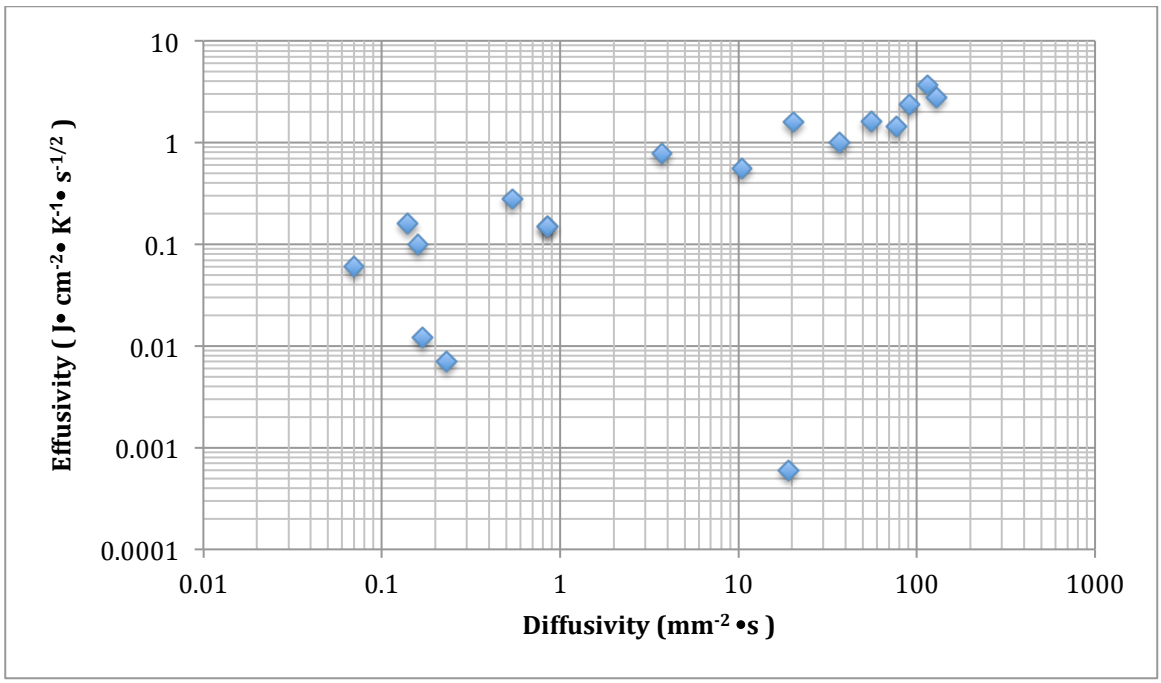


*Figure 6.* Plot of the diffusivity vs. the effusivity from the table of values in Clemens J.M. Lasance in the magazine Electronics Cooling. Nov. 1 2007. There are three outliers from the general trend. Air has a diffusivity of 19.2 $mm^{2} \cdot s^{-1}$ and was by far the furthest outlier. The other two outliers, balsa wood ( $\alpha$ = 0.17) and wool ( $\alpha$ = 0.23) have very low effusivity values, because they contain spaces that are filled with air. This makes these materials good insulators. Note: The units of effusivity are changed to $J \cdot cm^{-2} \cdot K^{-1} \cdot s^{-0.5}$.

## OBJECTIVE 3: EXTEND THE FRAMEWORK OF SYSTEM EQUIVALENT ANALOGIES

### Overview

"Still other analogies may be mentioned, and no doubt others will appear and existing ones will be greatly improved over the years." --(Schneider, 1955) pg. 357.

Analogies are often applied throughout physical concepts in order to help grasp a concept from a different vantage point. Most obvious are the similarities between the mass-spring-damper mechanical system with the capacitor-resistor-inductor circuit. Schneider devotes an entire chapter to the experimental-analogic method (Schneider, 1955). This technique was not only powerful for understanding problems, but it was a useful method for solving problems that could not be solved analytically or numerically with the computational technology of 1955. Though numerical solutions are easy to implement with today's technology, the analogies still serve the purpose of helping one to understand a problem. Parameters analogous to thermal inertia/thermal effusivity describe the effusion of molecular mass, fluid momentum, hydraulic discharge, displacement of a spring-damper, and alternating current. It was likely that many more analogies could further be described.

Each of the analogies described here begins with a transport law that describes the change in some quantity of flux with respect to distance. These equations are elliptical, steady state PDE's. Similar to Fourier's law for the conduction of thermal energy, Fick's law describes molecular diffusion; Newton's viscosity law describes shear stress in a viscous fluid, the dashpot equation describes the velocity of a damped system, Darcy's law describes the discharge rate of a hydrologic system, and Ohm's law describes the current in a circuit with a resistive element. Each of these equations was composed of

a conductivity term that describes the ease with which the principal quantity can flow through a unit volume.

A corresponding equation exists for each of these scenarios that describes the storage of each principal quantity. Similar to Joseph Black's equation for the specific heat that describes the increase in temperature with time, a simplistic definition of mass describes the increase in concentration with time, Newton's 2nd law describes the increase in velocity with time, a modified Hooke's law describes the change in spring force with time, the groundwater flow equation describes the change in head with time, and the capacitance equation describes the change in voltage with time. These equations contain a capacity term that describes the storage of the principal quantity. Through combination of the transport law and a storage equation, a corresponding diffusion equation was derived. The similarity between all of these diffusion equations was why they are commonly known as equivalent systems.

In this paper, the framework of equivalent systems was expanded to describe the similar effusivity terms. These diffusion equations of all the analogies described here are now solved using the same methodology applied to the heat diffusion equation in section 4 to derive their corresponding effusion equations with a corresponding effusivity terms. Each analogy was summarized below and detailed in Appendix A.

**Molecular diffusion**

The diffusion equation was used here in its simplest application. The diffusivity describes the concentration of molecules within a control volume. The conductivity term was called diffusivity in Fick's 1st law. For this analogy, there was no storage of molecules in space—at least within the current physical understanding, so the storage coefficient was simply one. Following the previous derivation for thermal inertia, the following equation was derived that describes the instantaneous diffusion flux. As with the

derivation for thermal inertia, the oscillating instantaneous diffusion flux was composed of the amplitude of the concentration, the square root of the diffusion, the square root of the frequency, and a cosine term. The proposed molecular effusivity was equal to the square root of the diffusion in this case. The instantaneous diffusion flux leads the concentration by $\pi/4$. This was the simplest linear case. For gases within a three dimensional control volume, Graham's law should be referenced.

$$J = \phi_{0_1}\sqrt{D}\sqrt{\omega}\cos\left(\omega t + \frac{\pi}{4}\right) \quad [\mathrm{mol}\cdot\mathrm{s}^{-1}\cdot\mathrm{m}^{-2}] \tag{65}$$

**Fluid momentum**

This analogy can be simulated with a fluid between two plates. One plate oscillates and applies a stress to the fluid which causes it to change velocity. A velocity gradient transmits through the fluid and reaches zero at the bottom plate. Newton's 2nd law was combined with Newton's law of viscosity, for an oscillating velocity boundary condition into equation ( 66 ). In this example, the fluid effusivity was proposed to equal the square root of density and viscosity. A maximum velocity of the boundary condition was the amplitude and left side of the equation was the shear stress.

$$\tau = u_{0_1}\sqrt{\rho\cdot\mu}\sqrt{\omega}\cos\left(\omega t + \frac{\pi}{4}\right) \quad [\mathrm{N}\cdot\mathrm{m}^{-2} = \mathrm{Pa}] \tag{66}$$

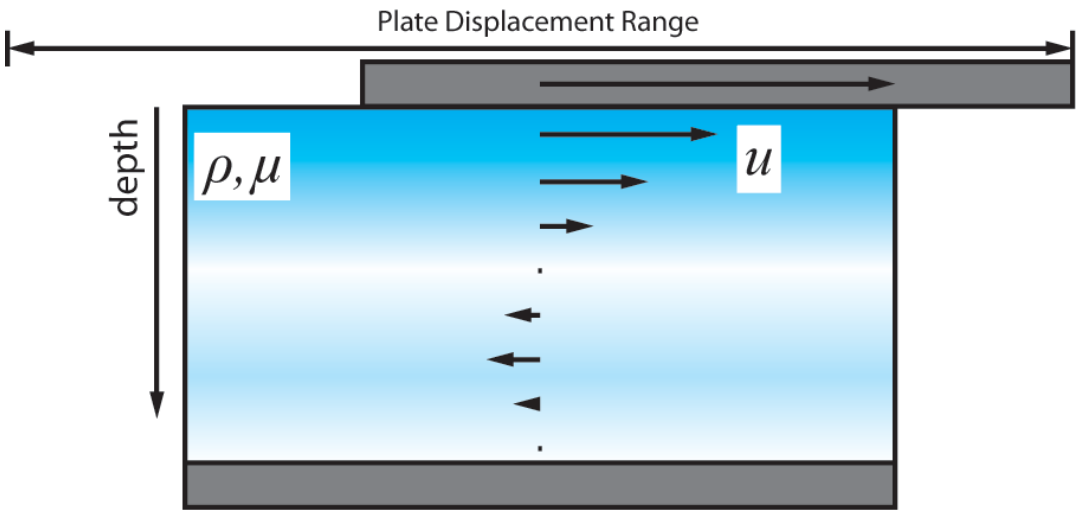


*Figure 7.* Cartoon of the velocity field of a fluid in between an oscillating plate and a semi-infinite steady state of no motion. The motion of the top plate accelerates the boundary fluid to a velocity $u$. The semi-infinite subsurface was characterized by ρ, μ. A velocity wave descends through the surface with decreasing amplitude. A "negative velocity wave" has a lower was transmitting down into the subsurface. Eventually, the amplitude of the wave becomes zero and the fluid at that depth has zero velocity.

**Groundwater flow**

The groundwater equation for the study of hydrology also provides an analogy. Electrical circuits were once used to study groundwater simulations as models of intermediate complexity—more sophisticated than analytical solutions, but more simplified than simulations via digital computer (Bouwer, 1967). Groundwater flow was also compared to heat flow. Here the hydraulic conductivity ($K$) in Darcy's law was similar to the thermal conductivity ($k$) in Fourier's law. Furthermore, the specific storage of the ground ($S_s$) in the groundwater equation was similar to the specific heat capacity ($c$). In a similar derivation, an equation for an oscillating groundwater system can be determined using a very simplistic model. This could perhaps be conceptualized as a cyclical charging (rain) and discharge (stream run-off) e.g. (Fetter, 2001).

Without any other non-cyclical sources or sinks, an oscillating head will produce the following discharge. The hydraulic effusivity was equal to the square root of the hydraulic conductivity multiplied by the specific storage.

Darcy's Law:

$$\Phi = -K\nabla h \tag{67}$$

Groundwater Flow Equation:

$$dQ = S_s \cdot v\frac{\partial \mathrm{h}}{\partial t}dt \tag{68}$$

$$\Phi = h_{0_1}\sqrt{K \cdot S_s}\sqrt{\omega}\cos\left(\omega t + \frac{\pi}{4}\right)\ [\mathrm{m} \cdot \mathrm{s}^{-1}] \tag{69}$$

**AC electrical circuit**

Electrical circuits are often used as analogies for mechanical systems and thermal systems. In this case, the current density varies an alternating voltage. Obviously, thermal conductivity was similar to electrical conductivity and thermal heat capacity was similar to electrical capacitance. Ohm specifically generated his equation as an analogy to Fourier's law. Here the proposed electrical effusivity was equal to the square root of the electrical conductivity per unit length multiplied by the capacitance per unit length. The circuit was driven with an alternating voltage source—similar to a wall outlet at 120V. This system was easily modeled with a series of resistors with parallel capacitors (*Figure 8*). Each unit cell—an RC circuit itself—becomes progressively more distant from the voltage source. Thus, the corresponding voltage amplitude was decreased and the corresponding phase was increased.

$$j = V_{0_1}\left(\frac{\sqrt{\sigma \cdot C}}{l^2}\right)\sqrt{\omega}\cos\left(\omega t + \frac{\pi}{4}\right)\ [\mathrm{A \cdot m^{-2}}] \qquad (70)$$

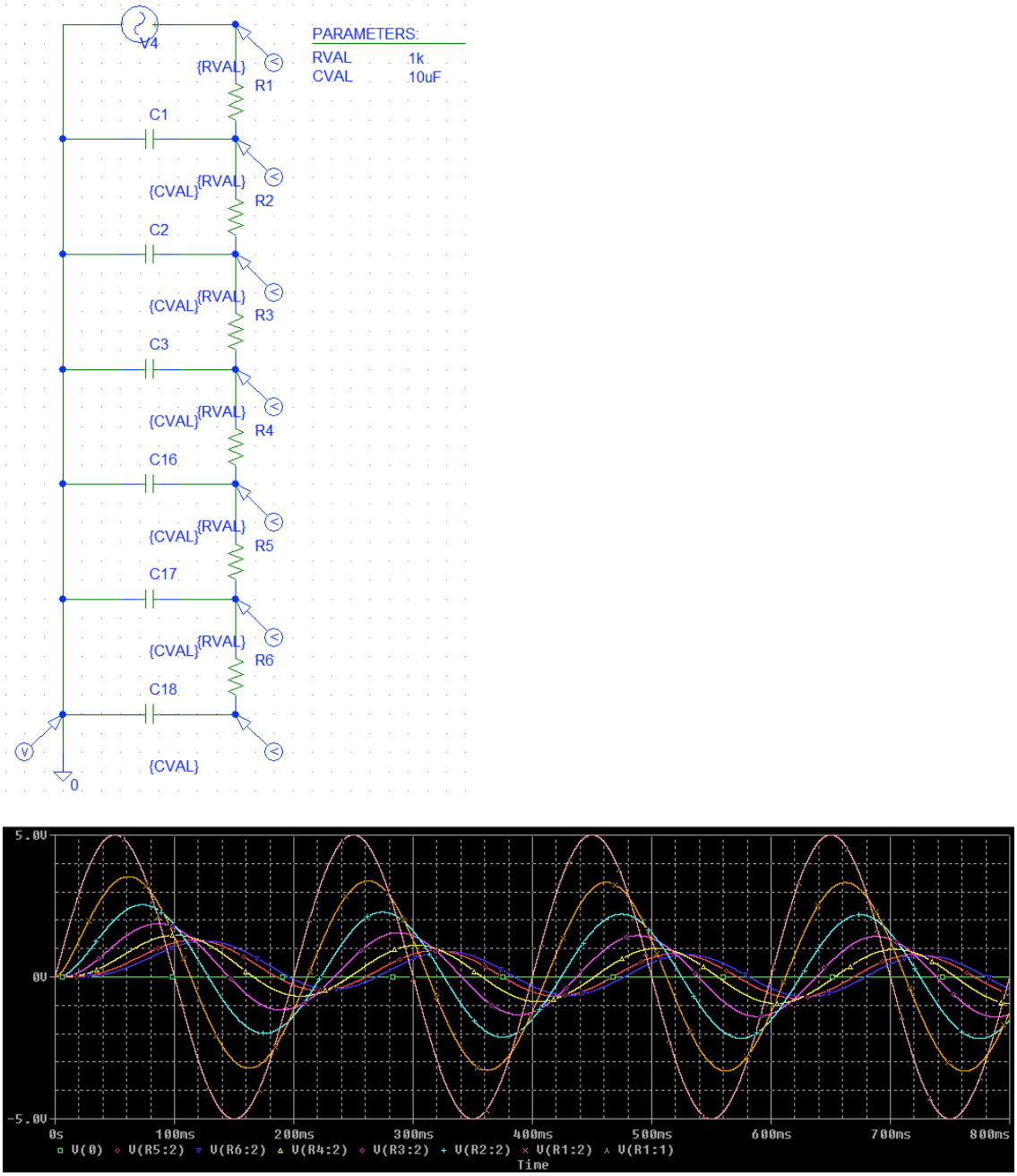


*Figure 8.* Electrical analogy created in PSPICE. The circuit was evaluated at different levels corresponding to unit cells in the thermal analogy. These nodes are represented by different colors on the left screen. Each successive unit cell has a decreased amplitude. There are four periods plotted.

**Translation**

One of the most common analogies used in system equivalence was the analogy between the mass-spring-damper problem and circuits; here the thermal system was compared to the spring-damper problem. For the storage equation, *Hooke's law* was modified by solving for $x$ and taking the derivative of both sides with respect to time. The compliance can also be used in place of the inverse spring constant. Equation ( 72 ) was in the form similar to the other storage equations.

The conductivity equation for this system was modified from the dashpot equation. The dashpot equation relates the damping ability and velocity to force. The derivative with respect to $x$ *was* taken for both of the velocity and the force. For a small section, the total dashpot coefficient must be considered per length scale. This was similar to the telegraph equation; for a long wire with a known resistance, the total resistance must be subdivided into the unit resistances. Here the same mathematical case was proposed for considering a "dashpot wire". The unit length was represented with an $l$. The derivative of velocity with respect to position was described with a capital upsilon. Also the dashpot coefficient can be replaced with its inverse term, the fluidity $\phi$. This term was normalized to the length scale when noted with a subscript.

No explicitly known examples of chains of spring-dampers are described here. Perhaps the best example was a viscoelastic material, where the spring constant and damping coefficient occur at the molecular level. Young's modulus was used in place of the spring constant and the viscosity was used in place of the damping coefficient. Many different spring damper models exist that attempt to model viscoelastic materials. This analogy, should be used with caution, but it was included nonetheless as it may help foster understanding.

Hooke's law:

$$F = k\Delta x \tag{71}$$

Modified Hooke's law:

$$dx = \frac{1}{k}\frac{\partial \mathrm{F}}{\partial t}dt \tag{72}$$

$$dx = S\frac{\partial \mathrm{F}}{\partial t}dt$$

Dashpot equation:

$$F = -Bv \tag{73}$$

Modified dashpot equation:

$$\Upsilon \equiv \frac{dv}{dx};\ \Upsilon = \frac{1}{-Bl}\nabla F \tag{74}$$

$$\Upsilon = -\phi_l \nabla F$$

$$\Upsilon = \mathrm{F}_{0_1}\left(\frac{\sqrt{\phi S}}{l^2}\right)\sqrt{\omega}\cos\left(\omega t + \frac{\pi}{4}\right)\ [\mathrm{m}^{-1}\mathrm{s}^{-1}] \tag{75}$$

## OBJECTIVE 4: PROPOSE A GENERAL EFFUSIVITY EQUATION AND GENERAL EFFUSION EQUATION

The derivations for thermal inertia and many similar analogies are now collectively classified. A general effusivity ($\varsigma$) term was proposed that was the square root of the conductivity term and the storage capacity term. Capital kappa was chosen as the general term for conductivity as many of the equivalent systems use a *k* for conductivity and there are not many terms that use kappa. Capital gamma was chosen for the capacity term as the letter *c* and the lower case gamma are widely used. A general effusion equation was developed that contains the amplitude of the potential term, the effusivity,

the square root of the frequency, and a cosine term that was leading by $\pi/4$. Though the frequency could be included in the effusivity for the units to become more sensible, the frequency does not describe the physical properties of the system; it describes the environment. The general effusivity equation and its corresponding general effusion equation are presented in equations ( 76 ) and ( 77 ).

General effusivity equation:

$$\varsigma_{Effusivity} \equiv \sqrt{K_{Conductivity} \cdot \Gamma_{Storage\ Capacity}} \tag{76}$$

General effusion equation:

$$\Phi_{Principal\ Flux} = \psi_{Potential\ Amplitude_{x=0}}\, \varsigma_{Effusivity} \cdot \sqrt{\omega} \cos\left(\omega t + \frac{\pi}{4}\right) \tag{77}$$

## CONCLUSIONS AND FUTURE WORK

The first goal of this paper was to familiarize the reader with the mathematics of thermal inertia through both analytical derivation and analogies. Thermal inertia was the square root of the product of thermal conductivity, density, and specific heat, because the square root was a mathematical result of solving the heat equation. Thermal inertia was a coefficient along with a coefficient for the temperature amplitude and the root frequency that describes the ability for heat to be exchanged through a material under a transient forcing function. Thermal flux and period being held equal, the temperature amplitude was inversely proportional to the thermal inertia for the simplest model of a single harmonic forcing function. The root of the frequency was typically excluded from the physical surface properties that define thermal inertia, but when combined, the two root seconds multiply to become a second. Analogies are presented of various similar diffusion scenarios. Extending the framework of equivalent systems, one must only switch out the variables for the corresponding system to understand how systems

governed by a conductive and a capacitive property behave when excited by a periodic forcing function.

The second goal of this paper was to persuade the reader that thermal inertia was thermal effusivity and fits within the general effusion equation proposed here. Thermal effusivity was already used in other fields of science and industry and was more consistent with thermal diffusivity. Furthermore, within the framework of system equivalence, inertia may be an entirely different parameter. The obvious question that arises when thinking about the electrical system was what would be the equivalent thermal term that represents inductance—which has equivalence to mass in the mass-spring-damper problem. If the *inertial* component was missing from these analogies it may give us pause to wonder if we are missing the *thermal inertia* component from our derivation. Perhaps *thermal inertia* was a different property all-together similar to mechanical mass or electrical inductance (Bouwer, 1967). This was the subject of the next chapter.

For now, the mathematical framework constructed here and the context of the greater scientific community and industry lead the author to suggest that the planetary science community ought to consider and to implement the term thermal effusivity when referring to the square root of the product of the thermal conductivity, the specific heat capacity, and the density. As an example of this utility, the knowledge that chemists measure the thermal effusivity of powders that are lithified into vitamins, may provide planetary scientists with new methods of experimentation and new innovations to study how mixtures of dust and sand become high thermal effusivity duststone and sandstone on the Moon, Earth, Mars, and other planetary bodies.

CHAPTER 3

# THERMAL INDUCTANCE: THE HYPERBOLIC THERMAL INERTIA

*I have done a terrible thing. I have postulated a particle that cannot be detected.* - *Wolfgang Pauli 1930.*

## INTRODUCTION

Thermal inertia was an important parameter for inferring thermophysical properties of planetary surfaces from orbit e.g. (Kieffer, 2013). In the planetary science literature, thermal inertia was defined as the square root of the thermal conductivity, density, and heat capacity. The derivation of thermal inertia was recently reviewed (Veto & Christensen, 2015). Other fields of science and industry often refer to this term as thermal effusivity, and it was suggested that the latter term be adopted in planetary science to refer to the mathematical definition. It may yet be appropriate to reserve the term thermal inertia for a general observation of heat lag that was equal to the thermal effusivity in the common planetary application. A framework of system equivalence was extended to propose similar terms of effusivity after reconstructing the similar conductivity and capacity terms. Thermal conductivity ($k$) was analogous to electrical conductivity ($\sigma$ or inverse resistance $1/R$); thermal heat capacity ($c$) was analogous to electrical capacitance ($C$). An obvious hole in the analogy was the thermal equivalent to electrical inductance ($L$) or mechanical inertia/mass ($m$).

This paper explores the thermal analogue to the Inductor-Resistor-Capacitor (LRC) circuit and the mass-spring-damper mechanical system. This was achieved with the addition of a thermal delay component initially called the thermal inductance i.e.(Bosworth, 1946)—though tangentially using the term to refer the phenomenon of

heat convection. This theoretical thermal equivalent parameter of heat conduction was used to explain the so-called non-Fourier heating which describes delayed conduction of heat as a wave. The phenomenon, mathematically postulated as early as James Clerk Maxwell (Maxwell, 1867), now attempts to reconcile the fact that heat cannot propagate at an infinite speed—as would be the case in the parabolic Fourier equation. Instead, heat behaves more like a wave with a finite propagation speed, not to exceed the speed of light. Though heat cannot conduct faster than light, heat was almost always assumed to instantly diffuse for most practical transient experiences according to the parabolic diffusion equation. This may be similar to the overwhelming majority of life experiences in which the omnipresent effects of general and special relativity are ignored in Newtonian mechanics.

Within the heat transfer literature, there are many scientists who have tried to either measure the effects or postulate the theory of thermal inductance. Maxwell even noted the term, but he ruled it out as heat conduction onsets so quickly that the term was ignored. A variety of experiments have attempted to measure this effect in the past hundred years with questionable repeatability and acceptance. Philosophical arguments contend that the updated equations are necessary; Fourier heat theory was used nearly unanimously and technically allows for instantaneous transfer of heat, but clearly heat itself cannot be transferred across space faster than light. If thermal inductance was real, then to only equate the thermal inertia with the thermal effusivity may be analogous to ignoring the induction of wires in a telegraph line, only considering the resistor-capacitor or to ignoring the mass of a car in designing a suspension system, considering only the spring constant and the shock resistance. Although the massless spring and the inductionless wire assumptions are valid in many problems, they fail in others.

This paper responds to a need to develop and to test hypotheses involving heat transfer within planetary science. The goal was to further develop heat transfer theory for models that may further elucidate the nature of planetary surfaces. This was attempted by deriving the relativistic thermal effusivity as a combination of the thermal effusivity and thermal inductance and creating a simple thermal model that shows the deviation of the proposed hyperbolic heat transfer from the contemporary parabolic heat transfer. A few terms and equations are presented as necessary background first.

## VARIABLES

A area, albedo, integration constant

B damping coefficient, integration constant

C integration constant, electrical capacitance

D diffusivity

F heat flux from radiative atmosphere, Force

I thermal inertia, electrical current

J diffusion flux, current density

K hydraulic conductivity, general conductivity

L latent heat, inductance

M mass

P period, momentum

Q heat, charge

R electrical resistance

S solar insolation, specific storage, compliance

U internal energy, integration parameter

V volume, voltage

X integration by parts parameter

Y integration by parts parameter

a hydraulic viscosity

c specific heat

d capacitive distance

h hydraulic head

i imaginary number, incidence angle

k thermal conductivity, spring constant

m mass

q time varying heat

r density

t time

u instantaneous internal energy

v specific volume, velocity

x displacement 1st Dimension

y displacement 2nd Dimension

z displacement 3rd Dimension, depth

Γ general capacitance

K general conductivity

Φ heat flux, hydraulic discharge flux

∇ spatial gradient

Δ change

α thermal diffusivity

β thermal skin depth

γ integration constant

δ thermal skin depth alternate

e emissivity

κ hydraulic permeability

μ viscosity

ν kinematic viscosity

ρ density

σ Steven-Boltzman constant, electrical resistivity

ς general effusivity

τ shear stress

θ instantaneous temperature

ϕ phase angle, concentration

ζ damping coefficient

ψ general amplitude for effusivity equation

ω angular frequenc

## BACKGROUND

### Thermal diffusivity

The thermal diffusivity is defined as the ratio of the thermal conductivity over the heat capacity. As the diffusivity is part of the heat diffusion equation, it can be thought of as the parameter that describes how quickly an unbalanced system reaches thermal equilibrium.

$$\alpha \equiv \frac{k}{\rho c} \left[\frac{m^2}{s}\right] \quad (78)$$

**Thermal effusivity**

Thermal effusivity was equated with thermal inertia in planetary science. Thermal inertia is often defined as the resistance of a surface to change temperature. In other fields of science and industry, thermal effusivity, being the square root of the product of thermal conductivity, density, and specific heat, is a definition for how well a material is able to transfer heat. Thermal effusivity is used in the pharmaceutical industry to quantify the mixing of drugs and used in textile industry to quantify the thermal utility of clothing. The everyday common effect of thermal effusivity is that metals feel cold at room temperature while insulated materials (e.g. wool) do not feel cold to the touch. A commercial tool exists to directly measure the thermal effusivity of a material. Dr. Nancy Mathis developed the TCi thermal conductivity sensor for her PhD thesis, and this device is used throughout various industries. Thermal conductivity is typically the most variable parameter within thermal effusivity in both household materials and martian surface materials (Piqueux & Christensen, 2009a). Realizing that thermal effusivity is a common thermal property in material science may help planetary scientists to advance their understanding of the property in laboratory experiments.

$$\boldsymbol{I = e \equiv \sqrt{k\rho c}} \quad [\, J \cdot m^{-2} \cdot K^{-1} \cdot s^{-0.5} \,] \tag{79}$$

**Parabolic heat equation:**

The parabolic nature of heat propagation is a result of Fourier's Law ( 80 ) which was derived from Newton's law of cooling (Fourier Joseph, 1822; Newton, 1701). The heat flow, or power ($dQ/dt$), is equal to the thermal conductivity ($k$) multiplied by the temperature gradient ($\nabla\theta$) and cross-sectional area $A$. Fourier's Law was combined with Black's equation for heat capacity ( 81 ) to derive the heat diffusion equation ( 82 ) [Black 1786]. Note that mass is density ($\rho$) multiplied with specific volume ($\upsilon$).

$$\frac{dQ}{dt} = -kA\nabla\theta \quad [J \cdot s^{-1} \; or \; W] \tag{80}$$

$$dQ = c\rho \cdot \nu \frac{\partial\theta}{\partial t} dt \;\; [\mathrm{J}] \tag{81}$$

$$\frac{\partial\theta}{\partial t} = \alpha\nabla^2\theta \tag{82}$$

**Non-Fourier effects of the parabolic equation:**

As a parabolic equation, the heat diffusion equation implies that all points within the domain instantaneously affect all other points within the domain. This physically implies that a heat source at one end a system will be instantly felt at the other end of the system. See the appendix. However, as Kranys notes, this contradicts Einstein's relativity as heat would travel faster than light—heat must have a finite propagation speed and travel as a wave (Kranyš, 1967; Maxwell, 1867).

Though not knowing the relativistic implications, Maxwell was the first to derive an equation that included a time derivative of heat. However, he zeroed out the term stating, "The first term of the equation may be neglected, as the rate of conduction will rapidly establish itself." For most practical applications Maxwell's assumption holds true, but eighty years later Peshkov claimed to have measured the velocity of a temperature wave in helium II to be 19 m/s at 1.4 K, providing the need to revisit this term (Peshkov, 1944). Later, Baumeister states, "Normally, the diffusivity is 10 orders of magnitude less than $C^2$." *C* is the speed of heat propagation; *C was* squared in this quote. "However, at very low temperatures or very short timescales, the effect of the finite propagation speed could be come important," he concludes (Baumeister & Hamill, 1969). It is possible that there is a third case existing outside of laboratory experiments: very large length scales. In these conditions, an "undisturbed region" of space has not been

affected by the heat wave traveling with a finite speed (*Figure 9*). The thermal wave produces a “thermal wake region”. The wavefront discontinuity has decreasing amplitude with time.

**The Cattaneo and Vernotte (C-V) equation:**

To account for the delay in heat conduction and reconcile the impossibility of instantaneous heat propagation, Cattaneo and Vernotte independently modified the Fourier equation (Cattaneo, 1958; Vernotte, 1958). A relaxation time ($\tau$), is equal to the diffusivity divided by the thermal wave speed ($C_{II}$). The speed of thermal wave is also referred to as the second sound speed (Chester, 1963; Peshkov, 1944).

Cattaneo and Vernotte equation:

$$\Phi + \tau \frac{\partial \Phi}{\partial t} = -k \nabla \theta \ [\mathrm{J \cdot s^{-1}} \text{ or } \mathrm{W}] \qquad (83)$$

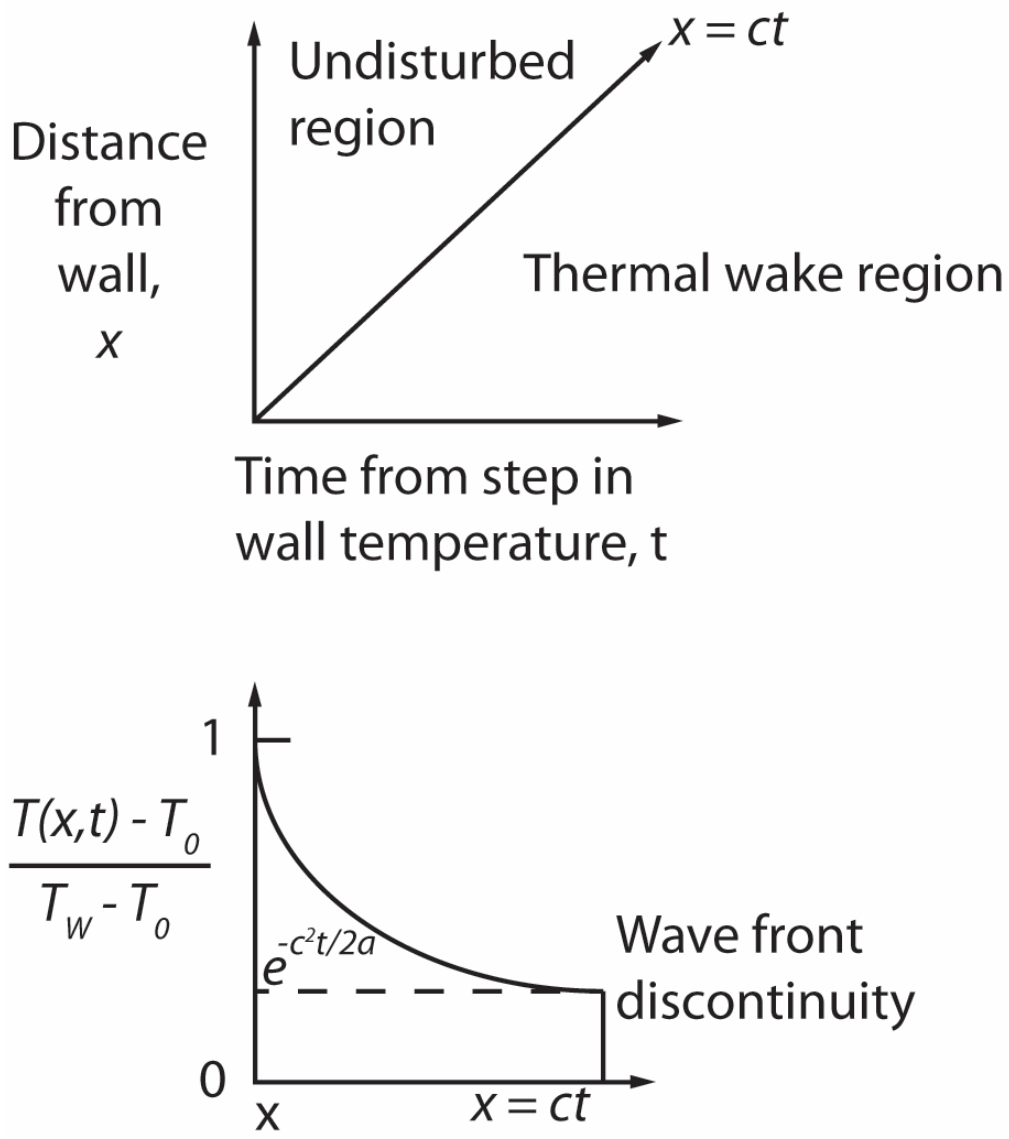


*Figure 9.* Hyperbolic heat wave depiction. Top) As a heat wave travels a distance *x* with time *t*, the region affected by the heat wave grows. Bottom) The temperature profile of a thermal wave. $T_w$ is the final wall temperature and $T_o$ is the temperature at infinity. The y-axis was normalized from zero to one. The wavefront travels a distance *x* equal to the wave speed *c* multiplied by time *t*. The discontinuity was equal to an exponential function. This was found by substituting $x = ct$ into the equation $T(x,t)$ i.e. $T(ct,t)$ and equation 24 of (Baumeister & Hamill, 1969) These plots are reproduced and modified from (Baumeister & Hamill, 1969).

**Hyperbolic heat equation:**

Combining the C-V equation with Black's equation produces a hyperbolic heat diffusion equation ( 84 ). The C-V equation then takes on the form of the telegrapher's equation. Both equations are hyperbolic partial differential equations. In a hyperbolic equation, a point does not instantaneously influence all other points in space as there was some limiting velocity of the information. A summary of the different classes of partial differential equations was presented in the appendix.

Hyperbolic heat equation:

$$c_p\rho\left(\frac{\partial\theta}{\partial t}+\tau\frac{\partial^2\theta}{\partial t^2}\right)=k\nabla^2\theta \qquad (84)$$

$$\frac{\partial\theta}{\partial t}+\tau\frac{\partial^2\theta}{\partial t^2}=\alpha\nabla^2\theta$$

$$\frac{\partial\theta}{\partial t}+\tau\frac{\partial^2\theta}{\partial t^2}=\frac{k}{\rho c}\nabla^2\theta$$

The hyperbolic heat equation was commonly compared to the telegraph equation that was used to quantify the voltage in telegraph lines equation ( 85 ) e.g. (Hong, Su, Chou, & Hung, 2011). Rearranging the telegraph equation to look more like the hyperbolic heat diffusion equation and substituting electrical conductance for the reciprocal of electrical resistance, an equation results that shows the analogy of the thermal time constant to the electrical inductance. The thermal time constant was analogous to the inductive term multiplied by the conductive term. The circuit representation of the hyperbolic heat equation was shown in *Figure 10*.

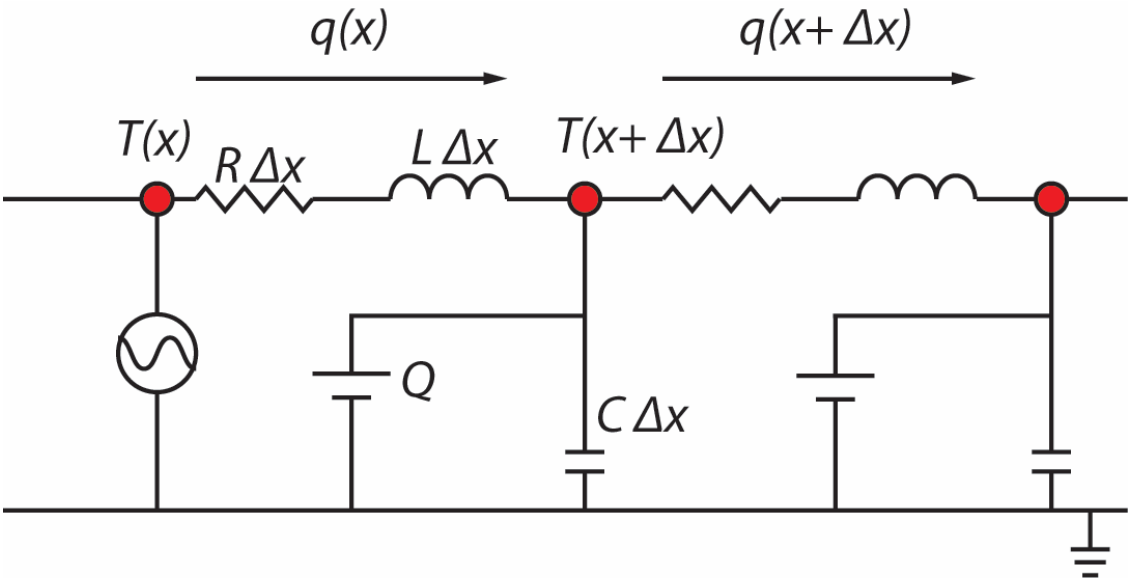


*Figure 10*. Hyperbolic thermal model represented as the analogous electrical circuit. A periodic, alternating current provides the surface boundary condition. Along each element, heat flow first conducts to the next element. In the hyperbolic model, there was some inertia to the heat flow modeled as an inductor. Each of the elements also holds some amount of charge/temperature modeled with the capacitor that does not pass to the next node. Finally, it was possible that there was some heat generated within each cell modeled as the DC battery term *Q*—though for our model this endogenic heating was assumed to be zero. The present modeling of heat transfer in a planetary surface does not account for thermal inductance/inertia and ignores internal heat generation. This figure was reproduced and modified from (Hong et al., 2011).

Telegraph equation:

$$\frac{\partial V}{\partial t} + \frac{L_l}{R_l}\frac{\partial^2 V}{\partial t^2} = \frac{1}{R_l C_l}\nabla^2 V \tag{85}$$

$$\frac{\partial V}{\partial t} + L_l \cdot \sigma_l \frac{\partial^2 V}{\partial t^2} = \frac{\sigma_l}{C_l}\nabla^2 V$$

**Definition of the delay constant**

Following Kaminski, there are three questions that must be addressed to describe this new constant (Kaminski, 1990). What was the physical meaning of $\tau$? What was the methods of experimental determination of $\tau$? When should the hyperbolic equation instead of the parabolic equation be used?

Using the thermo-electrical analogy, the thermal time constant $\tau$ was equal to the thermal inductance divided by the thermal resistance (Hong et al., 2011; Joseph & Preziosi, 1989). It was defined as the time needed to accumulate sufficient energy to propagate transfer to the next element. In a homogenous material it was suggested that this time depends on the interaction at the molecular or crystal structure level whereas for nonhomogeneous materials this was "at a different level and may take much greater value" (Kaminski, 1990).

Since *Peshkov* determined the second sound speed of helium II, many investigators have attempted to measure the second sound and relaxation time in gases, solids, liquids, and porous material. For the semi-infinite body, *Baumeister* calculated a theoretical value for $\tau$ based upon the second sound speed (Baumeister & Hamill, 1969). *Kaminski* describes an experimental apparatus to measure $\tau$. More recently *Roetzel et al.* provide a summary and commentary on these experiments noting their difficulty and potential for error (Roetzel, Putra, & Das, 2003). In their own experiments on non-homogenous materials, they found values for $\tau$ as a function of three material types,

pressure, temperature, and particle size. They determined a value of $\tau$ to be 2.26 seconds for synthetic sand with air as the pore filling gas at 1 bar with an average temperature inferred to be ~25°C. Furthermore, they show that the diffusivity varies strongly with gas pressure and weakly with temperature as was known in the planetary literature e.g. (Piqueux & Christensen, 2011). For synthetic sand, the relaxation time varies weakly with both pressure and temperature for Ar and $N_2$ gas. Helium gas however introduces strong variations as the pressure changes.

**Thermal inductance**

Mathematical analogies have significantly advanced our understanding of the physical world e.g. Ohm's Law as an analogy of Fourier's Law (Narasimhan, 1999; Ohm, 1827). More recently, contemporary scientists have searched for a thermal inductance term equivalent to an electrical inductance e.g. (Bosworth, 1946; Hong et al., 2011). Some researchers define the thermal inductance as related to energy stored in convective currents for fluids (Bosworth, 1946). For solids or non-homogenous mixtures of particles and atmosphere, the subject of this paper, thermal inductance was described as a measure of the interaction of the interior structure of a material in unsteady heat transfer processes (Kaminski, 1990). A review of the thermal literature shows that hundreds of investigators have look for a similar, but related, term: the thermal relaxation time ($\tau$). An annotated bibliography of the literature on heat waves and the relaxation time was presented by Joseph and Preziosi that accounts for the period 1867-1989 (Joseph & Preziosi, 1989). Though the interpretation and measurement of this term was still debatable, as of this writing, the seminal works (Cattaneo, 1958) and (Vernotte, 1958) have been cited 1065 and 926 times respectively (Google Scholar May 2018). Thermal inertia seems to be used as a general measure of transient temperature lag, and thermal inductance was invoked as a mathematical quantity to describe the observation

(Baumeister & Hamill, 1969; Hong et al., 2011; Kaminski, 1990); their definition used here was shown in ( 86 ). Either thermal inertia—synonymous with inductance—is mutually exclusive from the definition used in planetary science, or the thermal effusivity was the mathematical representation of the observed thermal inertia of a planetary surface. If thermal inductance is a real property of materials, then it must be added to either an expanded thermal effusivity definition or combined with the standard thermal effusivity into a greater representation of the observed thermal inertia. A diagram mapping the definition of the terms was presented in *Figure 11*.

Thermal inductance:

$$L_T = \frac{\tau}{k} = \frac{1}{\rho c \cdot {C_{II}}^2} \left[K \cdot m \cdot s^2 \cdot J^{-1}\right] \quad (86)$$

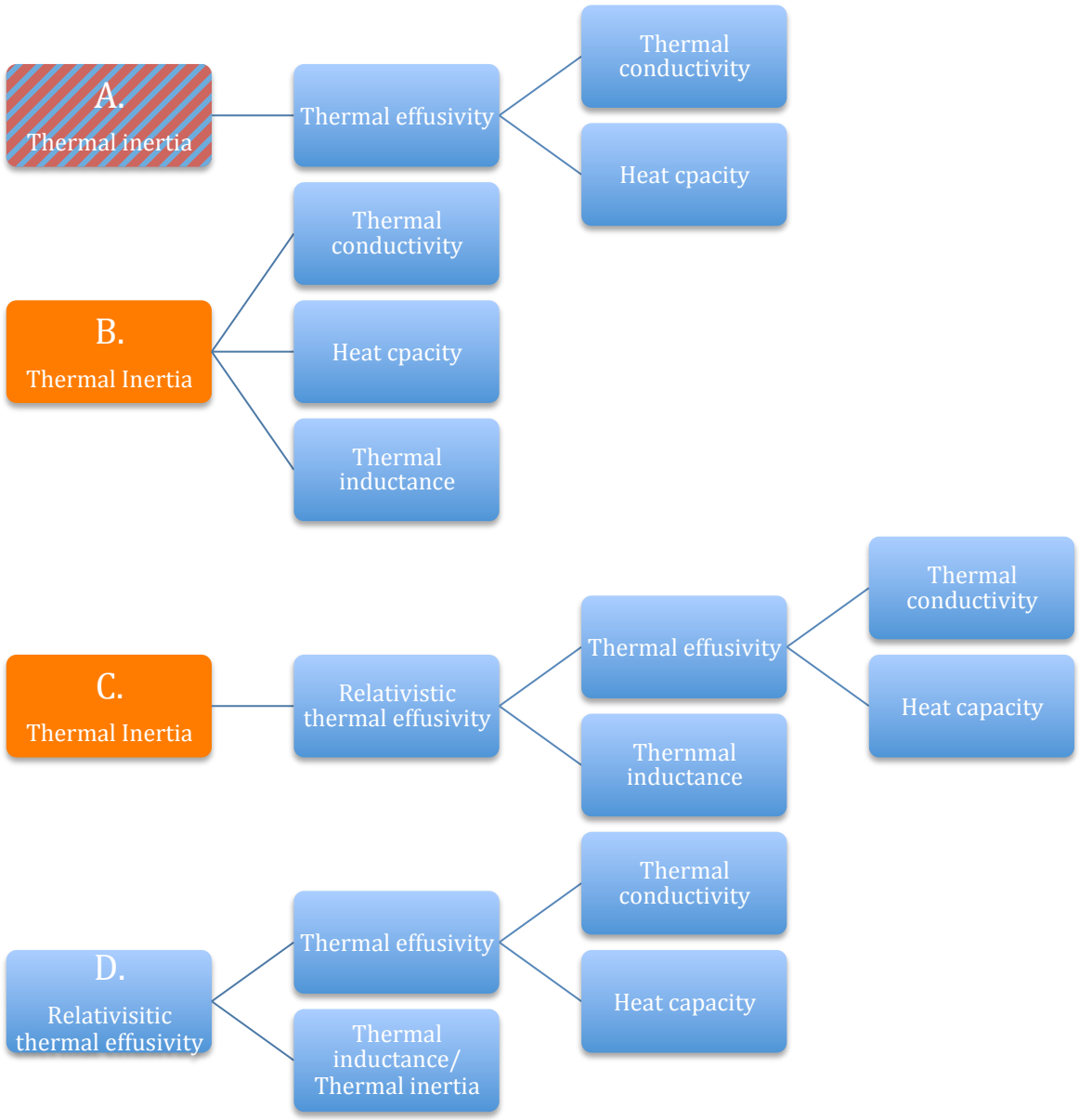


*Figure 11*. Various conventions to describe the defining terms. Blue boxes are physical properties or mathematical definitions. Orange boxes are observations or general terms that are further explained via properties or equations. A) The current definition used in planetary science. The thermal inertia is equal to the thermal effusivity. Thermal inertia can be both the general observation explained by the thermal effusivity or the commonly used equation in place of thermal effusivity. B) One definition inferred here from the

heat transfer literature. The thermal inertia is the observed delay of heat transfer from a combination of all of the thermal properties. C) The thermal inertia used in this paper. Thermal inertia is a general observation of a relativistic thermal effusivity undergoing a periodic forcing function. D) An alternate scheme for the derivations proposed here. The thermal inductance and the thermal inertia describe the same term that was under investigation, because inertia also describes the real quantity of mass (Joseph & Preziosi, 1989).Combined with the effusivity terms, thermal inertia/thermal inductance produces a relativistic thermal effusivity.

## APPROACH

The paper accomplished the following objectives.

1. Derive the relativistic thermal effusivity.
2. Test and or quantify the effects of relativistic thermal inertia in planetary science.

The thermal system was compared to the electrical system. The equivalent parabolic electrical system was augmented from the RC circuit to the hyperbolic LRC telegrapher's equation. The corresponding thermal equation was the hyperbolic heat diffusion equation derived from the C-V equation. Terms are manipulated, until an equivalent to electrical inductance was found in the augmented thermal heat equation. This term was referred to in literature as thermal inductance.

If a relaxation time was significant for the diurnal heat of a planetary surface, then an equation must be determined that defines a relativistic thermal effusivity to reconcile the relativistic propagation of heat. Previous derivations for the parabolic heat equation e.g. (Veto & Christensen, 2015) with (Carslaw & Jaeger, 1959; L. R. Ingersoll & Zobel, 1913; Kieffer, 2013; Schneider, 1955; Wesselink, 1948) are modified with hyperbolic derivations i.e. (Roetzel et al., 2003) to produce an equation for the hyperbolic heat flux at the surface was found. As $\tau$=0, this becomes the parabolic equation (Eq. 64).

### OBJECTIVE 1: DERIVE THE RELATIVISTIC THERMAL EFFUSIVITY

This section was broken into two parts. First a solution was found to the hyperbolic heat diffusion equation. Most of this work was transcribed from (Roetzel et al., 2003), who found a solution to use in their experimental analysis. In the second section, previous methods used to derive the thermal effusivity are applied to the hyperbolic heat equation in order to determine an upgraded relativistic thermal effusivity (Carslaw & Jaeger, 1965; Schneider, 1955; Veto & Christensen, 2015).

**Solve the hyperbolic heat diffusion equation.**

The hyperbolic heat equation was solved using the separation of variables method. The following steps are reproduced from (Roetzel et al., 2003) using his notation. Using the separation of variables method, the spatial and temporal components of U(x,t) are broken apart.

$$U(x,t) = X(x)Y(t) \quad (87)$$

$$Y(t) = e^{i\omega t} \quad (88)$$

$$X(x) = \xi(x) \quad (89)$$

$$U(x,t) = \xi(x) * e^{i\omega t} \quad (90)$$

After setting the integration constant equal to temperature, derivatives of this equation are taken and substituted into the hyperbolic diffusion equation.

$$\theta(x,t) = \xi(x) * e^{i\omega t} \quad (91)$$

First derivative with respect to t:

$$\frac{\partial \theta}{\partial t}(x,t) = \xi(x) * i\omega * e^{i\omega t} \quad (92)$$

Second derivative with respect to *t:*

$$\frac{\partial^2 \theta}{\partial t^2}(x,t) = \xi(x) * (i\omega)^2 * e^{i\omega t} \quad (93)$$

Second derivative with respect to *x*:

$$\frac{\partial^2 \theta}{\partial x^2}(x,t) = \frac{\partial^2 \xi(x)}{\partial x^2} * e^{i\omega t} \quad (94)$$

Substitution of the derivatives into the hyperbolic heat equation:

$$\xi(x) * i\omega * e^{i\omega t} + \tau * \xi(x) * (i\omega)^2 * e^{i\omega t} = \alpha * \frac{\partial^2 \xi(x)}{\partial x^2} * e^{i\omega t} \quad (95)$$

The exponential terms cancel.

$$\frac{\partial^2 \xi(x)}{\partial x^2} - \xi(x) * \left[\frac{i\omega}{\alpha} + \frac{\tau * (i\omega)^2}{\alpha}\right] = 0 \quad (96)$$

This was a common second order differential equation.

$$y'' - ay = 0 \ \rightarrow \ y = C_1 e^{-x\sqrt{a}} + C_2 e^{x\sqrt{a}} \quad (97)$$

$$\xi(x) = C_1 e^{-x\sqrt{\frac{i\omega}{\alpha} + \frac{\tau * (i\omega)^2}{\alpha}}} + C_2 e^{x\sqrt{\frac{i\omega}{\alpha} + \frac{\tau * (i\omega)^2}{\alpha}}} \quad (98)$$

is substituted into equation ( 91 ).

$$\theta(x,t) = \left[C_1 e^{-x\sqrt{\frac{i\omega}{\alpha} + \frac{\tau * (i\omega)^2}{\alpha}}} + C_2 e^{x\sqrt{\frac{i\omega}{\alpha} + \frac{\tau * (i\omega)^2}{\alpha}}}\right] * e^{i\omega t} \quad (99)$$

Now the boundary conditions are applied.

Boundary condition #1: The temperature at infinite distance has zero amplitude. Without an offset this was zero. The only way to satisfy this boundary condition was to have $C_2 = 0$.

$$\theta(\infty, t) = 0 \quad (100)$$

$$\theta(\infty, t) = [C_1 e^{-\infty} + C_2 e^{\infty}] * e^{i\omega t} = [C_2 e^{\infty}] * e^{i\omega t} = 0 \ \therefore C_2 = 0 \quad (101)$$

Boundary condition #2: The temperature at the surface was equal to the periodic forcing function with the specified amplitude $\theta_0$.

$$\theta(0,t) = \theta_0 * e^{i\omega t} \quad (102)$$

$$\theta(0,t) = \theta_0 * e^{i\omega t} = \left[C_1 e^{-0*\sqrt{\frac{i\omega}{\alpha}+\frac{\tau*(i\omega)^2}{\alpha}}}\right] * e^{i\omega t} \rightarrow \theta_0 = [C_1 * 1] \therefore C_1 = \theta_0 \quad (103)$$

The only way to satisfy this boundary condition was to have $C_1 = \theta_0$

$$\theta(x,t) = \left[\theta_0 * e^{-x\sqrt{\frac{i\omega}{\alpha}+\frac{\tau*(i\omega)^2}{\alpha}}}\right] * e^{i\omega t} \quad (104)$$

To make the derivation easier, the exponential terms are set to E.

$$\theta(x,t) = \theta_0 \left[e^{i\omega t} * e^{-x\sqrt{\frac{\omega}{\alpha}}*\sqrt{i-\tau\omega}}\right] = \theta_0 * E \quad (105)$$

The following steps are not explicitly enumerated in (Roetzel et al., 2003), but the same solution was reached.

$$e^{\sqrt{i-\tau\omega}} = e^{\sqrt{A+\sqrt{B}}} \quad (106)$$

$$A \equiv -\tau\omega \; and \; B \equiv -1$$

$$\sqrt{A+\sqrt{B}} = \frac{\sqrt{A+\sqrt{A^2-B}}}{2} + \frac{\sqrt{A-\sqrt{A^2-B}}}{2} \quad (107)$$

To simplify, a few terms are created.

( 108 )

$$\sqrt{A+\sqrt{B}}=\frac{\sqrt{\kappa}}{2}+\frac{\sqrt{A-\lambda}}{2}$$

$$\lambda \equiv \sqrt{(\tau\omega)^2+1}$$

$$\kappa \equiv \lambda + A$$

( 109 )

$$E = e^{i\omega t} * e^{-x\sqrt{\frac{\omega}{\alpha}}*\left(\frac{\sqrt{\kappa}}{2}+\frac{\sqrt{A-\lambda}}{2}\right)}$$

( 110 )

$$E = e^{i\omega t-x\sqrt{\frac{\omega}{\alpha}}*\left(\frac{\sqrt{\kappa}}{2}+\frac{\sqrt{A-\lambda}}{2}\right)}$$

( 111 )

$$E = e^{i\omega t-x\sqrt{\frac{\omega}{\alpha}}*\frac{\sqrt{\kappa}}{2}-x\sqrt{\frac{\omega}{\alpha}}*\frac{\sqrt{A-\lambda}}{2}}$$

Rearrange and pull *i* from the radical, which switches the signs of the $\lambda$ and $A$.

( 112 )

$$E = e^{-x\sqrt{\frac{\omega}{\alpha}}*\frac{\sqrt{\kappa}}{2}} * e^{i\left(\omega t-x\sqrt{\frac{\omega}{\alpha}}*\frac{\sqrt{\lambda-A}}{2}\right)}$$

A fundamental transform was used to convert the exponent to real cosine and imaginary sine.

( 113 )

$$E = e^{-x\sqrt{\frac{\omega}{\alpha}}*\frac{\sqrt{\kappa}}{2}} * \left[\cos\left(\omega t - x\sqrt{\frac{\omega}{\alpha}} * \frac{\sqrt{\lambda-A}}{2}\right) + i\sin\left(\omega t - x\sqrt{\frac{\omega}{\alpha}} * \frac{\sqrt{\lambda-A}}{2}\right)\right]$$

This expression was introduced back into equation ( 103 ), the imaginary part was dropped, and recognize equation ( 114 ), was used, to yield equation ( 115 ). This was the hyperbolic wave equation for the propagation of temperature as a function of both space and time. The equation for $\kappa$ was explicitly restated to show that if the time constant $\tau$ was zero, then $\kappa$ becomes one. Equation ( 115 )simplifies to the parabolic

equation for the propagation of temperature as a function of space and depth that was used to derive thermal effusivity.

$$\lambda - A = \frac{1}{\lambda + A} = \frac{1}{\kappa} \quad (114)$$

$$\theta(x,t) = \theta_{0_1} exp\left(-x\sqrt{\frac{\omega}{2a}\kappa}\right) cos\left(\omega t - x\sqrt{\frac{\omega}{2a}\frac{1}{\kappa}}\right)[K] \quad (115)$$

$$\kappa = \sqrt{(\tau\omega)^2 + 1} - \tau\omega$$

**Substitute the hyperbolic heat equation solution into the C-V equation.**

The previous equation was derived in the work of (Roetzel et al., 2003) to explain the propagation of a thermal wave with a relaxation time using the hyperbolic wave equation. The derivation presented in previous research was now used to determine the corresponding relativistic thermal effusivity (Veto & Christensen, 2015). One of the interesting effects of the hyperbolic heat equation was that (Roetzel et al., 2003) chooses a sinusoidal input into a semi-infinite medium. He states that an oscillating forcing function was necessary in order for the hyperbolic effects in experiments to persist for a long time.

Taking the derivative of the thermal wave equation with respect to position produces the following.

$$\frac{\partial\theta}{\partial x}(x,t) = \theta_{0_1}\begin{bmatrix} -x\sqrt{\frac{\omega}{2a}\kappa} * exp\left(-x\sqrt{\frac{\omega}{2a}\kappa}\right) * cos\left(\omega t - x\sqrt{\frac{\omega}{2a}\frac{1}{\kappa}}\right) + \\ -x\sqrt{\frac{\omega}{2a}\frac{1}{\kappa}} * exp\left(-x\sqrt{\frac{\omega}{2a}\kappa}\right) sin\left(\omega t - x\sqrt{\frac{\omega}{2a}\frac{1}{\kappa}}\right) \end{bmatrix}[Km^{-1}] \quad (116)$$

Set x=0 to describe the surface.

$$\frac{\partial\theta}{\partial x}(0,t) = -\theta_{0_1}\left[-\sqrt{\frac{\omega}{2a}}\kappa * cos(\omega t) + \sqrt{\frac{\omega}{2a}\frac{1}{\kappa}} * sin(\omega t)\right] [Km^{-1}] \quad (117)$$

Some simplifications are performed.

$$\frac{\partial\theta}{\partial x}(0,t) = -\theta_{0_1}\sqrt{\frac{\omega}{2a}}\left[\sqrt{\kappa} * cos(\omega t) - \sqrt{\frac{1}{\kappa}} * sin(\omega t)\right] [Km^{-1}] \quad (118)$$

This was then plugged into the C-V equation ( 83 ).

$$\Phi + \tau\frac{\partial\Phi}{\partial t} = -k * \left\{-\theta_{0_1}\sqrt{\frac{\omega}{2a}}\left[\sqrt{\kappa} * cos(\omega t) - \sqrt{\frac{1}{\kappa}} * sin(\omega t)\right]\right\} \quad (119)$$

The above was rearranged to a form more suitable for solving.

$$\frac{\partial\Phi}{\partial t} + \frac{1}{\tau}\Phi = \frac{\theta_{0_1} * k}{\tau}\sqrt{\frac{\omega}{2a}}\left[\sqrt{\kappa} * cos(\omega t) - \sqrt{\frac{1}{\kappa}} * sin(\omega t)\right] \quad (120)$$

The above equation was a difficult differential equation to solve. Wolfrum alpha was used to produce the solution ( 121 ).

$$\Phi(t) = \frac{\theta_{0_1} * k}{(\tau\omega)^2 + 1}\sqrt{\frac{\omega}{2a}}\begin{bmatrix}\sqrt{\kappa} * cos(\omega t) + \frac{\tau\omega}{\sqrt{\kappa}}cos(\omega t) \\ -\sqrt{\frac{1}{\kappa}} * sin(\omega t) + \tau\omega\sqrt{\kappa}\, sin(\omega t)\end{bmatrix} + Cexp\left(-\frac{t}{\tau}\right) \quad (121)$$

The solution was simplified.

$$\Phi(t) = \frac{\theta_{0_1}}{\lambda^2}\sqrt{kpc}\sqrt{\frac{\omega}{2}}\left\{\left[\sqrt{\kappa} * cos(\omega t) - \sqrt{\frac{1}{\kappa}} * sin(\omega t)\right] + \tau\omega\left[\frac{1}{\sqrt{\kappa}}cos(\omega t) + \sqrt{\kappa}\, sin(\omega t)\right]\right\} + Cexp\left(-\frac{t}{\tau}\right) \quad (122)$$

The following trigonometric identity ( 123) was used to simply equation ( 122 ).

$$A\, cos(\omega t) + B\, sin(\omega t) = \sqrt{A^2 + B^2}\cos\left(\omega t - \tan^{-1}\left(\frac{B}{A}\right)\right) \quad (123)$$

The first part of the brace in equation ( 122 ) becomes the following.

$$\sqrt{\kappa}\,cos(\omega t) + -\sqrt{\frac{1}{\kappa}}sin(\omega t) = \sqrt{\kappa+\frac{1}{\kappa}}\cos\left(\omega t - \tan^{-1}\left(\frac{-\sqrt{\frac{1}{\kappa}}}{\sqrt{\kappa}}\right)\right) \quad (124)$$

The second part of the brace in equation ( 122 ) becomes the following.

$$\tau\omega\left[\frac{1}{\sqrt{\kappa}}cos(\omega t) + \sqrt{\kappa}\,sin(\omega t)\right] = \tau\omega\left[\sqrt{\kappa+\frac{1}{\kappa}}\cos\left(\omega t - \tan^{-1}\left(\frac{\sqrt{\kappa}}{\sqrt{\frac{1}{\kappa}}}\right)\right)\right] \quad (125)$$

These simplifications are combined into equation ( 126 ).

$$\Phi(t) = \frac{\theta_{0_1}}{\lambda^2}\sqrt{k\rho c}\sqrt{\frac{\omega}{2}}\sqrt{\kappa+\frac{1}{\kappa}}\left\{\cos\left(\omega t - \tan^{-1}\left(-\frac{1}{\kappa}\right)\right) + \tau\omega\cos(\omega t - \tan^{-1}(\kappa))\right\} + Cexp\left(-\frac{t}{\tau}\right) \quad (126)$$

The tangent components are rewritten as follows. The negative in the first tangent was moved out.

$$\psi_1 \equiv \tan^{-1}\left(\frac{1}{\kappa}\right) \qquad \psi_2 \equiv \tan^{-1}(\kappa) \quad (127)$$

A final simplified hyperbolic heat flux equation for a harmonic forcing function was presented in equation ( 128 ). It was assumed here that the coefficient for the exponent term was $C$=0. This was because, as $t$ increases, the exponent will rapidly decrease. As $\tau$=0, this becomes the parabolic equation ( 130 ). Compared to the parabolic form, the hyperbolic form uses an added coefficient term $\Lambda$ as well as an added cosine term. These cosine terms, could be combined to a single term, however the equation was not as clean. It was more convenient to use multiple cosine terms to show how the equation simply reduces to a parabolic form when $\tau$=0 and thus when $\Lambda$=1.

Hyperbolic thermal effusivity equation:

( 128 )

$$\Phi_{q\_hyp} = \theta_{0_1}\sqrt{k\rho c} * \Lambda * \sqrt{\frac{\omega}{2}} * [\cos(\omega t + \psi_1) + \tau\omega\cos(\omega t - \psi_2)]$$

$$[\mathrm{J}\cdot\mathrm{m}^{-2}\cdot\mathrm{s}^{-1}]$$

$$\Lambda = \frac{\sqrt{\kappa + \frac{1}{\kappa}}}{(\tau\omega)^2 + 1} \qquad \kappa = \lambda + \mathrm{A} = \left(\sqrt{(\tau\omega)^2 + 1}\right) + (-\tau\omega)$$

Relativistic thermal effusivity equation, here denoted with an ash character.

$$æ \equiv \sqrt{k\rho c} * \Lambda \qquad ( 129 )$$

$$\Lambda = \frac{\sqrt{\kappa + \frac{1}{\kappa}}}{(\tau\omega)^2 + 1} \qquad \kappa = \lambda + \mathrm{A} = \left(\sqrt{(\tau\omega)^2 + 1}\right) + (-\tau\omega)$$

The parabolic heat effusion equation can be derived here. When the thermal inductance goes to zero, then the time constant will also go to zero. The limit of $\lambda$ as $\tau$ approaches zero was one and the limit of $\Lambda$ was one. Plugging in 1 for $\Lambda$ and zero for $\tau$ turns the hyperbolic heat flux equation into the parabolic heat flux equation. Unless the frequency was relatively high—perhaps on the order of single digit seconds or less depending on the materials—a small thermal inertia will have little effect on the heat flux.

( 130 )

$$\Phi_{q\_par} = \theta_{0_1}\sqrt{k\rho c} * (1) * \sqrt{\omega} * \left[\cos\left(\omega t + \frac{\pi}{4}\right) + (0) * \omega\cos\left(\omega t - \frac{\pi}{4}\right)\right]$$

$$\Phi_{q\_par} = \theta_{0_1}\sqrt{k\rho c} * \sqrt{\omega} * \left[\cos\left(\omega t + \frac{\pi}{4}\right)\right]$$

$$[\mathrm{J}\cdot\mathrm{m}^{-2}\cdot\mathrm{s}^{-1}]$$

## OBJECTIVE 2: APPLY RELATIVISTIC THERMAL EFFUSIVITY IN PLANETARY SCIENCE

### Significance for Mars

If thermal inductance was significant, its influence on the thermal modeling of planetary surfaces must be quantified. Equations ( 128 ) and ( 130 ) are used to compute the temperature profile for dry sand on Mars for the parabolic and hyperbolic case respectively (Roetzel et al., 2003; Schneider, 1955). For the parabolic case, $\Lambda \rightarrow 1$. A sinusoidal boundary condition was applied at the surface for temperature controlled by infrared radiation (de Breteuil & de Mairan, 1744). The thermophysical parameters for the martian dry sand are chosen from Mellon et al.'s chapter in (J. I. Bell, 2008) and the relaxation time was from (Roetzel et al., 2003). For this scenario there was no practical variation between the parabolic and hyperbolic equation (*Figure 13*).

### Heat flux vs. rotational period

The parabolic and hyperbolic surface heat fluxes ($\Phi$) from equations ( 128 ) and ( 130 ) are plotted at $t$=60 seconds for a range of rotational periods (*Figure 13*). When the rotational period becomes smaller than the time constant 2.26 seconds, then the hyperbolic heat flux equation damps to zero. This indicates that heat will not transfer at the surface when using the hyperbolic equation, but heat flux increases exponentially for the parabolic equation at time scales less than the time constant.

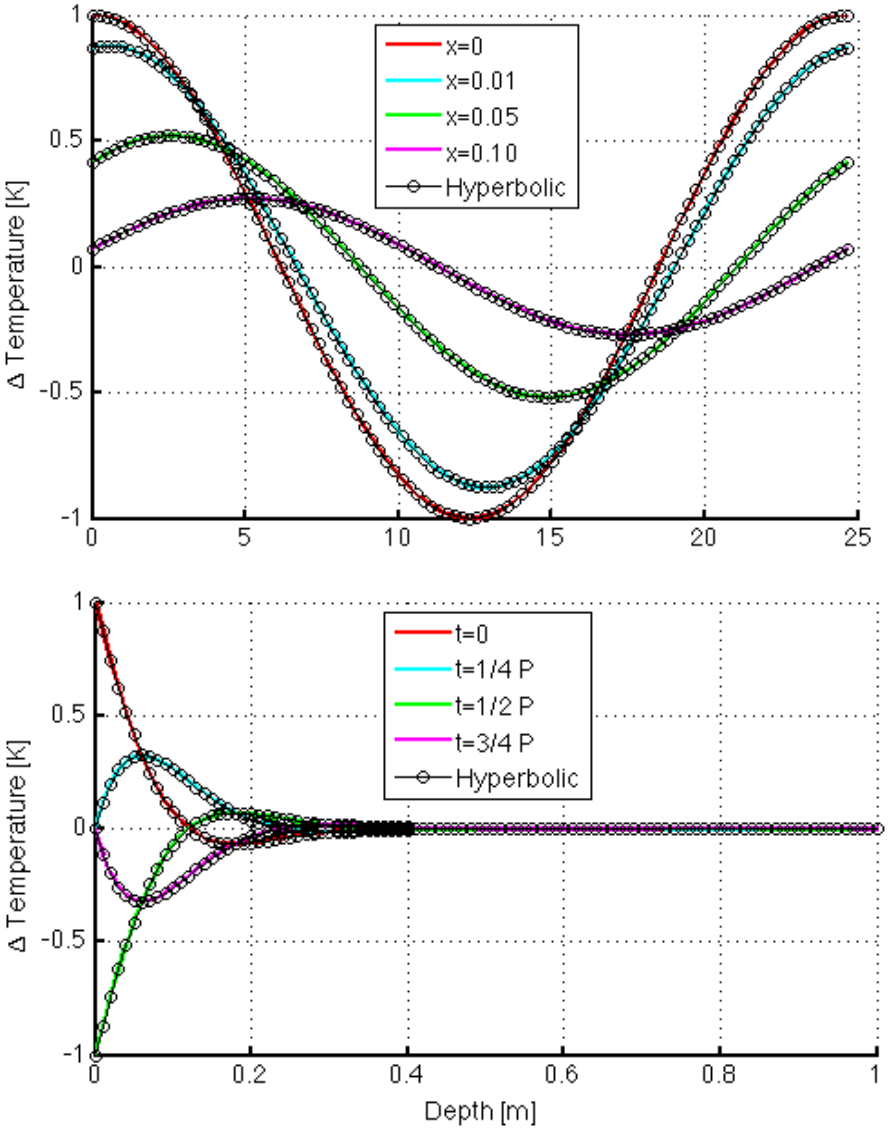


*Figure 12*. Diurnal temperature profile for dry sand on Mars. $k$ = 0.29 W m$^{-1}$ K$^{-1}$, $\rho$ = 1650 kg m$^{-3}$, $c$ = 850 J kg$^{-1}$ K$^{-1}$, $P$ = 24.6 hours, $\tau$ =2.26. A one Kelvin temperature amplitude normalizes the absolute result but does not affect relative results. Parabolic temperature profiles are solid lines, colorized for depth. Hyperbolic temperature points are plotted as circles. **A.)** Temperature trends versus time for different depth in meters. **B.)** Temperature trend versus depth at different times.

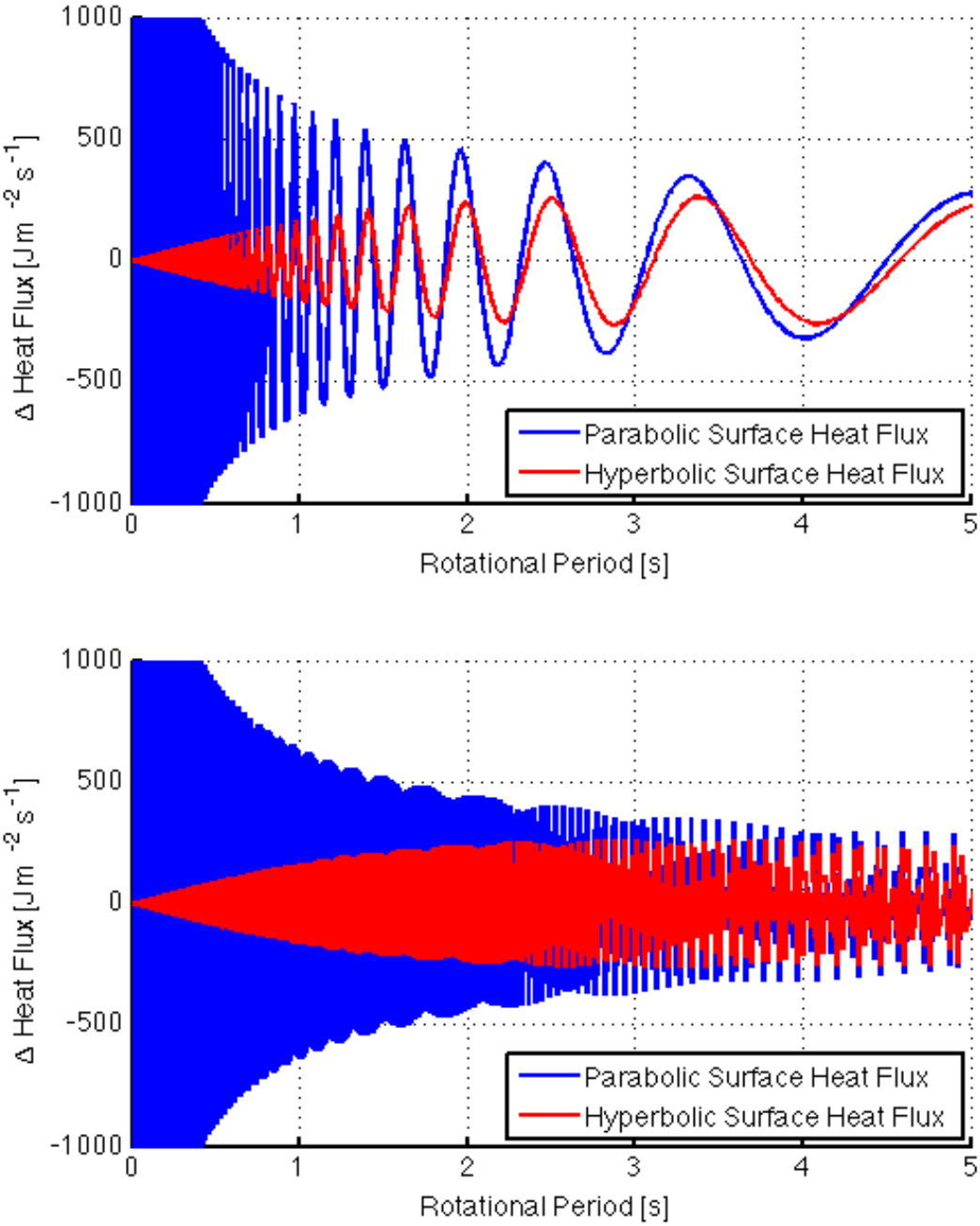


*Figure 13*. Surface Heat Flux for $x$=0. Top) $t$=60 seconds, Bottom) $t$=3600 seconds The same parameters are used from

*Figure 12*. As time increases from zero, the results from similar rotational periods diverge; thus, the perceived pseudo-frequency of the plotted sinusoid increases.

**The fastest spinning rocky body**

What was the fastest possible rotational speed for rocky object before it will become unstable and shed material? The force of gravity must be stronger than the centripetal force.

$$F_g \geq F_c \tag{131}$$

$$F_g = \frac{GMm}{r^2} \tag{132}$$

$$F_c = m\omega^2 r \tag{133}$$

$$\frac{GMm}{r^2} \geq m\omega^2 r \tag{134}$$

$$\frac{G\left(\frac{4}{3}\pi r^3 \rho\right)}{r^2} \geq \omega^2 r$$

$$G\left(\frac{4}{3}\pi r^3 \rho\right) \geq \left(\frac{2\pi}{P}\right)^2$$

$$G\left(\frac{1}{3}\rho\right) \geq \frac{\pi}{P^2}$$

$$P \geq \sqrt{\frac{3\pi}{\rho G}}\,[s] = \frac{3.7578 * 10^5}{\sqrt{\rho}}\sqrt{\frac{kg}{m^3}}[s] \tag{135}$$

First order estimates of the fastest stable rotational period for rubble piles of sand, basalt, and iron are made using density values from Mellon et al.'s Table 18.1 (J. I. Bell, 2008) and (Shackelford, Han, Kim, & Kwon, 2016).

( 136 )

$$P_{sand} \geq \frac{3.7578 * 10^5}{\sqrt{1650}} = 9251s \approx 2.6\ hours$$

$$P_{basalt} \geq \frac{3.7578 * 10^5}{\sqrt{2900}} = 6978s \approx 2\ hours$$

$$P_{iron} \geq \frac{3.7578 * 10^5}{\sqrt{7874}} = 4235s \approx 1.2\ hours$$

As shown in *Figure 13*, for the hyperbolic case to deviate from the traditional parabolic case, a body would need to have a diurnal period of less than 2 seconds! It was therefore, theoretically unlikely that there was a measurable difference on the surface temperature on planetary body that we currently know. While some asteroids rotate this fast, e.g. 2014rc at fifteen seconds, they are likely to be homogenous monoliths with small $\tau$ as a non-homogenous rubble pile would break apart.

## CONCLUSIONS AND FUTURE WORK

A body of literature exists that discusses the hyperbolic heat diffusion or C-V equation to reconcile the finite speed of heat waves using a relaxation time constant $\tau$. The equation was analogous to the electrical telegraph equation and a thermal inductance term was derived, but a physical explanation was not provided here other than the term appears to describe the internal interaction of transient heat across a material. A hyperbolic surface heat flux equation was derived and compared to the parabolic surface heat flux equation as a function of diurnal period. No significant

difference in the temperature profile between the parabolic and hyperbolic case was shown for planetary applications For relativistic effects to be realized, via this derivation and with the assumed parameters, Mars would need to have a diurnal period of ~2 seconds! While some asteroids rotate almost this fast, e.g. 2014rc at fifteen seconds, they are likely to be homogenous monoliths with small $\tau$, and a non-homogenous rubble pile would break apart.

There was still much work to be done to investigate this parameter. The Cattaneo and Vernotte have been cited 1065 and 926 times respectively, yet this was still an obscure problem. It seems that work on lasers in medicine lead the way for thinking about this application, but applications of this work within planetary science or astrophysics were not found. One of the difficulties may be that it was probably difficult to develop an experiment to test this theory on large scales. Still, future chamber experiments could be further designed to attempt to measure the thermal inductance. This may elucidate error in laboratory experiments that use pulsing heaters in simulated regolith. In parallel, the obvious next step was to wonder if there are any possible objects that are sufficient to observe hyperbolic heat transfer. The literature on second sound, the literature on hyperbolic heat conduction, and the results of this investigation point to three conditions that would express hyperbolic heat diffusion deviating from parabolic heat diffusion: small periods/high frequency, helium as a conductive medium, and cold temperatures.

There are no confirmed examples that are presented here that meet all the criteria. To entertain a thought of speculation, pulsars do rotate at speeds of less than one second and the first exoplanets discovered, orbited a pulsar. It is likely that pulsar planets are made of helium and hydrogen that reach very cold temperatures far from their star. And it is likely that some are bathed in an intense oscillating source of

radiation. If all of these possible circumstances combine, maybe hyperbolic heat transfer is observable on these worlds. Or maybe it a question of scale. Perhaps the spin of a dust grain near a star can be accelerated fast enough from a runaway Yarkovsky effect. Perhaps black holes are rotationally accelerating fast enough, as they collapse, to exhibit hyperbolic heat effects. Wondering further, the fact remains that parabolic, Fourier heat-transfer is incompatible over the vast distances of space where light has been traveling for billions of years. It is far beyond the scope of this PhD to investigate, but I can speculate that if parabolic heat transfer equations are used to model galaxies or the universe, then there could be errors that hyperbolic heat transfer could remedy. Further investigations and applications are being hypothesized.

Though it was once fitting to apply the term thermal inertia to describe the thermal effusivity, today, it may be more complete to include the thermal inductance with the thermal effusivity as a relativistic thermal effusivity that describes the overall observed thermal inertia. Although it is still questionable as to whether thermal inductance exists, it likely does not affect models of the planets that are currently being observed. Nevertheless, an awareness of thermal inductance in the heat transfer literature and the use of thermal effusivity in industry may provide new insight and inspiration for the modeling of planetary surfaces and beyond.

CHAPTER 4

# DEVELOPMENT OF A LONG-FAR INFRARED CAMERA FOR PLANETARY EXPLORATION

*"An expert is a [person] who has made all the mistakes which can be made, in a narrow field" – Niels Bohr*

## INTRODUCTION, GOALS, AND OBJECTIVES

### Scientific Exploration Background

Over the past 55 years, thermal infrared remote sensing instruments (~7-100 μm) have been engineered, built, and launched to collect data for scientific investigations of planetary bodies (See appendix for a table of instruments and references; See chapter 2 for discussion of thermal inertia science background). The development of these instruments typically follows a trend of increasing technological sophistication from radiometers to spectrometers to cameras to imaging spectrometers. Infrared instruments have been flown from the United States, the Soviet Union/Russia, the European Union, and India on missions of increasing complexity following the planetary exploration campaign strategy: telescopic observations, flybys, orbiters, landers, and rovers. The early infrared radiometers enhanced the telescopic measurements of the planets during flyby missions. These instruments measured the surface temperatures of planets in order to make broad initial discoveries such as the thermal heat balance of the planets and the composition of the polar caps of Mars and Triton. Spectrometers were then introduced to measure infrared spectra that help determine inferred mineral assemblages. These spectrometers were incorporated onto orbiters and eventually onto rovers on Mars.

Most recently, multispectral infrared cameras have been flown to Mars that are sensitive to ~7-13 μm, which is where the peak of the blackbody emission for the surface temperature of Mars lies (Table 1). The infrared cameras provide detailed mapping of the surface of Mars that enable higher spatial resolution mineral mapping—albeit at lower spectral resolution—and diurnal temperature maps that enable the derivation of thermal inertia to infer the physical nature (grain size) of the surface. The Thermal Emission Imaging System (THEMIS) is the longest operating instrument at Mars—celebrating more than 15 years in orbit. The Indian Thermal Infrared Imaging Radiometer TIS has recently entered into a highly elliptical orbit around Mars and the data are likely to offer a complimentary view of the martian surface as they become available. The current collection of infrared planetary data is rich, yet there is more that can be collected.

Future infrared instruments will explore icy bodies in the colder outer solar system, so infrared cameras are required to become more sensitive at longer wavelengths as the peak blackbody emission shifts to longer wavelengths with decreasing temperature. The investigation described here was initiated as a proposal to NASA's Planetary Instrument Definition and Development Program (PIDDP) in order to begin the development of a long-far wavelength infrared camera (8-50 μm) that can be used for any planetary body using a modular microbolometer-based detector assembly with custom filters and optics catered to the specific mission.

**The state of current IR cameras for space exploration**

Long-wavelength infrared cameras are currently operating at other planets. The Thermal Infrared Imaging System (THEMIS) orbits Mars on the *2001 Mars Odyssey* spacecraft (Christensen et al., 2004). The instrument has successfully acquired and downlinked over 226,733 infrared images and 227,625 visible images of Mars to Earth as of October, 30 2017. THEMIS uses 10 spectral bands with center wavelengths ranging

from 6.8 μm to 14.9 μm each with a FWHM of ~1 μm. The array consists of 320x240 microbolometers with a pixel pitch of 50 μm. Typical cooled detectors are a factor of 10-1000 more sensitive than microbolometer arrays. However, the advantage of microbolometer arrays is that they are relatively low-cost, low-power, low-volume, low-mass, low-risk, and low-complexity, largely because they do not require an active cooling apparatus. Furthermore, the THEMIS space-heritage has shown that microbolometer arrays are resilient and stable devices compared to cooled detectors. THEMIS is still healthy and operating at its pre-launch performance after 16 years of imaging without sign of degradation. Many cooled instruments exhibit catastrophic degradation as the cryogenic cooling systems begin to fail. The terrestrial instrument Advanced Spaceborn Thermal Emission and Reflection Radiometer (ASTER) consists of three sub-systems: visible and near-infrared (VNIR), the short-wave infrared (SWIR), and the thermal-infrared (TIR). As reported by the ASTER SWIR Data Status Report of March 13, 2009, the cryogenic cooled SWIR instrument performed nominally from 1999 to 2004, began to degrade from 2004 to 2007, and produced virtually no good data in 2008. The martian instrument Compact Reconnaissance Imaging Spectrometer for Mars (CRISM) also consists of two subsystems: a visible-near infrared detector and a shortwave infrared detector. The cryocooler degredation, from launch in 2006 to 2017, has resulted in a relatively large increase in thermal noise as the detectors have warmed ~15 K (Kreisch et al., 2017). Thus, while cooled detectors have increased sensitivity over microbolometer arrays, ASTER and CRISM show that cryocooled instruments degrade 5-10 years post-launch.

Joining *2001 Mars Odyssey* in orbit around Mars in 2014, India's *Mars Orbiter Mission* (*MOM*) caries the Thermal Infrared Imaging Spectrometer (TIS) as a science payload that offers promising infrared imagery at different scales to complement

THEMIS's consistent global mapping (Singh, Sarkar, & Kumar, 2015). *MOM*, being in a highly elliptical orbit, has an apoareon of ~77,000 km, so it is likely that TIS will capture large footprint images of Mars to provide infrared context images.

Over the past 16 years, microbolometer technology has continued to advance. The detector acquired for the experiment in this chapter was a 640 x 480 microbolometer array with 25 μm pixel pitch. FLIR now sells commercial 640 x 512 arrays with 17 μm pixel pitch detectors. Military grade detectors are rumored to be high definition. It was likely that these detectors have operated.

Because of their previously stated advantages, infrared cameras using microbolometer arrays are planned to launch on small student satellites for conducting proximity operations(Spencer, 2015; Veto & Christensen, 2016).

For planetary remote sensing, current infrared cameras are able to provide temperature data to infer the thermophysical properties of a planetary surface and multi-point spectra to determine mineral assemblages within the 7-14 μm spectral range. Using Wien's displacement law, this range corresponds to maximum wavelengths corresponding to 207 K to 414 K. Because this temperature range stretches from just above the sublimation temperature of $CO_2$ ice to above the boiling point of water, it is ideal for measuring the temperatures of planetary surfaces of the Earth and Mars. For outer planet bodies with colder temperatures, an infrared camera must be sensitive to longer wavelengths of light. Using the NASA Goddard planetary fact sheet for average surface temperatures, the peak wavelength was calculated using Wein's Law ( 138 ) and are tabulated in  Table 1 (Wien, 1894). The gas planets are calculated at 1 bar. An upgraded IR camera that is sensitive to 15-60 μm has utility for detecting the thermal variability of planetary surfaces in the colder, outer solar system.

$$\lambda_{max} = \frac{b}{T}\ [\mu m];\ b = 2898\ \mu m \cdot K \quad (137)$$

$$\nu_{max} = b * T\ [cm^{-1}];\ b = 1.916\ cm^{-1} \cdot K \quad (138)$$

Table 1

*The average surface temperature and corresponding peak radiative wavelength and wavenumber*

| Planet | Average Temperature (K) | Peak Wavelength (μm) | Peak Wavenumber ($cm^{-1}$) |
|---|---|---|---|
| Mercury | 440 | 6.8 | 843 |
| Venus | 737 | 4.1 | 1412 |
| Earth | 288 | 10.4 | 552 |
| Moon | 253 | 11.8 | 485 |
| Ceres | 168 | 17.8 | 322 |
| Mars | 208 | 14.4 | 399 |
| Jupiter | 163 | 18.3 | 312 |
| Io | 118 | 25.3 | 226 |
| Europa | 103 | 29.0 | 197 |
| Ganymede | 113 | 26.5 | 217 |
| Callisto | 118 | 25.3 | 226 |
| Saturn | 133 | 22.5 | 255 |
| Titan | 93 | 32.1 | 178 |
| Uranus | 78 | 38.3 | 149 |
| Neptune | 73 | 40.9 | 140 |
| Triton | 58 | 51.5 | 111 |
| Pluto | 48 | 62.3 | 92 |

Infrared cameras are also used to characterize the spectrum of a surface using multiple channels produced from filters or a diffraction grating. THEMIS produces nine point spectra of Mars that are used to map the mineralogical diversity of the surface. In parallel, Fourier Transform Interferometers are able to probe longer wavelengths—where diagnostic mineral absorption features are located. TES produces six single-point spectra with 143 samples per spectrum at 10 $cm^{-1}$ or 286 samples per spectrum at 5 $cm^{-1}$ to probe the region 6-50 μm(Christensen et al., 2001). Mini-TES with a singe point spectra that contains 167 samples per spectrum with 9.99 $cm^{-1}$ sample spacing probes the region 5.01-29.45 μm(Christensen et al., 2003). An improved IR imager has broad applications to map composition using the full infrared spectral range and to map the surface temperature of colder objects.

The potential disadvantages of microbolometer array-based IR cameras include decreases in sensitivity and slower frame rate. The FLIR LWIR mercury cadmium telluride (MCT) cameras have a typical noise equivalent delta temperature (NEDT) of 20 mK whereas the uncooled microbolometer cameras have a typical NEDT of <30 mK at 300K , f/1.0, 30 Hz. For most applications this is marginal. The thermal time constant for a microbolometer (9 ms) was considerably more than the MCT detector (3 μs)(Gruber, Moore, Tercha, & Bowe, 2012). The actual readout time for the microbolometer array with supporting electronics was limited to 30 Hz with standard commercial detectors. However, newer detectors at the time of writing this paper are being produced at 50-60 Hz.

In contrast, microbolometer arrays offer several advantages over MCT detectors. Microbolometer arrays can be implemented into IR camera systems with considerably less mass, volume, power, and expense over MCT systems. Furthermore, they do not require cryogenic cooling systems. While the microbolometer array onboard the

*Odyssey*-THEMIS instrument has been continuously working for over 16 years as of this writing. The absence of a cryogenic system ensures that an instrument can survive for longer missions to the outer solar system as well as conduct longer surveys to reduce noise or observe seasonal to decade-long trends. Microbolometer arrays, while less sensitive than cooled detectors, can theoretically detect energy at all wavelengths, whereas current cooled detectors are limited to wavelengths <15 μm.

**Motivation for enhanced thermal imaging**

There are three specific types of missions that have scientific benefits for enhancing the performance of a long wavelength IR cameras: missions to cold planetary bodies, missions to Mars and the Moon, and low-cost missions.

A long-far wavelength infrared camera will augment the exploration of cold planetary bodies for upcoming missions. Infrared cameras are able to detect temperature variations on planetary surfaces e.g. fractures in an icy surface on Europa, plumes from Enceladus, volcanism on Io, or the composition and dynamics of Titan's atmosphere. Thermal imaging will also assist in mapping the thermosphysical properties of the surface of moons, comets, and asteroids. Because these bodies, excluding Io, are much colder than the surface of Earth or Mars, the peak wavelength shifts to longer wavelengths. An infrared camera with longer wavelength capability will provide better SNR for detecting the thermal variation on the surface of cold bodies. ASU was currently designing an infrared camera for Europa based in-part on these results.

While the surface of Mars has been extensively mapped in the thermal infrared at 6.8-12.6 μm, multispectral remote sensing at wavelengths >15 μm would enhance the understanding of the surface composition by imaging the far infrared wavelength spectral absorptions of minerals that are not currently imaged at 100 meter per pixel scale. Figure 1 shows mineral absorption features in the 15-35 μm range that are not

currently mapped with THEMIS that could be mapped with a long-far wavelength infrared camera from orbit. A future instrument could also assist in measuring the thermophysical properties of the surface to assist with selection of candidates for a sample cache in a future rover and provide enhanced spectral capabilities for imaging the martian atmosphere.

Long-far wavelength multispectral cameras will enable future investigations that compliment near-infrared and visible imaging. These investigations may be half the payload of a small student cubesat mission, one of a variety of crucial payloads for medium NASA missions in the Discovery or New Frontiers class, or low-investment add-on augmentations for flagship class missions.

**Project Goals and Objectives**

This project responds to a need to determine the performance of IR cameras for planetary remote sensing applications. The specific goal of this project was to characterize microbolometer detectors for infrared cameras with enhanced spectral range at far wavelengths i.e. (15-100 μm). This goal was approached by accomplishing the following objectives.

**Objective 1: Retrofit a microbolometer sensing detector package (SDP) with a CVD diamond window.** The microbolometer array was retrofitted with a 0.5 mm thick, 1.01 in. x 1.01 in. CVD diamond window to provide long-wavelength transmission. Element Six produced the window and metalized the rim for bonding to the detector package. Raytheon Vision Systems installs the window onto the microbolometer focal plane.

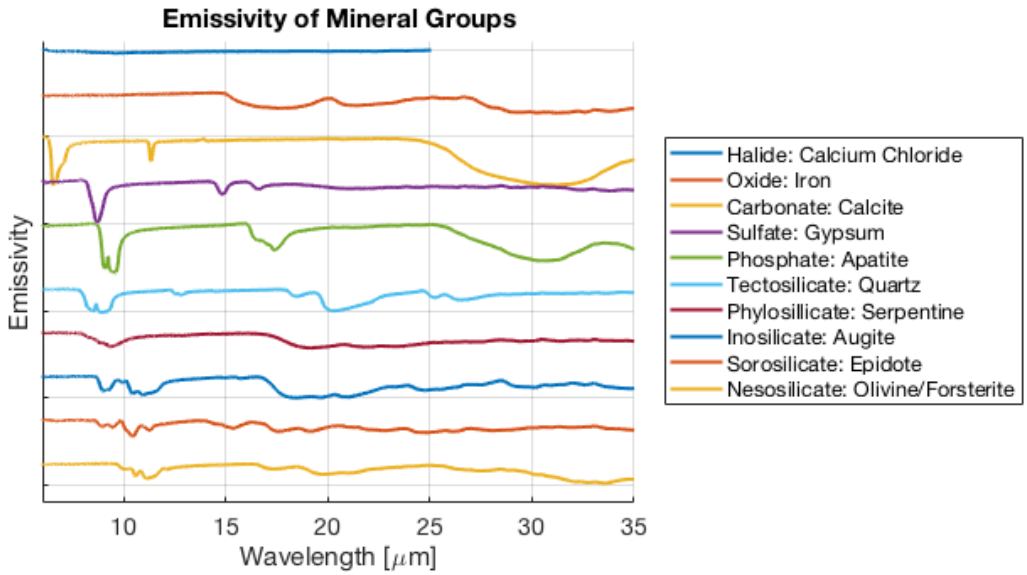


*Figure 14.* Emissivity spectra for mineral groups with absorption features in the 15-35 μm extended range of sensitivity using a diamond windowed microbolometer array. Spectra are offset. The calcium chloride sample was recently acquired for the dissertation work of Julie Mitchell. This spectrum only goes to 25 μm and shows the lack of any distinguishing features in the 6-15 μm spectral region that was used by THEMIS. All spectra are from the ASU spectral library (speclib.asu.edu).

**Objective 2: Develop a laboratory testbed for testing the performance of the microbolometer array.** This modified microbolometer was integrated with supporting electronics to produce a camera core. Two test methods are then used to collect data. First, the camera core was installed onto a lab bench at the ASU Infrared Instrument Optics Laboratory. Filter wheels are procured with ten band-pass filters that are used to take multispectral images of a well-calibrated blackbody source. Second, the camera core assembly was integrated onto a lab bench at the ASU infrared instrument optics laboratory using the engineering model (EM) interferometer assembly from the OSIRIS-REx Thermal Emission Spectrometer (OTES).

**Objective 3: Develop a calibration pipe-line for reducing the raw mircrobolometer DN values to an instrument response function.** The radiometric performance was determined using the calibration techniques developed at ASU for infrared instruments (Christensen et al., 2001; 2003; 2004).

**Objective 4: Collect data from the testbed in order to determine an instrument response function for the diamond retrofitted microbolometer array.** Data are collected using the instrument testbeds with the retrofitted microbolometer array; the data are calibrated using the respective calibration pipe-line. For the filter method, images are taken at each filter wheel method, then processed. For the interferogram method, data collection commences for a designated time in order to collect multiple interferograms that can be co-added over a period of hours. Experiments are iterated with incremental improvements to enhance the testing.

## INSTRUMENT BACKGROUND THEORY

A summary of the background of microbolometer arrays, their previous characterization, and interferometry equations are presented.

**Acronyms and variables**

| | |
|---|---|
| ASTER | Advanced Spaceborn Thermal Emission and Reflection Radiometer |
| ASU | Arizona State University |
| Cad-Tel | Cadmium Telluride |
| CRISM | Compact Reconnaissance Imaging Spectrometer for Mars |
| CVD | Chemical Vapor Deposited |
| DC | Direct Current |
| DFT | Discrete Fourier Transform |
| DMI | Displacement Measuring Interferometer |
| DN | Digital Number |
| FFT | Fast Fourier Transform |
| FLE | Fine Level Equalization |
| FLIR | Forward Looking Infrared |
| FPA | Focal Plane Array |
| FPGA | Field Programmable Gate Array |
| FWHM | Full Width Half Max |
| IR | Infrared |
| IRF | Instrument Response Function |
| LCR | Large Ceramic Package |
| LWIR | Long-wavelength Infrared |
| MCT | Mercury-Cadmium-Telluride |
| MOM | Mars Orbiter Mission |
| NEDT | Noise equivalent delta temperature |
| NESR | Noise equivalent signal resolution |
| NUC | Non-uniformity Correction |
| OTES | OSIRIS-REx Thermal Emission Spectrometer |
| PIDDP | Planetary Instrument Definition and Development Program |
| ROIC | Readout Integrated Circuit |
| RVS | Raytheon Vision Systems |
| SDP | Sensing Detector Package |
| SNR | Signal to Noise Ratio |
| SWIR | Shortwave Infrared |
| THEMIS | Thermal Emission Imaging System |
| TEC | Thermoelectric Cooler |
| TIS | Thermal Infrared Imaging Spectrometer |
| VI | Virtual Instrument |
| VNIR | Visible and Near-Infrared |
| ZPD | Zero Path Difference |

| | | | |
|---|---|---|---|
| $\Delta_{max}$ | optical path difference | I | Intensity or Radiance |
| | | N | number of points |
| $\delta$ | optical sampling distance | T | period |
| $\epsilon$ | emissivity | V | Voltage from FFT |
| $\lambda$ | wavelength | X | mirror travel distance |
| $\theta$ | phase shift | | |
| $\nu$ | wavemuber | f | frequency |
| | | k | discrete point in DFT |
| A | amplitude | m | spectrometer mode |
| B | Radiance | t | time, |
| E | Spectral Radiance | | |

**Microbolometer arrays**

A microbolometer is a single miniaturized bolometer that works by absorbing infrared radiation thereby changing its resistance measured as a voltage potential(Langley, 1880). Microbolometers were developed by Honeywell for the military (e.g. (Wood, 1993)). The miniaturization of the bolometer allows the construction of microbolometers into arrays of thousands of pixels that become a focal plane for infrared imaging. A material sensitive to IR radiation such as vanadium-oxide is the absorbent material that is suspended above a reflector and mounted onto a silicon substrate with a read-out integrated circuit (ROIC).

Rapid advances in microbolometer technology were made possible from the existing infrastructure and research for cooled infrared detectors for military applications. Microblometer array development advances beyond cooled detectors in that the removal of a requirement for cryogenic cooling, reduces the cost, mass, volume,

and complexity of the system, while increasing the utility. This is achieved at the expense of performance, though microbolometer arrays typically are sufficient to meet mission requirements. Declassification of the microbolometer array technology has allowed over a dozen companies to manufacture the microbolometer arrays integrated into infrared cameras for commercial use. Wood optimistically stated in 1993 that the then new commercial technology would allow infrared cameras to be sold for perhaps less than a few thousand dollars. Today FLIR sells small IR cameras as smart phone attachments for less than a few hundred dollars(Wood, 1993).

**Previous microbolometer array characterization**

This experiment builds on previous work interfacing microbolometer-based infrared cameras with spectrometers. An investigation incorporated an Infrared Solutions 160x120 pixel camera into a Nicolet Nexus 870 spectrometer (Malamas, Davis, U.S, & Physics, 2006). Using a step-scan spectrometer, a series of infrared images were collected of the internal glowbar. A single pixel was chosen to read-out the value at each step, and an interferogram was produced from stepping through a scan with the interferometers moving mirror. Averaging multiple frames at a given step improved the signal. The study proved that a commercial infrared camera could be integrated with a commercial spectrometer to capture interferograms.

Another investigation incorporated the FLIR Tau 320 IR camera with an interferometer assembly(Gruber et al., 2012). A number of useful design considerations are mentioned. They noted from a model that velocity of the moving mirror affects the signal level of the interferogram due to the time constant effect. They also noted that whereas microbolometer arrays are able to measure room temperature scenes, there must be a temperature difference between the scene and the detector in order to modulate the signal sufficiently. Significant steps in their data preprocessing include

removing the DC component, spatial co-adding of pixels from 1x1 to 9x9, resampling of the interferogram for off-axis pixel correction, and Forman phase correction using a FFTW transform.

Another investigation shows how the response of an infrared detector changed with incidence angle (Touvignon et al., 2014). The investigators noted that there was a shift in the minimum of the response from 4.6 μm to 3.5 μm when the angle of incidence was changed from 0˚ to 45˚. The results of this paper are later compared with these results (*Figure 38*).

An exploratory investigation was performed to replicate the work from these prior investigations using the ASU thermal emission spectroscopy lab's Nicolet 670 interferometric spectrometer (*Figure 15*)(Ruff, Christensen, & Barbera, 1997). A microbolometer array detector was integrated with the spectrometer to simulate the test method. Mounting hardware was fabricated at the ASU machine shop to fix the detector in the spectrometer. The detector was placed in the secondary detector position and focused onto a blackbody source at the sample end of the spectrometer. Images were captured of the blackbody radiation through the spectrometer. The object in the center of the IR image was the out of focus mirror for the scanning mirror laser. Although the scanning mirror velocity in this spectrometer cannot be tuned to a velocity compatible with the frame rate of the microbolometer array, the ZPD peak and smaller peaks were witnessed in the streaming video. Some of the peaks can be seen in the sampled data (*Figure 16*).

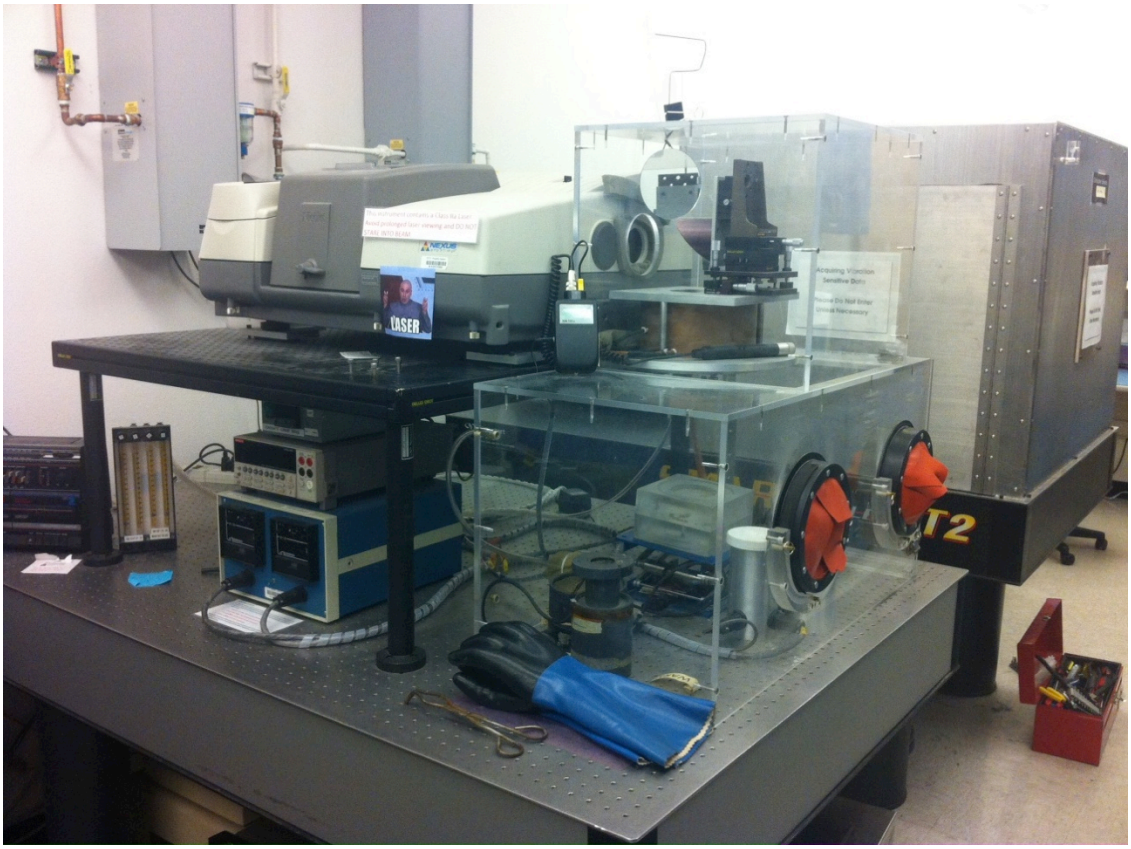


*Figure 15*. A) ASU Thermal Emission Spectroscopy Lab's Nicolet 670 interferometric spectrometer.

Caption for next page.

*Figure 16*. A) Infrared image of the blackbody source with laser mirror obscuration. B) The 8-bit value for a series of 600 images captured at 30 Hz. The overall contrast was only 14 DN in 8-bit mode. This was for 4 periods corresponding to 20 seconds of total data and 5 seconds per period with 125 data samples per period. However, only about 100 of these data points correspond to the double-sided interferogram, while the remaining 25 samples correspond to the retracting of the moving mirror.

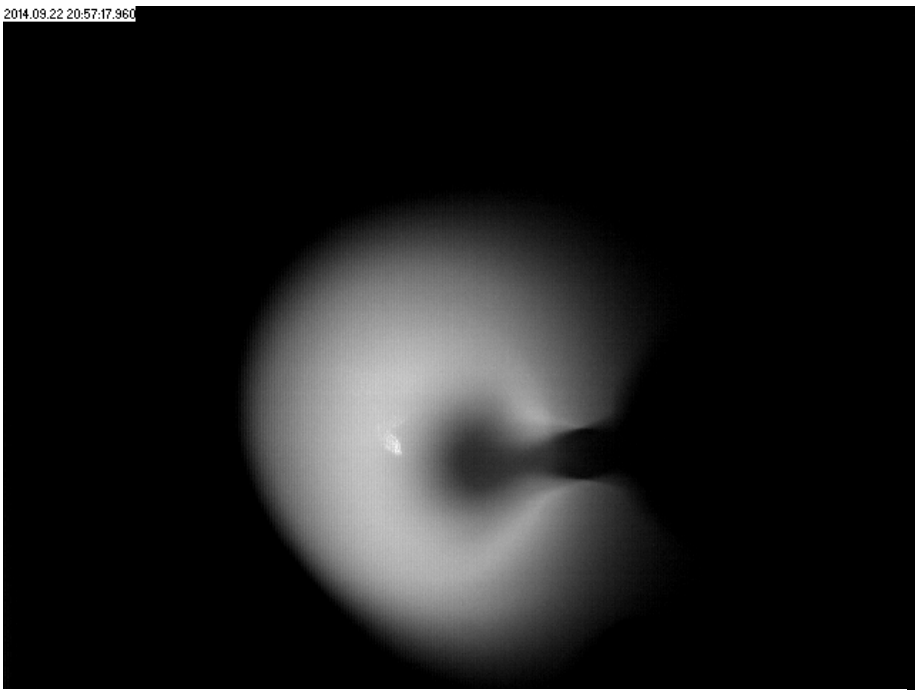
2014.09.22 20:57:17.960

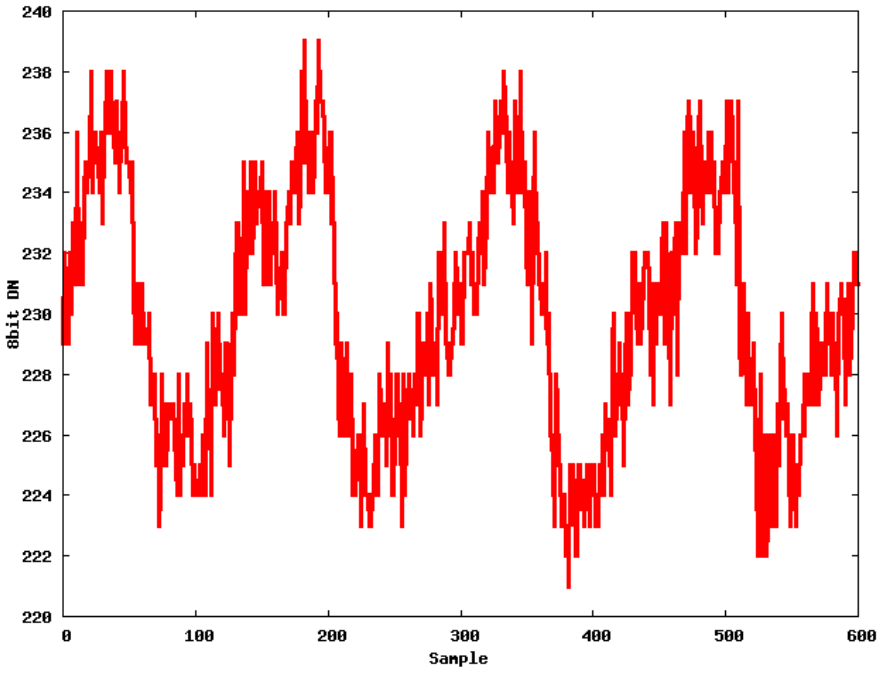
240
238
236
234
232
230
228
226
224
222
220
8bit DN
0
100
200
300
400
500
600
Sample

**Definition of terms**

Table 2
*Spectrometer terms and descriptions*

| Term | Symbol | Units | Description | Equation |
|---|---|---|---|---|
| Wavelength of Helium Neon moving mirror laser | $\lambda_{HeNe}$ | 632.8 nm or 15803 $cm^{-1}$ | - | |
| Total moving mirror displacement | $\Delta X$ | cm | Total distance moving mirror travels from ZPD. | |

| | | | | | |
|---|---|---|---|---|---|
| maximum useable wavenumber obtained | $\tilde{\nu}_{max}$ | $cm^{-1}$ | A function of how often the moving mirror was sampled. On the FFT, this falls in the middle of the full point raw FFT spectrum. If one included the mirror image of FFT, then the last point would be labeled $2^*\tilde{\nu}_{max.}$ This maximum wavenumber ($\tilde{\nu}_{max}$) was also called the Nyquist wavenumber. | $\tilde{\nu}_{max} = \frac{1}{2*d\delta}$ | ( 139 ) |
| spectral resolution | $\Delta\tilde{\nu}$ | $cm^{-1}$ | maximum wavelength that can be resolved by the interferometer, the inverse of the optical path distance, assuming a boxcar truncation function (Griffiths & De Haseth, 2007) pg. 28. | $\Delta\tilde{\nu} = \frac{1}{\Delta_{max}}$ | ( 140 ) |
| | | | | | |
| optical path difference or retardation | $\delta$ | cm | the difference in path length of light between the two arms of the interferometer through the whole system, equivalent to twice the displacement of the moving mirror. | | |
| maximum optical path difference. | $\Delta_{max}$ | cm | Maximum of $\delta$, i.e. when moving mirror fully displaced. $\Delta_{max} = 2 * \Delta X$ | $\Delta_{max} = 2 * \Delta X$ | ( 141 ) |

| | | | | |
|---|---|---|---|---|
| number of single-sided interferogram samples. | $N_s$ | N/A | The number of samples for half of an interferogram (ZPD to $\Delta_{max}$) For a full interferogram, $-\Delta_{max}$ to $\Delta_{max}$, 2*$N_s$ points; (Griffiths & De Haseth, 2007) pg. 62. For the FFT of a single-sided interferogram, the wavenumber x-axis of the spectrum was half of the wavenumber x-axis of a spectrum derived from a double-sided interferogram. | $N_s = N_{D_S} = \frac{2 * \tilde{\nu}_{max}}{\Delta\tilde{\nu}} = \frac{1}{\Delta\tilde{\nu} * d\delta}$ $N_{spectrum} = \frac{N_S}{2} = \frac{\tilde{\nu}_{max}}{d\tilde{\nu}_S}$ ( 142 ) |
| number of double-sided interferogram samples | $N_D$ | N/A | For the FFT of a double-sided interferogram, the numerator was two times the usable maximum wavenumber—also equal to the "nyquist" wavenumber. The negative points do not increase the maximum wavenumber, but increase the spectral sampling. | $N_D = \frac{2 * \tilde{\nu}_{max}}{d\tilde{\nu}_D}$ $N_{spectrum} = \frac{N_D}{2} = N_{D_S} = \frac{\tilde{\nu}_{max}}{d\tilde{\nu}_D} = \frac{\tilde{\nu}_{max}}{d\tilde{\nu}_S/2}$ ( 143 ) |

| | | | | | |
|---|---|---|---|---|---|
| Number of resolution elements | M | N/A | The number of resolution elements was equal to the maximum wavenumber divided by the spectral resolution (Griffiths & De Haseth, 2007) p. 65. This was half the number of data points plotted, which corresponds to the Nyquist criterion. | $M = \frac{\tilde{\nu}_{max}}{\Delta\tilde{\nu}}$ | ( 144 ) |
| sampling optical displacement | $d\delta$ | cm | the change in optical path difference between samples; m = 1 samples every zero crossing, $\tilde{\nu}_{\max}$ =15803 $cm^{-1}$; m = 2 samples every other zero crossing, $\tilde{\nu}_{\max}$ = 7901 $cm^{-1}$ (more common). See Nicolet-OMNIC user's guide and (Griffiths & De Haseth, 2007) pg. 63. | $d\delta = \frac{m*\lambda_{HeNe}}{2}$<br>$d\delta = \frac{\Delta_{max}}{N_s} = \frac{\overrightarrow{v_\delta}}{f_s}$ | ( 145 )<br>( 146 ) |
| spectral sampling | $d\tilde{\nu}$ | $cm^{-1}$ | This was the interval between points plotted on the final spectrum, it was the x-axis interval of a spectrum, it was half the spectral resolution for a double-sided interferogram. | $d\tilde{\nu}_{general} = \frac{\tilde{\nu}_{max}}{N_{spectrum}} = \frac{\tilde{\nu}_{max}}{N_{interferogram}/2}$<br>$d\tilde{\nu}_D = \frac{\Delta\tilde{\nu}}{2}$<br>$d\tilde{\nu}_S = \Delta\tilde{\nu}$ | ( 147 ) |

| | | | |
|---|---|---|---|
| period | $T$ | s | This was the period of the moving mirror. |
| optical velocity | $\overrightarrow{v_\delta}$ | cm·s$^{-1}$ | This was the optical velocity of the moving mirror. |
| moving mirror velocity | $\overrightarrow{v_x}$ | cm·s$^{-1}$ | This was the physical velocity of the moving mirror |

**Calibration equations**

For an in-depth guide to interferometer calibration see (Christensen et al., 2017). A summary of the techniques used for this investigation are presented.

**Phase correction: Mertz method.** The interferograms are corrected for phase using the Mertz Method. The Fourier transformed interferogram was complex with both real and imaginary parts ( 148 ), also as ( 149 ). The phase information can be calculated from the inverse tangent of the imaginary divided by the real part of the spectrum ( 150 ). The cosine and sine of the phase are multiplied to real and imaginary part of the spectrum respectively (Griffiths & De Haseth, 2007). Though the phase was typically calculated for only a small sample of points around the ZPD, so a nearly single-sided interferogram can be collected, for this study a double-sided interferogram was processed into the whole spectrum for phase.

$$B(\tilde{\nu}) = B'(\tilde{\nu})e^{-i\theta_{\tilde{\nu}}} \quad (148)$$

$$B(\tilde{\nu}) = Re(\tilde{\nu})\cos\theta_{\tilde{\nu}} + Im(\tilde{\nu})\sin\theta_{\tilde{\nu}} \quad (149)$$

$$\theta_{\tilde{\nu}} = tan^{-1}\left(\frac{Im(\tilde{\nu})}{Re(\tilde{\nu})}\right) \quad (150)$$

**Apodization Filter.** An apodization filter was applied to the final result. A triangle wave with a peak amplitude of one and a final amplitude of zero was applied to the interferogram in order to reduce the amplitudes of the wing information.

**Calibrated radiance.** The DN of a specified temperature was predicted using the following equation for a given temperature *t*. The observed signal/voltage was equal to the difference in radiance between the target and the instrument ( $\varepsilon B_{ins}$ ) multiplied by the instrument response function (*IRF*). Because the sample target was a blackbody

(*BB*), the reflectivity was zero, and the term was excluded here e.g. (Christensen et al., 2017; Ruff et al., 1997).

$$V_t = (BB_t - \varepsilon B_{ins}) * IRF \quad (151)$$

**Instrument Response Function.** As outlined in objective 3, the instrument response function was required in order to determine the performance of the detector. In order to do this, the methods used for the ASU spectral laboratory and past instruments were used (Christensen et al., 2001; 2003; 2004; 1992; Ruff et al., 1997). If two known blackbody targets are measured, then a system of equations can be solved for the following *IRF*, where the radiance from the instrument cancels.

$$IRF = \frac{V_{hot} - V_{warm}}{BB_{hot} - BB_{warm}} \quad (152)$$

**Instrument energy.** The offset contribution of the instrument can then be calculated using the following equation.

$$\varepsilon B_{ins} = BB_{hot} - \frac{V_{hot}}{IRF} \quad (153)$$

**Emissivity derivation.** Next, the emissivity of the sample can be calculated. The sample temperature was known, so a theoretical blackbody curve was calculated for $B_{samp}$. The radiance of the environment was assumed to be negligible considering the temperature of the blackbody targets, but this was an assumption that needs a bit more investigation. The emissivity and the room temperature are not calculated in this investigation. If geologic samples were measured, then the temperature of the environment would be required to calibrate the emissivity.

$$\epsilon_{PE} = \frac{\frac{V_{PE}}{IRF} + B_{inst} - B_{env}}{B_{samp} - B_{env}} \quad (154)$$

## EXPERIMENTAL DESIGN: DETECTOR DEVELOPMENT AND TEST OF PERFORMANCE APPROACHES

### Microbolometer array retrofit

**CVD diamond acquisition.** An infrared camera that incorporates a retrofitted diamond window was produced through a number of steps. First, a diamond window was designed for use in the existing RVS microbolometer array. The x-y dimensions and metallization layers were acquired from Raytheon Vision Systems (RVS) and relayed to Element 6. The rim of the diamond was coated with layers of specific metals in order to bond the diamond with the metal stand off. The CVD diamond window was fabricated and metalized at E6 and sent to ASU (*Figure 17*).

The diamond window transmission was measured with ASU's Nicolet spectrometer before the diamond was sent to RVS to be retrofitted onto one of their detectors (*Figure 18*). The window was placed over one of the sample cups used to measure powders. The transmission spectrum was the ratio of the spectrum of the diamond and the sample cup over the sample cup alone (*Figure 19*).

**Retrofit of diamond window.** RVS was contracted to retrofit the diamond window onto a detector. Once the detector arrived at ASU, it was inserted into the thermal electric cooler (TEC) board (see *Figure 19*). The system was powered up, but the electronics were not configured properly with the new window. The proper non-uniformity correction (NUC) tables were uploaded onto the electronics and an image was acquired. The tables and parameters had to be reconfigured in the electronics package in order to allow the new detector to capture a clean image. After successfully capturing an image, the detector package was integrated into the optical design (*Figure 20*).

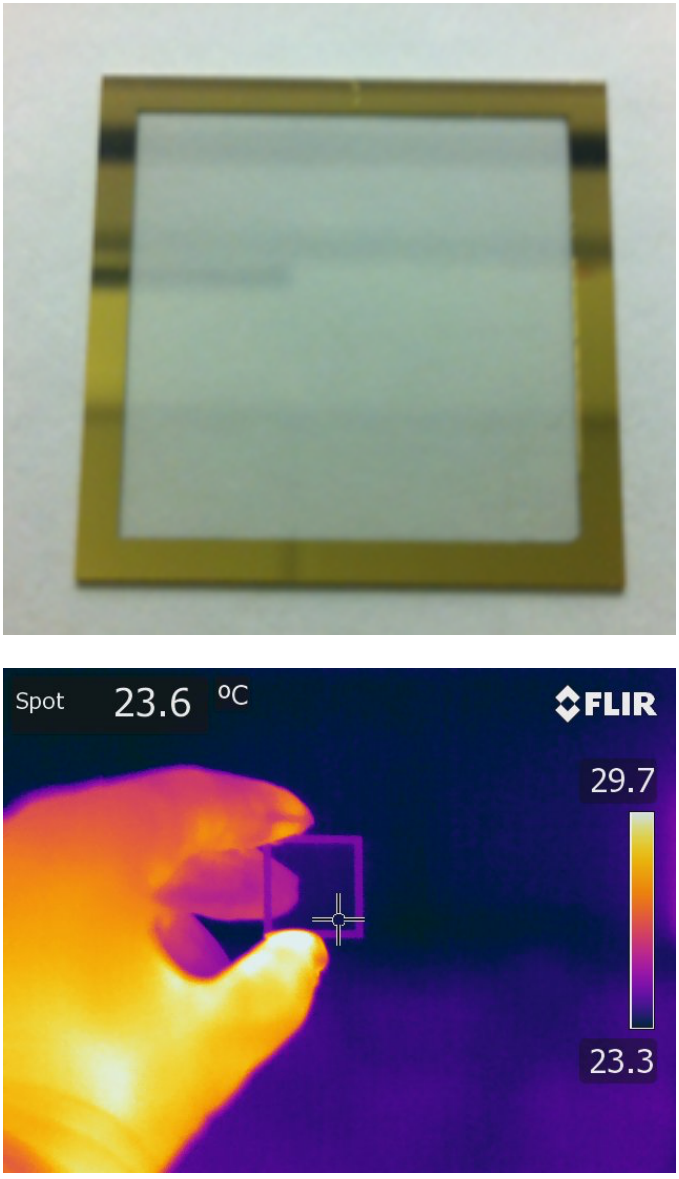


*Figure 17*. CVD Diamond Window. Top) Visible image of the CVD during initial inspection. The rim was metalized for bonding to the microbolometer array. Each side measures 1.01 inches and the diamond was 0.5 mm thick. Bottom) A FLIR IR image of the CVD diamond window. It can be seen that the window was transparent within the sensitivity range of the commercial 8-12 μm FLIR camera. The metalized rim was reflecting the foreground scene temperature.

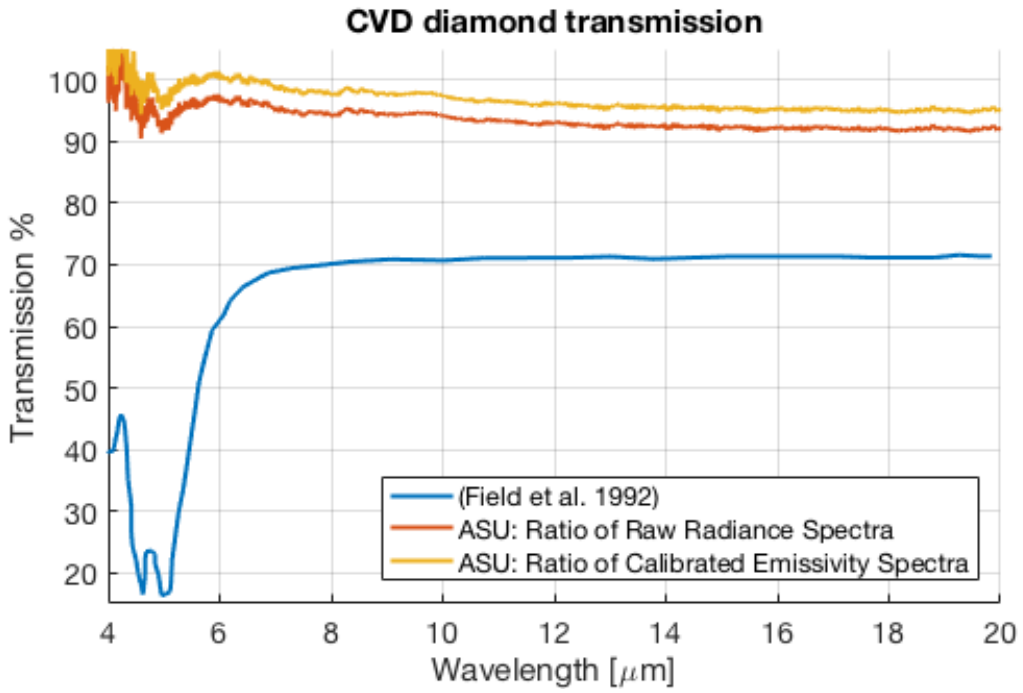


*Figure 18*. Comparison of CVD diamond transmission. The ASU diamond derived here has a lower absorption than that reported by Field presumably due to thickness. Spectra were calculated using a simple ratio of the raw uncalibrated radiance between the sample with and without the diamond. The raw radiance spectra were also calibrated using the ASU spec lab techniques and the output emissivity spectra were then ratiod. The calibrated data assume a point on the spectrum was equal to one, which may artificially inflate the overall diamond transmission. The major absorption doublet centered ~5 μm was observed. The shape of the spectrum was mostly consistent with the CVD spectrum of Field (Field, 1992). A prior experiment had an inversion of the doublet that may have been from emission of the diamond if it were hotter than the blackbody.

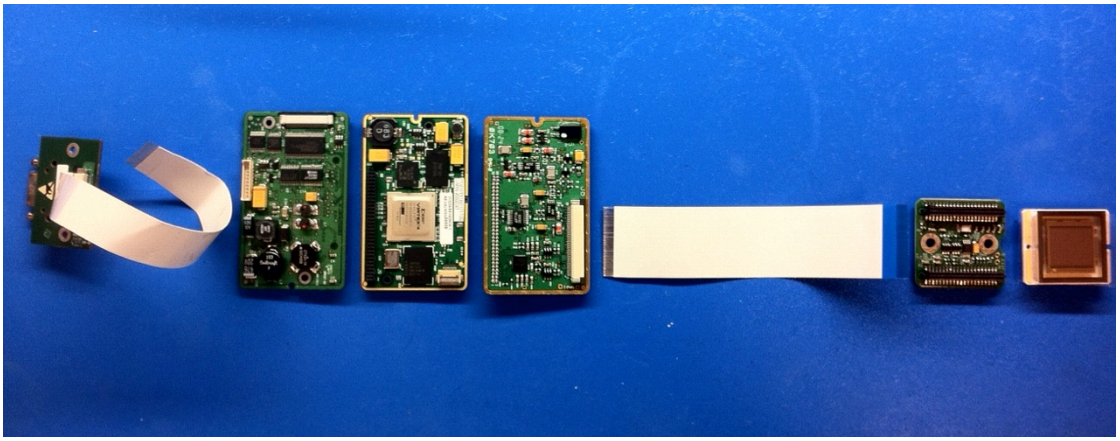

*Figure 19*. From Right to Left 1) Dewar: FPA and TEC in a vacuum package, this particular dewar was an LCP (Large Ceramic Package). 2) Carrier card: analog bias decoupling and output buffer 3) Flex Cable: a few control signals, and many analog signals 4) Analog card: analog to digital conversion, bias generation, and shutter drive circuits. 5) Digital card: digital signal processing in Virtex 4 FPGA, TEC power circuit. (Beige connector was JTAG) 6) Power supply card: input power conditioning and camera link processing chips 7) Flex cable: camera link signals 8) Camera link adapter card: Convert from flex to standard camera link connector.

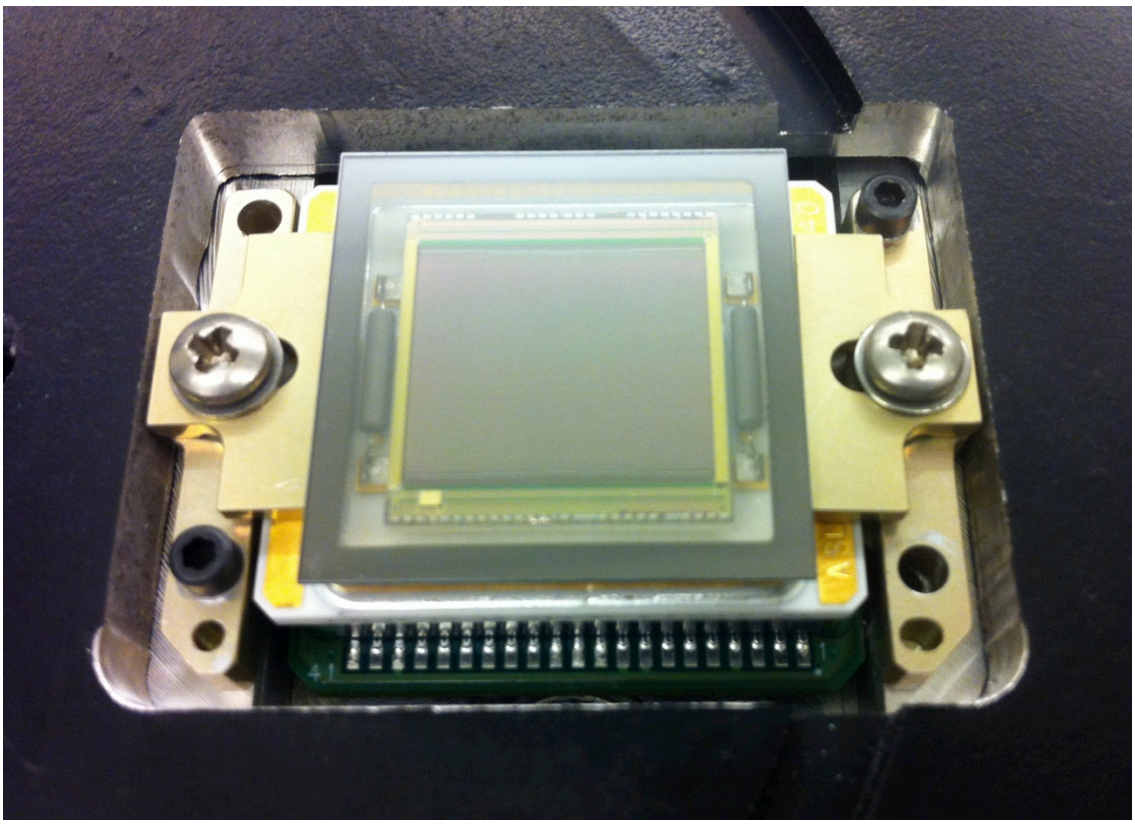

*Figure 20*. Microbolometer array with diamond window. The diamond was 1.01” square and has a metallic frame that was soldered to the “can” that supports the vacuumed seal. The actual detector array was ~2/3 the size of the window.

**Approach 1: Filter method**

**Filter Apparatus, Trades, and Modeling**. The first test apparatus was developed for testing the response using band-pass filters. The optical setup to test the filters with the diamond retrofitted microbolometer array is shown in *Figure 21*.

A filter assembly was necessary to measure spectral response at discrete wavelengths until a sufficient spectrometer would be available. Five filters were initially chosen: 25 μm, 30 μm, 49 μm, 68 μm, and 93 μm. An optical bench was created that emitted blackbody radiation through the filters onto the detector. A broken 50 μm filter was replaced with a 45 μm filter during testing.

The filter functions for the first set of filters were obtained from Thorlabs and multiplied by the theoretical blackbody curve for 100˚ C. As expected, *Figure 23*.A shows that the contribution of the 100˚ C blackbody response at the measured wavelengths was relatively small to the peak. *Figure 23*.B shows that there was a significant contribution of signal outside of the nominal bands for each filter. The longer filters are completely compromised, as the leakage was more significant than the band. The shorter filters, while yielding more in-band signal, still have significant out-of-band-leakage.

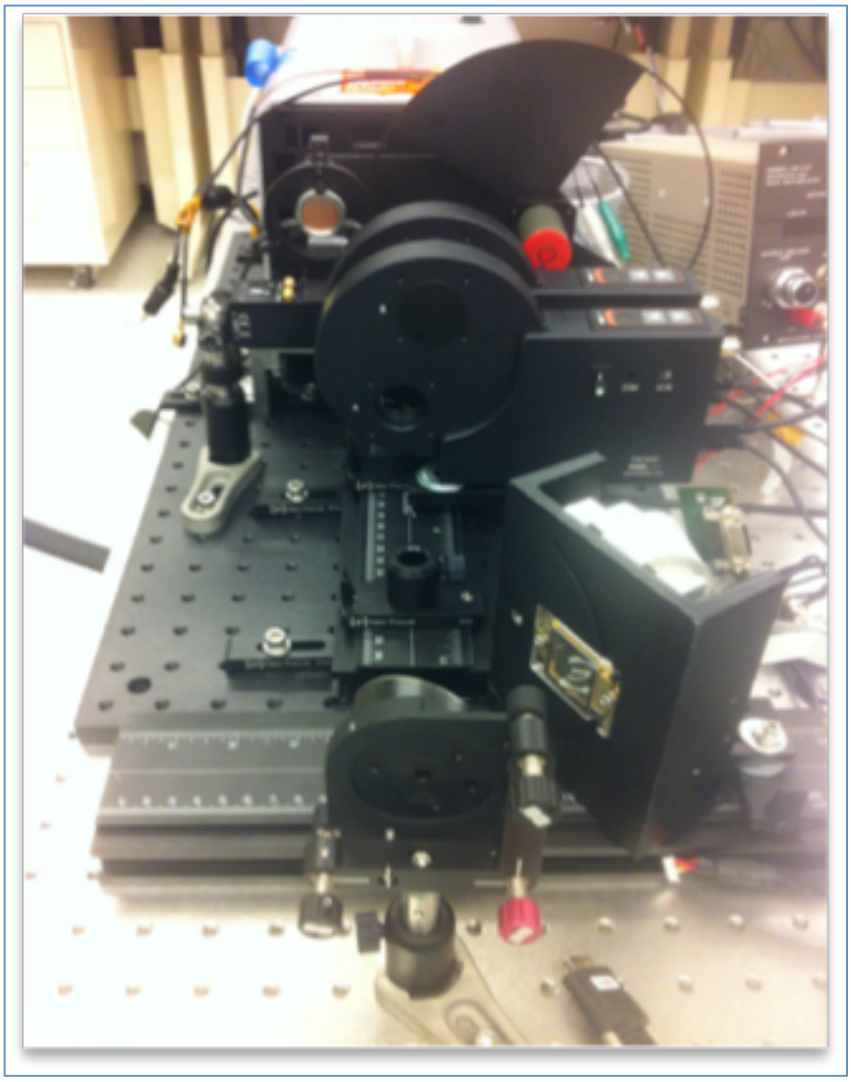

*Figure 21*. Filter test bench setup. A blackbody source radiates energy along the optical path. A chopper was integrated to allow the radiation to be easily blocked during testing. The 30 μm long-pass filter was mounted into a servo arm that allows it to be dropped in and out of the optical path. Two automated filter wheel carousels allow the filters to be set in the optical path. The filtered light passes onto a parabolic mirror that focuses the energy onto the microbolometer array.


*Figure 22*. Gold THz band-pass filters in filter wheel. As a practical concern, extreme caution was necessary with the filters.

Table 3

*THz Filters*

| Position | Filter Center Wavelength | FWHM | Transmission |
|---|---|---|---|
| 1.1 | Open | Atmosphere | Atmosphere |
| 1.2 | 25.82 μm | 0.096 | 0.816 |
| 1.3 | 29.6 μm | 0.161 | 0.888 |
| 1.4 | 43.62 μm | 0.143 | 0.886 |
| | 49.0 μm | 0.187 | 0.885 |
| 1.5 | 67.64 μm | 0.188 | 0.808 |
| 1.6 | 93.23 μm | 0.211 | 0.813 |
| 2.1 | Open | Atmosphere | Atmosphere |
| 2.2 | 14.32* μm | 0.159* | 0.874* |
| 2.3 | 33.89* μm | 0.116* | 0.854* |
| 2.4 | 61** μm | 0.16** | 0.88* |
| 2.5 | 80.47 μm | 0.223 | 0.927 |
| 2.6 | 101.37 μm | 0.258 | 0.815 |

* Estimates from measured spectra

** Digitized sample transmissions from website.

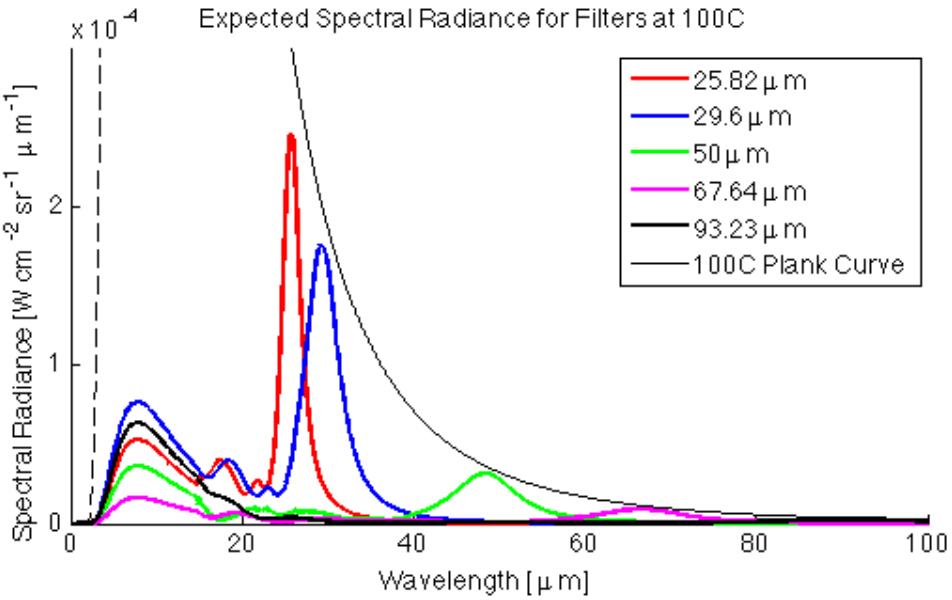


*Figure 23*. Expected spectral radiance of filters for a 100˚ C blackbody. It was evident that there was out of band leakage at the peak of the plank curve.

**Long-pass filter design.** A long-pass filter was incorporated to block the out-of-band leakage. QMC has >15 μm, >24 μm, >30 μm, and >50 μm long-pass options. The later three were digitized and used to determine how much leakage they would prevent. The 30 μm filter was chosen, because much of the leakage at longer filters occurs at wavelengths greater than 20 μm. *Figure 24* shows the resulting expected throughput of a 100˚ C theoretical blackbody using these digitized long-pass filters with the band-pass filters. The plot shows that 1) the 24 μm long-pass filter was sufficient for blocking the leakage for the 30 μm filter, but still allows leakage for the longer filters, 2) the 30 μm long-pass filter blocks the 30μm band-pass filter while blocking most of the leakage from the longer band-pass filters with minimum degradation to the desired signal, and 3) the 50 μm long-pass slightly improves the leakage blocking for the 90 μm and 100 μm band-pass filters, but it significantly cuts into the 50 μm band-pass filter. The 30 μm long-pass filter was chosen, because it was the best compromise of blocking leakage while maintaining response for the longer (50+ μm) band-pass filters. The analysis was shown in *Figure 24*.The 30 μm long-pass filter was ordered and integrated into the optics assembly (see *Figure 21*).

**Long-pass Filter Testing.** The band-pass filters were placed into the Nicolet sample chamber with the 30 μm long-pass filter in order to measure the effect of blocking the shortwave response. The radiation that leaks through wings of the band-pass filters was compared before and after the filter was inserted into the optical path for each filter.

The measured filter spectra, shown in *Figure 25*, show the effects of using the long-pass filter. The spectra clearly show measured response leaking outside of the filter bands. This leaked signal was mostly suppressed with the 30 μm long-pass filter. There was some residual leakage in the 45+ μm filter when analyzed, however the leakage

<30μm was significantly reduced compared to the leakage that was previously present. The measured remaining leakage for the 60+ μm filters was expected to still be significant, as was modeled in the previous section. For the filters >45 μm, the limitation of the Nicolet's far wavelength response does not allow us to compare the measured leakage to the expected in-band response. Further analysis of the >45 μm region will require another long-pass filter or multiple band-pass filters. The response of the 45 μm filter was nearly entirely within band. From the model in the previous section, an additional long-pass filter at ~50 μm would be required to suppress the leakage when viewing a 100° C blackbody. Using multiple band-pass filters was an alternative strategy.

**Calibration Pipeline.** A response function was created with band-pass filters. For each filter, the detector was FLE'd with both open filters and an image was captured of the flag, the filter was then placed in front of the detector and an image was captured of the blackbody, finally the filter was removed and the flag was reimaged. This process allowed the drift to be measured for each filter and the average value between the imaging of the flags before and after the filter was subtracted to determine the ΔDN from the ambient flag. Furthermore, performing FLE through each filter independently on the flag ensures that any reflections of the detector are calibrated out. The calibration pipeline was shown in *Figure 26*.

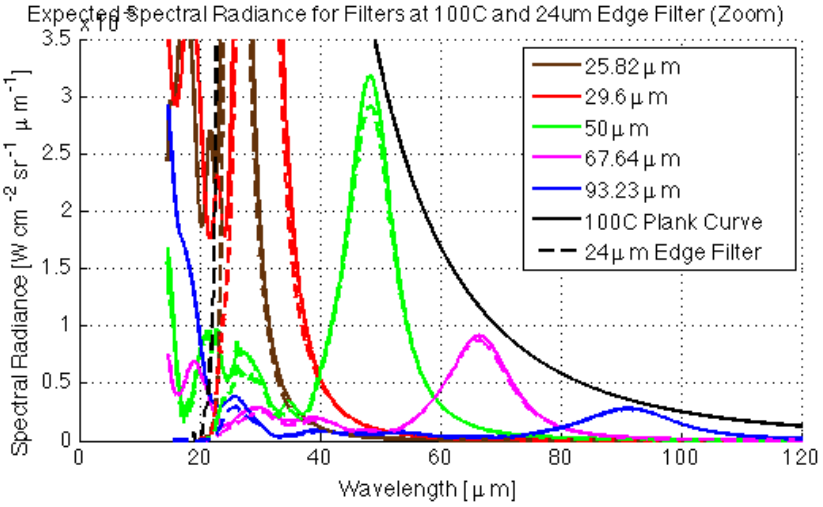
Expected Spectral Radiance for Filters at 100C and 24um Edge Filter (Zoom)
x 10^-5
Spectral Radiance [W cm^-2 sr^-1 μm^-1]
Wavelength [μm]
25.82μm
29.6μm
50μm
67.64μm
93.23μm
100C Plank Curve
24μm Edge Filter

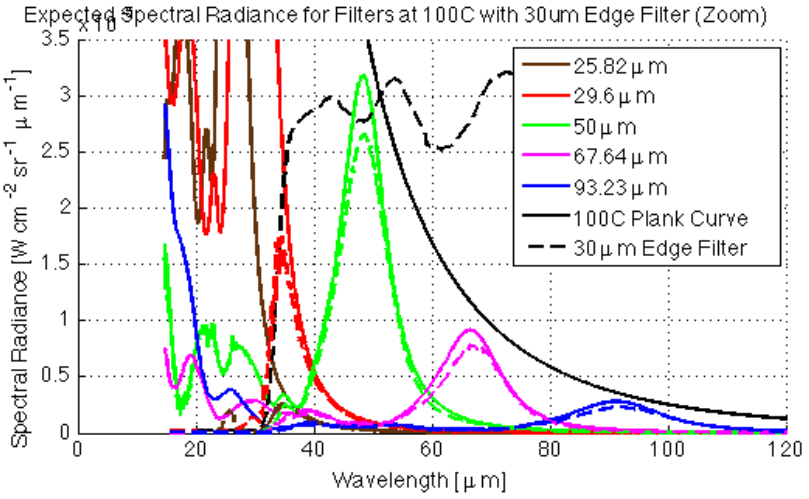
Expected Spectral Radiance for Filters at 100C with 30um Edge Filter (Zoom)
x 10^-5
Spectral Radiance [W cm^-2 sr^-1 μm^-1]
Wavelength [μm]
25.82μm
29.6μm
50μm
67.64μm
93.23μm
100C Plank Curve
30μm Edge Filter

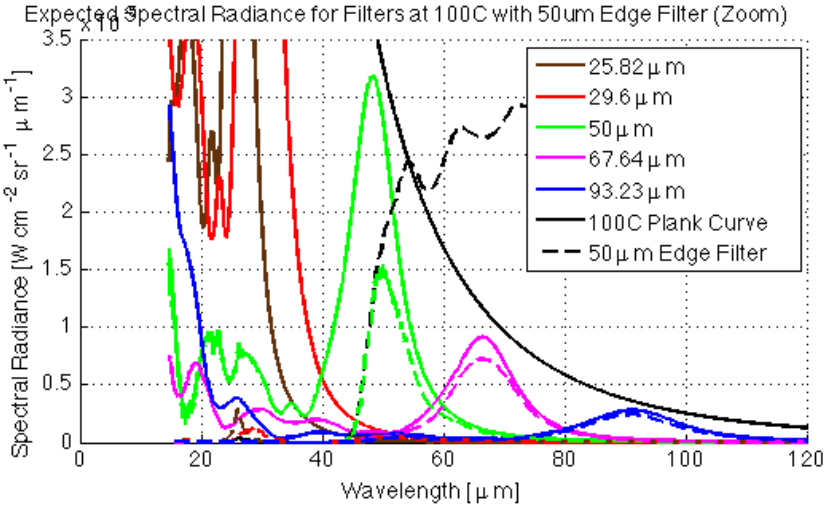
Expected Spectral Radiance for Filters at 100C with 50um Edge Filter (Zoom)
x 10^-5
Spectral Radiance [W cm^-2 sr^-1 μm^-1]
Wavelength [μm]
25.82μm
29.6μm
50μm
67.64μm
93.23μm
100C Plank Curve
50μm Edge Filter

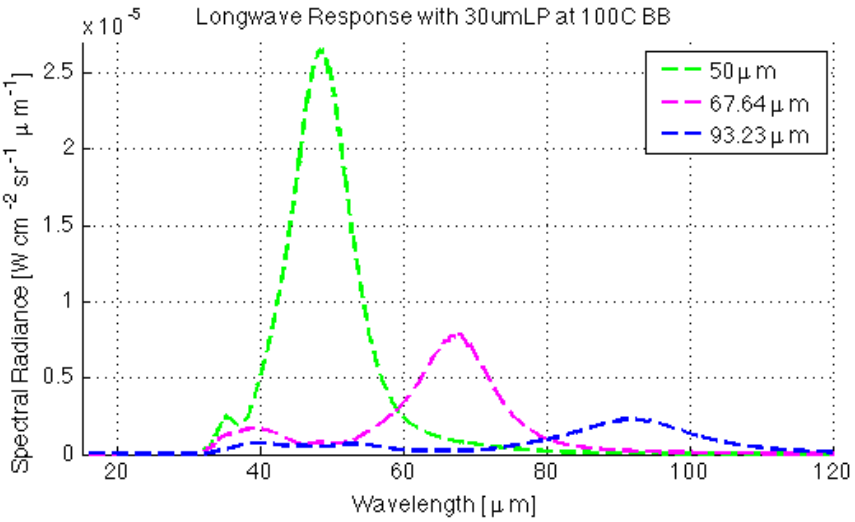


*Figure 24.* Expected spectral radiance of filter functions with and without long-pass filter. The plots are from top to bottom using a 24 μm, 30 μm, and 50 μm filter. The dashed lines represent the multiplication of the edge filter with the filter function and the theoretical 100C blackbody. The plots are zoomed to focus on the effects of the longer (50 μm, 70 μm, and 90 μm) wavelength filters. The transmission function of the filters was divided by 1E5, 3E5, and 3E5 respectively in order to show its relative effect on the response. Finally, the response of the 30 μm long-wavelength filter with the longer band-pass filters was shown alone to show the relative contributions of the band-pass and the leakage.

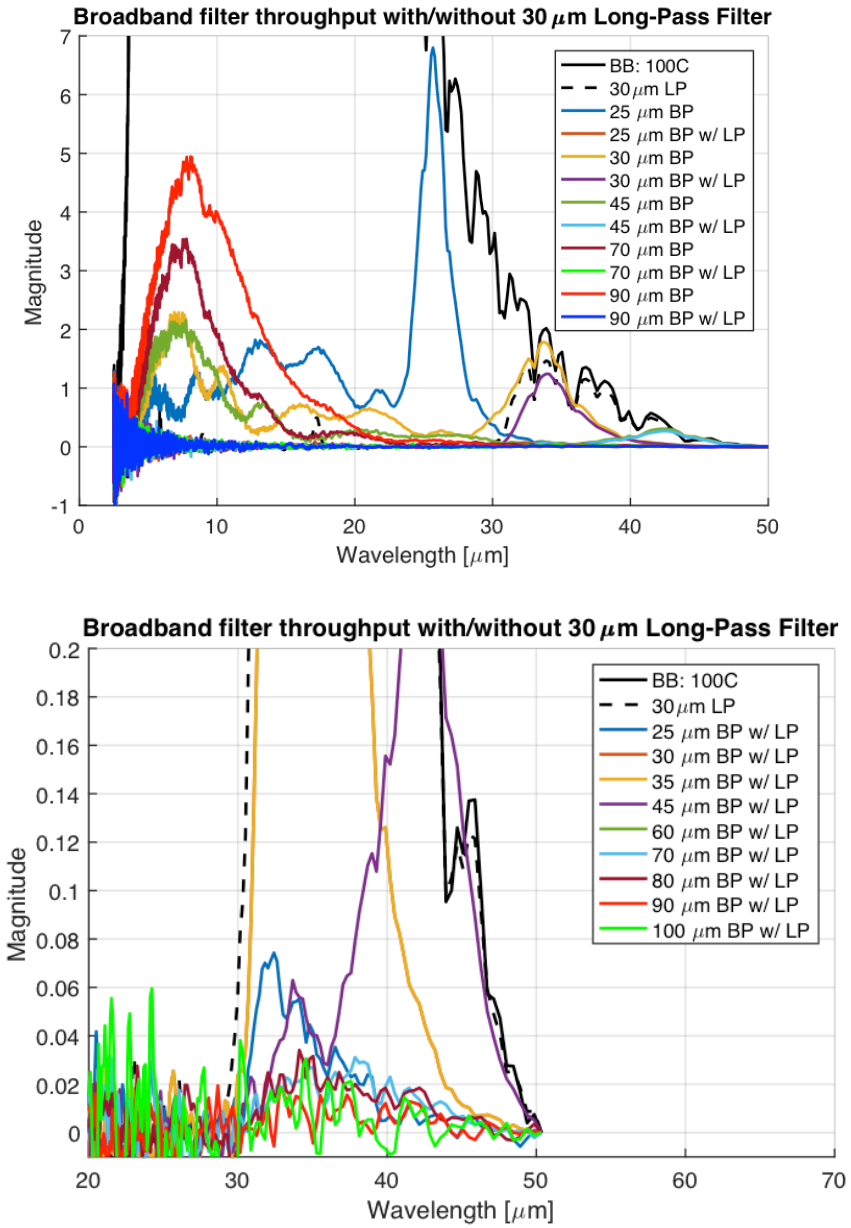


*Figure 25.* Response and transmission for 100° C blackbody with the 30 μm long-pass. Top) The response of select bandpass filters with and without the longpass filter. Bottom) All band-pass filters are plotted with the long-pass filter. There was still leakage for the band-pass filters even with a long-pass filter. This may be insignificant for the shorter filters (e.g. 45 μm), but the remaining leakage may be comparable or greater than the response of the longer filters (e.g. 60+ μm).

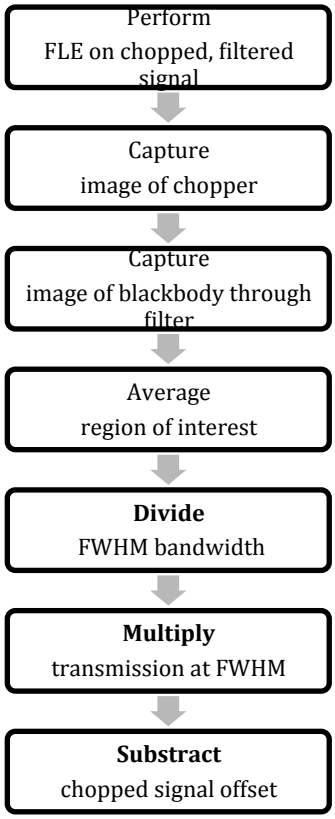


*Figure 26*. Calibration pipeline for filter exploration.

**Approach 2: Interferometer method**

The second experimental apparatus integrates the diamond microbolometer array and electronics with the OTES diamond interferometer. A schematic was shown in *Figure 27*, and an image was shown in *Figure 28*. The blackbody source emits light onto a fold mirror that passes light through a field stop to a collimating mirror. The collimated light passes into the interferometer. Half the recombined energy was reflected off a focusing mirror to a fold mirror that focuses the light on the microbolometer array.

Because the maximum sampling interval was limited by the frame rate of the camera core, the interferogram was sampled at 30 Hz or 0.033 seconds. Typical interferometers are sampled at equal intervals of distance—when there was a zero crossing of the moving mirror laser. Instead of triggering the image capture at laser zero crossings, images are captured at known time intervals. This does require a very well controlled moving mirror velocity, so there was some resultant error associated with the subtle errors in the moving mirror velocity from either the waveform generator. The distance of the mirror was measured with an auxiliary interferometer.

A LabView VI controls the system, to observe the data, and to save desired data (*Figure 29*). The VI provides centralized control of the following systems: the waveform generator for the moving mirror, the microbolometer array electronics, and computer data acquisition. The VI also provided a custom all-in-one readout of the following data: infrared image of the blackbody through the field stop, pixels that are averaged for the interferogram, histogram counts of the images, charts of the running values of the moving mirror displacement and the interferogram, graphs of all the collected data, an on-the-fly FFT. The interferograms are collected for ~3 hours to produce ~100 interferograms viewing a 140˚ C, 300˚ C, and 600˚ C blackbody (*Figure 30*). The interferogram-processing pipeline was shown in *Figure 31*.

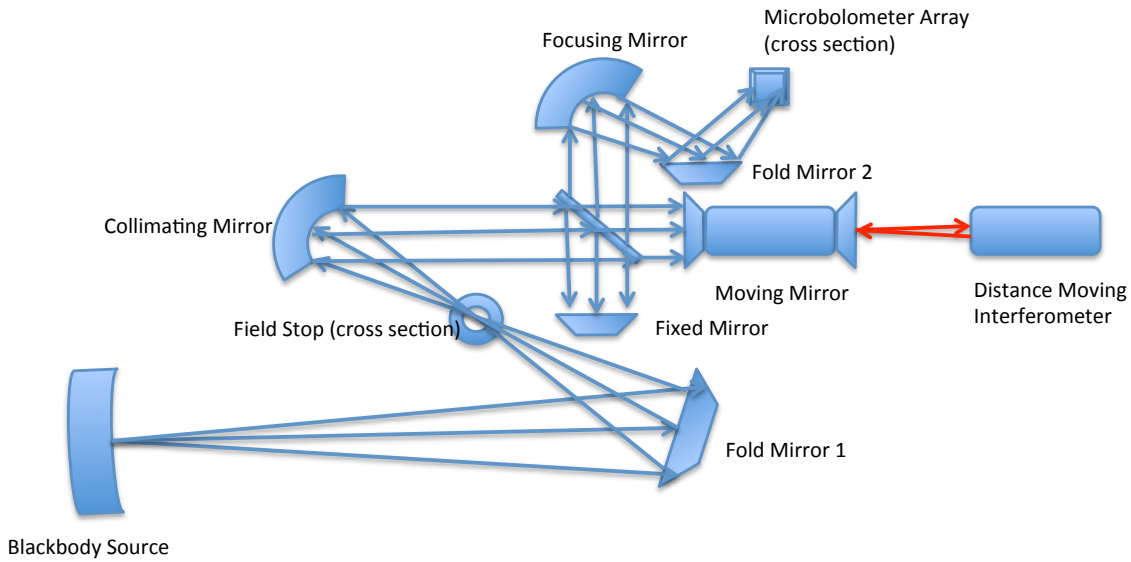


*Figure 27.* Simplified schematic of the optical path from a blackbody source through OTES engineering model to the microbolometer array.

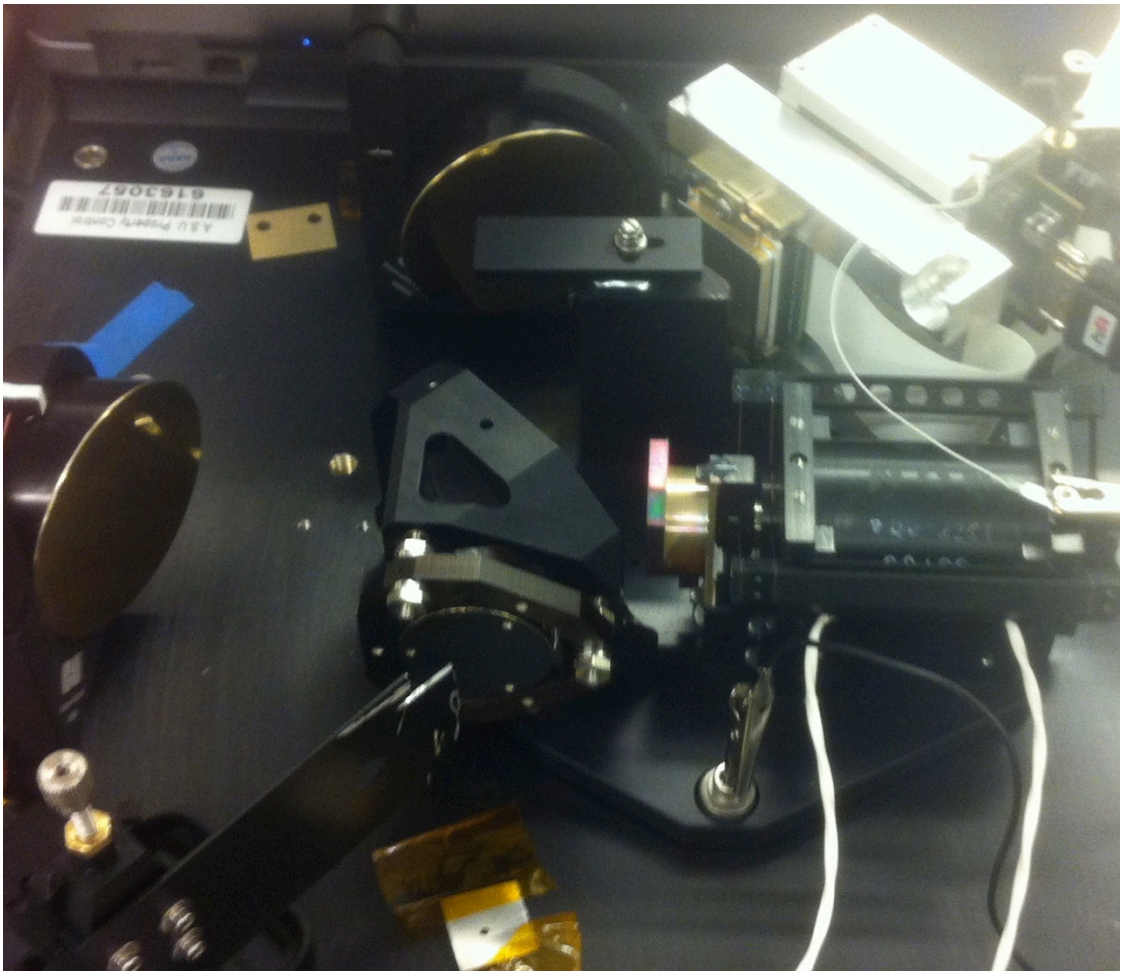

*Figure 28*. The interferometer test setup.

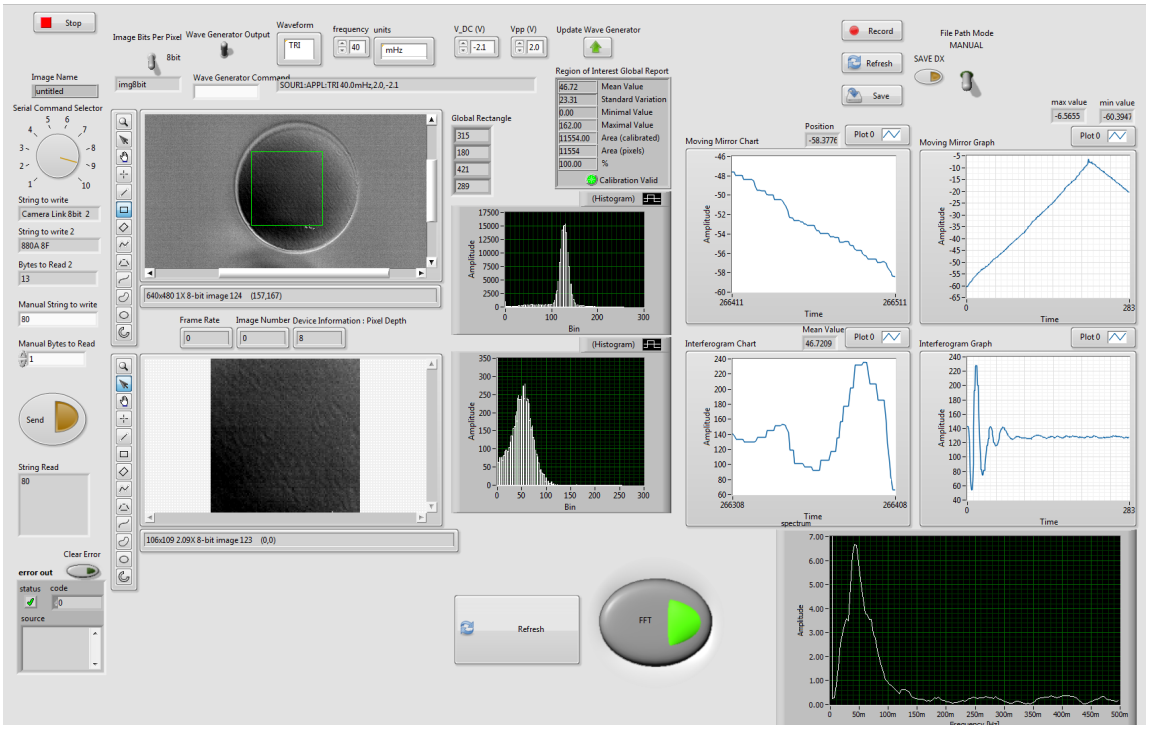


*Figure 29*. LabVIEW frontpanel.

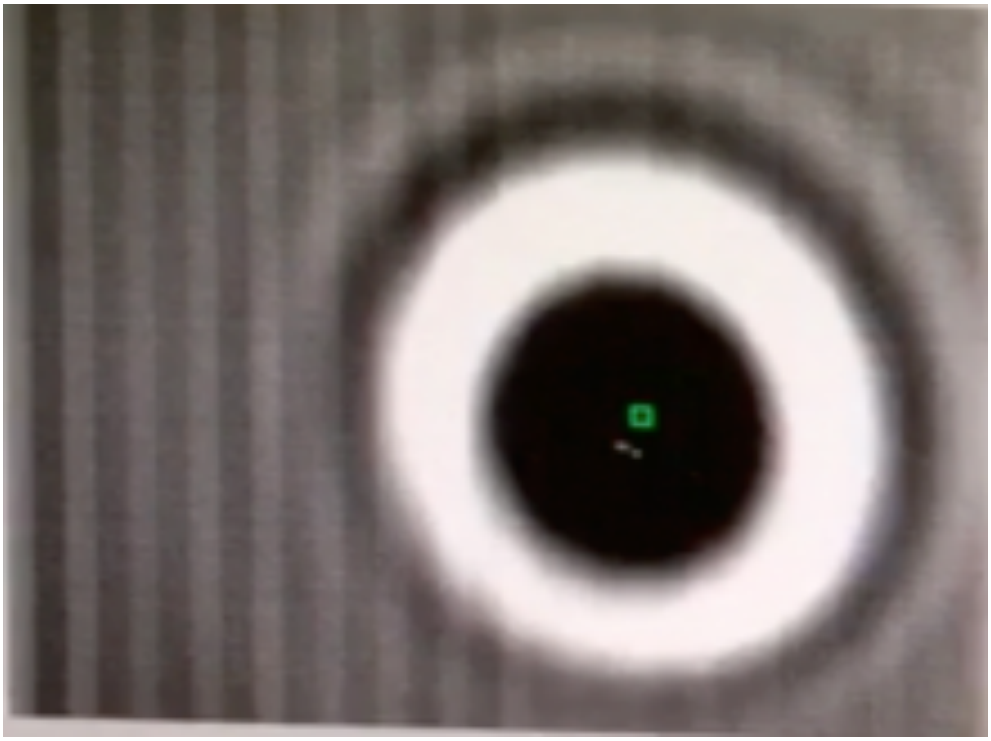

*Figure 30*. A screenshot of the frontpanel showing the real-time interferogram. An example of the final interferogram alignment, shown in the top left image, was much sharper and geometrically improved than the first image captured. The bright doughnut around the dark circle in the center corresponds to the ZPD peak. This was the first known image of an interferogram captured with a diamond microbolometer array.

Caption for next page.

*Figure 31*. Processing pipeline of interferogram data.

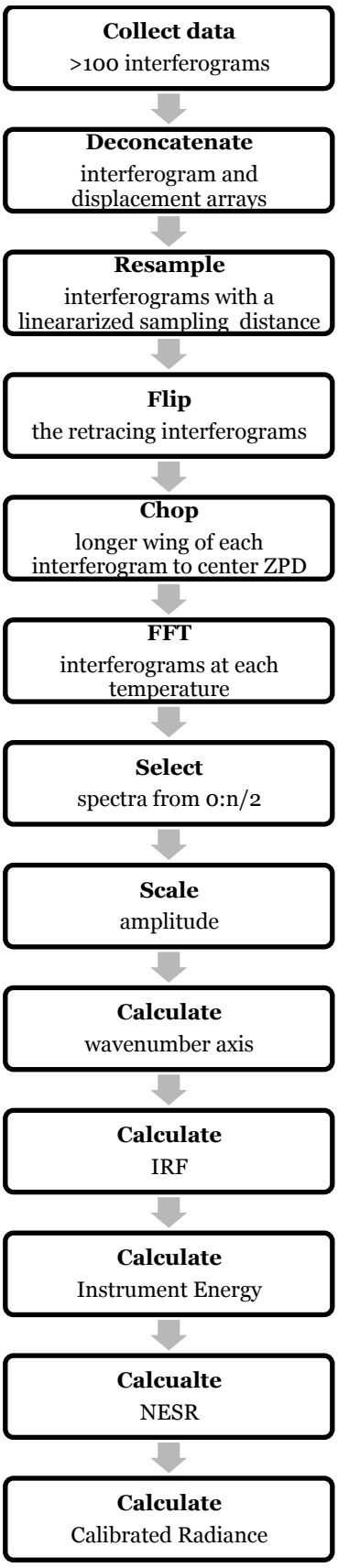
Collect data
>100 interferograms
Deconcatenate
interferogram and displacement arrays
Resample
interferograms with a linearized sampling distance
Flip
the retracing interferograms
Chop
longer wing of each interferogram to center ZPD
FFT
interferograms at each temperature
Select
spectra from 0:n/2
Scale
amplitude
Calculate
wavenumber axis
Calculate
IRF
Calculate
Instrument Energy
Calcualte
NESR
Calculate
Calibrated Radiance

## RESULTS FOR FILTER METHOD

Filtered images were processed to produce a spectrum (*Figure 32*). A 100˚ C blackbody at similar wavelengths was plotted, and the axes are scaled for comparison. The measured response trend matches the plank curve better than initial tests without the long-pass filter; however, there was some small variation at long wavelengths that may be attributed to further leakage. Only one temperature was collected for the final test of the long-pass filter, so an IRF was not computed. The images are included in the appendix.

The results indicate that 30 μm long-pass filter blocked most of the response, as expected, that leaked through the bandpass wings. However, it appears that there was residual leakage of the shorter 15 μm and 25 μm filter, so obtaining a ~10 μm long-pass filter was useful to better calibrate these short response bands. While the majority of the leakage in the longer filters appears blocked, the signal was weak, and it was impossible to determine how much of the signal was residual leakage. Obtaining a ~50 μm long-pass will be useful to better calibrate the long filters in conjunction with the 30 μm long-pass. Alternatively, multiple filters of the same bandpass could be stacked. In addition, capturing the data at a higher bit depth could help differentiate the small signals. More filters and higher bit depth will likely expand the results to produce a filter-based IRF.

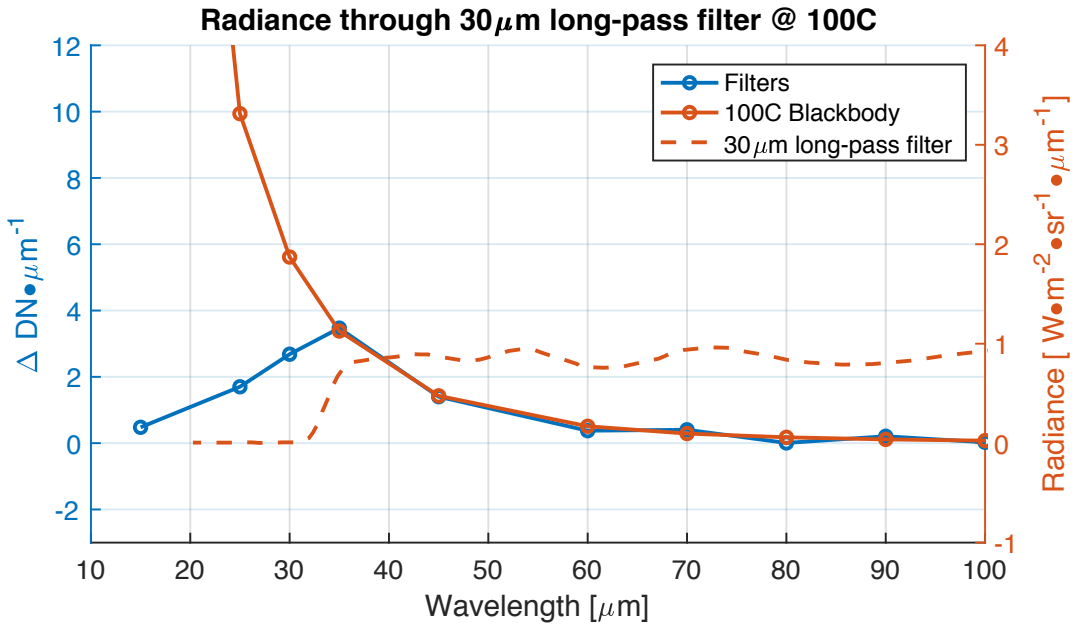


*Figure 32*. A DN radiance spectrum was produced via the calibration pipeline for pixels averaged in rows 175-200 and columns 330-350. The response can be scaled to almost identically match the blackbody spectrum—though two temperatures are truly needed to compute the IRF. Furthermore, the long-pass filter transmission was plotted. The filtered response, below the long-pass filters, was significantly, but not totally, reduced. This likely further leakage from the exponential increase input radiance.

## RESULTS FOR INTERFEROGRAM METHOD

### Detector Performance

An IRF was produced that characterizes the whole optical system: the interferometer, the optics, and the detector. The IRF shows that the peak response begins to decrease at ~500 $cm^{-1}$ or ~20 μm and reaches its minimum at ~285 $cm^{-1}$ or ~35 μm (*Figure 37*).

To achieve this, interferograms were recorded with the microbolometer array (*Figure 33*). The interferograms were processed into spectra following the pipeline (*Figure 35*). The standard deviation of the DN spectra was produced (*Figure 36*). For this experiment, the standard deviation increased with temperature.

The IRF in wavelength space was produced and shows the deep absorption ~5 μm and the return to peak transmission at ~3.5 μm (*Figure 38*). The IRF was compared with microbolometer array response of Touvignon et al. and the transmission of CVD from Field(Field, 1992; Touvignon et al., 2014). The shape of the IRF produced here reasonably matches the response of the previous microbolometer array response between the intervals that microbolometer arrays are typically designed (7-13 μm). The far wavelength response was extended to at least 20 μm before beginning to decrease.

The IRF and the RI are used in order to predict the response of the opposite blackbody temperature. While the calibrated response closely matches the expected blackbody for much of the region of interest in long wavelength infrared spectroscopy, the prediction begins to diverge ~1400 $cm^{-1}$. This was where the IRF was significantly reduced and where the diamond transmission begins to decrease.

The noise equivalent signal resolution (NESR) quantifies the precision of the instrument. Because of thermal instabilities of the detector, a reasonable estimate of NESR was difficult to obtain.

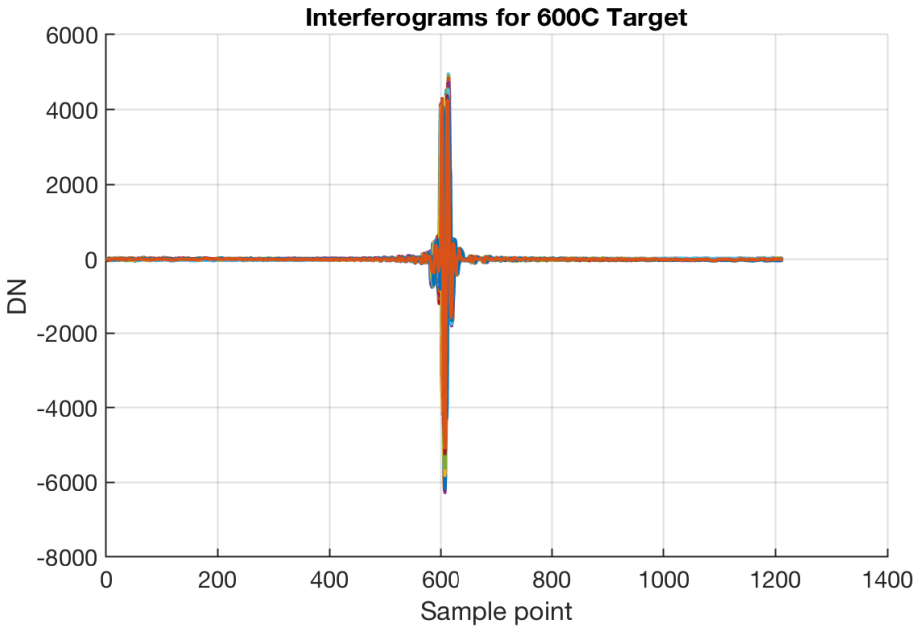


*Figure 33*. Processed re-sampled interferograms for a 600˚ C target.

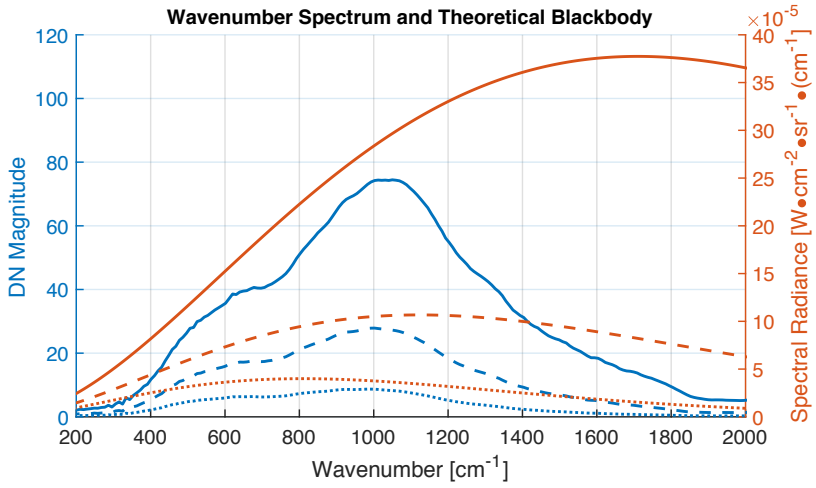


*Figure 34*. The DN magnitude plotted with the corresponding blackbody radiance for the three tests in the wavenumber range of interest. The solid line was 600˚ C, the dashed line was 300˚ C, and the dotted line was 140˚ C. The deep decrease in response was the absorption of diamond

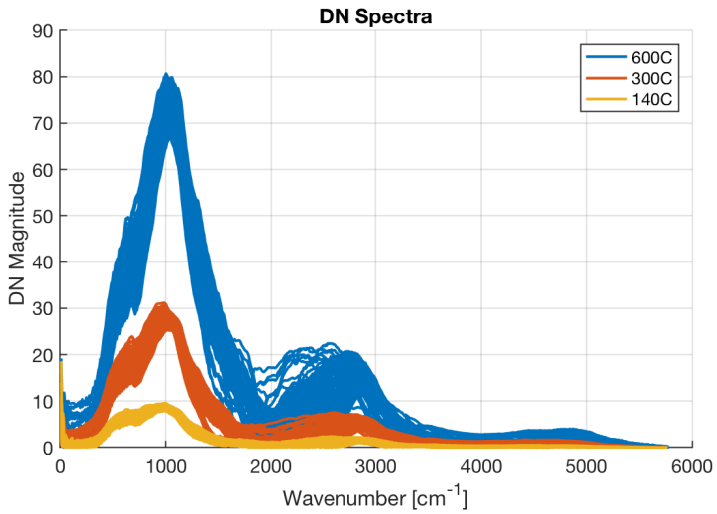


*Figure 35*. Top) The 10mHz waveform spectra for a 140° C, 300° C, and 600° C blackbody. These spectra were resampled before being Fourier transformed. The resampling corrects for the moving mirror non-linearity. The effect was to lower the response at long wavenumbers.

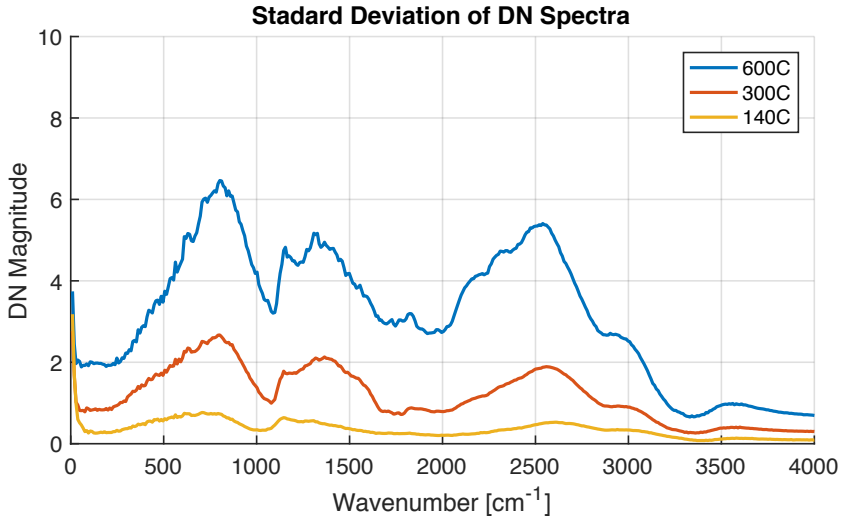


*Figure 36*. Standard deviation of DN spectra.

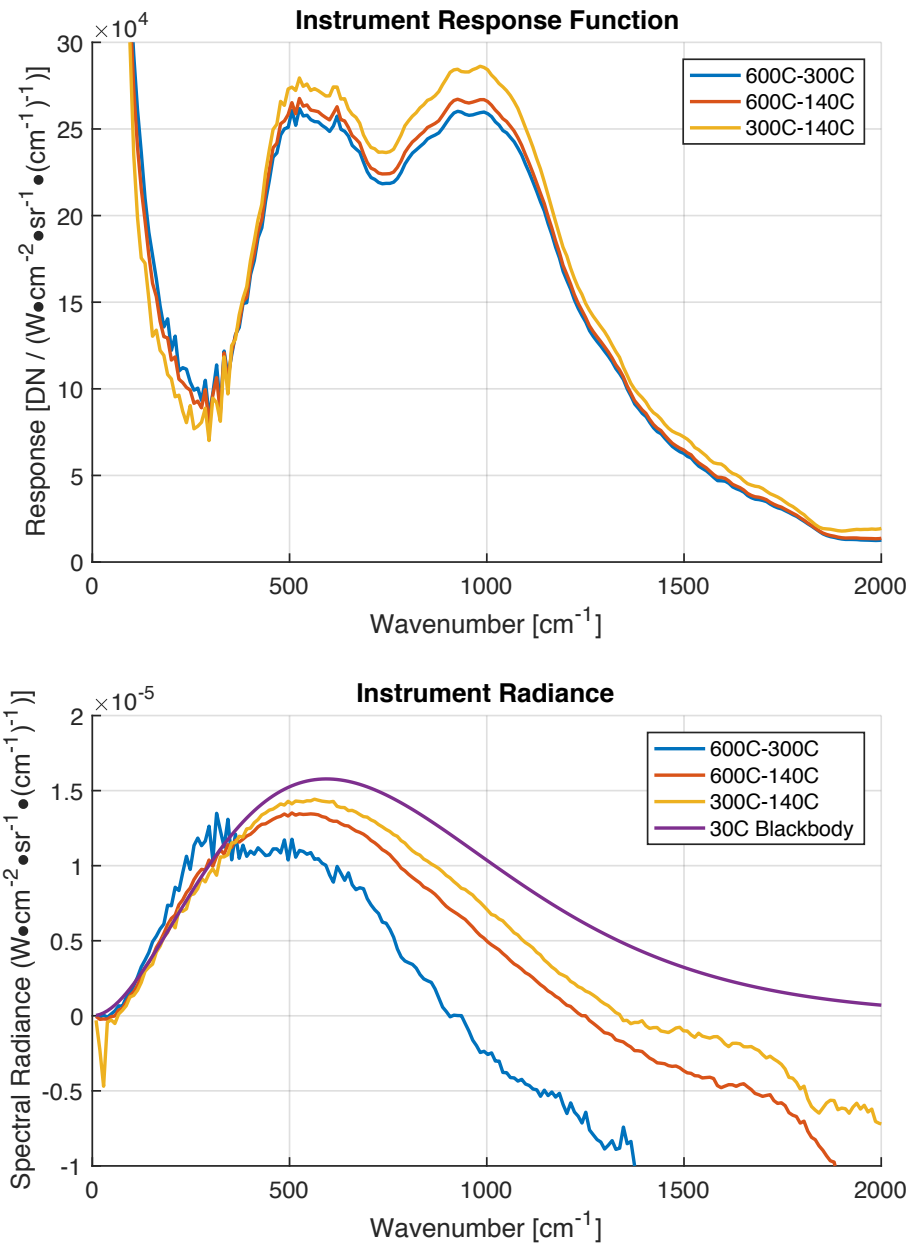


*Figure 37*. Top) The IRF from three permutations of temperatures. Bottom) The instrument radiance from the three permutations of temperatures. A 30° C blackbody was plotted as well to show that the instrument radiance nearly matches the blackbody. The instrument temperature was not recorded though, so this temperature could be +/- 10° C. At wavenumbers >1000cm$^{-1}$, the diamond transmission blocks the instrument radiance.

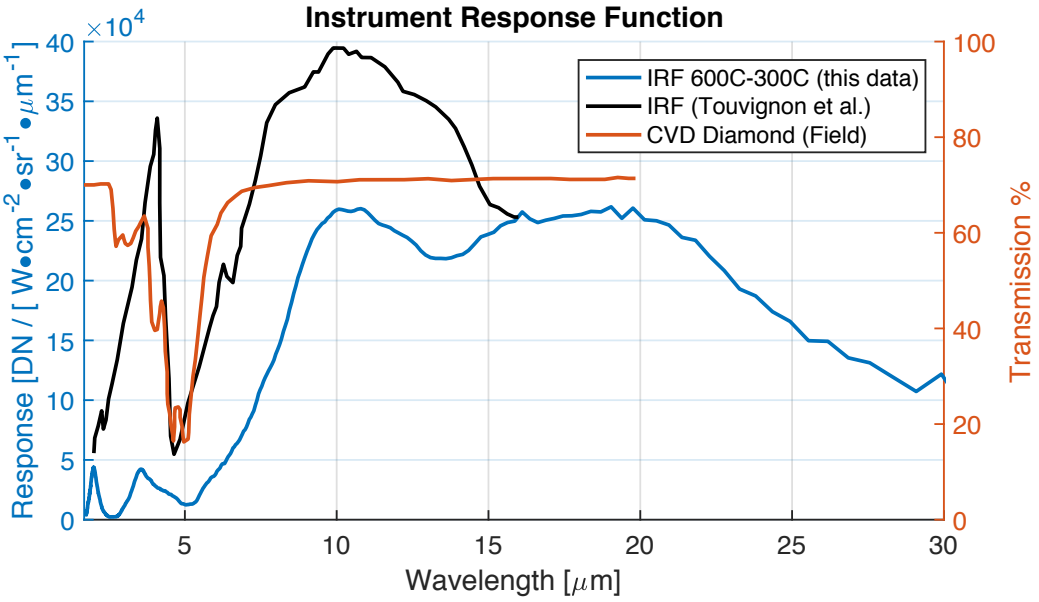


*Figure 38*. The wavelength IRF from this research compared to the wavelength response (reported as 0-100%) of Touvignon et al.(Touvignon et al., 2014). A CVD diamond spectrum for a 1.2 mm thick diamond was presented as well (Field, 1992). The IRF axis produced in this research was chosen to provide enough offset to compare the spectra. The shape of the spectra look similar between 7-13 μm. The broader absorption in the data centered on 6 μm was likely from the diamond window. The peak in Touvignon et al. was ~4 μm, while the peak in this data was ~3.5 μm. This was likely a result from the diamond transmission. The IRF from Touvignon et al. continues to decrease for wavelengths above 13 μm, whereas it does not begin to decrease in the IRF produced here until ~20 μm.

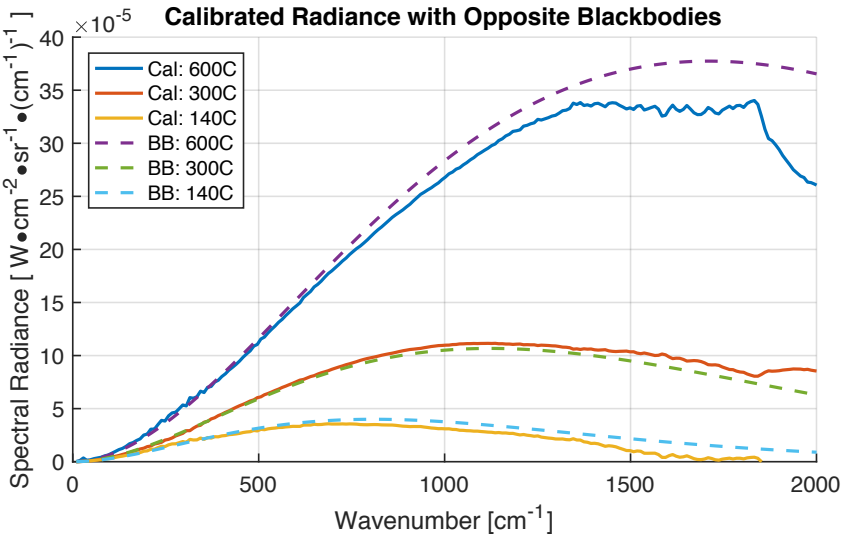


*Figure 39*. Calibrated blackbody response. The IRF and the RI from *Figure 37* are used to predict the blackbody radiance of the third temperature. The divergences of the data was likely a result of the diamond transmission function and the decrease in instrument response.

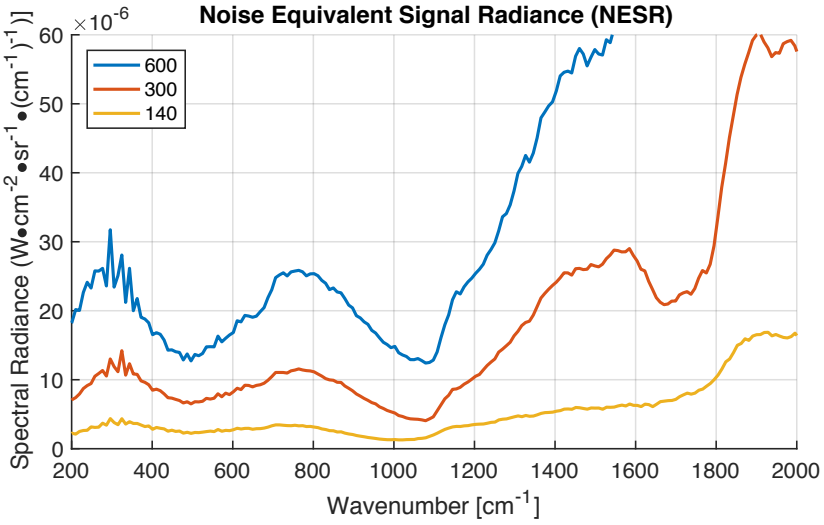


*Figure 40*. Noise equivalent signal radiance. The standard deviation from *Figure 36* was divided by the IRF from *Figure 37*.

**Sources of experimental error**

**Peak to peak variation.** There was observed drift of the minimum and maximum points on the interferogram. This could either be a long-term drift in the temperature of the detector, or it could be associated with a sampling bias. Thermal drifts are a characteristic of infrared detectors, and the temperature of the detector was not measured. The detector may not have imaged the interferogram at exactly the same position. The moving mirror did not use a laser for high precision measurement. Instead the microbolometer array relied on the imaging frequency, which may have fluctuated as well. In any case, the errors certainly decreased the precision of the spectra as evidenced by the NESR.

**Scan mirror inconsistencies.** The moving mirror displacement was not linearly sampled by the DMI (*Figure 42*). It was assumed that the images are sampled linearly at a constant frequency. When the interferograms were resampled to a modeled linear interferogram for the analysis in this paper, the response at ~5000 $cm^{-1}$ in the spectrum dropped. The effect of vibrational sinusoidal sampling error was to create false peaks in the response at greater wavelengths pg. 73 (Saptari, 2004).

**Thermal drift.** Detectors drift was observed during the experiments. It was likely that thermal drift of the detector, witnessed from the peak variation, was responsible for much of the noise. The detector could become more stable to make it easier to measure the NESR. A better estimate of the NESR, through better temperature control of the detector, will also increase the expected SNR of future instruments.

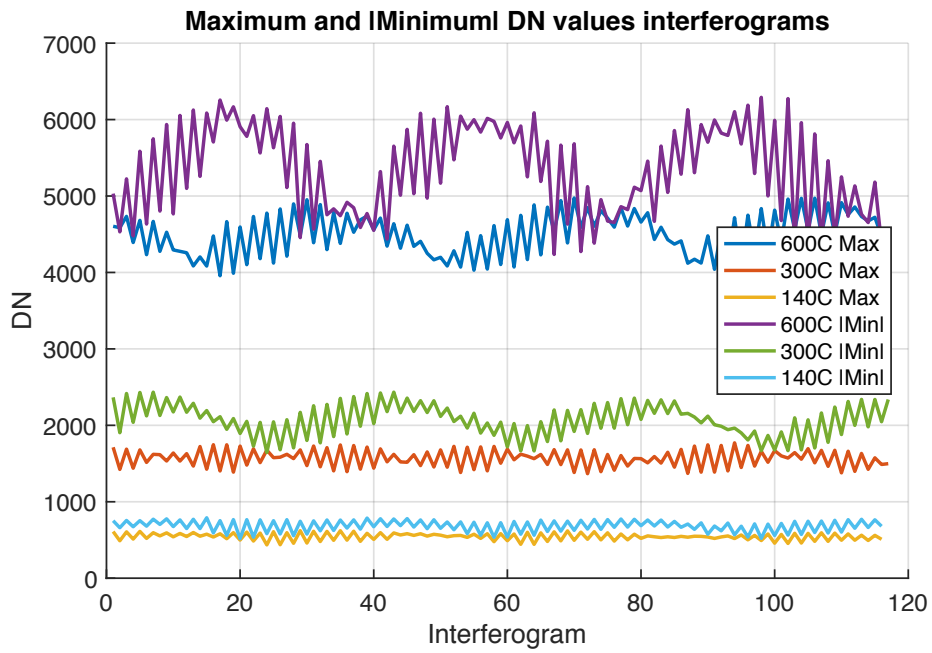


*Figure 41*. The maximum and absolute value of the minimum of each raw interferogram. The maximum and minimum values oscillate at a period of ~40 interferograms.

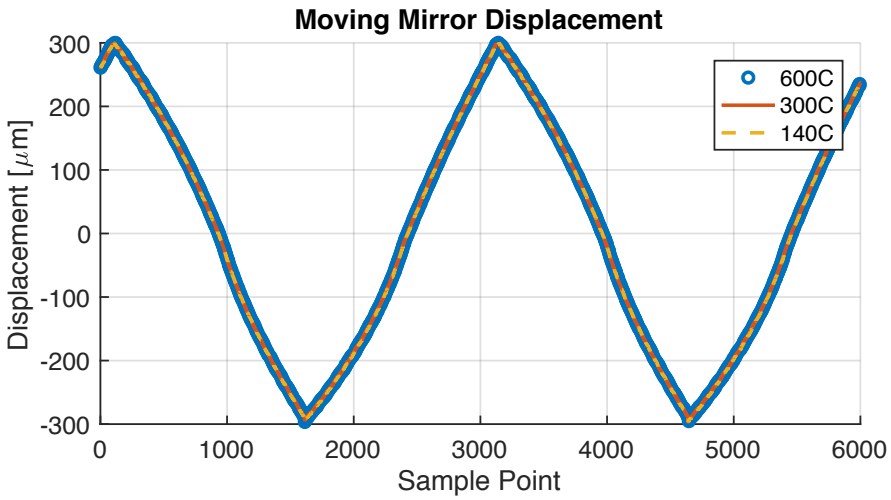


*Figure 42*. Moving mirror displacement for four interferograms show unsteady moving mirror velocity.

**Summary of successful points**

1. Instrument Response Functions are produced from averaged spectra at three different temperatures.
2. This IRF shows that the peak response begins to decrease at ~500cm$^{-1}$ or ~20 μm and reaches its minimum of ~40% at @285 cm$^{-1}$ or ~35μm.
3. Interferogram images were captured with the diamond retrofitted microbolometer array.

**EXAMPLE APPLICATION: A LONG-FAR INFRARED CAMERA FOR EUROPA**

One of the principal motivations for this project was to develop an infrared camera that would be suitable for cold bodies in the outer solar system such as Europa. An example would be Europa with a surface temperature of ~100 K, where the peak emission was 29μm/197cm$^{-1}$.

The instrument response function produced here was plotted along with a plank curve for Europa (*Figure 43*). Although the peak energy lies outside of the response function produced here, there was energy that intersects the instrument response function. The reliable region of overlap was ~10-30 μm. Based upon this information, possible filters can be chosen for a multispectral infrared camera.

Table 4

*Filter Possibilities*

| Justification | Filter Center Wavelength | FWHM % | $\Delta\lambda$ (μm) | $\lambda_{min}$ (μm) | $\lambda_{max}$ (μm) | Trans. |
|---|---|---|---|---|---|---|
| Proven Heritage Response | 14.32* μm | 0.159* | 2.28* | 13.18 | 15.86 | 0.874* |
| Intersection of IRF and Radiance | 21.39** μm | 0.125** | 2.68** | 20.156 | 22.835 | 0.820** |
| Peak Europa Radiance | 29.6 μm | 0.161 | 4.77 | 27.22 | 31.98 | 0.888 |
| Greatest Integrated Radiance | 30 μm Long-pass | N/A | | | | ~1 >30 μm |

* Estimates from measured spectra; ** Digitized sample transmissions from website.

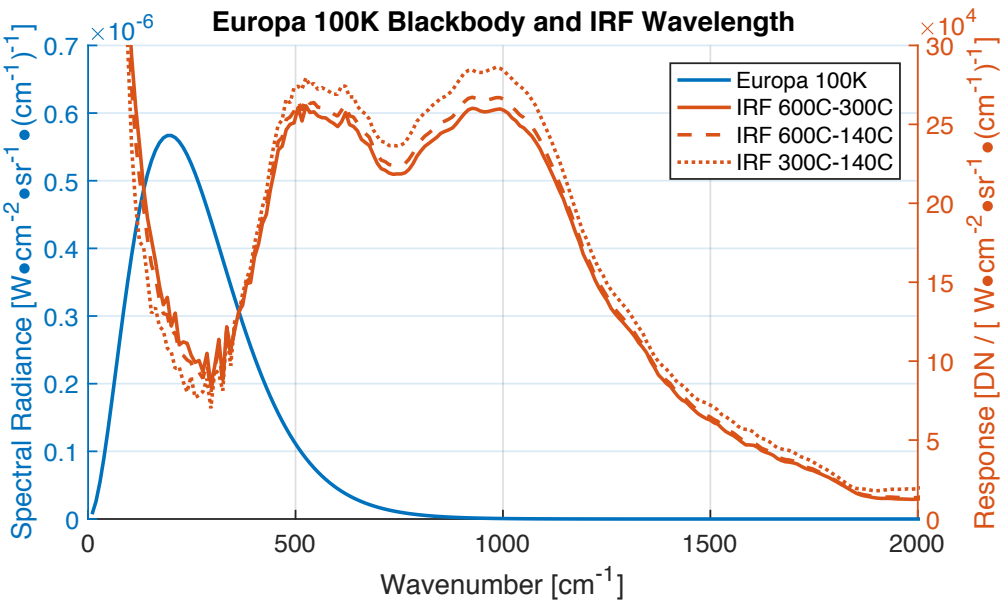


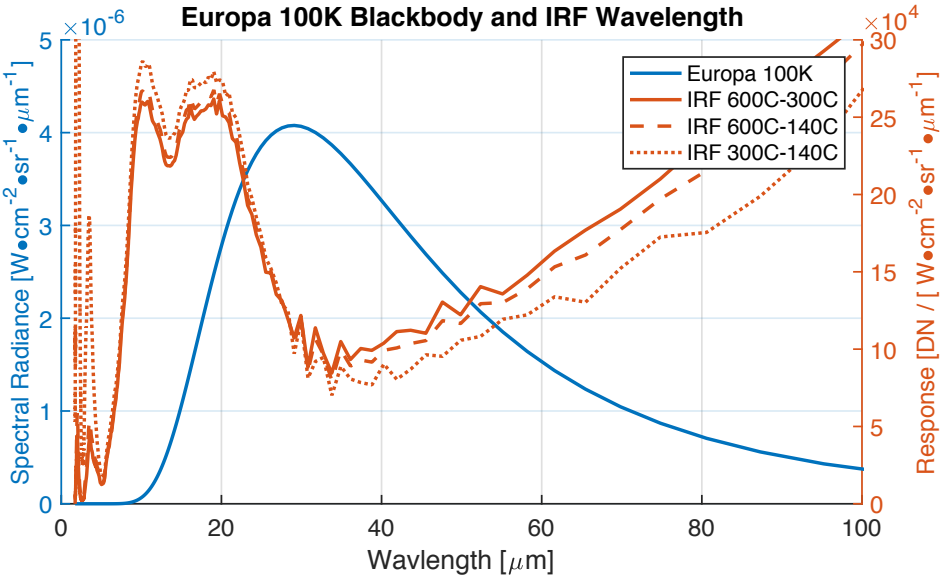


*Figure 43*. Instrument response functions and 100K blackbody.

## CONCLUSIONS AND FUTURE WORK

The goal of this project was to characterize the long-far wavelength spectral response of a microbolometer array using a retrofitted diamond window in order to develop future thermal infrared cameras for planetary exploration in the 15-100 μm range. Two laboratory test beds were developed to test the performance of the microbolometer.

First, the microbolometer array response was initially tested with THz filters. The results indicated that response was detected up to 45 μm with the filters. However some uncertainty remains due to leakage in the filters of the wings. A long-pass filter proved that energy was leaking through the wings. A second long-pass filter or multiple band-pass filters are necessary to block out-of-band leakage at additional wavelengths in order to produce a filter-based IRF. A 10 μm and a 45 μm long-pass filter are suggested.

The second approached involving integration of the diamond microbolometer array with the OTES diamond interferometer provided the opportunity to record interferograms with a diamond microbolometer array, for perhaps the first time ever, in order to produce an instrument response function. Through a series of tests, the spectra generated were gradually improved. The final IRF shows that the peak response was extended to ~500 $cm^{-1}$/~20 μm. The response then begins to decrease to ~25% at ~285 $cm^{-1}$/~35 μm. Thermal instability of the detector was a likely source of error that inhibits the confident analysis of the IRF beyond 35 μm. Further testing is being completed by the OTES engineering team to refine these results with an upgraded system that will reduce noise and errors in the interferograms collected for this investigation. As a result of this experiment it was determined that modulation efficiency significantly affects the instrument response function, 14-bit data is essential for measuring the strong ZPD

signal compared to the small fluctuations in the wings, and closed-loop moving mirror servo would likely increase the quality of the spectra.

Finally it should be mentioned that there was a trade-off between the two techniques used here. The interferometer approach provides a better spectral shape. When the IRF was well-characterized, then the filter method can be used to design an instrument system with higher SNR. This was especially important when looking at very cold targets where the signal may be below the NESR for an interferometer instrument system. In short, the interferometer method was better for characterizing the detector, and the filter approach was better for using the characterized detector to study a scene at low temperatures.

The initially scouting of a long-far infrared response function of diamond microbolometer arrays was a success. More detailed analyses are building upon the results produced here to design a long-far infrared camera for the exploration of Europa. Future missions to Mars and other planetary bodies can take advantage of the extended performance of diamond windowed microbolometer arrays. In the future perhaps, as the cost of CVD diamonds continues to decrease from~$5K at present to hundreds of dollars, all infrared cameras may switch to using diamond windows.

# CHAPTER 5

# THE THERMAL-CAMERA SYSTEM FOR EXPLORATION, SCIENCE, AND IMAGING SPACECRAFT (THESIS) FOR THE *PROX-1* MICROSAT MISSION

*"Jackson and Stacy both considered the Rocket Project's success more important than their own academic progress. It took Stacey eight years to earn his PhD; Jackson never would get his. Stacey's 1954 PhD dissertation, 47 pages of mathematical equations with occasional English interruptions, was a theoretical piece arguing for the superiority of something he called the 'Ideal Control.' A type of servomechanism, the Ideal Control was the Rocket Project's intellectual foundation."* – From Jars to the Stars: How Ball Came to Build a Comet-Hunting Machine *by Todd Neff*

## INTRODUCTION

The THermal-camera for Exploration, Science, and Imaging Spacecraft (THESIS) was an instrument system consisting of an infrared camera, a visible camera, and an instrument computer to be integrated as a payload element for the *Prox-1* microsatellite mission. The mission was collaboration in which students of PI David Spencer (Georgia Tech Professor) and Phil Christensen (THEMIS Principal Investigator) have worked together to design, build, integrate, and test a Microsatellite-class spacecraft (10-100 kg) for the University Nanosatellite Program (UNP) sponsored by the Air Force Research Laboratory (AFRL). In this program students compete against other universities and must demonstrate over a two-year period of several reviews that the mission fits within the goals of the customer (AFRL), that sufficient engineering analysis has been conducted through detailed documentation subsystem reports, and that progress can be

shown on the development of flight hardware. *Prox-1* was selected as the winner of the UNP-7 microsatellite competition in 2012.

The mission objectives are to demonstrate the use of continuous thrust propulsion and autonomous safe trajectory control during proximity operations. Image-based observations were proposed for the navigation and closed-loop attitude control of *Prox-1*, relative to a deployed CubeSat—the Planetary Society's *LightSail-B* (Schulte & Spencer, 2016; Spencer, 2015; Walker, 2012). A secondary objective was to verify the deployment of *LightSail-B's* solar sails. If these objectives are accomplished, the instrument and spacecraft teams hope to capture infrared and visible imagery of the Earth as a third objective of the instrument science team
(Veto & Christensen, 2016; Védie, Spencer, Walker, & Veto, 2013). Finally a fourth, passive objective of the instrument science team was to improve the TRL of potential imaging payloads for Planetary Science missions. *Prox-1* must also meet all UNP-7 program constraints, including staying within a size and mass envelope of 50cm × 50cm × 60cm and 50kg. The *Prox-1* mission and spacecraft design was led by students at the Georgia Institute of Technology, while the instruments were designed and built at ASU which specializes in developing infrared instrument systems.

THESIS was the instrument suite developed at Arizona State University for this PhD dissertation. THESIS incorporates mentorship from Phil Christensen's Infrared Instrument Laboratory (IRIL). THESIS was capable of acquiring thermal infrared images to track *LightSail-B* and visible images to provide context. The instrument system also contains an instrument computer that controls the cameras through preconstructed commands that the spacecraft computer initiates. THESIS has a mass of 2.04kg including all of the harnessing. The infrared camera was sensitive to 8-12 μm emitted radiation and the visible camera was a RGB bayer pattern color camera. The

instrument system consumes 7W of power in standby and 7.4W during image capture. In ambient laboratory conditions of 25.5˚C while staring at a 70˚C and 100˚C blackbody target, the standard deviation or Noise Equivalent Delta Temperature (NEDT) for most pixels was <30mK, and peaks at ~20mK. This meets the 1K requirement. The signal to noise ratio (SNR) was 737 and 457 respectively in these conditions, and this meets the requirement of 10:1. The radiometric temperature accuracy was theoretically +/- 5K as specified by FLIR. Preliminary testing indicated error of up to 15K, but when the lens transmission was multiplied, then the error drops to <2K for these conditions. The radiometric accuracy requires further testing to build confidence in this claim.

*Prox-1*—THESIS was developed from the unselected UNP-6 *Rapid Reconnaissance and Response ($R^3$)* mission(Walker & Spencer, 2010). The infrared instrument point design in 2010 was the subject of the ASU undergraduate Barrett, The Honor's College thesis for Michael Veto and Sean Marshall. Subsequent development of the point design to a completed and delivered instrument system was performed in partial fulfillment of this PhD thesis. THESIS image performance characterization also served as part of a PhD dissertation chapter for Amber Keske; THESIS preliminary environmental testing was completed in the PhD project TVAC chamber of Sylvain Piqueux and Andrew Ryan. The development of THESIS was performed in ASU's 100K cleanroom on the 1st floor of SESE's ISTB4 in front of thousands of children and members of the public. THESIS was presented at the TEDx Maricopa in front of a live audience of elementary students and retirees.

**Acronym List**

| | | | |
|---|---|---|---|
| AFRL | Air Force Research Lab | CAD | Computer Aided Design |
| ASU | Arizona State University | CCD | Charge-coupled device |
| C&C | Command and Control | CDH | Command and Data Handling |

CDR Critical Design Review

CG Center of Gravity

COTS Commercial off-the-shelf

CPU Central Processing Unit

DITL Day-in-the-life

EM Engineering Model

EPS Electrical Power System

FCR Flight Competition Review

FLIR Forward Looking Infrared

FMS Full Mission Success

FOV Field of view

FPA Focal plane array

FPS Frames Per Second

GS Ground System

GT Georgia Institute of Technology

GNC Guidance, Navigation, and Control

GPIO General Purpose Input/Output

GPU Graphics Processing Unit

GSD Ground Sample Distance

IFOV Instantaneous field of view

IPA Image Processing Algorithm

IR Infrared

IRIL Infrared Instrument Laboratory

ISTB4 Interdisciplinary Science and Technology Building 4

ITAR International Traffic in Arms Regulations

LEO Low Earth Orbit

MD Mission Design

MoE Measure of Effectiveness

MOI Moment of Inertia

MP Megapixel

NEDT Noise Equivalent Delta Temperature

OTES OSIRIS-REx Thermal Emission Spectrometer

PI Principal Investigator

PIR Pre-integration Review

PDR Preliminary Design Review

PSR Pre-ship Review

$R^3$ Rapid Reconnaissance and Response

ROI Region of Interest

S/C Spacecraft

SESE School of Earth and Space Exploration

SIRR Spacecraft Integration Readiness Review

SME Space Mission Engineering(Wertz, Everett, & Puschell, 2011)

| | |
|---|---|
| SNR | Signal to Noise Ratio |
| SS | Space Systems |
| THEMIS | Thermal Emission Imaging System |
| TRL | Technology Readiness Level |
| TVAC | Thermovacuum |
| UHF | Ultra High Frequency |
| UNP-7 | University Nanosat Program 7 |
| USB | Universal Serial Bus |
| UTC | Coordinated Universal Time |
| VEFC | Visible Early Full Color 8bit .jpg |
| VEFR8 | Visible Early Full Raw 8bit .pgm |
| VEFR16 | Visible Early Full Raw 16bit .pgm |
| VEFM | Visible Early Full Mono 8bit .jpg |
| VESM | Visible Early Summed Mono 8bit .jpg |
| VETM | Visible Early Thumbnail |

**Variable List**

| | | |
|---|---|---|
| $\epsilon$ | emissivity | [N/A] |
| $\tau$ | transmission | [N/A] |
| f | frequency | [Hz] |
| h | altitude | [km] |
| r | reflectivity | [N/A] |
| v | velocity | [km/s] |
| B | Radiance | [$W*m^{-1}*sr^{-1}*\mu m^{-1}$] |
| D | Diameter | [mm] |
| HFOV | Horizontal Field of View | [degrees/radians] |
| IFOV | Instantaneous Field of View | [degrees/radians] |
| Q | Heat | [Joules] |
| S | Recorded counts at detector | [counts] |
| T | Temperature | [Kelvin] |
| U | Cubesat Unit | [10 cm] |
| VFOV | Vertical Field of View | [degrees/radians] |
| W | Radiated Thermal Flux | [counts] |

## BACKGROUND

### Prox-1 Mission and Spacecraft

*Prox-1* will demonstrate automated trajectory control in low-Earth orbit relative to the deployed *LightSail-B* CubeSat for an on-orbit inspection application(Spencer, 2015). To achieve this, *Prox-1*—equivalent to a 75U CubeSat—has been designed, built, integrated, and tested at the Space System Design Lab at the Georgia Institute of Technology under PI David Spencer. The primary objectives of the mission are to 1) flight qualify new technologies including THESIS, a microsatellite control moment gyroscope unit, and a 3-D printed propulsion system 2) deploy the Planetary Society's *LightSail-B* CubeSat, and 3) test on-board guidance algorithms for implementing automated trajectory control for proximity operations(Spencer, 2015). *Prox-1* was planned to launch on the SpaceX *Falcon Heavy* launch vehicle in 2017 and carry the Planetary Society's *LightSail-B* as a payload within an integrated P-POD deployment system.

### THESIS Instrument Suite Overview

The THESIS instrument suite consists of an infrared camera, a visible camera, and an instrument computer. It was designed, built, and tested at the class 100K clean room facilities at Arizona State University by integrating commercial off the shelf (COTS) and custom components into an instrument system. The architecture of the THESIS instrument system was inspired by THEMIS and uses instrument science calibration practices developed for THEMIS while engineering expertise and advisement was lent by the OSIRIS-REx Thermal Emission Spectrometer (OTES) Engineering Team (Christensen et al., 2004; 2017).

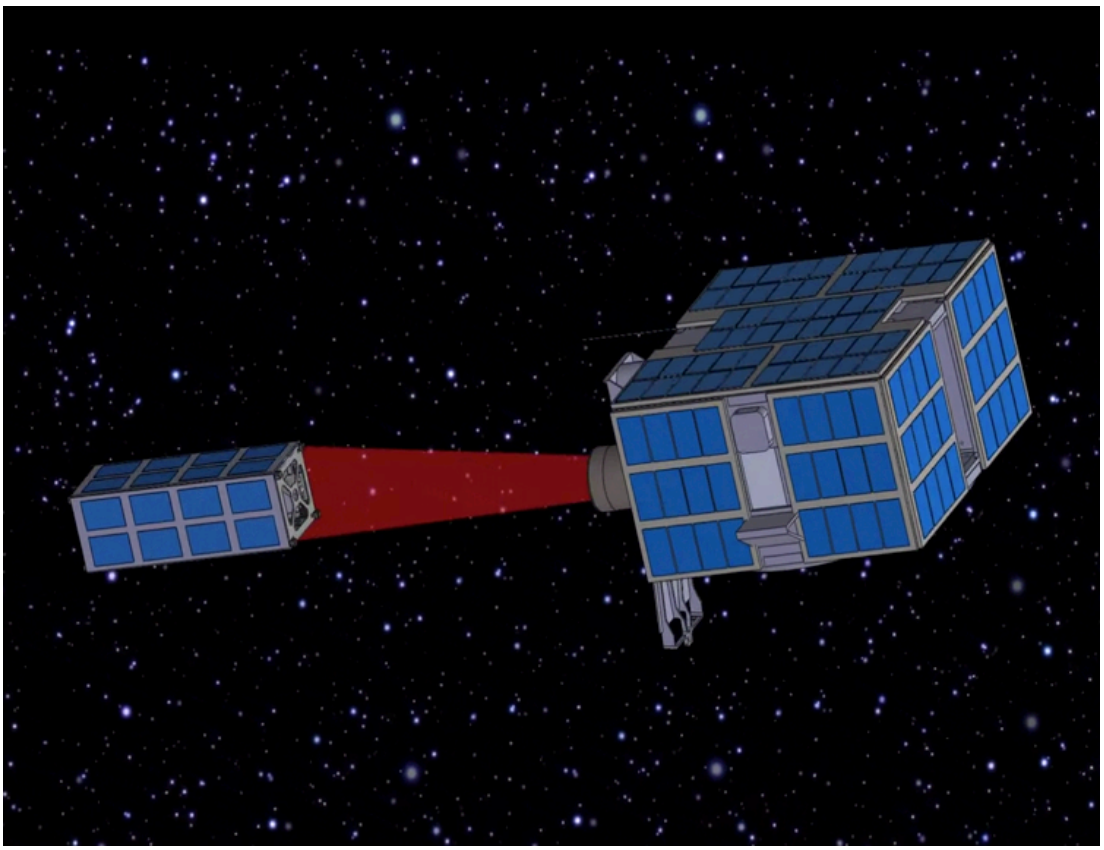

*Figure 44*. The *Prox-1* microsat mission captures infrared images of the *LightSail-B*.

Image from Georgia Tech and posted as "*Prox-1* Concept of Operations" on youtube.com

**Project purpose: learn space mission engineering**

The goal of space mission engineering was to design a space mission to meet a set of broad, often poorly defined objectives at a minimum cost and risk(Wertz et al., 2011). THESIS addresses three explicit innovative solutions for approaching this goal.

First, THESIS fosters understanding of the basic objectives of the community. The University Nanosatellite Program (UNP) was a hybrid program that bridges the basic objectives of the military, education, and smallsat space communities. *Prox-1*—THESIS provides the USAF with a competitive advantage over adversaries; trains the next generation of scientists and engineers; and demonstrates the applicability of small, rapid, low-cost missions. These objectives are addressed in the first two goals of THESIS: verify *LightSail-B* deployment and demonstrate proximity operations. The additional extended and passive goals of THESIS incorporate the basic objectives of the earth science and interplanetary communities. *Prox-1*—THESIS gathers visible and infrared imagery to learn about the changing Earth and tests infrared detector technology to incorporate into future interplanetary missions. In parallel, *Prox-1* was planned to launch on the first commercial launch of the SpaceX *Falcon Heavy*. Thus, *Prox-1*—THESIS interplays with launch community—helping to seed the development of a new launch system of a relatively young company. The various parties involved with *Prox-1*—THESIS have the opportunity to become familiar with the objectives outside of their respective community.

Second, THESIS creates an opportunities for multiple communities to work together. The joint development and demonstration of a small spacecraft system capable of autonomous proximity operations was a combined effort of the previous mentioned communities. The military community was interested in developing this technology for counterspace efforts and the interplanetary community was interested in developing

autonomous systems for detecting, tracking, and rendezvousing spacecraft as required for the *Mars Sample Return – Orbiter* (*Report on Technology Horizons: A Vision for Air Force Science and Technology During 2010-2030*, 2010; "Vision and Voyages for Planetary Science in the Decade 2013-2022," 2012).

Finally, THESIS applies technologies, processes, and methods between communities. Cross-community flow of technology, process, and methods was inherent to this project. The AFRL and ASU-OTES provide mentoring to students. The students—within the context of a smallsat project—test innovative, low-cost, and risky ideas that could validate/invalidate technologies to the military and interplanetary communities.

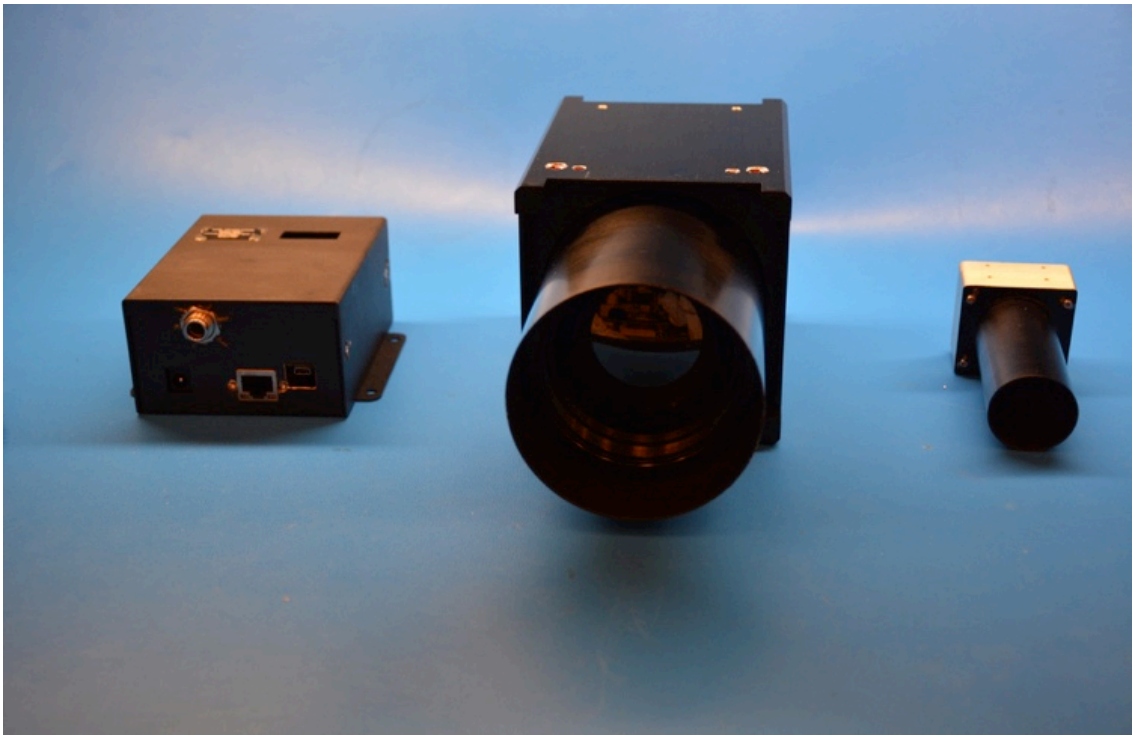

*Figure 45*. The completed THESIS suite of instruments. Left) The instrument computer commands the instruments to capture images and captures the data. The instrument computer interfaces to the spacecraft computer via Ethernet. Middle) The infrared camera captures infrared images that are used for target tracking. The structure was designed with a 1.5U CubeSat dimensions with lens and solar shade extending outward. Right) The visible camera with solar shade to prevent lens flare.

## *PROX-1*—THESIS MISSION-INSTRUMENT DESIGN

### *Mission objectives and constraints*

#### Prox-1 mission statement and Instrument Objectives

The mission statement outlines the qualitative goal of the mission.

The Prox-1 mission will demonstrate automated safe trajectory control during proximity operations for on orbit inspection. Passive, image-based observations will be used for the navigation and closed-loop attitude control of *Prox*-1 relative to *LightSail-B*.

The four goals of the THESIS instrument system are to support Prox-1 as follows:

***Verify LightSail-B deployment.*** After *Prox-1* deploys the Planetary Society's *LightSail-B* from the P-POD, the THESIS instruments will capture images of *LightSail-B* that will be downlinked to show its ejection. *Prox-1*-THESIS will also capture visible and infrared images of the solar sail deployment of the *LightSail-B*. While *LightSail-A* successfully deployed its sails and captured a self-image, *Prox-1*-THESIS will capture third-perspective images of a solar sail deployment in space for the first time.

***Demonstrate proximity operations.*** The THESIS instruments will also capture IR images that will be used in conjunction with image processing algorithms to determine the relative range and range-rate of *LightSail-B* with respect to *Prox-1*. The resulting relative orbit determination will be used to conduct automated proximity operations(Schulte & Spencer, 2016; Spencer, 2015).

***Conduct Earth remote sensing.*** Should all the mission objective be accomplished, THESIS will be able to support visible and infrared remote sensing of Earth in order to provide opportunities for scientist to further conduct investigations of scientific scenes of interest such as the gulf stream (Védie et al., 2013; Walker & Spencer, 2010), polar caps, urban heat islands (Stefanov et al., 2004), anthropogenic heat sources (i.e. possibly aircraft), wildfires, and volcanoes.

***Demonstrate small satellite instrument technologies for future planetary missions .*** As an implicit goal, THESIS will also demonstrate COTS instrument technology for future planetary missions. Should THESIS be successful, a similar architecture of instruments could be deployed to study the Moon and Mars.

### THESIS Stakeholders and their objectives

The various stakeholders of THESIS have both explicit objectives outlined in the mission statement as well as implicit, though influential, hidden objectives.

### Timeline

The total time span from initial conception to spacecraft delivery at Kirtland Air Force Base was 10 years. The *R³* concept development was completed over a two-year period. The *Prox-1* concept to delivery was completed over an additional eight-year period.

### THESIS estimate of qualitative needs, requirements, constraints

The estimates of the needs, requirements, and constraints determined during the concept study are presented in Table 7.

## Alternative Concepts

### Alternative Instrument Architecture

The THESIS instrument architecture was adapted from the mission architecture. The instrument architecture was specified strictly for THESIS-*Prox-1*. Many of the THESIS architecture segments could be adapted for other missions using THESIS. The other principal parties (GT, AFRL, SpaceX) have authority to trade in some of the following segments that ASU cannot for *Prox-1*. Although it was possible that ASU could trade in those segments if THESIS were retrofitted onto a different mission. The instrument architecture was shown in Table 8 and for the mission con ops shown in *Figure 46*.

Table 5.

*Stakeholders and objectives*

| Stakeholder | Objective | Community |
|---|---|---|
| Instrument Provider: ASU-SESE | Conduct remote sensing for Earth science; provide educational experience for PhD dissertation; gain academic prestige; proof-of-concept for future missions; inspire public via clean lab visibility | Education; Interplanetary; Earth science |
| Primary/Operator: Georgia Institute of Technology | Use imagery for in-flight proximity operations; use images for publicity; promote cross-university collaboration | Education; Interplanetary |
| Secondary: AFRL | Demonstrate proximity operations of Smallsats to enhance national defense; educate students for future workforce | Military and Intelligence |
| End User: Planetary Society | Obtain images to verify light sail deployment; use images for publicity | Alternative Space |
| End User: Smallsat Community | Trade knowledge | Smallsat |
| End User: Space X | Acquire launch ballast and AFRL funding for maiden commercial Falcon Heavy; use images for publicity | Launch |
| End User: Public | Use imagery for student/citizen science | Public |

Table 6.

*THESIS Approximate Timeline*

| Phase | Goal | Major Milestone | Final Outcome | Duration |
|---|---|---|---|---|
| *R³* | | | | |
| Concept Development | Create a proposal and prototype, win AFRL contract | Flight Competition Review | Not Selected | ~24 months 2008-2009 |
| *Prox-1* | | | | |
| Concept Development | Create a proposal and prototype, win AFRL contract | Flight Competition Review (FCR) | AFRL awards 1st Place | ~24 months 2010-2011 |
| Detailed Design | Revise concepts, review, converge on final solution | Subsystem Integration Readiness Review (SIRR) | Design locked; Begin flight fabrication | ~24 months 2012-2013 |
| Fabrication and Subsystem Integration | Complete THESIS flight hardware | Pre-Integration Review (PIR) | THESIS delivery to GIT | ~30 months 2014-2016 |
| Spacecraft Integration and Test | Integrate subsystems onto spacecraft, complete day-in-the-life | Pre-ship Review (PSR) | Deliver Prox-1 to AFRL | ~18 months 2016-2017 |

Table 7.

*THESIS Estimates*

| Constraint | THESIS Original Estimate | Justification |
|---|---|---|
| Functional Requirement | | |
| Performance | Sufficient resolution to detect cubesat from ~50 to ~200 meters at all times. | Preliminary optical estimates indicate that the highest powered available IR optics can detect a 3U up to ~200 meters. At <~50 meters the out-of-focus blur becomes significant. This was a reasonable range for the prox-ops maneuvers as well. |
| Coverage | Field of view was larger than pointing accuracy of spacecraft. Image was available for image processing within less than 1 second of commanding. Sufficient memory was available for ~thousands of images. | The spacecraft must be detected even if the pointing accuracy was significant and/or either spacecraft drifts. |
| Interpretation | Sufficiently discriminate the whole target cubesat pixels from the background (space, sun, Earth, etc.) | The images most provide reasonable discrimination of the cubesat, so the image processing algorithms can discern the target with confidence. |
| Timeliness | If image processing was conducted on the instrument computer, the processing should be completed in <2 seconds. | The image processing algorithms require the image to be processed in order to produce an output vector. This vector was needed every ~2 seconds for the proximity operations algorithm. |
| Secondary Missions | Conduct Earth remote sensing; test technology for future missions | Conduct $R^3$ investigation with existing asset after completing primary mission; education opportunity for science students; prepare for future |

Continue on next page.

| | | |
|---|---|---|
| Operational Requirement | | |
| Commanding | Image thumbnails and telemetry are automatically collected at ~1 minute intervals by the instrument computer. The prox-ops commanding can be triggered on the order of ~2 seconds. | S/C computer was not responsible for scheduling telemetry gathering. S/C does need to trigger instrument computer when the spacecraft was ready for prox-ops or specific imaing of an ROI. |
| Mission Design Life | Several months | Preliminary estimate. |
| System Availability | Backup camera, routine telemetry, and routine imaging | Because volume and mass are not vastly limited for the microsat, a backup camera could be designed. Routine telemetry and thumbnail imaging could be saved and downlinked to investigate issues. |
| Survivability | LEO | Survive in low earth radiation environment |
| Data Distribution | Rapid data transfer to s/c computer | Images or range vectors need to be rapidly transferred to the spacecraft computer as inputs for the prox-ops algorithm. |
| Data Content Form, and Format | Raw images, compressed images, thumbnails, telemetry, select beacon data. Vectors if processing on instrument computer. | Images can be compressed to reduce data budget. Telemetry was reduced to most-necessary in beacon. |
| User Equipment | Laptops and server | All data can be analyzed and post-processed on a laptop and optionally stored on server. |
| Constraint | | |
| Mass | 5 kg | Mass budget of proposed subcomponents; initial CAD models with thick walls for radiation shielding; margin |
| Volume | IR: 10 in. x 5 in. x 4 in.<br><br>VIS: 44mm x 29mm x 87mm | Volume budget of proposed subcomponents; initial CAD models |

Continued from previous page.

| | | |
|---|---|---|
| Power | 10 W | Power budget of proposed subcomponents with 25% margin |
| Cost | $500K | Cost of subcomponents, graduate student stipend for 5 years, labs, and travel with 25% margin |
| Schedule | 5 years | 2 years concept;<br>2 years development;<br>1 year I&T;<br>2015 launch |
| Risk | Cost, schedule, technology readiness | Some COTS parts are not available at time of initial design. |
| Regulation | Export Control Technology; ITAR | IR technologies subject to US export control; some AFRL material was ITAR |
| Politics | Directly responds to Air Force need for conducting proximity operations in space. A hidden political objective was to demonstrate proximity operations with IR cameras to promote future possibility of space rendezvous for Mars Sample Return. | The mission goal was linked to one of the customer's (AFRL) needs in order to win the competition. Aspects of future needed concepts that are desired by the investigator, e.g. Mars Sample Return, are unofficial demonstrated. |
| Environment | Design to protect from solar illumination | Spacecraft attitude will operate prox-ops regardless of solar vector, therefore optimize shading of optics. |
| Interfaces | Simple to interface with s/c computer | The s/c team does not have time and resources to troubleshoot interface, therefore make this simple to integrate. |
| Development Constraints | Schedule: AFRL review milestones, SpaceX launch; Remote design | Design and testing progress must be meet key deadlines. Georgia Tech and spacecraft are across the country, thus limiting interface testing. |

Table 8.

*THESIS Instrument Architecture for Prox-1*

| Segment | Description | Can be traded in a study? | Justification | Options |
|---|---|---|---|---|
| Mission Instrument Concept | Data delivery, tasking, communication, timeline | Yes | Explore possibilities. | See Table 9 |
| Subject | Radiation from LightSail-B and regions of interest on Earth | Yes | LightSail-B and Earth can be imaged using a variety of camera wavelengths | Infrared<br>Visible |
| Instrument Payload Elements | IR camera, VIS camera system | Yes | Variability for detectors, bands, optics, aperture, interface, adjustable optics with moving parts. | |
| Instrument Bus | Instrument Computer | Yes | Central vs. distributed payload command and control:<br>INS computer functionality incorporated into spacecraft computer? | Distributed:<br>instrument computer C&C<br>Centralized:<br>spacecraft computer C&C |
| | Power scheme | Yes | Centralized vs. distributed instrument power.<br>Camera power controlled by instrument computer or spacecraft EPS. | Distributed:<br>INS power control<br>Centralized:<br>EPS control |

| | | | | |
|---|---|---|---|---|
| Ground System | Primary: GT GS<br>Secondary: ASU GS<br>via Prox-1's S-Band, UHF | No | GT provides GS.<br>ASU provides option for backup capability. | N/A |
| Mission Operations | Onboard Image Processing Algorithms (IPAs) | Yes | Centralized vs. distributed data processing:<br>Image processing occurs on which bus. | Distributed:<br>instrument computer processing |
| | | | | Centralized:<br>spacecraft computer processing |
| | Instrument Autonomy | Yes | Prox-Ops<br>Instrument system captures images on its own or waits for capture commands. | No autonomy |
| | | | | Semi-autonomy: Images are commanded on s/c computer |
| | | | | Full autonomy |
| | | | Earth Remote Sensing<br>Instrument system captures images on its own or waits for capture commands. | No autonomy |
| | | | | Semi-autonomy: images are target via ground |
| | | | | Full autonomy |
| | GT and ASU students | No | Students from GT and ASU involved in Mission Ops. | N/A |
| Command, Control, and Communications Architecture | Store and dump; Where store images and when transfer? | Yes | The images could be stored for downlink on a computer. | Store on INS computer |
| | | | | Store on S/C computer |

| | | | | |
|---|---|---|---|---|
| | Cameralink vs. USB for Data latency. Thumbnails? Image compression? | | | Do not store |
| | | | The images could be compressed for low data budget. | Send raw images |
| | | | | Compress images: Thumbnail, JPG, 8-bit, etc. |
| | | | Data transfer scheme | USB |
| | | | | Cameralink |
| Orbit | Classified<br>Designed for 720 km orbit | No | AFRL defines orbit. | N/A |
| Launch | SpaceX first commercial<br>Falcon Heavy | No | AFRL determines launch vehicle. | N/A |

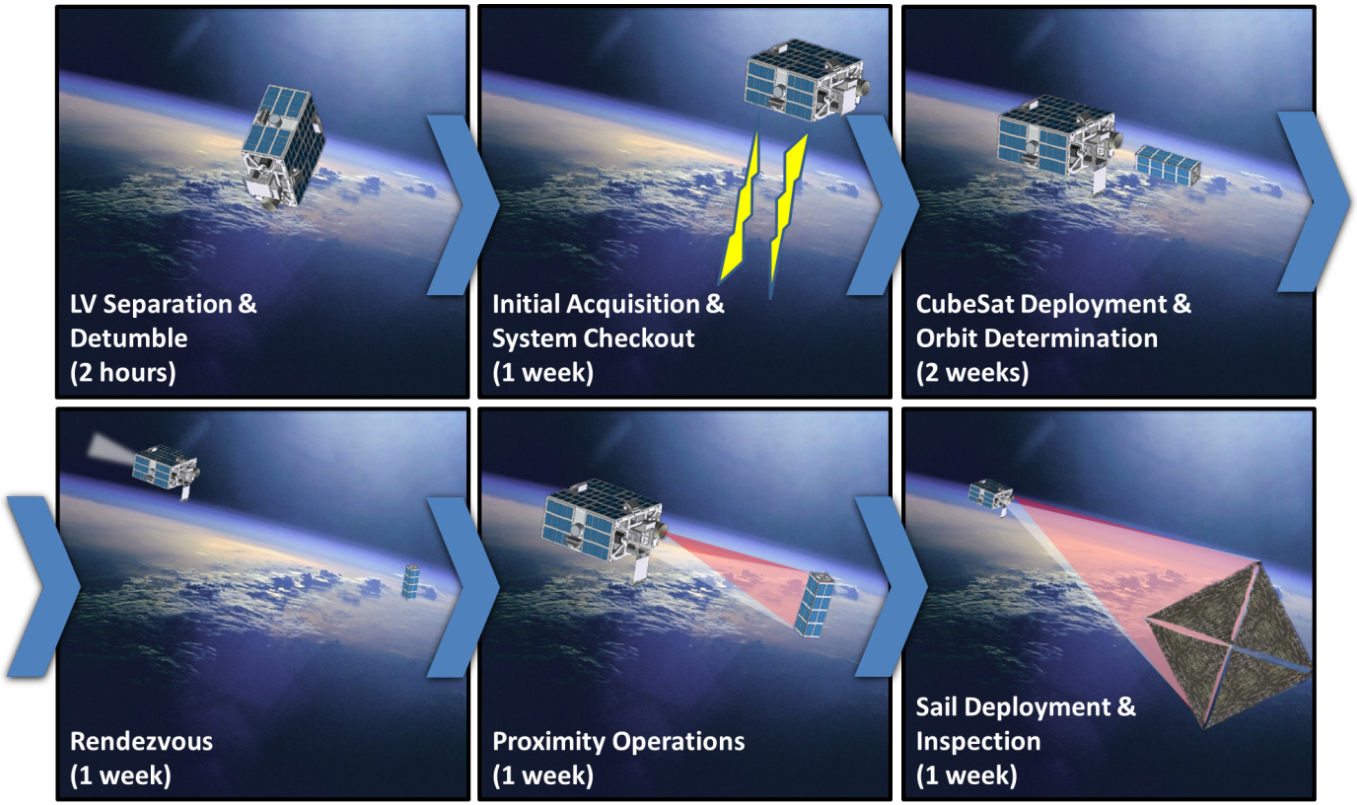


*Figure 46*. The *Prox-1* Concept of Operations. Image credit Georgia Tech.

### Alternative Instrument Concepts

The architecture outline given in Table 8 was used to create four instrument concept options that are given in Table 9. The first key trade involves selection of the wavelength of camera to be used. While visible cameras are simpler, cheaper, and smaller than infrared cameras, an infrared camera will be able to detect the target in Earth shadow. The data delivery method was the second key trade. While centralized processing may be easier for a nanosat mission, the complexity, requirements, and expanded resources of a microsat mission may converge on a better solution with distributed processing with some built-in autonomy and on-board data processing. An advantage of the distributed processing scheme, dubbed "Performance-IR", was that the dedicated instrument computer can schedule automatic tasks such as image capturing and telemetry archiving that was independent of the spacecraft computer. Because image capturing, processing, and storing was a moderately intensive process, the distributive process frees the spacecraft computer from these responsibilities. Furthermore, the development and testing the camera control software can be done in parallel to, and was independent of, the spacecraft flight software development; the spacecraft flight software team was provided with executable functions that the instrument computer will accept and execute. The "Performance-Efficient-IR" concept involves two additive enhancements to optimize the performance of the spacecraft. First the image processing automatically occurs on the instrument computer. The spacecraft computer pulls the resulting output vector. Second, the subcomponents of the instrument system are independently powered through the spacecraft EPS, so power usage can be reduced.

Table 9.

*Instrument Concept Options*

| Segment | Option A Simple-IR | Option B Simple-VIS | Option C Performance-IR | Option D Performance-Efficient-IR |
|---|---|---|---|---|
| Mission Instrument Concept | Infrared camera was commanded directly from centralized s/c computer, using available COTS components, to sense emitted radiation from LightSail-B. | Visible camera was commanded directly from centralized s/c computer, using available COTS components, to image reflected light from LightSail-B. | Infrared camera was controlled through a distributed instrument computer, utilizing COTS components in development, to sense emitted radiation from LightSail-B; prox-ops are triggered by s/c computer to instrument computer, and image processing was performed on s/c computer. Camera draws power from instrument computer. | Infrared camera was controlled through a distributed instrument computer, utilizing COTS components in development, to sense emitted radiation from LightSail-B; prox-ops are triggered by s/c computer to instrument computer, and image processing was immediately performed on the instrument computer. Power was distributed to each system independently to save power. |
| Subject | Emitted infrared radiation from LightSail-B | Reflected solar illumination from LightSail-B | Emitted infrared radiation from LightSail-B | Emitted infrared radiation from LightSail-B |
| Instrument Payload | IR camera | VIS camera | IR camera | IR camera |
| Instrument Bus | Command through spacecraft computer | Command through spacecraft computer | Instrument Computer | Instrument Computer |
| | Power drawn through | Power drawn | Distributed instrument | Centralized instrument |

| | | | | |
|---|---|---|---|---|
| | spacecraft computer USB | through spacecraft computer USB | subsystem power: Infrared camera power supplied through instrument computer | system power: Independent instrument subcomponent power control through EPS |
| Ground System | GT provides GS.<br>ASU provides option for backup capability. | | | |
| Mission Operations | Image processing on s/c computer | Image processing on s/c computer | Image processing on s/c computer | Image processing on INS computer |
| | No autonomy | No autonomy | Semi-Autonomous | Semi-Autonomous |
| | Students from GT and ASU involved in Mission Ops. | | | |
| Command, Control, and Communications Architecture | Images stored on s/c computer; No image compression; USB data transfer | Images stored on s/c computer; No image compression | Images stored on s/c computer; No image compression; Camera link data transfer | Images stored on INS computer; Image compression; Camera link data transfer |
| Orbit | AFRL defines classified orbit;<br>Designed for 720 km orbit | | | |
| Launch | AFRL determines launch vehicle: SpaceX first commercial Falcon Heavy | | | |

### Key Parameters, System Drivers, and Key Requirements

The following key parameters are analyzed within the proposed instrument concepts in order to determine the influential system drivers.

***Resolution.*** First and foremost, the instruments are required to detect the target spacecraft at an adequate resolution to determine its range. Thus, the resolution was driven by a number of drivers including the optics, detector, and distance between the two satellites.

***Target precision.*** The precision of the pixels was important for feeding into the algorithm to determine its size. The more precise the histogram of pixels, the better the algorithm can determine the overall size of the target and thus its distance. Visible light may not uniformly reflect off of *LightSail-B*, whereas the spacecraft's nearly uniform emissivity should produce a more uniform signal of emitted infrared energy.

***Sensitivity Time.*** The ideal scenario was to be able to track *LightSail-B* at all times. Visible light, requires a source of illumination—either the sun or the Earth's reflection of the sun. The emitted infrared energy can be tracked at all times.

***Data Budget and Processing Speed.*** The spacecraft data budget was significantly constrained and the time required to process and output images to feed into the spacecraft GNC was on the order of seconds.

***Mass.*** The instrument allocation of the mass budget was set to 2kg. Each component/structure element was estimated with +25% margin when prefabricated/pre-procured, +15% margin when massed with EM hardware, and +5% margin when massed with flight hardware. Thus, the instrument subsystem was designed to be no greater than 2 kg, but the spacecraft systems engineer reserved 2.10 kg for margin. For *Prox-1*, the mass of THESIS was a moderate constraint.

***Volume.*** The volume of THESIS was generally accommodating by the spacecraft and was not a chief concern. The placement of the instrument subsystems was chiefly driven by the ability to accommodate the harnessing. The instrument computer had to be carefully positioned and the harnessing had to be designed with angles to avoid spacecraft walls. The only major explicit constraint on the volume of the instruments was to limit the length of the IR solar shade, so as to not protrude from the spacecraft's volume limit within the launch vehicle. For *Prox-1,* the volume of THESIS was a low constraint.

***Power.*** The overall power constraint for the spacecraft was a function of the power generated through solar panels minus the power consumed through subsystems. During the design phase, the addition of a Honeybee control moment gyro that consumed a relatively large amount of power, constrained the available power budget to the instrument system. The spacecraft power budget cannot allocate 8 W at all times to the instruments. For *Prox-1*, the power draw of THESIS was a major constraint.

***People.*** The initial allocation of people for *Prox-1* consisted of graduate students at Georgia Tech and the lead author as an undergraduate working on THESIS. Throughout the mission development, *Prox-1* transitioned to an undergraduate project with relatively high turnover. THESIS became ~50% of the graduate work for the lead author. Graduate student Amber Keske assisted with characterization of the visible camera and infrared camera images. Graduate student Andy Ryan assisted with thermovacuum testing of the EM. The OTES team provided mentorship. For *Prox-1,* the allocation of people was a major constraint.

***Cost.*** As a smallsat student project, cost was usually a limiting resource. This class of missions was touted for low-cost. The AFRL and GT did not supply any funding

to ASU for the development of THESIS. Funding was wholly provided through ASU funding. For *Prox-1*, the cost of THESIS was a major constraint.

***Laboratory Space.*** Laboratory space was provided for *Prox-1* at GT. The spacecraft was built in clean tent. THESIS was the first project to be allocated space in the newly constructed class 100K clean lab at ASU. For *Prox-1*, the allocation of laboratory space for THESIS was a low constraint.

***Schedule.*** The overall time constraint consisted of a proposal phase of ~2 year, a design phase of ~2 years, a build phase of ~2 years, and an integration and test phase of ~1 year. For *Prox-1,* the time schedule was a major constraint.

***Technology.*** The camera link interface between the infrared camera and the instrument computer was not commercial available during the early stages of development. Thus, this technology was not available until later in the development that imposed risk and schedule delays.

***Risk.*** As a student microsat mission, the overall driving constraint was cost. Because the project was operating on a relatively low budget with students, the project inherently accepts risks that are not otherwise accepted on a professional NASA or Air Force mission. The *Prox-1* team and THESIS team follows the UNP user's manual and provides any analyses that are required by AFRL; however, the project assumes risk without funding dedicated professional engineers, test equipment, tools, travel, and the highest grade spacecraft hardware. Cheap equals risk. For *Prox-1*, lack of funding presented a pervasive risk to the project, but THESIS was completed within the cost constraints through ASU funding.

***Descoped parameters.*** Key parameters that could be traded for planetary missions also include the visible SNR, infrared NEDT, and the infrared accuracy. However, these parameters are not critical for *Prox-1* and were descoped for analysis.

The key parameters are computed using identified system drivers in Table 10. The system drivers can be thought of as the dials for the design and the key parameters are the gauges. The key parameters that critically affect the instrument system design are specifically singled out in Table 11.

Table 10.

*Instrument Key Parameters, Algorithms, and System Drivers*

| Key Parameter | First Order Algorithm Simple-IR | First Order Algorithm Simple-VIS | First Order Algorithm Performance-IR | First Order Algorithm Performance-Economic-IR | System Drivers |
|---|---|---|---|---|---|
| Performance | | | | | |
| Resolution | Distance*[Infrared Pixel Pitch / Infrared Focal Length] | Distance*[Visible Pixel Pitch / Visible Focal Length] | Distance*[Infrared Pixel Pitch / Infrared Focal Length] | Distance*[Infrared Pixel Pitch / Infrared Focal Length] | LightSail-B distance, focal length, pixel pitch |
| Target precision | % of LightSail-B uniformly emitted | % of LightSail-B uniformly reflected | % of LightSail-B uniformly emitted | % of LightSail-B uniformly emitted | Reflectivity and Emissivity of LightSail-B, |
| Sensitive Time | 100% | % time receiving sunlight or earth-shine | 100% | 100% | time in sunlight, time in earth shine |
| Image Processing Time | [USB speed*VIS ROIC speed + s/c processing speed] * image size | [USB speed*IR ROIC speed + s/c processing speed] * image size | [Camera link speed*IR ROIC speed + image transfer speed via Ethernet +s/c processing speed] * image size | [Camera link speed*IR ROIC speed +INS processing speed ] * image size + vector transfer time via Ethernet | ROIC speeds, data transfer speeds, image size, INS processing speed, s/c processing speed |

| | | | | | |
|---|---|---|---|---|---|
| Mass | IR detector + IR Optics + Solar Shade | VIS detector + VIS Optics + VIS Solar Shade | IR detector + IR Optics + Solar Shade + Computer | IR detector + IR Optics + Solar Shade + Computer | Size of optics and structure |
| Volume | IR detector + IR Optics + Solar Shade | VIS detector + VIS Optics + VIS Solar Shade | IR detector + IR Optics + Solar Shade + Computer | IR detector + IR Optics + Solar Shade + Computer | Solar shade length, harnessing configuration, components |
| Power | IR detector | VIS detector | IR detector + Computer | [IR detector * period ON] +Computer | IR power, VIS power, Computer power, period ON |
| Solar Shade Angle | ATAN (Lens diameter / [Length of IR lens shading + length of allowable IR extension to spacecraft boundary]) | ATAN (Lens diameter / [Length of visible lens shading + length of allowable visible extension to spacecraft boundary]) | ATAN (Lens diameter / [Length of IR lens shading + length of allowable IR extension to spacecraft boundary]) | ATAN (Lens diameter / [Length of IR lens shading + length of allowable IR extension to spacecraft boundary]) | Lens diameter, length of as-is shading, allowable shade length, |
| Target precision | % of LightSail-B uniformly emitted | % of LightSail-B uniformly reflected | % of LightSail-B uniformly emitted | % of LightSail-B uniformly emitted | Reflectivity and Emissivity of LightSail-B, |
| Sensitive Time | 100% | % time receiving sunlight or earth-shine | 100% | 100% | time in sunlight, time in earth shine |
| Cost | | | | | |

| | | | | | |
|---|---|---|---|---|---|
| People Cost | [Graduate student stipend x years x number of students] | | | Cost of graduate student, time of project development, number of students | |
| Hardware Cost | VIS camera x number of copies | IR camera x number of copies | [IR camera + INS computer] x number of copies | [IR camera + INS computer] x number of copies | Cost of hardware, number of subcomponent copies |
| Travel Cost | Number of trips * cost of trip | | | Number of trips, cost of trip | |
| Schedule | | | | | |
| COTS subcomponent development time | N/A | N/A | Time to develop COTS Camera link interface | Time to develop COTS Camera link interface | Sub component availability |
| Instrument System Development time | Visible development time | Infrared development time | Infrared development time + instrument computer development time subcomponent + time to develop custom data harnessing | Infrared development time + instrument computer development time + time to develop custom data harnessing + time to develop custom EPS harnessing | Individual subcomponent development times, harnessing development times |
| EM Schedule impact time | | [Development time * number of EM] - time savings on lessons learned – time development savings in-parallel | | Number of EM, time spent in parallel processes, time saved troubleshooting EM | |

Table 11.

*Critical Requirements*

| Requirement | What it affects |
|---|---|
| Resolution | LightSail-B must be resolved with as many pixels as possible for algorithms to determine distance. |
| Timeliness of Image Processing | The distance must be determined with a couple seconds. |
| Power | The instrument system must fall within the allocated power budget. |
| % Sensitive Time | The instruments must be able to detect LightSail-B, preferably at all times. |
| % Target precision | The instrument must have precise whole target measurements that feed into the image processing algorithms to adequately model the distance. |

## Mission Analysis: Evaluation of Concepts

### Feasibility Assessment

The feasibility of THESIS was assessed by comparison with THEMIS heritage; past experience designing, building, integrating, and testing ground-based and underwater robotics; and confidence in the available mentoring expertise and resources. This quick-assessment showed that the THESIS instrument can be successfully designed and integrated to a spacecraft in order to meet the mission objectives within the available cost, schedule, and risk.

### Sizing Estimate

The systems engineering sizing estimates for THESIS on *Prox-1* the same as those developed for visible and infrared camera system for $R^3$ for the author's undergraduate Honor's thesis (Veto, 2010). The figures incorporate estimates for the optics from the optical analysis that was performed by Sean Marshall for his undergraduate Honor's thesis. These estimates were determined using subsystem

component specific sheets for a system scaled down from THEMIS using COTS components and refractive optics.

Table 12.

*Sizing Estimate for Visible and Infrared Camera*

| Parameter | Visible Camera | Infrared Camera |
|---|---|---|
| Mass (no radiation shielding) | ~0.25kg | 1.5kg |
| Mass (with radiation shielding) | N/A | 5kg |
| Volume | 10 x 10 x15 cm | 20 x 15 x 15 cm |
| Power | ~3.0 W | ~2.0 W |
| Interface | IEEE 1394b and/or GPIO | RS 232 and/or Camera link |

**Point Design**

***Overview.*** A point design was produced from a prototype infrared and visible camera. The prototype infrared camera consists of a Raytheon 640x480 (~0.3 megapixel) microbolometer focal plane array with supporting electronics, an Ophir 100mm lens, a custom calibration flag, and custom mechanical structure. Data was output in either 8-bit or 14-bit format via a camera link interface. A visible camera provides context images for images acquired by the infrared camera. The visible camera acquires a 1.4 megapixel image to complement the 0.3 megapixel infrared image. The visible camera outputs 8-bit data over a Firewire interface. Selection of the detectors and optics are detailed in the Honor's Thesis of Michael Veto and Sean Marhsall and are not detailed here. Subsequent component selection involved the design of a calibration flag and a mechanical structure to interface the infrared components.

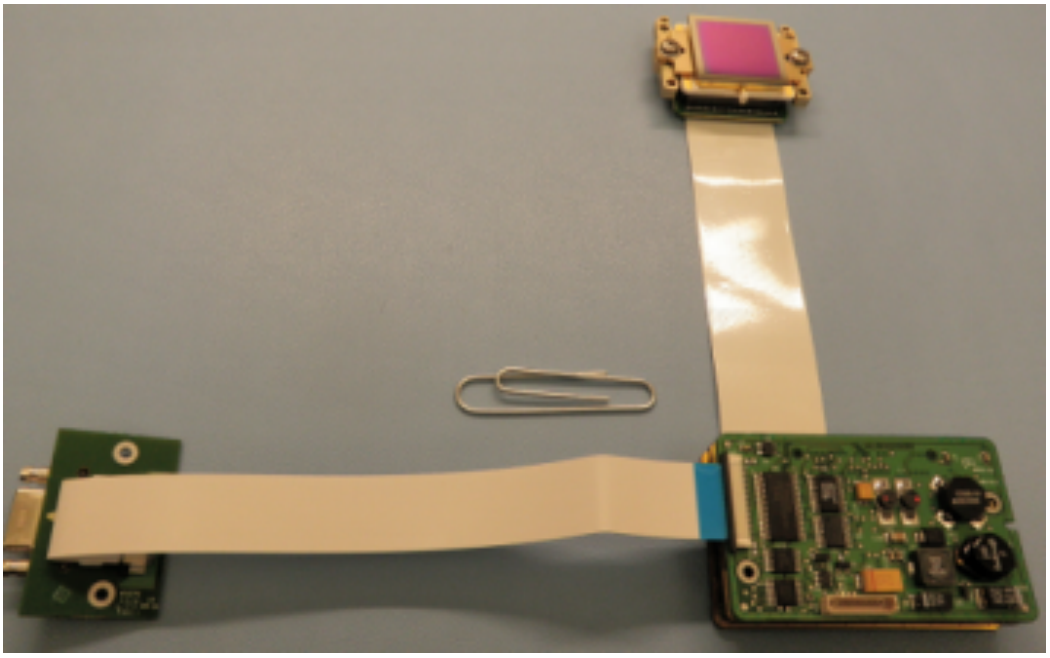

*Figure 47*. The Raytheon 640x480 Focal Plane Array with supporting electronics boards and camera link interface board.

***Calibration Flag.*** A calibration flag was necessary in order to take calibration images and flat field the detector. The calibration flag will close in front of the FPA to capture an image of a known temperature. The blade was painted with a specialized absorbing paint, so that it will have the characteristics of a black body. A thermocouple was mounted to the blade, so that the temperature of the blade can be measured. The infrared camera takes an image of the blade to determine both individual pixel offsets as well as a point calibration that was used in order to derive the temperatures of the scene.

In addition to calibration, the shutter can be closed if the imager was pointed toward the sun to protect the detector from solar radiation. While this was a consideration for the prototype, it will ultimately be removed for the flight model.

Selection of the shutter took several factors into account. A Brandstrom Instruments A1071 shutter was selected for as the strongest motor with the greatest travel. The shutter swings open when a +3.3V signal was pulsed with a pulse width of ~133 ms and closed with a corresponding -3.3V pulse.

As there were no commercially available shutter blades that would fit the geometry of our assembly, it was determined that a custom shutter blade would be designed and fabricated at Arizona State University. The shutter was designed to completely block the full dimension of the rear optic to be conservative.

***Infrared Camera Structure.*** In order to relay the optical path precisely onto the detector, a structure made of aluminum was created. The structure was a box with channels in the bottom to support the detector mount and the shutter mount. In addition, a hole was cut in the front panel to allow the optics to be mounted. A structure was fabricated that holds the supporting electronics boards, and a structural element was created to mount the calibration flag (*Figure 50*).

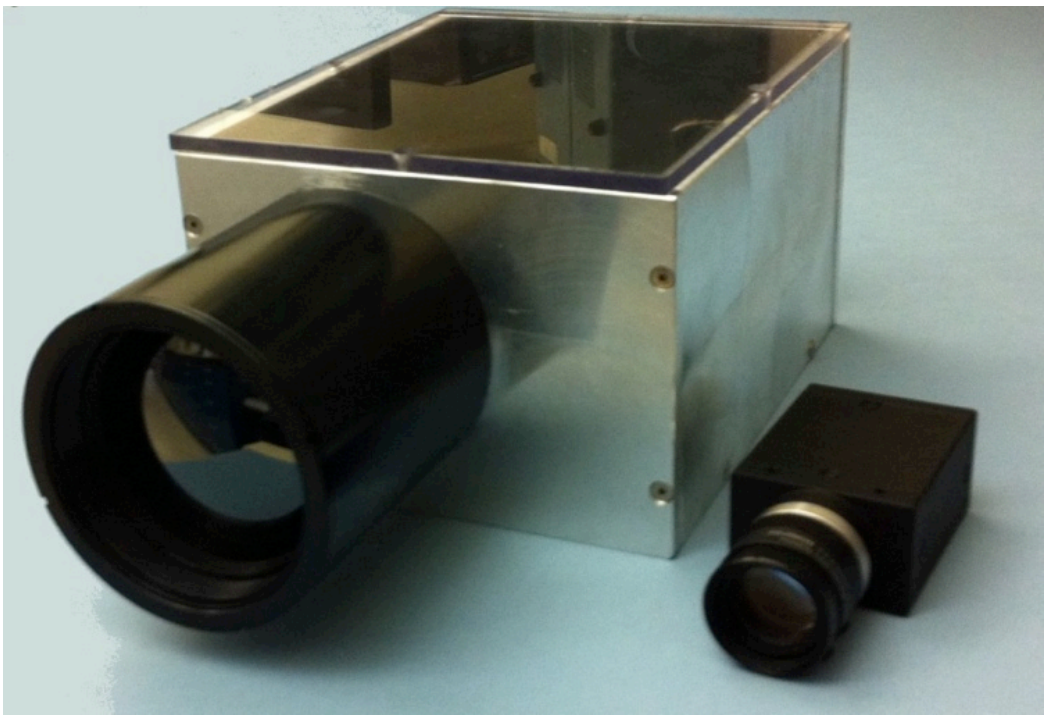

*Figure 48*. The Ophir 680026 IR lens attached to the prototype aluminum structure. The Grasshopper and Fujinon lens combined are much smaller in comparison. The variation in diameters of the visible and infrared lens illustrates the effect of the diffraction limit on the diameter as a function of wavelength. The diameter of the infrared optics was 62.5 mm and the diameter of the visible optics was 17.85mm.

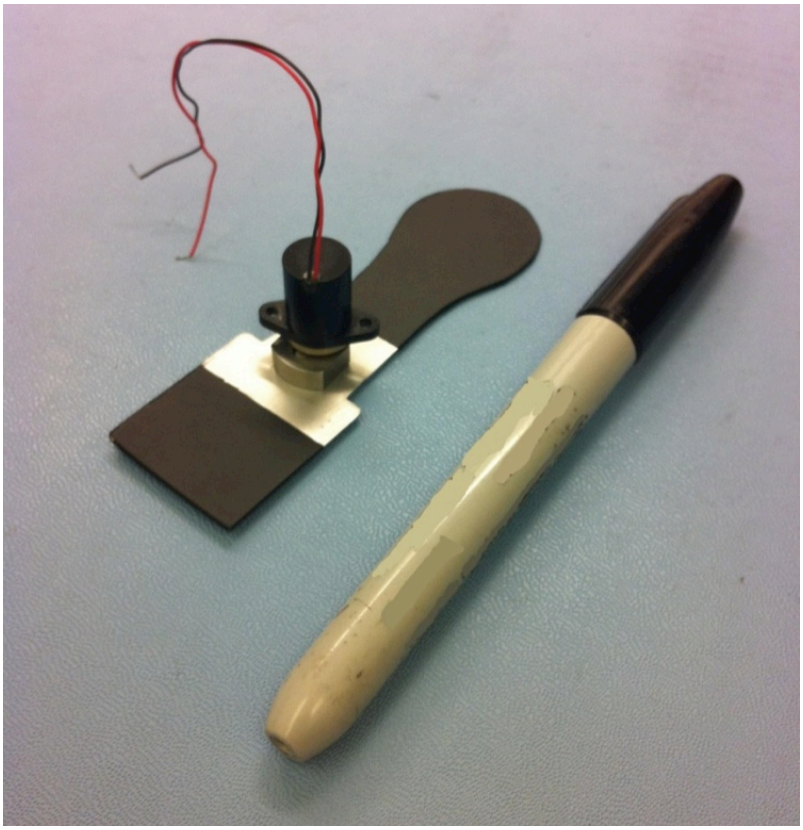

*Figure 49*. Calibration shutter blade with the Brandstrom Instruments A1071 servomotor attached.

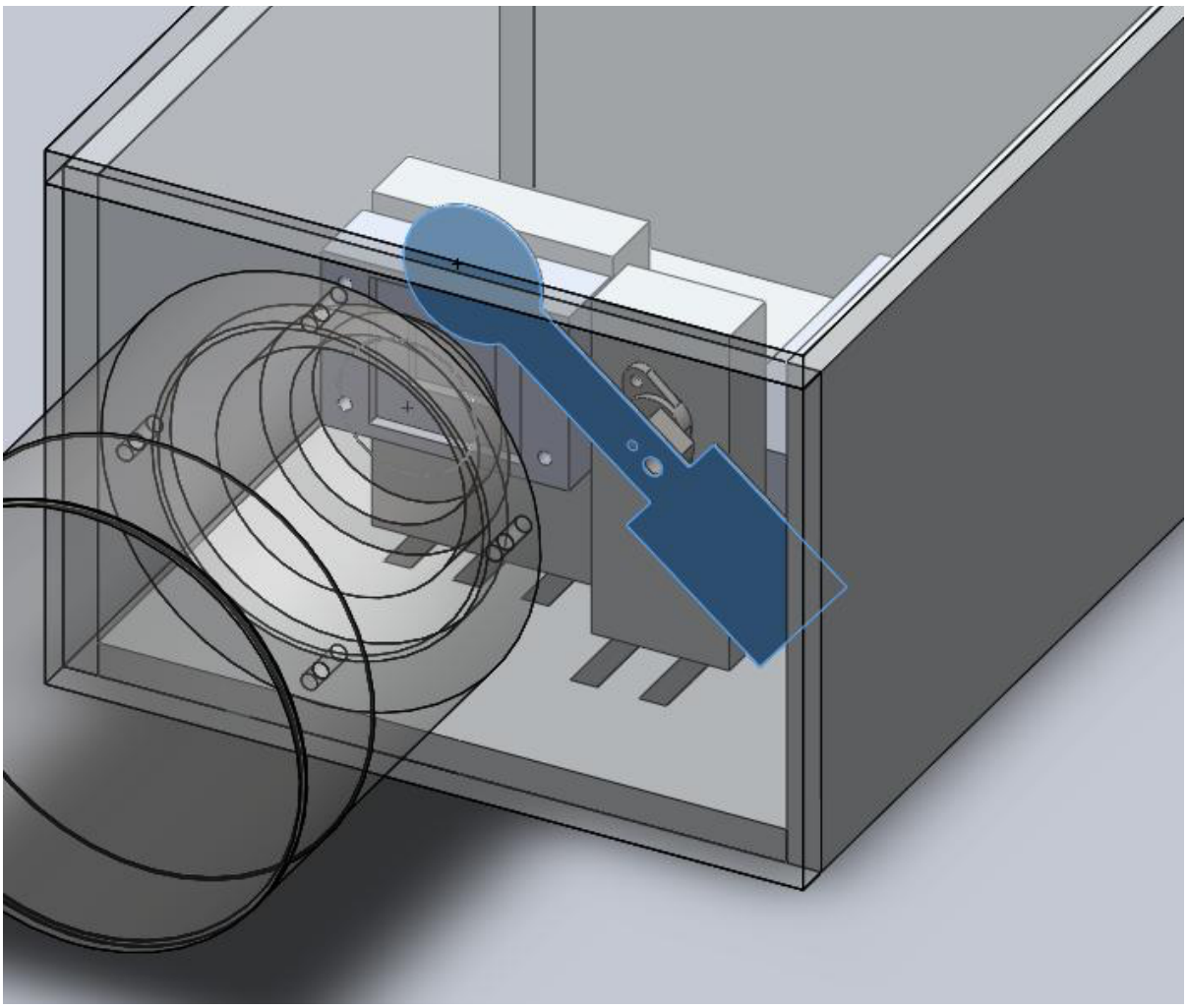

*Figure 50*. CAD model showing the highlighted calibration flag in the open position. The lens assembly and front structural panel are rendered transparent.

### Subsystem Trade Studies

Subsystem trade studies were performed in order to determine hardware selection and software schemes for the instrument system. A brief description of these trades and where there are found was shown in Table 13. For the trade studies below, underlined items are either optimal or there was not a significant difference between the cameras; unformatted items are less desirable, but workable options; and striked items are not acceptable options for the overall instrument system design.

***Infrared Detector Upgrade.*** The primary challenge in developing the flight IR camera was the redesign to transition from a benchtop model to a flight unit. During the concept exploration of this project, the FLIR Tau 2 camera core became available. This camera has a fully integrated shutter that was housed in an aluminum structure along with the detector and possesses a mounting ring to attach a lens. The Tau 2 also contains development software that allows a user to change settings and program the infrared camera. Specifications are compared in Table 14. After comparing the parameters, it was determined that the FLIR Tau 2 would replace the Raytheon OWL-IR.

***Visible Camera Interfaces and Upgrade.*** Subsequent to the procurement and testing of the grasshopper camera for the point design, the command and data handling subsystem team for the spacecraft determined that it would be better to use a USB 2.0 interface rather than the IEEE 1394 FireWire 800 interface. It was determined that implementing FireWire would be too costly and complicated. The onboard color processing and higher transfer speeds are not as desirable as the ease of interface to the flight computer. A trade study was conducted to evaluate possible new options (Table 15). The Point Grey Chameleon camera was chosen as a replacement and has been procured. The main differences are shown in the table below

***Processing architecture.*** The time to process an infrared image was critical to provide vectors for the navigation algorithms to control the spacecraft during proximity operations. The infrared cameras are limited in their ability to stream images over USB. Images currently must be transferred via camera link in order to achieve the request speed for prox-ops of 1-2 seconds. The USB interface took several seconds to transfer an image, and this was unacceptable for the GNC team. A trade study was conducted to evaluate possible alternatives (Table 16). Because the spacecraft flight computer does not contain a camera link interface, it was decided that an instrument computer would be needed that incorporated a camera link interface. This also allows the instrument subsystem to be completely developed independent of the spacecraft. The spacecraft computer simply connects over Ethernet to the instrument computer and executes preprogrammed shell scripts on the instrument computer.

It was also decided that in order to further increase the computation speed, the images would automatically be processed onboard the instrument computer to output the range vector. This eliminates the need to transfer images over the Ethernet to the spacecraft computer and this takes advantage of the Minnowboard's significantly greater processing power over the spacecraft computer's Beagleboard to run the computations. In effect, the instrument computer was similar to a video card. The spacecraft "CPU" offloads all image processing onto a "GPU".

Table 13.

*Subsystem Trades*

| Trade | Description | Where traded | Result |
|---|---|---|---|
| Imaging Subject | Visible reflectance or infrared radiation from LightSail-B and regions of interest on Earth? | Inferred from Resolution Tests Section | Infrared camera used for prox-ops; visible camera used for context and backup |
| Infrared Camera Optics | Focal length? Options? Fixed/focusing? | Sean Marshall Honor's Thesis | Ophir 680026: 100mm lens, fixed focus, Athermalized lens |
| Infrared Camera Detector | Raytheon 640x480, FLIR Tau 2 Performance, FLIR Tau2 Industrial | Table 14 | FLIR Tau 2 |
| Visible Camera Detector | Point Grey Grasshopper or Chameleon | Table 15 | Point Grey Chameleon |
| Visible Camera Optics | Keep Fujinon 25 mm optics? | Sean Marshall Honor's Thesis | 25 mm from Point Design |
| Power Architecture | Centralized vs. distributed instrument power. Camera power controlled by instrument computer or spacecraft EPS. | Table 26 | Distributed instrument power Centralized power from s/c EPS. |
| Processing Architecture | Instrument Computer. Central vs. distributed payload command and control: Instrument computer functionality could be incorporated into spacecraft computer. | Table 16 | Distributed processing with an instrument computer |
| Onboard Image | Centralized vs. | Table 16 | Distributed data |

| | | | |
|---|---|---|---|
| Processing Algorithms (IPAs) | distributed data processing:<br>Image processing occurs on which bus. | | processing on the instrument computer similar to a GPU. |
| Prox-ops Instrument Autonomy | No autonomy, semi-autonomy: s/c commands images, full autonomy | Table 16 | Semi-Autonomous: Images are captured every 5 minutes and auto-processed; s/c can command image on the fly |
| Image Storage | Store and dump; Where store images and when transfer? INS, S/C, none? | Table 16; Table 33; | Images stored on instrument computer |
| Infrared Image Data Transfer | USB? Cameralink? | Table 16 | Serial communication performed over USB 2.0; Image data transferred over Camera Link |
| Image Compression | Compress? Thumbnail? | Table 33; | Visible default was Color JPG (option for RAW in PNG)<br>Infrared default was 14bit in 16bit-TIF (option for 8 bit in 8 bit-TIF) |

Table 14

*Infrared camera comparison*

| Parameter | Raytheon OWL-IR | FLIR Tau 2 Industrial |
|---|---|---|
| Pixel Array | 640 x 480 | 640 x 512 |
| Pixel Size | 25 µm | 17 µm* |
| NEDT | <50mK | <30mK |
| Spectral Range | 8.5µm to 12.5µm | 7.5µm to 13.5µm |
| Frame Rate | 30 Hz | 30 Hz |
| Detector Size | 0.640 in x 0.480 in. | 0.428 in. x 0.343 in. |
| Interface | 14 bit Camera link | USB 2.0, Camera link (optional) |
| Power | 2.5 W | 1.2 W |
| Mass | ~100 g | ~70 g |
| Volume | ~1.5 in. X ~3 in. x ~1.5 in. | 1.75 in. x 1.75 in. x 1.18 in. |
| Price | ~~Unknown~~ | ~$10,000 |
| Integrated shutter | ~~No~~ | Yes |
| Programing Support | ~~No~~ | Yes |
| Customer Service | ~~Poor~~ | Excellent |

*During testing of the final hardware, it was found that perhaps the smaller pixel size of the FLIR Tau 2 may be contributing to some diffraction limiting blur. In subsequent work to this dissertation, the 17 µm pixel size of the FLIR may be less desirable than the 25µm pixel size of the Raytheon detector for these optics.

Table 15

*Visible camera comparison*

| Parameter | Grasshopper | Chameleon |
|---|---|---|
| Pixel Array | 1384 x 1032 | 1296 x 964 |
| FOV | 14.6° x 10.9° | 11.0° x 8.2° |
| IFOV | 38.0 arcseconds | 30.5 arcseconds |
| Detector Size | 1/2” | 1/3" |
| Interface | ~~IEEE 1394 Firewire 800~~ | USB 2.0 |
| Transfer Rate | 800 Mbit/s | 420 Mbit/s |
| Color Processing | On-camera | On-camera |
| Mass | 104 g | 37 g |
| Volume | 58 mm x 44 mm x 29 mm | 25.5 mm x 44 m x 41 mm |
| Price | $1295 | $295 |

Table 16

*Processing Architecture Trades*

| Parameter | Centralized Options | Distributed Options |
|---|---|---|
| Computer | S/C computer commands cameras | Instrument computer commands cameras through s/c computer |
| High Speed Camera Link Image Transfer | ~~Not available with Beagleboard~~ | Available on Minnowboard with interface cards |
| IPA processing | ~~Full 14-bit Image was transferred to S/C and processed on CPU.~~ | Image was automatically processed on "GPU". Only vector was transferred. |
| Image Storage | Possible, but increases writes on s/c data card | Dedicated space for images prevents s/c issues |
| Instrument Autonomy | Possible, but may interfere with s/c routines | Autonomous routines run independent of s/c |
| Mass | No added mass | Instrument computer added |
| Volume | No added volume | Instrument computer added |
| Power (Instrument Computer) | No added power | Instrument computer added and requires power mitigation. |
| Price | No added volume | Instrument computer added, Expensive custom harness |
| Schedule | No added schedule | Significant development time and custom harness design |
| Verdict | ~~Fails to accomplish GNC requirement. Not an option~~ | Accomplish all requirements but costs resources to instrument team and requires special power mitigation. |

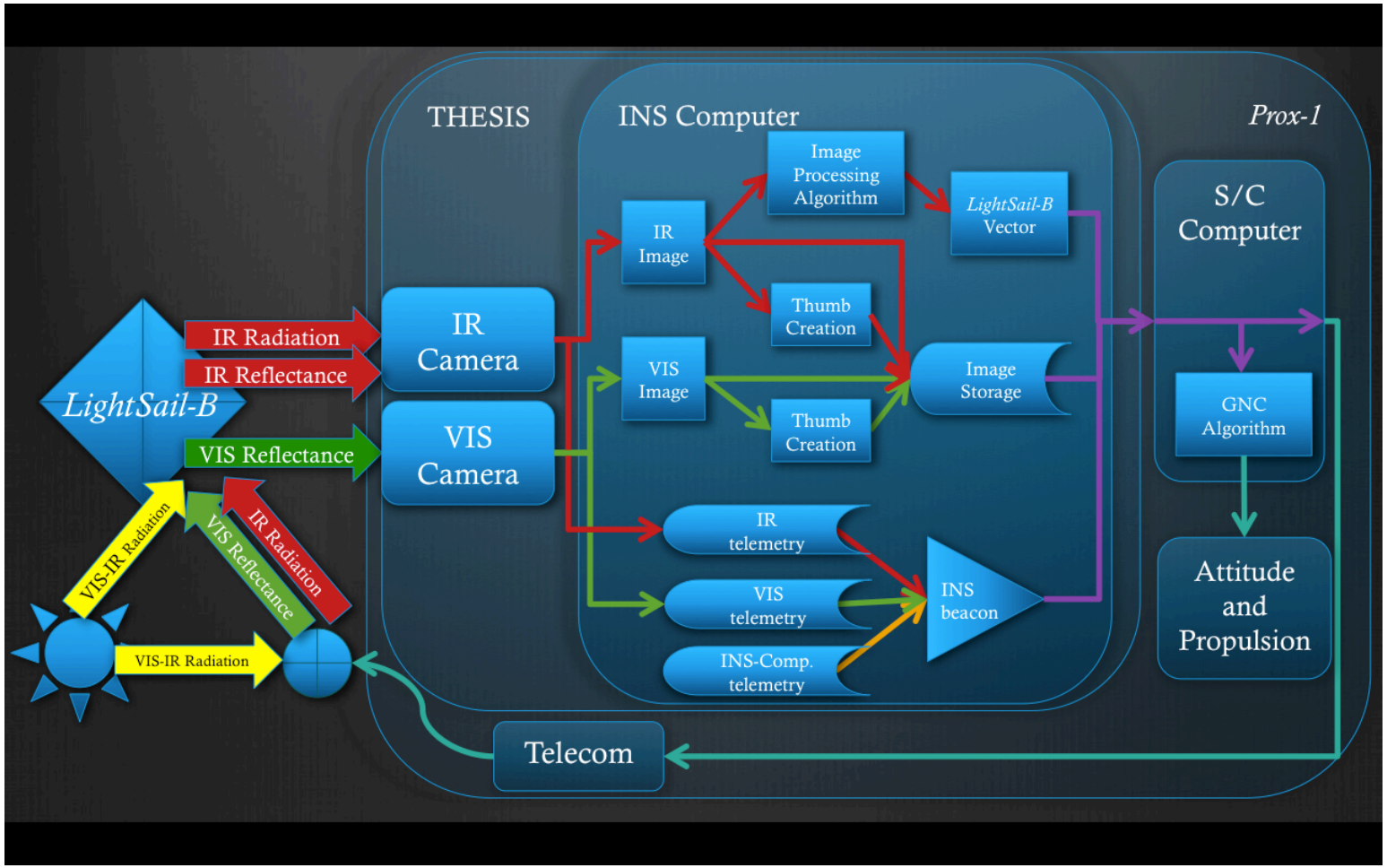


*Figure 51*. THESIS Data-Flow Diagram. Yellow was solar radiation. Green was visible light or visible data from the VIS camera. Red was infrared light or infrared data from the IR camera. Purple was data from the instrument computer. Teal was data from the spacecraft computer.

### Performance Assessments

***Overview.*** THESIS was evaluated for both its performance and utility. The performance assessment was quantitative comparison of possible trades to verify that the mission and spacecraft requirements can be met. The subsystem utility assessment quantifies the validity of the options to meet the end-user's objectives.

***Resolution Simulation 1: Proof of Concept for Preliminary Design Review (PDR).*** An initial resolution test confirmed that the blackbox CubeSat (*Figure 52*) could be detected as near as 23 meters with the chosen optics when focused at that distance (*Figure 53*)

***Resolution Simulation 2: Proof of Distance Determination for Critical Design Review (CDR).*** An analysis was performed that showed the measured number of pixels was comparable to the calculated number of pixels for a given distance. The visible image estimate versus measured corresponded to 3% error. The infrared image estimate versus measured was equal in this test. The test suggests that calculated and measured pixel counts are likely to be sufficiently close when the cameras are focused at the given target's distance.

*Figure 52*. The sample blackbox CubeSat. (10 x 10 x 30 cm).

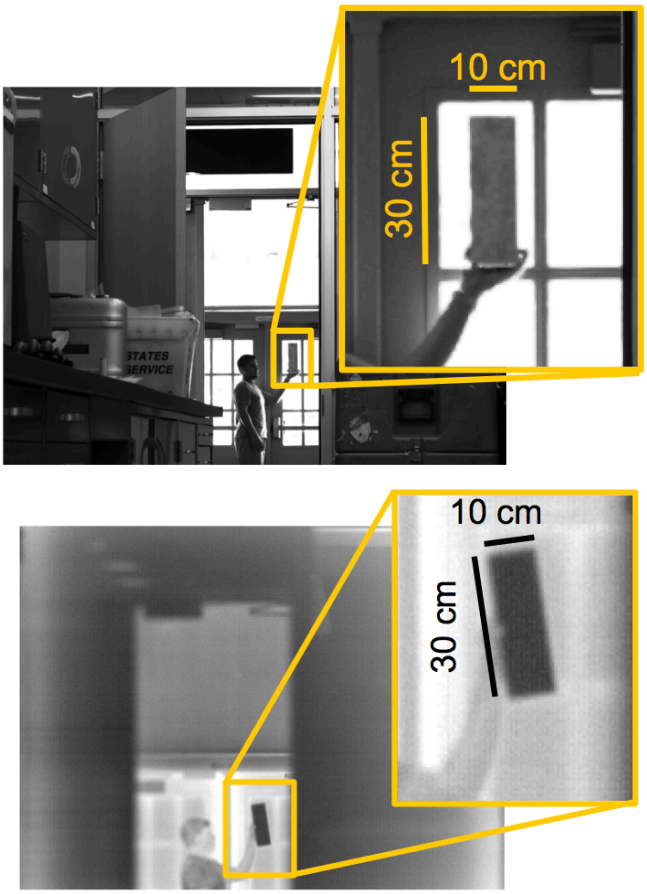


*Figure 53*. Visible and infrared test images of the edge-on CubeSat at ~75 feet or ~23 meters.

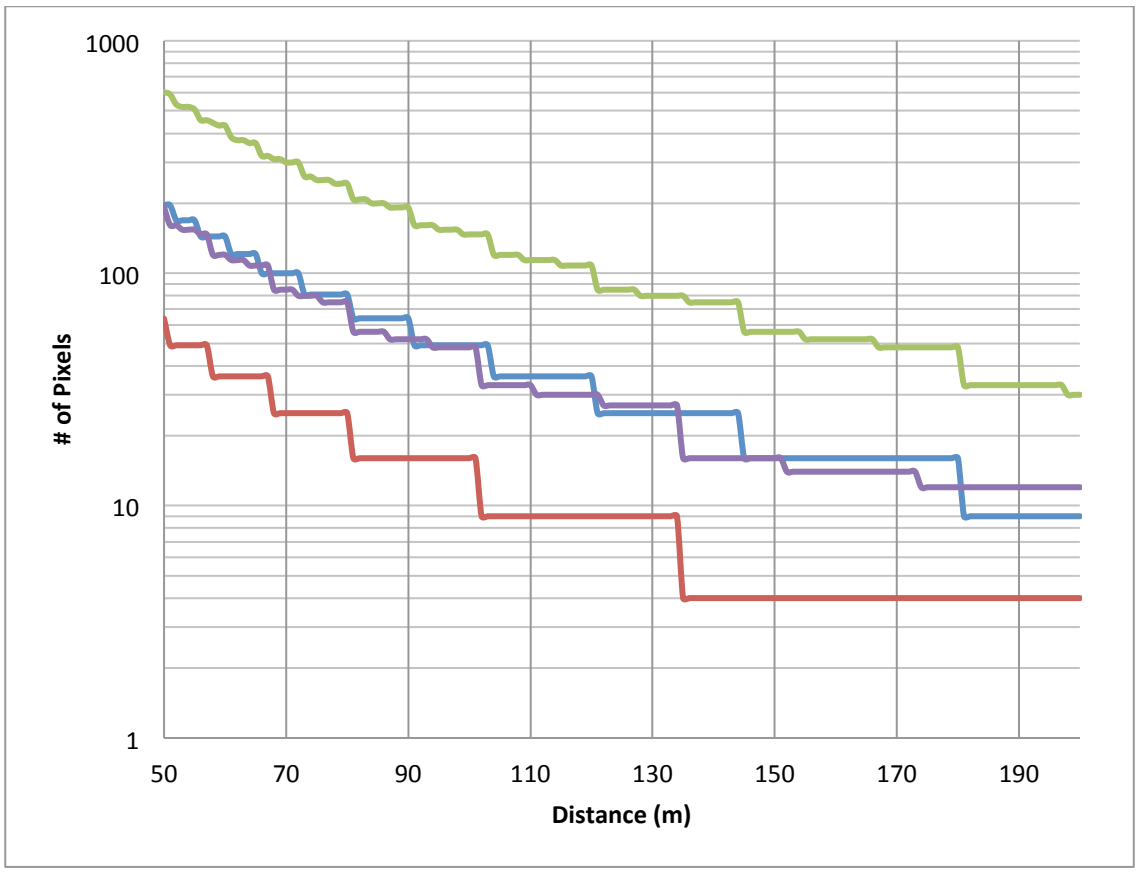


*Figure 54* Calculated resolution of the CubeSat for two views for the visible and thermal imager. Green) Visible camera 30x10cm side. Blue) Visible camera 10x10cm side. Purple) Infrared camera 30x10cm side. Red) Infrared camera 10x10cm side.

*Figure 55*. Visible and infrared image of the blackbox CubeSat at 48 meters. The blackbox CubeSat was heated in an oven to increase its temperature to ~80° C. These images were uncropped to show the relative size of the cubesat. The images were not co-aligned, so they are offset in the figure. A cat entered the building during infrared testing and was seen escaping through the door in the scene.

Table 17.

*Calculated and measured pixel values for initial 48m test and full range resolution test.*

| Camera | Target Distance [meters] | Pixels | | | | | | Error |
|---|---|---|---|---|---|---|---|---|
| | | X-direction | | Y-direction | | Total | | |
| | | Calculated | Measured | Calculated | Measured | Calculated | Measured | |
| IR | 48 | 8 | 8 | 25 | 25 | 200 | 200 | 0% |
| VIS | 48 | 11 | 11 | 33 | 34 | 363 | 374 | 3% |
| IR Near Focus | 50 | 8 | 9 | 24 | 25 | 192 | 225 | 17% |
| IR Near Focus | 200 | 2 | n/a | 6 | n/a | 12 | n/a | n/a |
| IR Far Focus | 200 | 2 | 1 | 6 | 5 | 12 | 5 | 58% |
| IR Far Focus | 50 | 8 | n/a | 24 | n/a | 192 | n/a | n/a |

***Resolution Simulation 3: Range of Distance at Infinite Focus for Preliminary Qualification Review (PQR).*** This test compares predicted versus measured pixel counts at multiple distances between 50 and 200 meters (*Figure 56* and *Figure 57*). The results indicated that there was significant error for both the near and far limits of 50m and 200m for differing reasons. Error was minimalized when the optics were focused at the target's distance, but the error was significant when the target was placed in the near (50m) or far (200m) field while focused at the opposite (Table 18).

***Resolution Simulation 4: Comparing various distances at 100m focus for Flight Competition Review (FCR).*** A fourth test was undertaken that tried to resolve the blackbox CubeSat while the focal plane was focused at an intermediate (100m) focus (*Figure 58*). For the IR images, all of the distances were overestimated. The conclusions made from this test are 1) Bayer processing should be activated for any visible images that are processed for the range estimate, 2) focusing the optics at infinity yields better overall results and will provide in-focus images of Earth, 3) a correction factor was needed for the CubeSat at near distances.

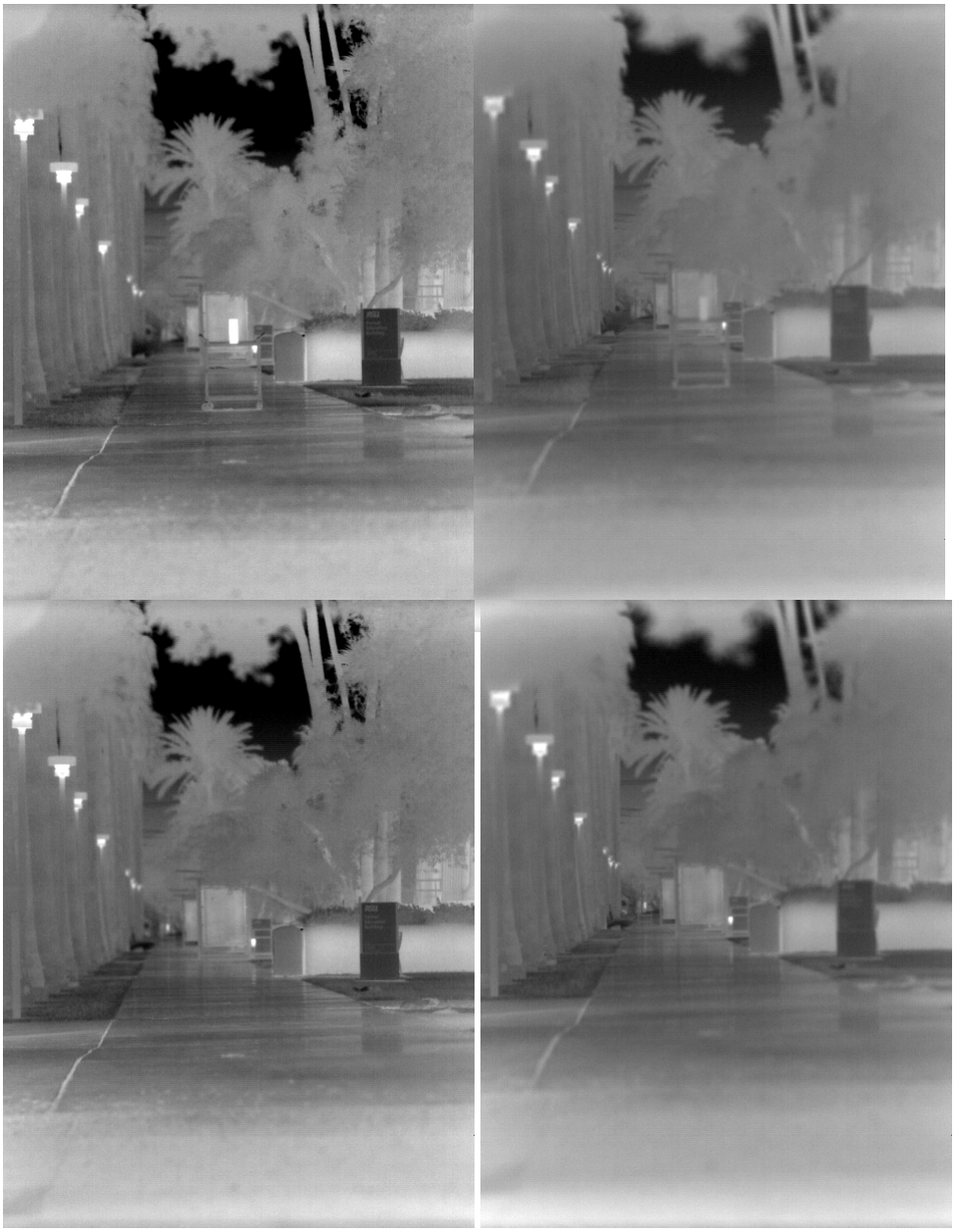

*Figure 56*. Left images are focused at 50 meters. Right images are focused on the background. Top images show target at 50 meters. Bottom images show target at 200 meters.

*Figure 57*. Visible images of CubeSat focused at 100 meters at distances of a) 50 meters, b) 100 meters, c) 200 meters.

Table 18.

*Calculated and measured pixel values for second full range resolution test.*

| Camera | Target Distance [meters] | Pixels | | | | | | Error |
|---|---|---|---|---|---|---|---|---|
| | | X-direction | | Y-direction | | Total | | |
| | | Calculated | Measured | Calculated | Measured | Calculated | Measured | |
| Vis | 50 | 10 | 14 | 41 | 44 | 410 | 616 | 50% |
| Vis | 100 | 5 | 7 | 20 | 23 | 100 | 161 | 61% |
| Vis | 200 | 2 | 5 | 10 | 12 | 20 | 60 | 200% |
| IR | 50 | 8 | 11 | 24 | 26 | 192 | 267 | 39% |
| IR | 100 | 4 | 7 | 12 | 14 | 48 | 70 | 79% |
| IR | 200 | 2 | 4 | 6 | 7 | 12 | 25 | 108% |

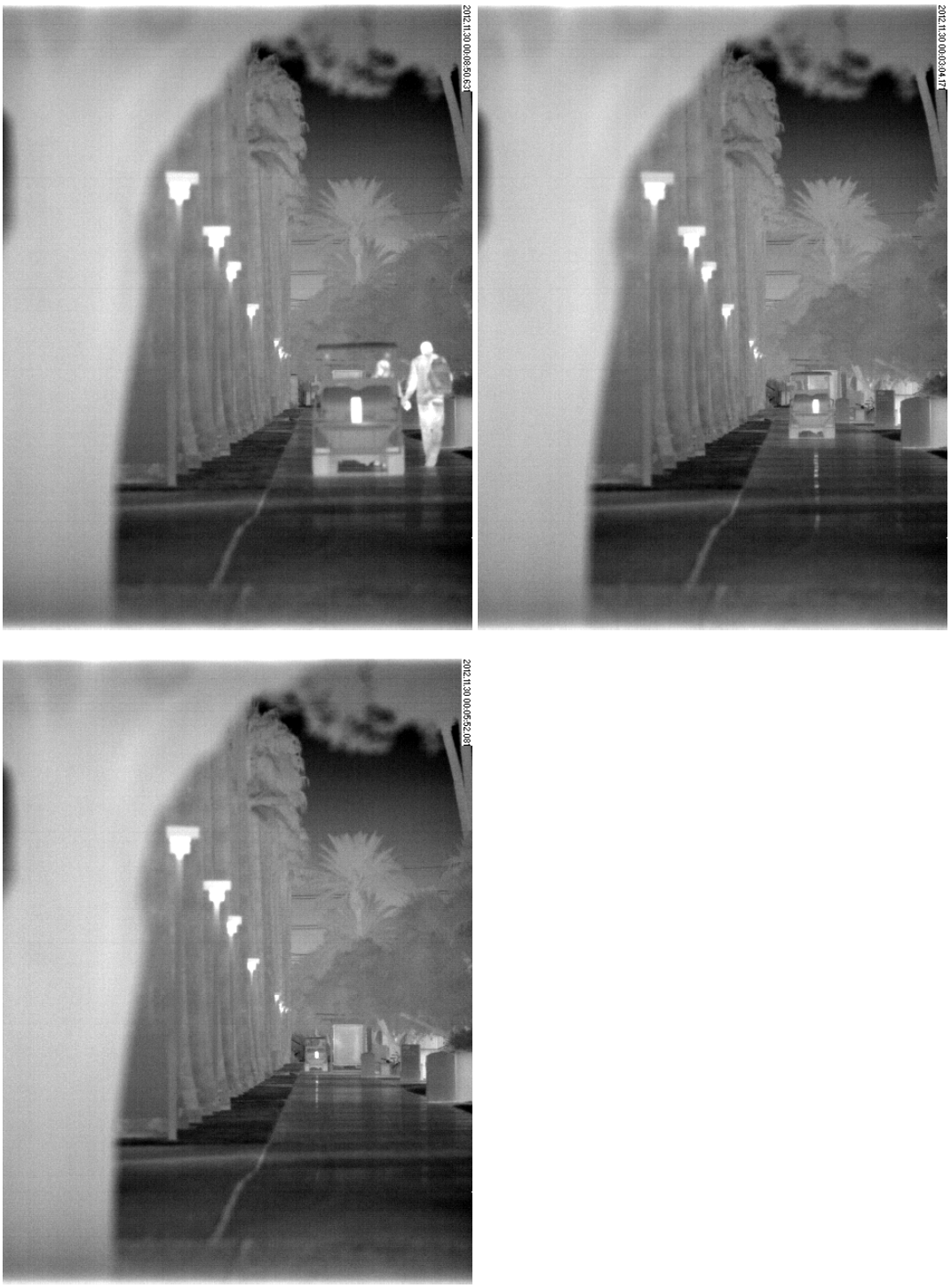

*Figure 58* Infrared images of CubeSat focused at 100 meters at distances of a) 50 meters, b) 100 meters, c) 200 meters.

***Ground Sampling Algorithms for Earth Remote Sensing.*** The visible and infrared cameras each consist of a detector package and an optical assembly. The detectors were reevaluated through the prototyping phase to arrive at the Point Grey Chameleon and the FLIR Tau 2. The optic element was carried over from point design as they continued to be the best options. The 100 mm infrared optics were the highest focal length available in order to maximize resolution, where as the 25 mm visible optics were chosen in order to provide comparable resolution to the infrared camera. The overall specifications of the detector packages and the optics are shown in Table 22 based upon a best estimate orbital altitude of 720 km. The calculations of the resolution are subsequently provided.

The anticipated best theoretical resolution for the visible camera was calculated as follows assuming an altitude of 720 km and IFOV

$$Ground\ Sampling\ Distance = IFOV * Altitude \quad (155)$$

$$Visible\ GSD = 0.148\ mRad * 720km = 107m$$

$$Infrared\ GSD = 0.169\ mRad * 720km = 122m$$

***Pixel Smear Adjustment Algorithm:*** The worst case along track pixel smear due to the velocity of the spacecraft was calculated as follows. This assumes that the detector was integrating for the entire duration of the frame rate interval.

Re = 6378km [equatorial radius of Earth]

$\mu_E$ = 398600 km^3/s^2 [standard gravitational parameter for Earth]

h = 720km [altitude]

fs_IR = 30 Hz or 1/30s. [Infrared Camera frame rate]

fs_Vis = 18 Hz or 1/18s. [Visible Camera color frame rate]

$$v_{s/c} = \sqrt{\frac{\mu_E}{R_e + h}} = 7.494\ km/s \quad (156)$$

$$d\theta = \frac{v_{s/c}}{(R_e + h) * f_s} \quad (157)$$

$$d\theta_{Vis} = 5.87 * 10^{-5}\ Radians$$

$$d\theta_{IR} = 3.52\ * 10^{-5}\ Radians$$

$$dx_0 = d\theta * R_e \quad (158)$$

$$dx_{0_{Vis}} = 374\ meters$$

$$dx_{0_{IR}} = 225\ meters$$

***Image swath width Algorithm:*** The swath width for each image was equal to the ground sampling distanced multiplied by the number of pixels.

$$Swath\ Width = Ground\ Sampling\ Distance * number\ of\ pixels \quad (159)$$

$$Visible\ Swath\ Width = 107\ meters\ per\ pixel * 1290\ pixels$$

The swath width of the visible camera was 138.0km.

$$Infrared\ Swath\ Width = 122\ meters\ per\ pixel * 640\ pixels$$

The swath width of the infrared camera was 78.1km.

***Visible camera: Cross-track, Along-track, and Instantaneous Field-of-View.*** The Point Grey Chameleon's detector was a Sony (Type 1/3, 6mm diagonal) array with an Active Pixel Array of 1280 x 960 pixels and a pixel size of 3.75 μm x 3.75

μm. This corresponds to a 4.8 mm x 3.6 mm array. The focal length of the Fujinon Optics was 25 mm.

$$HFOV_{Visible} = \tan^{-1}\frac{4.8mm}{25mm} = 0.1897Rad = 10.87°$$

$$VFOV_{Visible} = \tan^{-1}\frac{3.6mm}{25mm} = 0.1430Rad = 8.19°$$

$$IFOV_{Visible} = \frac{189.7mRad}{1280\ pixel} = 0.148\ mRad = 0.00848°$$

The visible camera IFOV was 0.148 mRad, however the HFOV was probably rounded. Assuming that only the pixel pitch (3.75 μm) and the focal length (25 mm) are used for small angle approximation, the IFOV was 0.15 mRad.

***Infrared Camera Cross-track, Along-track, and Instantaneous Field-of-View.*** The Ophir Specification Sheet states that the HFOV for a 17 μm pixel pitch detector was 6.2°. The array size was 640x512.

$$HFOV_{IR} = 6.2°$$

$$VFOV_{IR} = 6.2° * \frac{512}{640} = 4.96°$$

$$IFOV_{IR} = \frac{6.2°}{640\ pixels} = 0.0097°\ per\ pixel * \frac{\pi}{180°} = 0.169\ mRad$$

The infrared camera IFOV was 0.169 mRad, however the HFOV was probably rounded. Assuming that only the pixel pitch (17μm) and the focal length (100mm) are used for small angle approximation, the IFOV was 0.17 mRad.

***Image Processing Simulation.*** The performance of the IPA and GNC system was tested through simulation of real images provided from the instrument subsystem. Images captured at ASU—used for resolution analysis within the instrument subsystem team—were also sent to GT in order to validate that the IPAs me their requirements and that that GNC could successfully simulate using a real image to navigate. The details of these GNC simulations are detailed in the PhD dissertation of Peter Schulte. The IPAs were completed as the Master's thesis for Nathalie Vedie.

***Radiometric Target Emission Simulation.*** A simple radiometric simulation was performed to show how the heated CubeSat, with black paint, radiates as compared to blackbodies using a nicolet spectrometer. This was not the spectrum of the actual cubesat, but it was necessary to show the spectrum was similar to a blackbody for subsequent image testing. *Figure 60* shows the energy radiated from the target and an estimated integrated energy, using the midpoint rectangle method and the bounds of the infrared camera's range.

Spectra were also collected for a variety of materials initially thought to be used on *LightSail*. There were many problems with collecting this data, so it should not be referenced. However, it does represent a first attempt to quantify the emissivity of materials that may be used on *LightSail*.

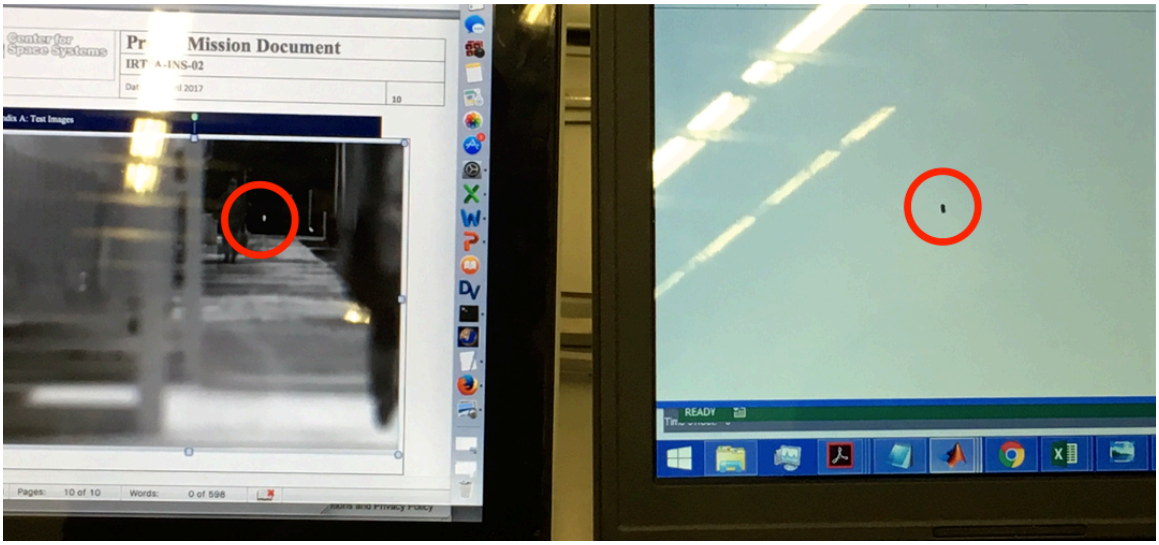


*Figure 59*. Left) Real images captured with the IR camera at ASU of the mock cubesat. Right) A post-processed image from ASU was used in MATLAB simulations for the GNC navigation algorithms.

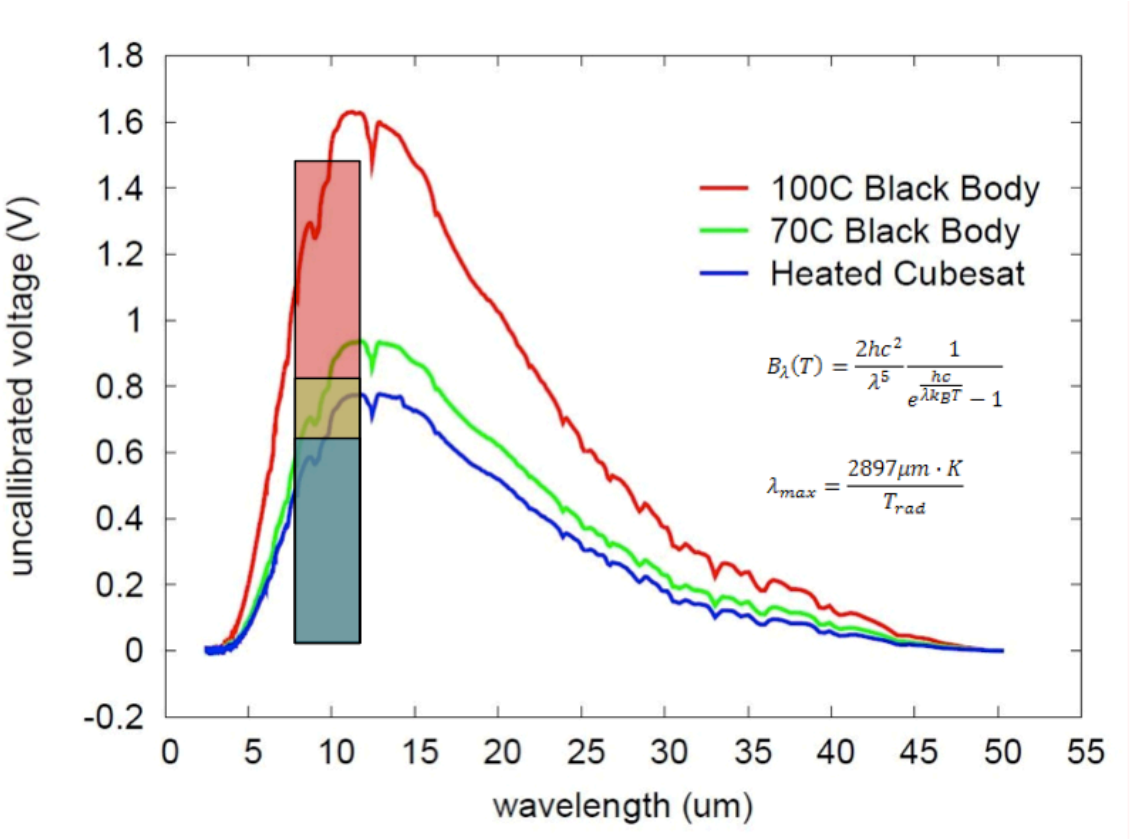


*Figure 60*. The raw spectra of the 100˚ C blackbody target, 70˚ C blackbody target, and a heated CubeSat are shown. The mock cubesat with black paint was heated to 80˚ C in an over and was subsequently cooled to <70˚C. The microbolometer's corresponding range was used along with the midpoint rectangle method of calculus to show an estimated amount of integrated radiance. In reality, the measured energy was integrated over an infinitely small wavelength region dλ.

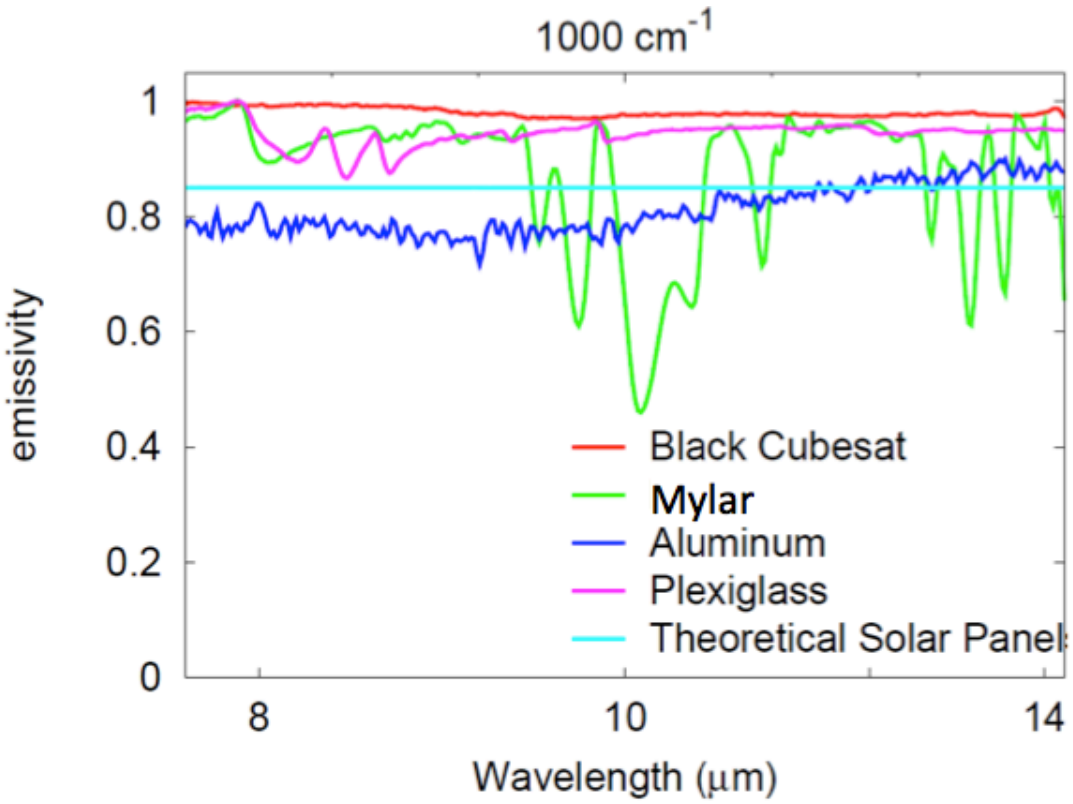


*Figure 61*. The emissivity of a variety of materials was measured that may represent materials used on *LightSail*. The blackbody CubeSat has an emissivity of nearly one. The emissivity of a Mylar space blanket was measured. We also measured a transparent plastic—noted here as plexiglass. Finally, bare aluminim was measured. Since we know aluminum has a very low emissivity, it's likely that this spectrum was a reflection of the instrument. While, this data should not be referenced, it does represent a first cut attempt of trying to identify the emissivity of materials used on *LightSail* that was necessary to make sure tht the spacecraft will be detected.

In order to obtain an initial idea as to what the *LightSail* would look like with visible and infrared images, a simulation was performed at Ecliptic—the company constructing *LightSail* based out of NASA Ames Research Park. This trip was carried out as a side trip from the American Geophysical Union conference in San Francisco and occurred on December 10th. First, a heat gun was used to bring the solar cells up to a temperature that would differentiate them from the equilibrium room temperature *Figure 62*. The prototype LightSail was imaged outside to see how the different surfaces behaved in solar illumination *Figure 63*.

The conclusion of these preliminary tests was that LightSail solar cells and boards have a sufficiently high emissivity, such that they should be identifiable with the infrared camera. The sails have a very low emissivity, such that they will probably appear very cold compared to the spacecraft. With the Earth in the background, the spacecraft may be hard to identify, but the sails will likely be very cold and easy to detect. With space in the background, the spacecraft will be easy to detect, while the sails still probably still be identifiable against the background of space however with illumination via the sun or the Earth. Thus the optimum conditions for tracking the spacecraft before deploying are probably with space in the background. Deployment was probably best image with space in the background as well, but fully deployed images with the Earth in the background will probably emphasize the sails.


*Figure 62*. Visible and infrared images of the prototype LightSail being heated with a heat gun. One of the solar cells very readily heats up when heat was applied.

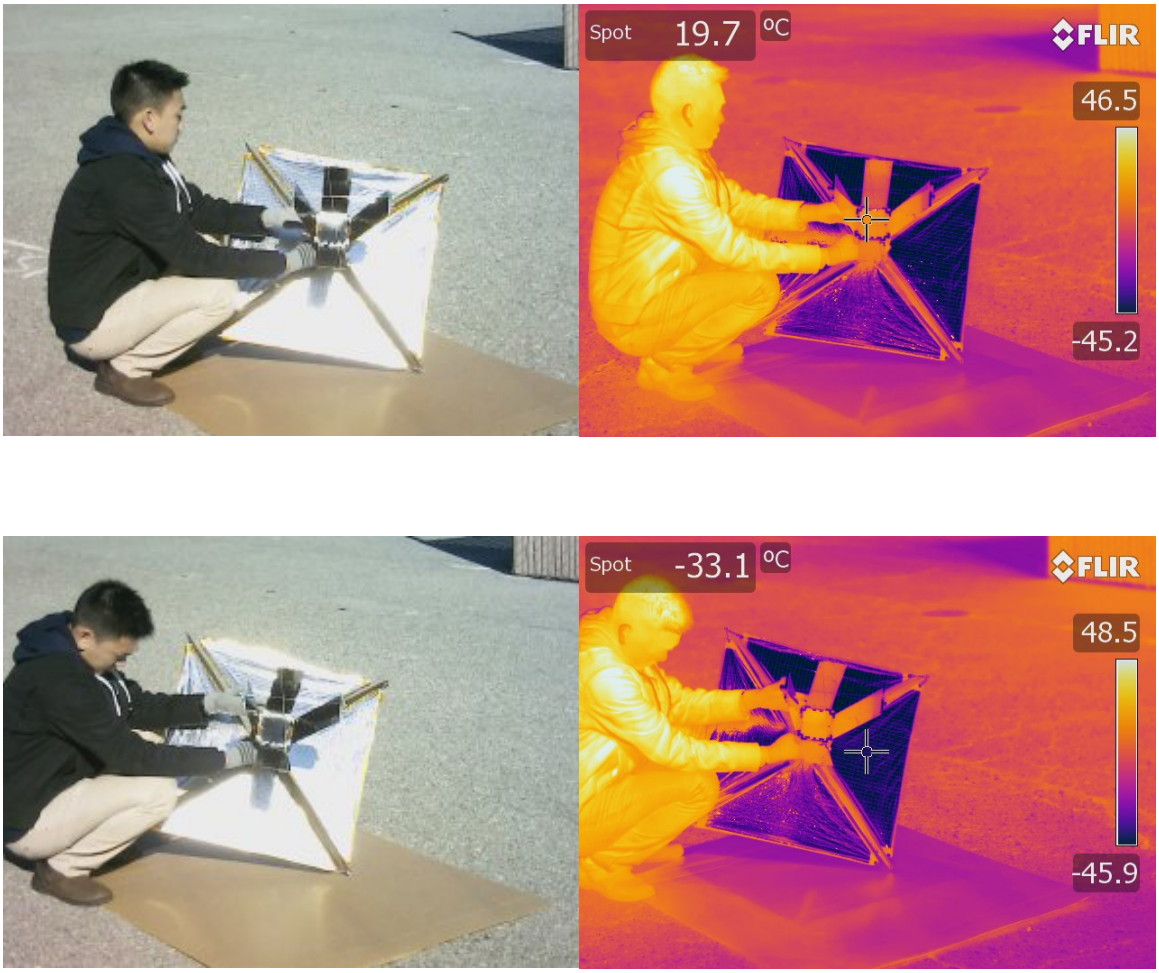


*Figure 63*. The LightSail was placed out in the sunlight. The temperature of the top face was 19.7˚ C. The sails measure ~-33.1˚ C, the diffusive Mylar's low emissivity was partially reflecting the atmosphere and the sun. Thus, the brightness temperature reading was ~50˚C colder than the kinetic temperature.

**Evaluate Instrument Utility**

Is it worth it? The instrument system utility was evaluated to determine if the performance parameters are sufficient and if the system successfully contributes to the overall mission objectives.

The performance of the THESIS instruments for the *Prox-1* mission was measured by five key performance parameters that characterize the instrument system.

Beyond the actual performance parameters, the instrument system was evaluated for its ability to meet the mission objectives. Does the infrared camera produce sufficient images to detect *LightSail-B*? Does the infrared camera produce sufficiently high resolution and clear images to produce a useful image vector? Are image vectors produce fast enough?

The goal oriented measures of effectiveness (Wertz et al., 2011) are detailed within the scope of education. The AFRL would be able to better evaluate the instrument system within the scope of military. Besides improving technology for future missions and providing scientific opportunities for students, there was not a focused utility within the scientific scope. Finally, this mission was not intended for commercial purposes.

Ultimately, the baseline design was attempted. A block wiring diagram shows how the subsystems are interfaced to each other and to spacecraft subsystems *Figure 64*. The specifications are presented in Table 22.

Only the resolution verification test post-vibe and the TVAC radiometric calibration testing were not baselined. These tests are descoped to the threshold design of in-flight calibration, while pre-delivery images are used for resolution characterization.

Table 19.

*Instrument Performance Parameters and Measures of Effectiveness*

| Performance Parameter/MoE | Description | Value |
|---|---|---|
| Performance | | |
| Pixel Scale | This was the length of a pixel at various distances? | 8.5 mm @ 50 meters<br>34.0 mm @ 200 meters |
| Image vector generation speed | This was the time that passes once the image capture command was issued until a vector to LightSail-B was produced. | <2 seconds |
| Radiometric Temperature Accuracy | This was the ability to determine the temperature of LightSail-B in orbit. While a TVAC radiometric test was not completed, the theoretical value on the Tau 2 specification sheet was used until an in-flight calibration was completed. | Theoretically +/- 5K;<br>Radiometric accuracy characterization descoped to in-flight calibration |
| Radiometric Temperature Precision | This was the ability to determine the temperature variation of LightSail-B in orbit. While a TVAC radiometric test was not completed, the theoretical value on the Tau 2 specification sheet for the NEDT was used until an in-flight calibration was completed. | Theoretically <30mK;<br>Radiometric precision characterization descoped to in-flight calibration |
| Power | Independent power methodology saves 3.2W by turning off cameras. Without this savings, the visible camera would not fit within the s/c budget. | 7.4W fully operational;<br>3.8W computer standby; 3.2W combined VIS and IR |

| | | |
|---|---|---|
| Measure of Effectiveness | | |
| Probability of detecting LightSail-B | Is LightSail-B detected in an image with the image processing algorithms? | Simulations from the image processing team, indicate that LightSail-B was detectable in 100% of images with space in the background ad 68% of images with the Earth in the background. [Bellet internal report]. |
| Probability of accurately estimating LightSail-B range | How effective was the combination of the images and algorithms are at determining the range of LightSail-B? | Using real and simulated test images, the range was typically estimated to within 20% accuracy (Walker, 2012). |
| Image vector response time for guidance algorithm effectiveness | How fast are images captured and processed to determine the range vector? | The GNC team desired an image vector input at a frequency of less than 10 seconds from correspondence of their simulations. Range vectors are produced at 5x the necessary value for conducting proximity operations. |
| Goal Oriented Measures of Effectiveness | | |
| Measure of Utility | Did the project provide an opportunity to learn how to design, build, test, and launch an experiment?<br>Was the cost of the project manageable? | Partial success. This project successfully provided an opportunity to design, build, and test spaceflight hardware for students. The instruments were completed within an allowable budget of seed funding from ASU. However no funding was received from customers. |
| Measure of Success | Was the hardware delivered and launched? | Partial success. Instrument was delivered to the primary contractor, the AFRL. Mission was canceled, so s/c-payload was not launched. |

| | | |
|---|---|---|
| Impact of Outcome | What was the quality of education?<br>How many students are going into space science and engineering? | Success. Students received professional education from OTES scientists and engineers in parallel to development. This project prepared the lead author, Michael Veto, for a career in space mission analysis whom acquired an undergraduate Honor's thesis, PhD, and a professional job. The early analysis prepared Sean Marshall for graduate school. Analysis on the camera data helped Amber Keske to acquire a professional industry job. The Phoenix undergraduate cubesat mission, designed by dozens of ASU undergraduates, was spun-off from this project. |
| Level of Preparedness | What was the ability to educate the next generation of scientists and engineers? What was the ability to inspire children and the public in space sciences? | Success. This project created new ways to educate graduate students in space sciences. This project was presented at a TEDx Maricopa in front of hundreds of students and retirees to educate future scientists and engineers. The instrument subsystem was designed, built, and tested in ASU's class 100,000 clean lab in front of thousands of visiting children to demonstrate the excitement of engineering of spaceflight hardware. |

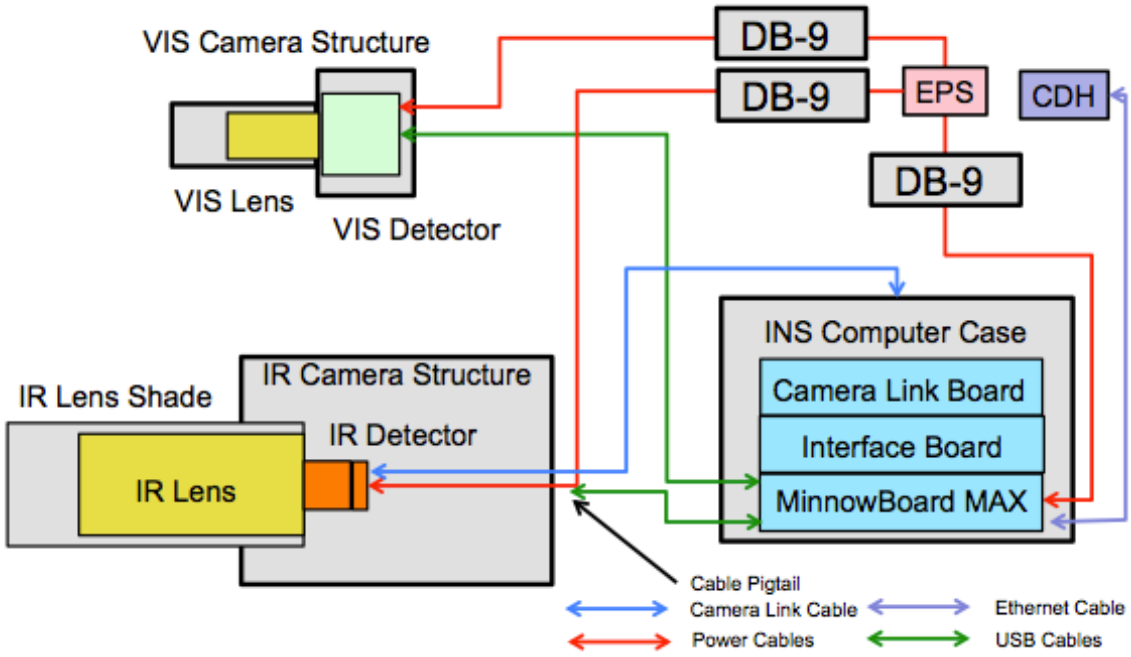


*Figure 64*. Instrument block wiring diagram of THESIS consisting of three major components: the visible camera, the infrared camera, and the instrument computer. All three of the instrument systems are connected to the spacecraft's EPS via DB9 connections. The instrument computer interfaces to the CDH computer via an Ethernet cable. A USB cable that comes out of the IR detector was pigtailed into separate power and data lines that run to the EPS and INS computer system respectively.

### Define Baseline Instrument Concept and Architecture

The THESIS threshold design consists of the minimum threshold system that will meet the requirements. The simple VIS and simple IR from Table 9 are eliminated, as they will not achieve the objectives. The performance-IR requires an instrument computer that will pull the images over high-speed camera link. Calibration of the infrared camera was reserved for in-flight, as a TVAC campaign costs time and money.

A baseline design approach attempts to make the instrument system more efficient and adds a visible camera as a backup imager. All three subsystems are independently powered in order to conserve power when cameras are not in use but the instrument computer functionality was desired. A TVAC campaign was added to perform calibration of the instruments on the ground before flight.

### Revise the quantitative requirements and constraints

The original estimates are revised. The performance requirements and the functional requirements remain the same, but the constraints changed from the point design to the detailed design. The changes are tabulated in Table 21. The complete final specifications are tabulated in Table 22.

Table 20.

*Threshold and Baseline Instrument Concept*

| Segment | Threshold<br>Performance-IR | Baseline<br>Performance-Efficient-IR with VIS Backup |
|---|---|---|
| Mission Instrument Concept | Infrared camera was controlled through a distributed instrument computer, utilizing COTS components in development, to sense emitted radiation from LightSail-B; prox-ops are triggered by s/c computer to instrument computer, and image processing was performed on s/c computer. Camera draws power from instrument computer. TVAC characterization of radiometric performance. | Infrared camera was controlled through a distributed instrument computer, utilizing COTS components in development, to sense emitted radiation from LightSail-B; prox-ops are triggered by s/c computer to instrument computer, and image processing was immediately performed on the instrument computer. Power was distributed to each system independently to save power. A visible camera was a backup. |
| Subject | Emitted infrared radiation from LightSail-B | Emitted infrared radiation from LightSail-B; reflected solar radiation as backup |
| Instrument Payload | IR camera | IR camera; VIS camera backup |
| Instrument Bus | Instrument Computer | |
| | Distributed instrument subsystem power: Infrared camera power supplied through instrument computer | Centralized instrument system power: Independent instrument subcomponent power control through EPS |
| Ground System | GT provides GS. | |
| Mission Operations | Image processing on INS computer | |
| | Semi-Autonomous | |
| | Students from GT and ASU involved in Mission Ops. | |
| Command, Control, and Communications | Images stored on INS computer; No image compression; Camera link data transfer | Images stored on INS computer; Image compression; Camera link data transfer |

| | | |
|---|---|---|
| Orbit | AFRL defines classified orbit;<br>Designed for 720 km orbit | |
| Launch | AFRL determines launch vehicle: SpaceX first commercial Falcon Heavy | |
| Radiometric Calibration | In-flight calibration of radiometric performance. | TVAC characterization of radiometric performance. |
| Resolution Verification | In-flight calibration of resolution post-vibration test. | Resolution testing at AFRL post-vibration test and pre-launch. |

Table 21.

*THESIS Revised Constraints*

| Constraint | THESIS Original Estimate | THESIS Revised |
|---|---|---|
| Mass | 5 kg | 2 kg |
| Volume | IR: 10 in. x 5 in. x 4 in.<br>VIS: 44mm x 29mm x 87mm | IR: 21.68 cm x 10 cm. x 10 cm<br>VIS: 44mm x 41mm x 100mm<br>INS-computer: 2.2 in. x 4.4 in. x 4.6 in. |
| Power | 10 W | IR: 1.5W<br>VIS: 1.7W<br>INS-computer: 3.8W standby, 4.2W imaging |
| Cost | ~$50K | ~$500K |
| Schedule | 5 years | 7 years<br>plus 1 year for writing dissertation |
| Risk | Cost, schedule, technology readiness | Student turnover |
| Regulation | Export Control Technology; ITAR | Launch vehicle requirements, AFRL standards |
| Politics | Directly responds to Air Force need for conducting proximity operations in space. A hidden political objective was to demonstrate proximity operations with IR cameras to promote future possibility of space rendezvous for Mars Sample Return. | Mission objectives reprioritized to accommodate prioritized payloads. |
| Environment | Design to protect from solar illumination | N/A |
| Interfaces | Simple to interface with s/c computer | N/A |
| Development Constraints | Schedule: AFRL review milestones, SpaceX Falcon Heavy launch; Remote design | Milestone slips allow more schedule within launch vehicle development slips |

Table 22.

*Instrument Specifications*

| Parameter | Visible Camera | Infrared Camera | Instrument Computer |
|---|---|---|---|
| Detector and Electronics Boards | Point Grey Chameleon | FLIR Tau 2 | n/a |
| Electronics Boards | n/a | Camera Link Board | Minnowboard-MAX; SilverJaw Lure; PIXCIe |
| Sensor Type | CCD Array | Microbolometer Array | n/a |
| Active Pixel Array Resolution (Cross-track x Along-track) | 1290 x 960 | 640 x 512 | n/a |
| Pixel Pitch | 3.75 µm | 17 µm | n/a |
| Spectral Range | RGB Bayer Pattern 390nm – 750nm | 7.5 – 13.5 µm (Detector) 8 – 12 µm (Optics) | n/a |
| Maximum Frame Rate | 18 FPS | 30 FPS | n/a |
| Optics | Fujinon HF25HA-1B | Ophir 680026 | n/a |
| Focal Length | 25 mm | 100 mm | n/a |
| f/# | 1.4 | 1.6 | n/a |
| diameter | 17.86 mm | 62.5 mm | n/a |
| Field of View FOV (Cross-track x Along-track) | 10.87° x 8.19° | 6.2° x 4.96° | n/a |
| Instantaneous Field of View | 0.0085° or 0.15 mRad | 0.0097° or 0.17 mRad | n/a |

| | | | |
|---|---|---|---|
| IFOV | | | |
| Theoretical Ground Sample Distance @ 720km altitude | 107 m | 122 m | n/a |
| Worst Case Along-track Pixel Smear @720km | 374 m | 225 m | n/a |
| Swath Width | 138.0 km | 78.1 km | n/a |
| Imaging Scheme | Framing Camera | Framing Camera | n/a |
| Instrument Pointing Control System | Fixed to Spacecraft | Fixed to Spacecraft | n/a |
| Spacecraft Attitude Control System | Torque Rods & CMGs | Torque Rods & CMGs | n/a |
| Pointing Accuracy | 30 degrees/axis | 30 degrees/axis | n/a |
| Look Angle | Along-track direction | Along-track direction | n/a |
| POST-DETAILED-DESIGN | | | |
| Physical Parameters | | | |
| Envelope dimensions | 44mm x 41mm x 100mm | 10cm x 10cm x 21.81 cm | 2.2in. x 4.4in. x 4.6in. |
| Mass | 135 g | 1296 g | 253 g |
| Moving Parts | None | Internal calibration flag | None |
| Electrical Power | | | |
| Voltage | 5V | 5V | 5V |
| Standby, operating power | 1.7W, 1.7W | 1.5W, 2.5W (calibration) | 3.8W, 4.2W |

| Operations | | | |
|---|---|---|---|
| Operating modes | 6<br>VEFR16: Visible Early Full Raw 16bit .pgm<br>VEFR8: Visible Early Full Raw 8bit .pgm<br>VEFM: Visible Early Full Mono 8bit .jpg<br>VEFC: Visible Early Full Color 8bit .jpg<br>VESM: Visible Early Summed Mono 8bit .jpg<br>VETM: Visible Early Thumbnail Mono 8bit .jpg | 5<br>IR8L: Low Gain, 8-bit<br>IR8H: High Gain, 8-bit<br>IR16L: Low Gain 14-bit<br>IR16H: High Gain 14-bit<br>IR8TH: Thumbmail 8-bit | 1<br>Automatic telemetry and thumbnail storage,<br>Manual image capture |
| Boot Time | 3 seconds | 3 seconds | 30 – 55 seconds |
| Duty cycle | VEFC: <1.5 seconds | IR16H: <2 seconds | Telemetry recorded every 5 minutes |
| Need for eclipse operation | Yes | Yes | Yes |

| | | | |
|---|---|---|---|
| Telemetry and Commands | | | |
| Number of command and telemetry channels | 5 imaging commands<br>71 telemetry channels<br>1 beacon channel | 4 imaging commands<br>24 telemetry channels<br>3 beacon channels | 7 auto commands<br>16 telemetry channels<br>5 beacon channels |
| Command memory size and time resolution | VEFC frame rate: 18 Hz | IR16H frame rate: 30 Hz | Linux telemetry in 0.001 seconds |
| Thermal Control | | | |
| Non-operating temperature limits | -30˚C – 60˚C | -55˚C – 95˚C | 0˚C – 70˚C |
| Operating temperature limits | 0˚C – 45˚C | -40˚C – 80˚C | 0˚C – 70˚C |
| Heat rejection | Conduction to spacecraft | Conduction to spacecraft | Conduction to spacecraft |

## DEFINITION OF REQUIREMENTS

The requirements for the instruments flow down directly from the mission statements of *Prox-1*. The requirements flow down presented detail the mission objectives, the Level 1: Mission Requirements, the Level 2: System Requirements, and the Level 3: Instruments Requirements. The Instrument requirements are presented in Table 23 for the infrared camera and Table 24 for the visible camera.

Table 23

*Requirement verification matrix for the infrared camera*

(Next page)

| INS | | Science Instruments | Source | Verification Method | Flight Verification Source Document and LINK (test procedure, analysis report, etc.) |
|---|---|---|---|---|---|
| INS-1 | | The Prox-1 satellite shall use an infrared camera to acquire thermal images of the target. | FMS-1 | Testing | 022_DITL_TestingReport |
| | INS-1.1 | The infrared camera shall provide the spatial and thermal resolution necessary for the image processing algorithms to correctly identify targets. | INS-1 | Analysis, Testing | INS_IR_Resolution_Report (Predelivery), INS_In-Flight_Resolution_ Test_Report |
| | INS-1.1.1 | The infrared camera shall consist of a 640 x 512 pixel array. | INS-1 | Inspection | INS_Specification_Sheet |
| | INS-1.1.2 | The infrared camera shall be able to resolve the target to within at least three contiguous pixels at a range of 200 m. | INS-1 | Analysis, Testing | INS_IR_Resolution_Test_Report |
| | INS-1.1.3 | The infrared camera shall have a noise equivalent temperature difference (NETD) of 1 K. | INS-1 | Analysis, Testing | INS_In-Flight_Radiometric_ Test_Report |
| | INS-1.1.3.1 | A calibration shutter shall be integrated into the microbolometer thermal imager assembly to acquire calibration temperatures. | INS-1 | Inspection, Testing | INS_Specification_Sheet |
| | INS-1.1.3.2 | The temperature of the infrared camera environment shall be monitored to assist in calibration. | INS-1 | Testing | INS_Specification_Sheet |
| | INS-1.2 | The infrared camera shall produce images with a signal to noise ration of greater than 10:1 in order to ensure images of sufficient quality to assist attitude control based upon onboard processes. | INS-1 | Analysis, Testing | INS_In-Flight_ Radiometric_Test_Report |
| | INS-1.3 | The infrared camera shall be protected from incident solar radiation with a solar shade. | SS-3.1 | Analysis, Inspection | INS_Solar_Shade_Report |

Table 24.

*Requirement verification matrix for the visible camera.*

| INS | | Science Instruments | Source | Verification Method | Flight Verification Source Document and LINK (test procedure, analysis report, etc.) |
|---|---|---|---|---|---|
| INS-2 | | The Prox-1 satellite shall use a visible camera to acquire visible images of the target. | FMS-1 | Testing | 022_DITL_TestingReport |
| | INS-2.1 | The visible camera shall provide the spatial resolution necessary for the image processing algorithms to correctly identify targets. | FMS-1.1 | Analysis, Testing | INS_Visible_Resolution_Test_Report (Predelivery), INS_VIS_In-Flight_Resolution_Test_Report |
| | INS-2.1.1 | The visible camera shall consist of a 1296 x 964 color CCD array. | MD-4,INS-2.1 | Inspection | INS_Specification_Sheet |
| | INS-2.1.2 | The visible camera shall be able to resolve the target within to within at least three contiguous pixels at a range of 200 m. | MD-4,INS-2.1 | Analysis, Testing | INS_Visible_Resolution_Test_Report |
| | INS-2.2 | The visible camera shall produce images with a signal to noise ration of greater than 10:1 in order to ensure images of sufficient quality to assist attitude control based upon onboard processes. | FMS-1.1,FMS-3,FMS-4 | Analysis, Testing | INS_Visible_Thermal_ Performance_Report |
| | INS-2.3 | The visible camera shall be protected from incident solar radiation with a solar shade. | SS-3.1 | Analysis, Inspection | INS_Solar_Shade_Report |

# INSTRUMENT FLIGHT HARDWARE DETAILED DESIGN AND FABRICATION

## Overview of Flight Hardware Development Timeline

The following figure shows the status of the hardware development along each of the review milestones. In general, the instrument hardware was about one review behind of the desired status. However, the baseline instrument design was completed and ready for spacecraft level testing at the preship review (PSR). The calibration was descoped to the threshold requirement of an in-flight calibration rather than a TVAC radiometric campaign and a post-vibration resolution testing. The instrument system worked as designed with flight harnessing on the spacecraft with simplified functional testing with each of the spacecraft subsystems. Some concerns arose during simplified integrated testing. The spacecraft was never tested as a whole with the instruments, and the grounding of the instruments with the spacecraft EPS team was not adequately completed to rule out ground loops. In summary, a fully functional instrument system was delivered that achieved all of the requirements. Fully integrated spacecraft level testing was required to demonstrate that the instruments, within the spacecraft system, survive vibration testing, adequately mitigate heat within the space environment, and successfully avoid ground loop interferences. Baseline level instrument performance characterization was descoped to a threshold in-flight checkout phase. Each of the instrument subsystem designs was subsequently described.

*Subsytem Integration Readiness Review (SIRR): Nov. 6,7 2013*

- Prototype Infrared Camera Hardware
- Switched to Chameleon Cmaera
- Procuring cameralink to USB interface device to connect IR to CDH

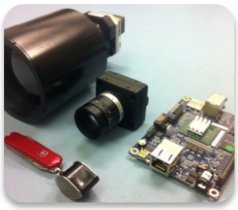

*Pre-Integration Review (PIR): April 8, 2015*

- Switched and procured FLIR IR Tau 2 camera
- Designed Instrument computer on Beagleboard
- Switched Instrument Computer to Minnowboard
- Interfaced INS computer with CDH computer
- CDH computer commands visible imgae capture over INS computer

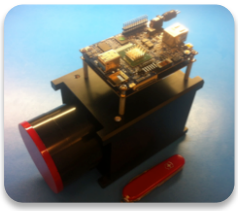

*Pre-Integration Review Redo (PIR2): December 16, 2015*

- All Instrument hardware procured and tested
- High speed interface boards for infrared camera procureed and tested
- Only conformal coating, staking remain
- Basic software functionality
- Enginineering model harnessing works

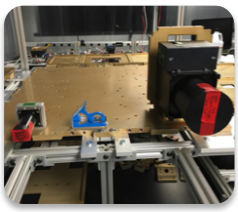

Pre-Pre-Ship Review (PPSR): May 20, 2016

- Instruments are hard-mounted to the spaceraft bottom plate
- Some software updates implemented
- Design of flight harnessing in-progress

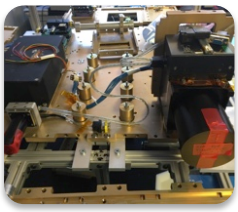

Pre-Ship Review (PSR): April 21, 2017

- Flight software is implemented
- Flight harnessing is installedephasize
- Calibration is descoped for possibly environmental testing at AFRL

*Figure 65*. Progress of the instruments throughout the various reviews after FCR in 2012.

## Mechanics

### Infrared Camera Housing Assembly

The completed infrared camera system was 10 cm wide by 10 cm high and 21.75 cm long. The infrared camera structure was designed with a CubeSat form factor in mind to ease integration with the spacecraft and provide modularity for future mission concepts. A 1.5U CubeSat structure was reduced to 1.4U structure in order to fit within the Prox-1.

The recess for the 100 mm lens and solar shade was 3.75 cm deep and the lens shade was 11.5 cm long. The length of the infrared camera structure was 14 cm. The lens shade provides 2.7 cm of extension over the lens assembly. This was the maximum length provided to the INS subsystem from the spacecraft structures team to meet the microsat volume requirement from AFRL. The lens shade also has a wall thickness of 0.3 cm in-between the structure and the lens. Thus, without the shade, the length of the infrared camera was reduced by 3 cm to 18.75 cm.

The spacecraft team sent the interfacing part files to ASU electronically, and they were machined on campus for fit checking the instrument components before integration of the instruments at Georgia Tech. This technique proved very successful.

### Visible camera housing assembly

The visible camera housing assembly was essentially an aluminum version of the existing Chameleon plastic case that was upgraded with a solar shade. The mounting configuration from the original factory case are preserved and were given to Georgia Tech. The *Prox-1* structures team designed a special mounting ring that fastened the visible camera to the spacecraft's bottom plate. The length of the visible camera was 100 mm. There was ~0.5 mm of paint thickness at the end of the solar shade for a total

length of 100.5 mm The width of the visible camera was 44 mm. The height of the visible camera was 41 mm

**Instrument computer housing assembly**

A computer housing assembly was designed that encases the computer electronics boards for protection and provides mounting fixtures for harnessing and holes for integration to the spacecraft.

The final measurements of the instrument computer are 4.525 inches long by 4.125 inches wide by 2.250 inches tall. This includes the mounting tabs, the harnessing fastening points that protrude from the case, and the bumper support for the cantilevered camera link harness.

The instrument computer was designed to be mounted on top of the infrared camera for *Prox-1*, however it can be mounted in a different location for other spacecraft configurations. Custom configurations may require a redesign of the harnessing.

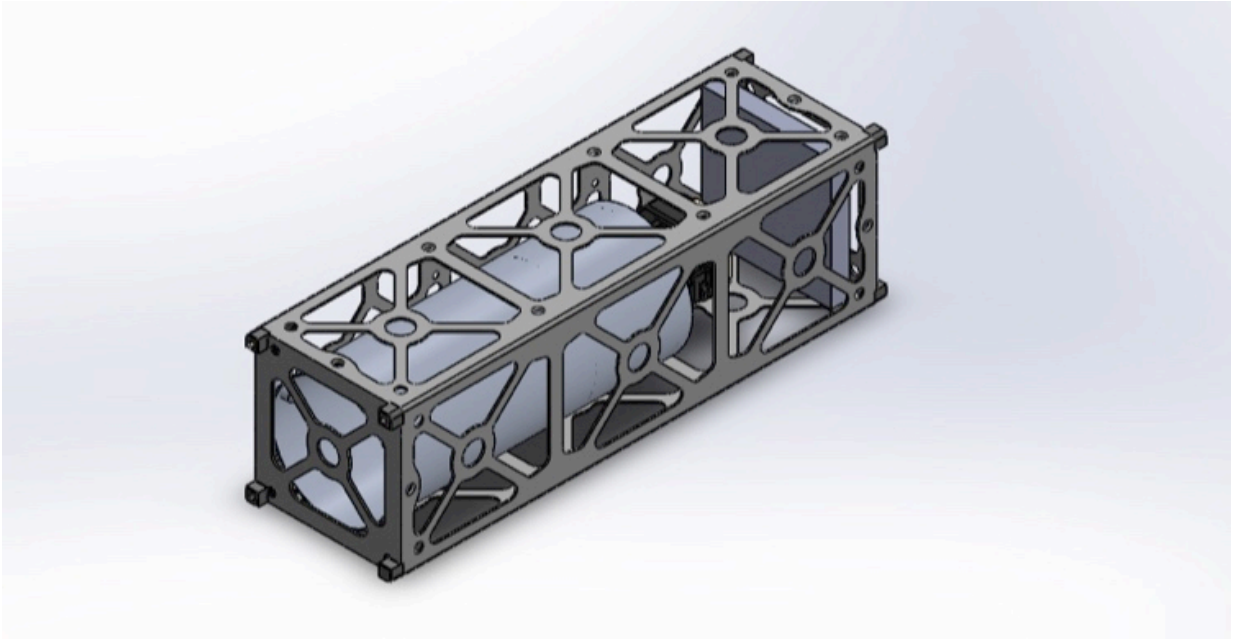

*Figure 66*. Early concept model for the infrared camera. The original intent was to contain the full infrared camera within a 3U CubeSat (10 cm x 10 cm x 30 cm). Due to the spacecraft volume limitations, the solar shade was reduced. However, the IR structure was modeled after a modified 1.5U structure and the whole volume nearly fits within a 2U structure.

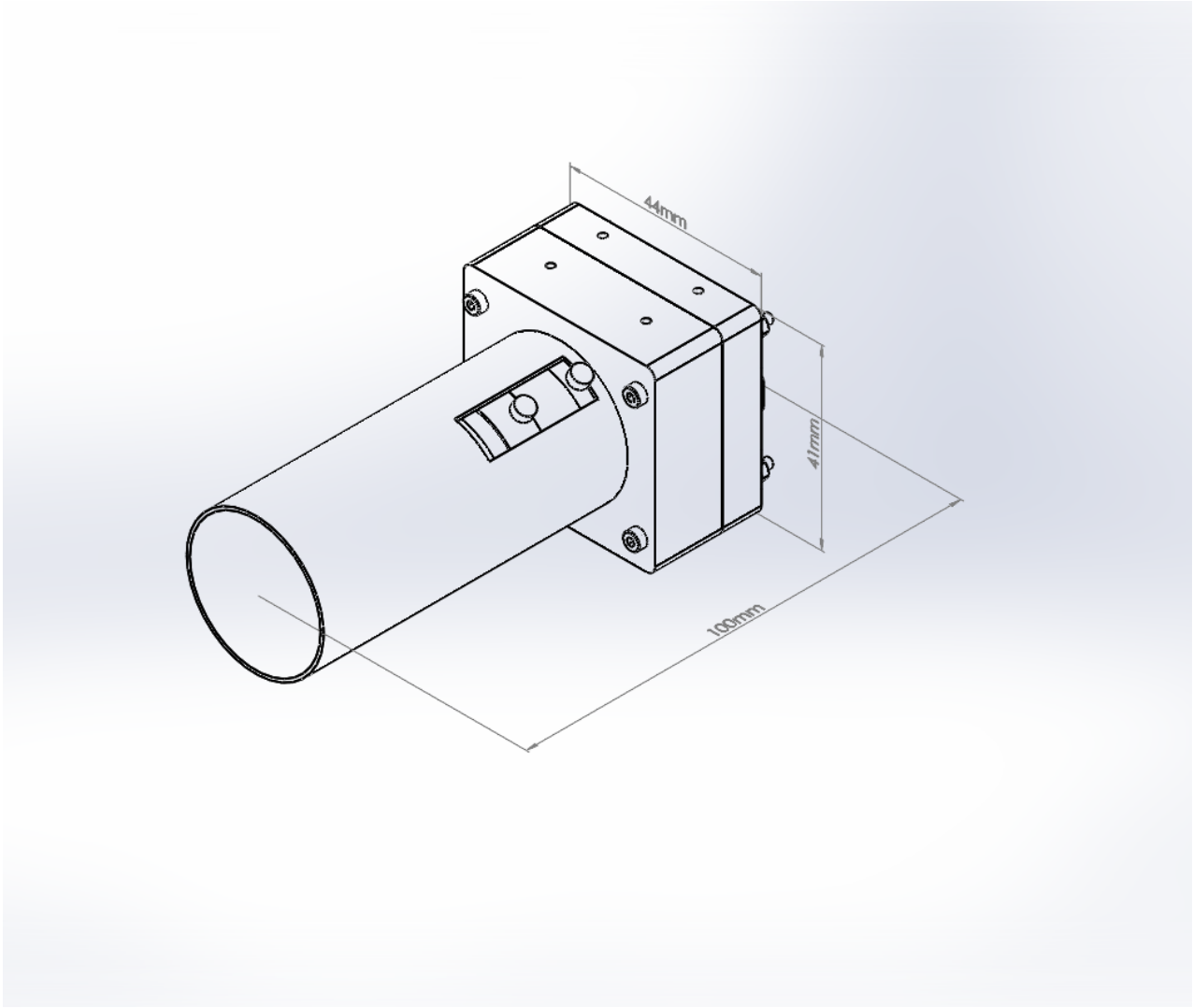


*Figure 67*. Visible camera assembly.

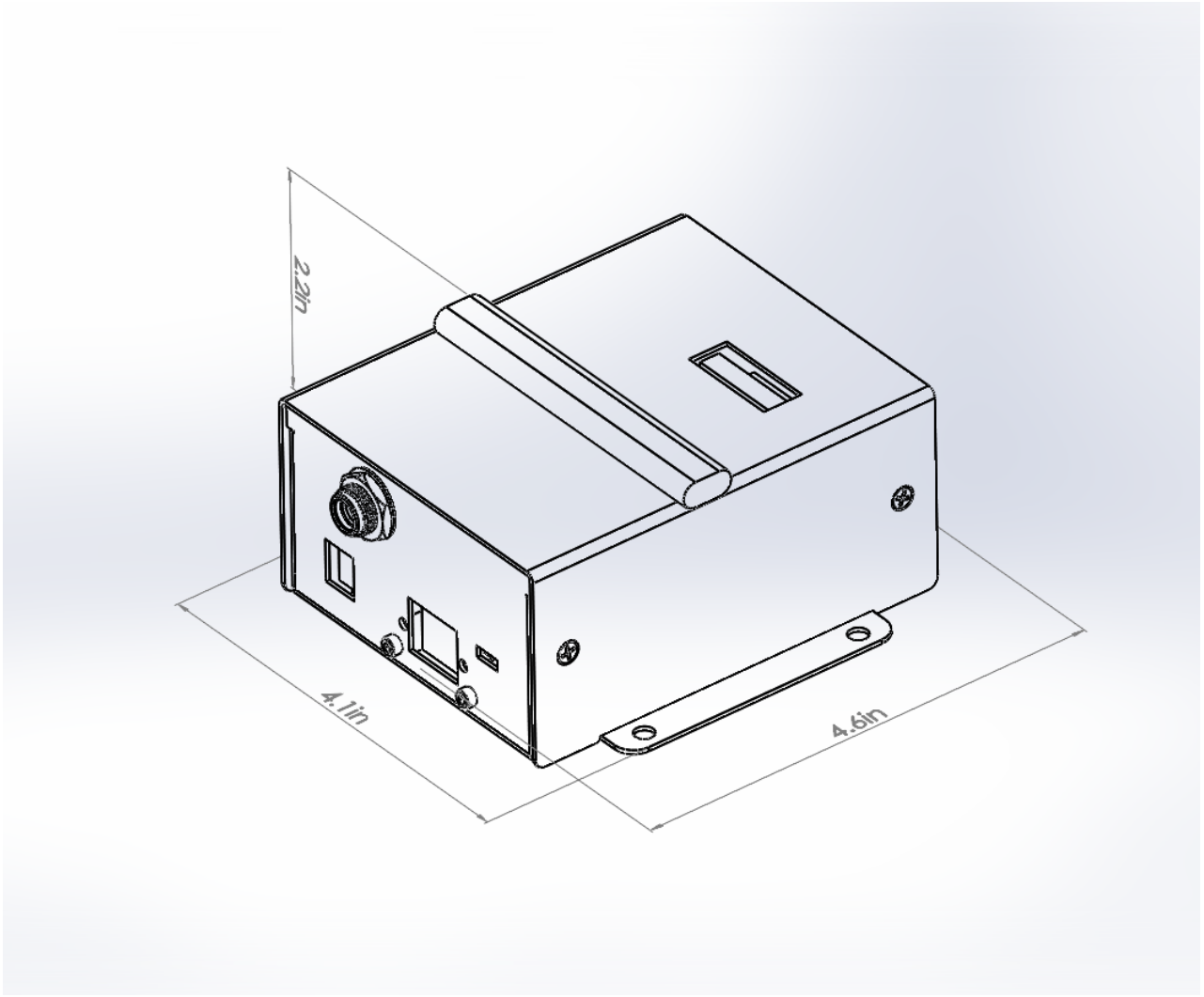


*Figure 68*. The instrument computer assembly.

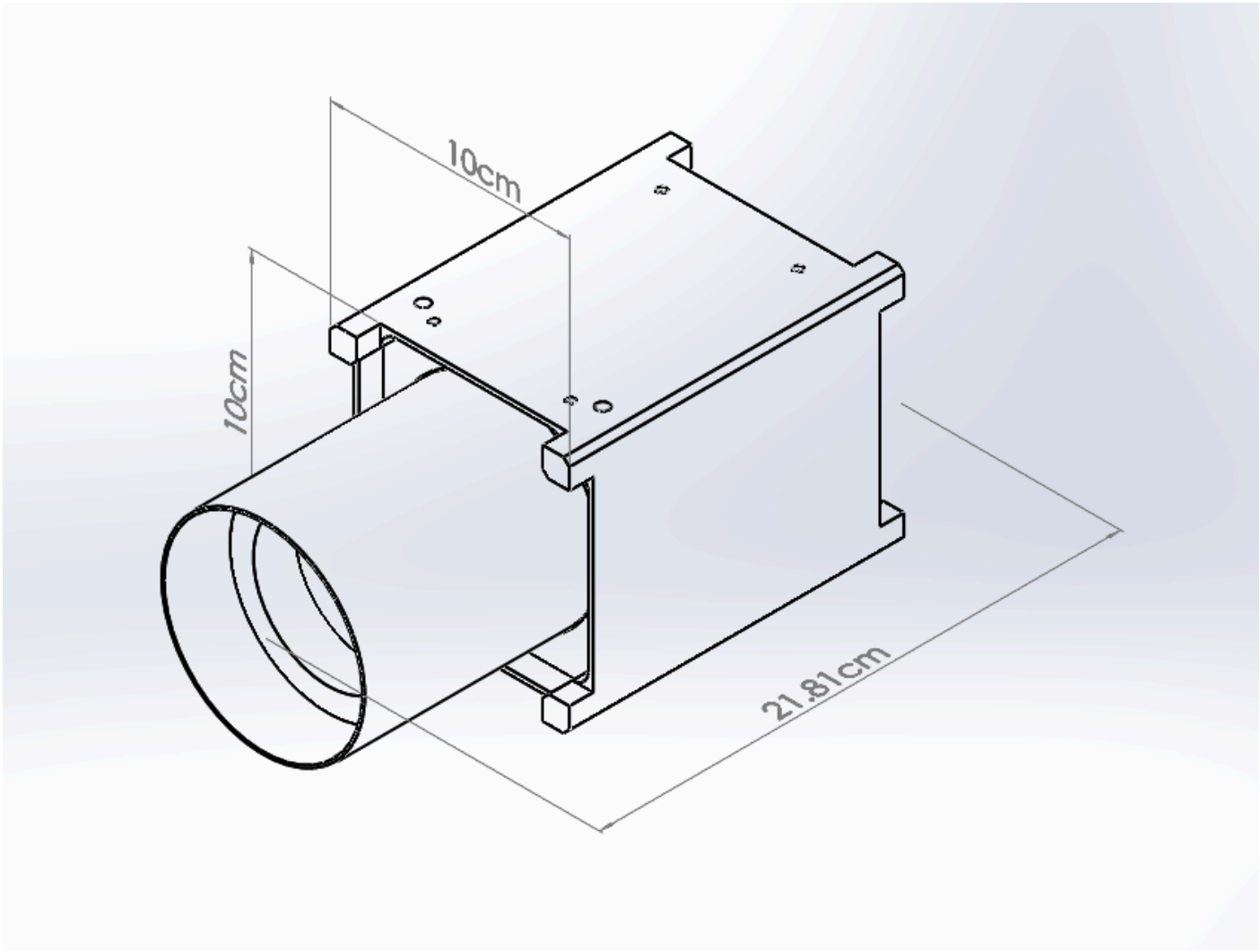


*Figure 69*. The infrared camera assembly.

### Instrument Computer Case Assembly

The case protects the instrument computer, provides the fastening mounts for the harnesses, and provides flanges for the computer to be mounted within the spacecraft. A CAD model was constructed of the instrument computer stack and sent to a company called Protocase. This company created a drawing for a case and supplied a corresponding CAD file of the case. The Protocase CAD file was imported into the instrument computer model to verify the compatibility. The drawing was approved for the case completed with black anodize. After delivery, the instrument computer was mounted into the case. Later, the case was modified to incorporate harnessing mounts.

### Helicoil Inserts

In order to conform to spacecraft standards for back-out protection, locking helicoils are inserted into infrared camera structure. Six 1/4"-20 locking helicoils were inserted at the structure to lock the spacecraft bolts. Four 8-32 locking helicoils are inserted into the top of the infrared structure to lock the bolts that fasten the instrument computer to the infrared camera structure.

The bolts used to attach the visible camera to the spacecraft structure were too small for locking helicoils.


*Figure 70*. The instrument computer case sitting next to the instrument computer showing corresponding holes for harness connections.

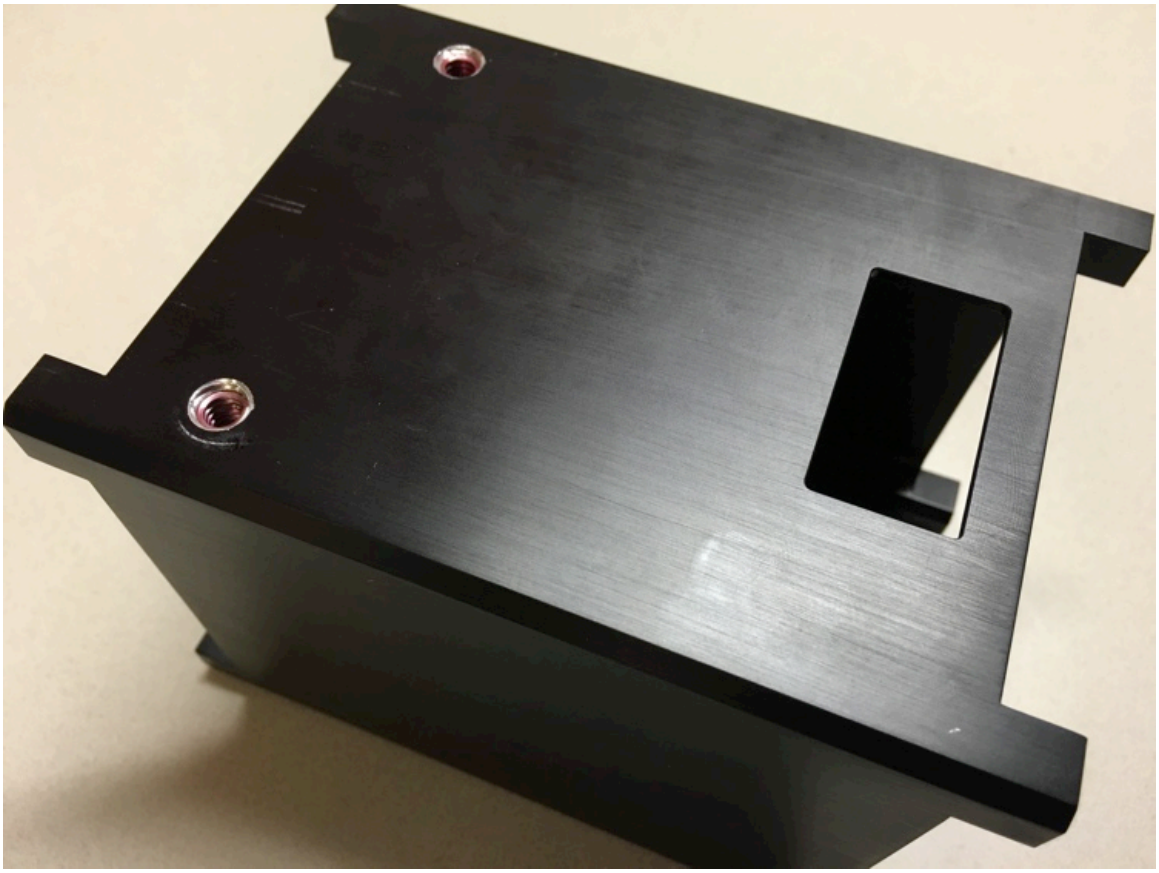

*Figure 71*. The infrared camera structure, with bottom face pointing up, shows the maroon locking helicoil inserts that lock the ¼”-20 bolts from the bottom plate of the spacecraft structure.

### Chromate conversion and Anodizing

The aluminum structures were treated for protection. First all of the parts were treated with the chemical chromate commonly known by the eponym Alodine. This process protects the aluminum from corrosion but maintains the electrical conductivity.

The structural elements are then prepared for anodize. The surfaces of the two visible camera structure elements that come into contact are then masked. In addition, the inside of the solar shade was masked. The feet of the infrared camera structure are masked as well. Masking these elements prevents the anodization process on these designated surfaces to preserve the electrical conductivity and provide clean surfaces for painting.

The parts are then andoized. By applying an electrical current into an electrolyte bath, the surface of the aluminum was oxidized to create a protective coating that has a hardness equal to sapphire. The anodized surface treatment was stronger and creates an electrical insulation. In addition, a black coloring was included. All anodized surfaces on THESIS are black. All Alodined surfaces are gold.

### Paint

The inside face of the solar shades was painted in order to minimize any reflections into the optical system. Aeroglaze flat black Z306 was chosen for its common use in the Aerospace industry as well as the familiarity of use with the vendor.

*Figure 72*. Visible camera parts after alodine treatment. Green masking compound was applied to protect surfaces that will not be anodized.

**Mass**

The mass estimate of the instrument subsystem has evolved throughout the course of the project. At the onset of the mission, the budget for the instrument subsystem was 5 kg. During the design phase, the structure of the spacecraft was determined to provide sufficient radiation shielding for the subsystems, thus the structure of the instruments was reduced. Prior to subsystem integration, the instrument mass estimate was reduced down to 2 kg. The mass of each of the instrument subsystems components was measured prior to integration to the spacecraft bottom plate. The total mass of the major instrument subsystem components (i.e. without harnessing or fasteners) was ~1.68 kg. The instruments were 16% under-budget for mass prior to modification and harnessing.

After de-integration of the instruments from Prox-1, the instrument masses were re-measured for a final mass measurement. The modifications increased the mass by 13 grams. The harness masses were also measured to 326 grams. This does not include the harnessing from the EPS that connects into the INS DB9 connectors that provide power to the instruments. The harnessing from EPS that traverses most of the distance to the instruments was the responsibility of the spacecraft harnessing team and was not included in the INS mass budget. The harnessing fasteners to the instruments as well as the hardware to mount the instrument computer to the infrared camera was estimated to total ~30 grams. This estimate was derived from measuring de-integrated fasteners with 15% added conservatism for re-integration. The final total measured mass of the THESIS major subsystem components, harnessing, and fasteners for harnessing was ~2.04 kg. Although this was 2% over the original budget estimate, some of the harnessing and fastener mass was likely budgeted elsewhere in the spacecraft mass budget. The final INS subsystem mass measurements fall closely within the original mass estimate of 2 kg.

Table 25.

*Instrument Subsystem Mass*

| Subsystem | Pre-integration Mass (g) | Modification Delta Mass (g) | Final Mass (g) |
|---|---|---|---|
| Instrument Computer | 241 | 12 | 253 |
| Infrared Camera | 1295 | 1 | 1296 |
| Visible Camera | 135 | 0 | 135 |
| Systems Sub Total | 1671 | 13 | **1684** |
| Power to INS Computer | | | 25 |
| Power to Vis Camera | | | 19 |
| Power to IR Camera (Y) | | | 49 |
| IR data to INS Computer | | | 97 |
| IR serial data to INS Computer (Y) | | | See (Y) |
| VIS data to INS Computer | | | 34 |
| INS Computer to S/C Computer | | | 102 |
| Harnessing Sub Total | | | **326** |
| Harnessing Hardware Estimate | | | **~30** |
| **TOTAL** | | | **2040** |

### Fasteners and Torque

A list of all the fasteners and their torques was found in the appendix. In general, high strength A286 was used when available. However, many of the fasteners could not be found in the high strength steel and were ordered from McMaster. All of the hardware was torqued and then staked for extra backout protection. The hardware to mount the instruments to the spacecraft was owned by the spacecraft team.

### Harnessing mount modifications

Harnessing mounts were retrofitted onto the instrument computer case and the camera link card in order to provide ruggedized fixtures for the USB cables and the Ethernet cables. These parts were fabricated from aluminum, alodined, and fastened to the structure. The harnessing fastening screws provide a hard attachment that prevents backout of the connector.

### Glass Fracture Control

The optical elements for the visible and thermal imagers of the Prox-1 mission must comply with the UNP user's guide section 6.7.12 states, “Use of glass should be minimized. Where glass must be used, it should be non-pressurized and subject only to inertial loading. (Ref. NASA -STD-5003, Section 4.2.3.6).” A study of the NASA standard reveals that the optical components of the visible camera are non-fracture critical, while the optical components of the infrared camera are fracture critical. In order to comply with NASA-STD-5003 section 4.2.3.6, it was determined that optical component of the infrared camera should be tested to vibration levels higher than expected during the mission as outlined in section 4.2.3.6.2.d. This will satisfy the fracture control requirements—pending the approval of the fracture control authority, whom it was assumed to be the UNP.

Although NASA-STD-5003 was specified for payloads to be used on the Space Shuttle, section 1.3.b details that this document was suitable for payloads aboard other vehicles if the program/project management has determined that the suitability of this document. The University Nanosat Program, being the program management, has specified in the UNP user's guide that NASA-STD-5003, section 4.2.3.6 was the required standard for glass components.

As detailed in section 4.2.3.6.1, “a glass component shall be considered fracture critical if it was loaded by either external or pressure loads or if it fails to meet the “low release mass part” or “contained part” requirements specified in 4.2.2.1 and 4.2.2.2. The lenses for the visible camera are shown to be non-fracture critical, whereas the IR lens was shown to be fracture critical. Based upon the following criteria.

***External Loads and Pressures.*** The lenses do not have external loading or pressures applied to them. They only have inertial loading.

***Low Release Mass Part.*** The visible lens qualifies as a low release mass part because it meets requirement 4.2.2.1. It has a mass of less than 113 grams, it does not support any weight, and it was not preloaded in tension. Thus, the visible camera lens was non-fracture critical. The IR lens however fails to be classified as a low release mass part, because it has a mass greater than 113 grams.

***Contained Part.*** If a part fails the low release mass part designation, then it must be shown that the part can be fully contained with the payload as to not cause catastrophic hazard as outlined in requirement 4.2.2.2. The IR lenses are not fully contained within the spacecraft and are fracture critical.

Because IR lens was fracture critical, a method must be used to mitigate effects of fracturing. Section 4.2.3.6.2.d of NASA-STD-500 states:

"If the component has only inertia loading during mission phases, including launch and landing, and does not meet either requirements of 4.2.2.1 and 4.2.2.2, a vibration test of the component, in excess of flight levels, followed by a rigorous visual inspection may satisfy fracture control requirements. Effects of humidity and/or cleanliness during the tests shall be considered. Use of this option shall be approved by the responsible fracture control authority."

Thus, a vibration test in excess of the flight vibration levels will serve to meet the NASA standard if approved by the program management—UNP.

***Approval.*** Fracture control requirements can be satisfied if the fracture control authority approves of a vibration test as outline in section 4.2.3.6.2.d of NASA-STD-500. It was assumed that UNP has the authority of fracture control for the nanosat mission.

The optical elements for the visible and thermal imagers of the Prox-1 mission will require the use of glass materials. The UNP user's guide section 6.7.12 states, "Use of glass should be minimized. Where glass must be used, it should be non-pressurized and subject only to inertial loading. (Ref. NASA -STD-5003, Section 4.2.3.6)." A study of the NASA standard reveals that the optical components of the visible camera are non-fracture critical, while the optical components of the infrared camera are fracture critical. In order to comply with NASA-STD-5003 section 4.2.3.6, it was determined that optical component of the infrared camera should be tested to vibration levels higher than expected during the mission. According to 4.2.3.6.2.d, this will satisfy the fracture control requirements—pending the approval of the fracture control authority. It was assumed that UNP has the authority of fracture control. Thus, this memo was requesting UNP to grant approval of vibrational testing to satisfy UNP requirement 6.7.12.

**Vent Hole Analysis and Modification**

A vent hole was required for a sealed container to sufficiently evacuate air as to avoid a pressurized vessel. An analysis was completed to determine he size of the vent holes necessary to limit the pressure difference on the Ophir lens for the infrared camera.

For NASA spaceflight missions, an analysis has been done on space shuttle payloads to determine the adequate vent hole sizing for spacecraft payloads (Mironer & Regan, 1983). The basic rule of thumb was that a quarter inch diameter hole was required for each cubic foot of volume to limit the maximum pressure difference during ascent to less than 0.5 psi. We follow the example and take a ratio of the volume of the lens structure to a cubic foot. This was a very conservative estimate, as we took the outer dimensions of the lens to calculate a cylinder for the volume of the lens cavity and use the full length of the lens with margin to support the air gap up to the microbolometer surface.

Using the method, we need a vent hole with a diameter of 0.037 inches. Alternatively, we can drill 2 holes with diameter of 0.0185 in. This was larger than a 1/64 bit (0.1562) but smaller than a 1/32 (0.03125). We shall drill two 1/32 holes.

( 160 )

$$(0.25\ in.) * \sqrt{\frac{\pi * \left(\frac{8.2cm}{2}\right)^2 * 11.8cm}{(12\ in.)^3} * \frac{1\ in.^3}{16.387\ cm^3}} = 0.037\ in.$$

Recommended Area: π * (0.037 in. / 2 ) ^2 = 0.001 in.²

Used Area: 2 holes * π * (0.03125 in. /2 ) ^2 * = 0.0015 in.²

Ratio of Areas: 1.5

Ratio of Diameters: 1.2

Two holes are drilled at 1/32” diameter. This was 1.5 times the required amount for an overestimated cavity volume that was around half the calculated volume. These two factors ensure that the vent hole mitigation approach was very conservative. The holes are antipodal to each other at the prescribed locations from the vendor’s suggestion. Subsequent testing in vacuum confirmed that the lens chamber successfully vented.

**Camera Solar Shade Design**

**Overview**

Solar shades are helpful to protect the system from unwanted out of field light. An analysis was completed that shows how far the shade must extend from the current lens in order to block out incident solar radiation as a function of the solar vector. The following section characterizes the testing of the necessity for the Solar Shades as well as the actions taken.

First, we calculate the desired lengths of the solar shades for the lenses. We determine that the visible shade should ideally extend 40.7mm beyond the visible lens and the IR solar shade should ideally extend 121.5mm beyond the IR lens. However, the visible camera extension was reduced to 35mm to allow for conservatism in blocking the FOV, and the IR solar shade was reduced to 27mm as a spacecraft volume requirement.

Second, we test a test unit solar shade on the visible camera to determine how well this shade enhanced the stray light. The camera was mounted on a motor-controlled pan-tilt unit and pointed toward a solar-spectrum integrating sphere. This experiment rigorously tested the chosen length of the shade by collecting images at each angle and using the average signal obtained from images to produce signal curves with the shade and without. For this experiment, the opening of the integrating sphere was reduced to a size simulating the angular diameter of the sun. The results of this test show that the use

of a shade allows for the lens to be oriented at an angle of 18° from the sun without being affected by lens flare, as opposed to 22.5° without the shade. Qualitative testing with the IR camera reveals that only when a hot source comes very near to the FOV does it affect the scene. This could be further quantified, but it was not expected that stray light will be significant for the IR camera. The IR stray light could be further characterized during Radiometric testing.

Thirdly, we then design the solar shades and integrate them into the cameras.

**Visible Camera Solar Shade Analysis**

I calculate the radius of the VIS FOV as a function of the distance from the Entrance Pupil. The hard limit of the solar shade was assumed to be the outer diameter of the lens—as the simplest form of solar shade was produced: a cylinder with inner diameter equal to approximately the outer diameter of the lens. The following figure shows that the ideal solar shade would extend ~48.3 mm beyond the entrance pupil. Given that the edge of the lens structure was 7.62 mm from the entrance pupil, the solar shade would extend the 40.7 mm beyond the edge of the lens (see *Figure 73*).

A solar shade extension of 40.7 mm was reasonable on the spacecraft. In order to build conservatism into this design, the solar shade was reduced by 1 mm to 39.7 mm. The paint thickness added 0.5mm back to the total length. This will account for any tolerance issues in the machining and paint thickness. We then calculate the worst-case direct stray light to compare the ideal shaded case, the conservative shaded case and the unshaded case. It was predicted that our shaded visible camera will prevent stray light up to 22.4˚, whereas the unshaded case will only prevent stray light up to 67˚. There was a total reduction of 44.5˚ of maximum stray light angle. The ideal case, only saves another 2˚. However, the conservatism ensures that the filed of view will not be blocked

from machining errors or paint was worth the marginal gains and sufficient stray light was still blocked.

( 161 )

$$As\ Is\ Maximum\ Stray\ Light\ Angle$$
$$= tan^{-1}\left(\frac{Lens\ Diameter}{Length_{Structure\ limit\ to\ EP}}\right)$$
$$= tan^{-1}\left(\frac{17.85\ mm}{7.62mm}\right) = 66.9^{\circ}$$

( 162 )

$$Shaded\ Maximum\ Stray\ Light\ Angle$$
$$= tan^{-1}\left(\frac{Lens\ Diameter}{Length_{Structure\ limit\ to\ EP} + Length_{maximum\ extension}}\right)$$
$$= tan^{-1}\left(\frac{17.85\ mm}{7.62mm + 40.68mm}\right) = 20.3^{\circ}$$

( 163 )

$$Shaded\ Maximum\ Stray\ Light\ Angle\ with\ Margin$$
$$= tan^{-1}\left(\frac{Lens\ Diameter}{Length_{Structure\ limit\ to\ EP} + Length_{marginal\ extension}}\right)$$
$$= tan^{-1}\left(\frac{17.85\ mm}{7.62mm + 35.68mm}\right) = 22.4^{\circ}$$

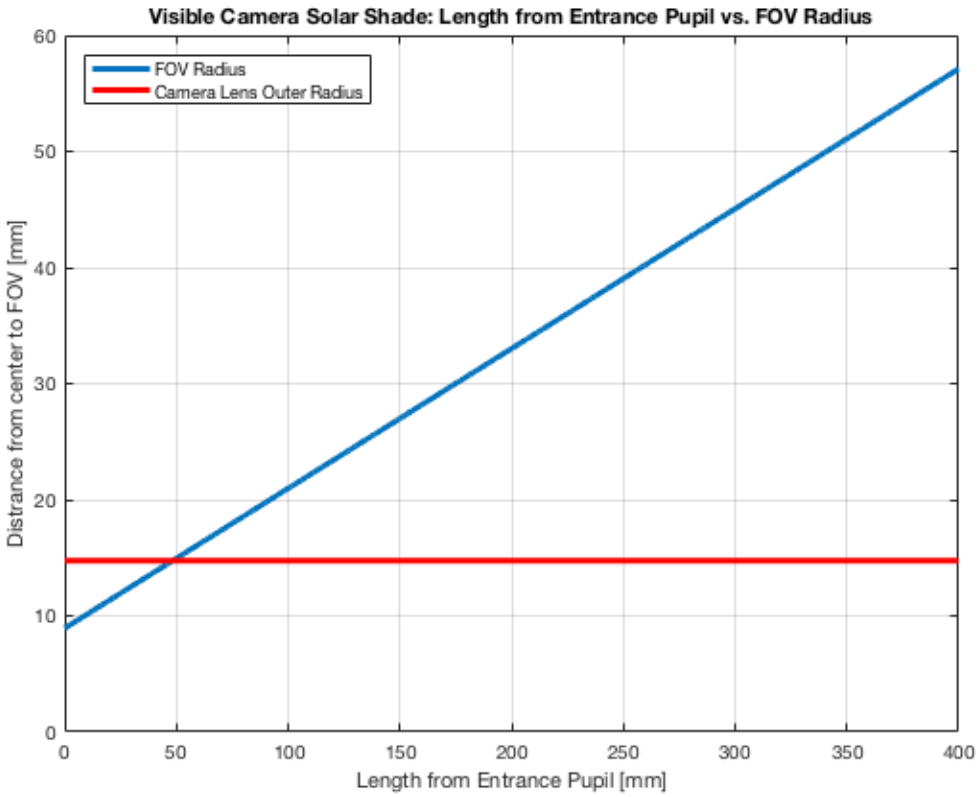


*Figure 73*. The radius of the FOV of the visible camera was equal to the outer radius of the lens (14.75mm) at a distance of 48.3mm. This was the ideal case for a cylindrical solar shade.

**Infrared Camera Solar Shade Analysis**

The radius of the IR FOV as a function of the distance from the Entrance Pupil. The hard limit of the solar shade was assumed to be the outer diameter of the lens—as the simplest form of solar shade was produced: a cylinder with inner diameter equal to approximately the outer diameter of the lens. The following figure shows that the ideal solar shade would extend ~139 mm beyond the entrance pupil. Given that the edge of the lens structure was 17.5 mm from the entrance pupil, the solar shade would extend the 121.5 mm or about 12 cm. Unfortunately, the structures team would not allow this—as the solar shade would protrude beyond the volume boundary of the spacecraft. There were only 2.7 cm of extension available from the end of the lens. This would provide 34.5 mm of shading from the entrance pupil.

The following calculations show the maximum angle for incident stray light. The off-the-shelf camera lens introduces stray light at angles of a minimum of 74.4˚. With the added solar shade, the angle was reduced to 54.5˚. Stray light was calculated as any light entering from the top of the plot that reaches the opposite edge of the opposite side of lens (this would be -31.25mm). In practice this calculation was unreasonably conservative, but it was the extreme case assuming any impingement on the lens will reach the detector.

$$As\ Is\ Maximum\ Stray\ Light = tan^{-1}\left(\frac{Lens\ Diameter}{Length_{Structure\ limit\ to\ EP}}\right) \quad (164)$$

$$= tan^{-1}\left(\frac{62.5\ mm}{17.5mm}\right) = 74.4^{\circ}$$

( 165 )

$$Shaded\ Maximum\ Stray\ Light$$

$$= tan^{-1}\left(\frac{Lens\ Diameter}{Length_{Structure\ limit\ to\ EP} + Length_{maximum\ extension}}\right)$$

$$= tan^{-1}\left(\frac{62.5\ mm}{17.5mm + 27.1mm}\right) = 54.5^{\circ}$$

Thus the inclusion of a solar shade will reduce any stay light from a total FOV of 148.8˚ to 109˚.

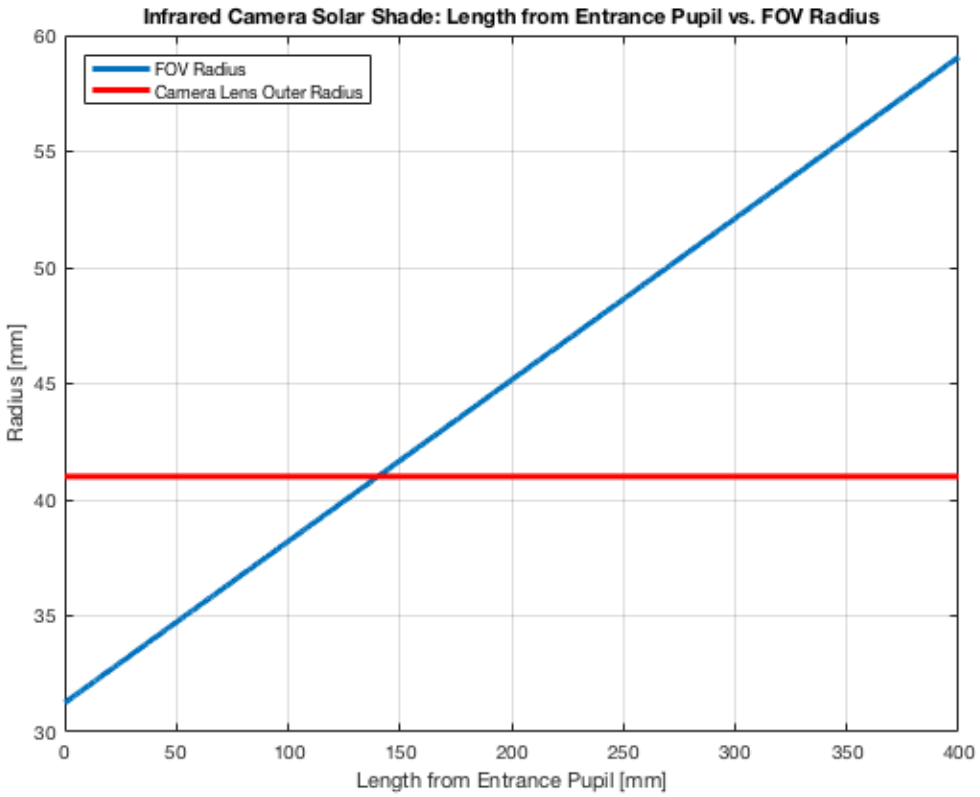


*Figure 74*. The radius of the FOV from the entrance pupil was equal to the radius of the lens at the entrance pupil and extends at 7.96˚ half angle of the diagonal. An ideal solar shade would trace the FOV radius. Our design was limited as a cylinder at the outer diameter of the mechanical lens fixture of 41mm. Thus our ideal shade would extend to the intersection but not block any of the FOV at ~139mm.

**Visible Camera Design Solution:**

Given that the lens was 35mm long and the maximum length of the shade can be 40.68mm, the maximum length of the solar shade from the base of the lens was ~75mm. We conservatively remove 5mm to account for any errors induced from machining and paint thickness. Thus, the length of the baffle was designed to be 70 mm long from the base of the lens, which was also the point at which the structure opens to encase the electronics.

**Testing for IR lens stray light**

Preliminary tests have shown that only when a soldering iron, emitting a significant amount of radiation compared to the scene, gets very close to within the field of view, was there significant stray light. Thus, the system appears to sufficiently block stray infrared radiation. Future testing was needed to quantify this effect, but for the moment, based upon analysis and functional testing, only a very strong emitter, such as the sun, at near FOV angles, would be sufficient to cause interference within the images. Because it was relatively easy to implement, and because the spacecraft structure limits the extension of the baffle to only 2.71 cm, we proceed with the design.

**Infrared Camera Design Solution:**

The structures team only allowed for an extension of 27.1mm from the edge of the camera lens, so this was the maximum extension of the solar shade. The lip on camera lens was 26mm from the edge, so the maximum extent from the lip was 53mm. We add 1 mm of clearance, when boring out the solar shade to make sure that the mounting faces are at the base of the solar shade.

**Integrated Solar Shades**

The integrated solar shades are shown in the figure below.

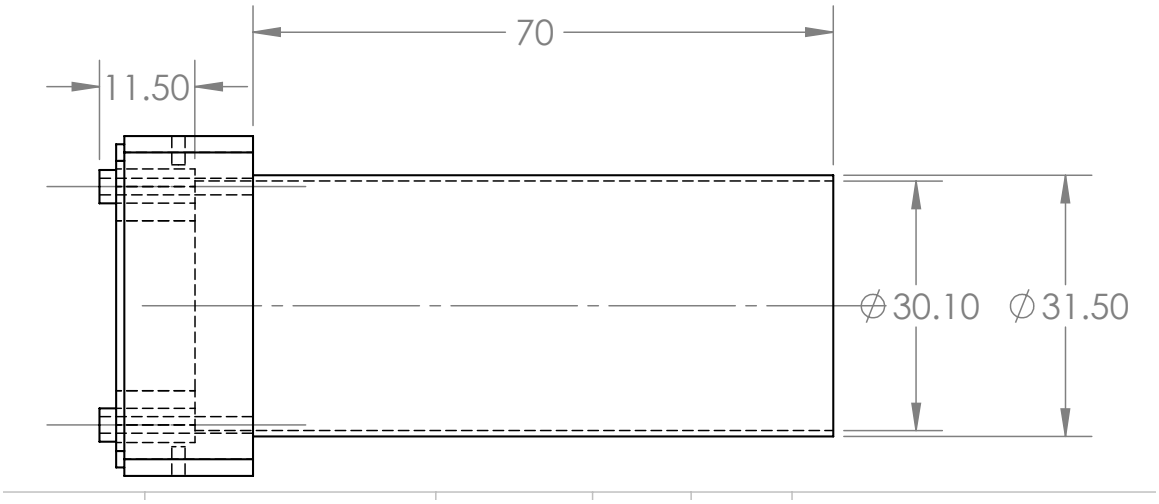


*Figure 75*. Cross section drawing of the visible solar shade and front camera casing.

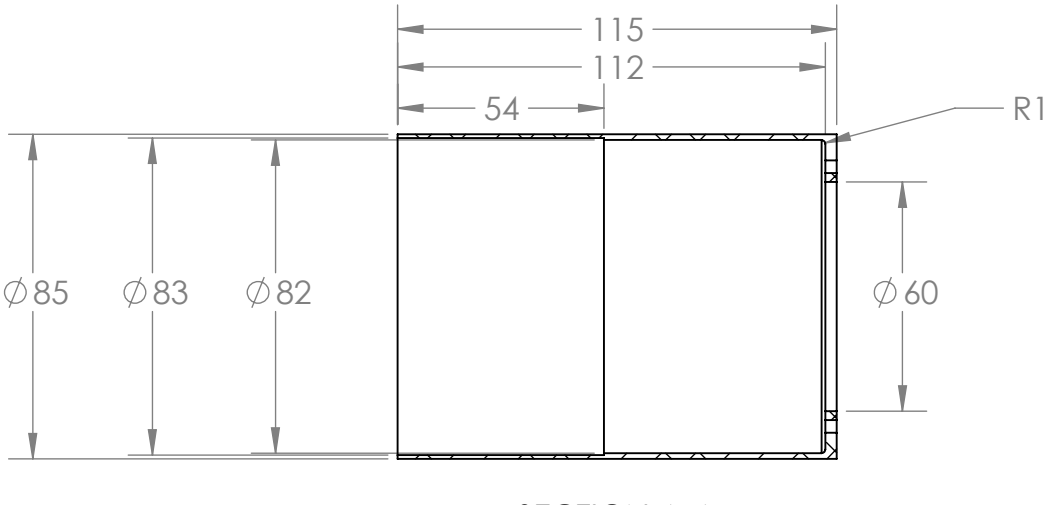


*Figure 76*. Cross-section drawing that was used to machine the solar shade. Units are in mm.

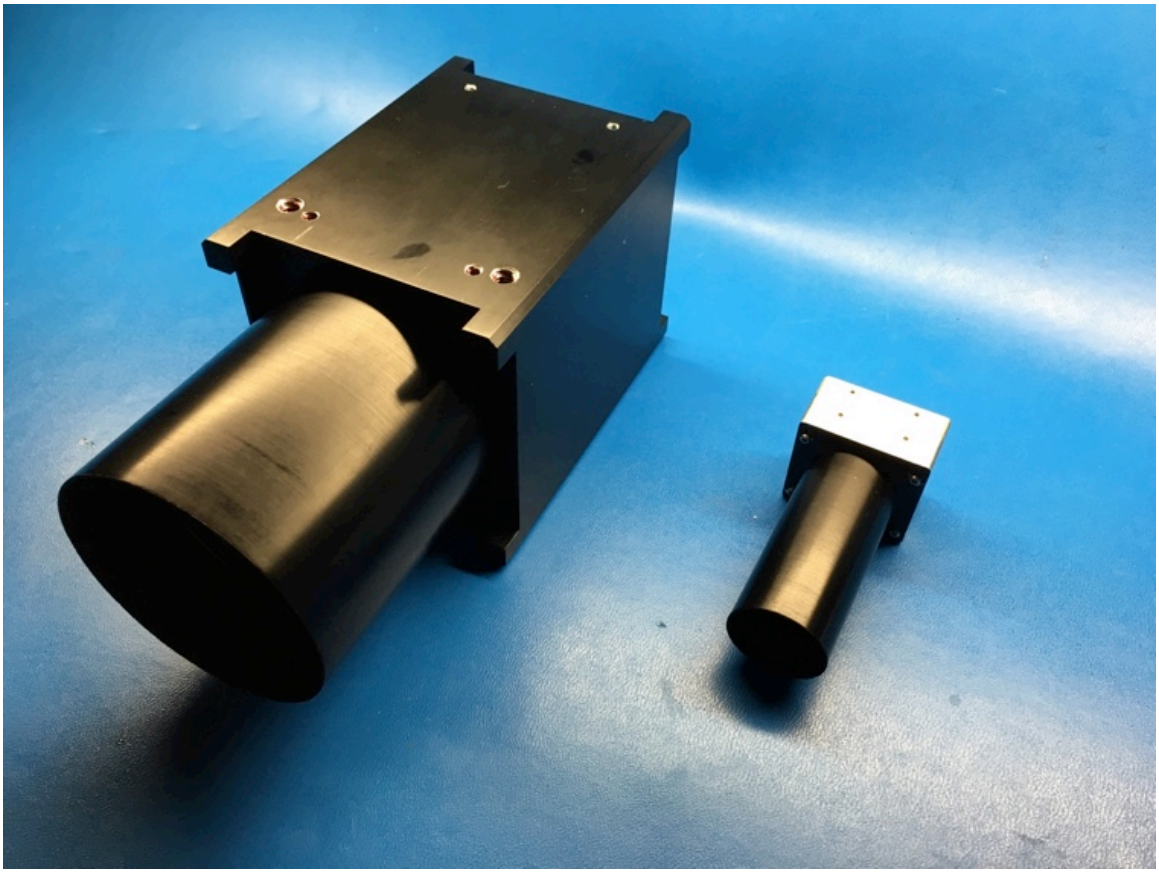

*Figure 77*. The infrared and visible camera with integrated solar shades.

## Electronics and Electrical

### Power

The infrared camera, visible camera, and instrument computer each require applied power from the EPS. The visible camera and the infrared camera detectors are typically powered via the USB connection to a computer. Originally, we planned to have the instruments powered from the instrument computer. However, the addition of the Honeybee CMG unit significantly altered the spacecraft budget. Consequently, the decision was made to independently power the instruments such that they could be turned off to conserve energy without descoping the visible camera. A special USB cable was created that allowed the instrument computer to command imaging without supplying power and tests were performed to determine power consumption.

The power consumption for a variety of idle test cases was measured (Table 26). After boot, the computer draws ~750mA at 5V for ~3.8W when ON and idle. The visible camera draws ~330mA at 5V for ~1.7W when ON and idle. The infrared camera draws ~290mA at 5V for ~1.5W when ON and idle. The total power with all systems ON and idle was ~7W. The total power draw of the computer when turning off the cameras was 3.8W with a savings of 3.2W.

The power consumption while imaging was also measured. The computer draws ~840mA at 5V for ~4.2W when capturing. The visible camera draws ~340mA at 5V for ~1.7W when capturing. The infrared camera draws ~290mA at 5V for ~1.5W when capturing with a spike of 2.5W for shutter. The total power during visible and infrared imaging was ~7.4W.

These tests further showed that the cameras can sufficiently be powered using 1 amp lines and the computer should use a 2 amp line. The website FAQ for the

MinnowBoard-MAX states, “We recommend the use of a 5V, 2.5A power supply with MinnowBoard-MAX.” So, it can be inferred that the 2A was sufficiently current-limited.

Special harnessing was required for the visible camera to be powered independently. Because the visible camera power defaults power drawn from the computer when there was not a higher voltage source supplied over the GPIO, it was at first thought not possible to power the visible camera via a secondary source. It was assumed that USB 5V was required for starting the communication between the computer and the visible camera. The USB 5V cannot be turned off from the computer easily if at all in software. After contacting the vender it was determined that the Camera did not need the 5V power from the USB2 line. Power was required for USB3, but that was not used here. A USB2 cable was cut open and the $V_{bus}$ 5V wire was cut. The GPIO cable was then plugged into the camera with a 5V power supply. The camera turned on as expected. The image capture command was issued to the camera, and the camera indeed captured an image! This test confirmed that the camera can be powered separately over a 5V line that can be turned on/off over the EPS line in order to preserve power when not imaging without any power connection required over the USB to the computer. A special USB2 cable was designed for the final harnessing of the visible camera to the computer without a power wire. A USB2 cable was designed that does not have any power wires, and the visible camera draws power from the GPIO connector. With this implementation we save 1.7W with the visible camera powered off.

A similar modification to the infrared camera power harnessing was required. However, the infrared camera must be powered through its USB-mini port. Consequently a Y-cable was created that splices the USB-mini into data only USB-line to the instrument computer and power lines to the EPS. More of this will be described in the data interfaces and harnessing sections.

Testing and modifying the power delivery architecture to the instruments proved that during non-imaging configurations (i.e. non imaging) provided a method for conserving power by ~46%.

### Data Interfaces

After selecting the flight detectors and designing the independent power architecture, the following data interfaces were finalized.

### Electrolytic Capacitors

The capacitors used on the electronics boards must be verified for space flight worthiness, as the use of wet capacitors in space application was strictly prohibited as outlined in MIL-STD-1547B. The vendors of the electronics boards were asked to survey the boards for electrolytic capacitors to verify that none were used. Only one of the boards used electrolytic capacitors. Because these capacitors are solid polymer, as opposed to wet/fluid capacitors, we tested the board in a thermal vacuum chamber in order to verify that the capacitors would continue to operate. This analysis was shown in the subsequent thermal section. The Minnowboard-MAX contains four solid polymer electrolytic capacitors (indicated with 300µF label) with the following vendor information: Aluminum Polymer Electrolytic Capacitor , SM, 330uF, 20%, 2.0V, 7mΩ from Panasonic EEF-SX0D331XE.

Table 26.

*Instrument Power Specifications via Testing*

| Experiment | Voltage (V) | Current (A) | Power (W) |
|---|---|---|---|
| Computer powered Visible Camera | | | |
| Comp. only | 5 | 0.75 | 3.8 |
| Comp. + Vis Idle | 5 | 0.96 | 4.8 |
| Comp. + Vis Capture | 5 | 1.2 | 6 |
| Comp. + Vis Idle post-capture | 5 | 1.1 | 5.5 |
| Computer and Independent Visible Camera | | | |
| Comp. Capture w/o Vis power | 5 | 0.84 | 4.2 |
| Comp after capture, w/o Vis power | 5 | 0.76 | 3.8 |
| Visible Idle | 5 | 0.33 | 1.7 |
| Visible Capture | 5 | 0.34 | 1.7 |
| Computer and Independent Infrared Camera | | | |
| Comp. Capture w/o IR power | 5 | .8 | 4 |
| Infrared Idle | 5 | 0.29 | 1.5 |
| Infrared Capture | 5 | 0.29 | 1.5 |
| Infrared Calibration (<1 sec) | 5 | 0.50 | 2.5 |
| All Independent y Powered Subsystems | | | |
| COMP ONLY | 5 x1 | 0.76 | 3.8 |
| ALL ON IDLE | 5 x3 | 0.76, 0.33, 0.29 | 7 |
| ALL ON CAPTURE | 5 x3 | 0.84, 0.34, 0.29 | 7.4 |

Table 27.

*Data Interfaces*

| Instrument | Instrument Interface | Computer Interface | Cable | Application |
|---|---|---|---|---|
| Infrared Camera | USB 2 mini Type B | USB 2 Type A | USB 2 : single twisted pair | Serial Commands |
| Infrared Camera | Camera Link SDR | Camera Link SDR | Camera Link | Infrared Data |
| Visible Camera | USB 2 mini Type B | USB 2 Type A | USB 2 : single twisted pair | Serial Commands and Visible Data |
| Computer (INS) | RJ45 (INS) | RJ45 (CDH) | Ethernet: 4 twister pairs | Instrument System Command and Data to Spacecraft |

### Electrical Grounding

Following NASA-HDBK-4001, a proper grounding strategy was essential for minimizing noise and disturbance to other subsystems such as magnetometers. The system used for THESIS employs a Multiple-Point Ground system e.g. While data systems share grounding through the USB connectors and Camera link connectors, the power was returned to the spacecraft EPS, which was harnessed to the spacecraft chassis. The individual boxes for each of the subsystems are also grounded to the chassis.

One of the difficulties with the design of THESIS was isolating the subsystem boxes. The instrument computer case was anodized, so it was initially electrically insulated. However, it was noticed that upon torqueing the attachment bolts to their required values, the bolts scratched into the anodize and established an electrical path. Prior to spacecraft delivery, an attempt was made to isolate the instrument computer box from the infrared camera box (*Figure 78*). However, when the bolts were torqued, there was inevitably a contact between the bolts and the case flange. There was some flexing of the case flange observed, so it's probable that the case flange warped while torqueing and touched the bolt. As this was a last minute attempt to fix the grounding prior to delivery that appeared to compromise the torque settings of the bolts, it was determined that instead, the case should be grounded to the infrared camera structure. Attempts were made to then isolate the instrument computer boards from the instrument computer case. Kapton tape was used to block all of the harnessing points from touching the case and the board standoff holes were covered with tape as well. When the bolts were gently tightened, there was no electrical conductivity between the boards and the case. However, when the screws were torqued to the desired values, the standoffs tore through the tape to establish a ground path. There was insufficient time to remedy this problem before delivery. Future work would verify a solution for this problem.

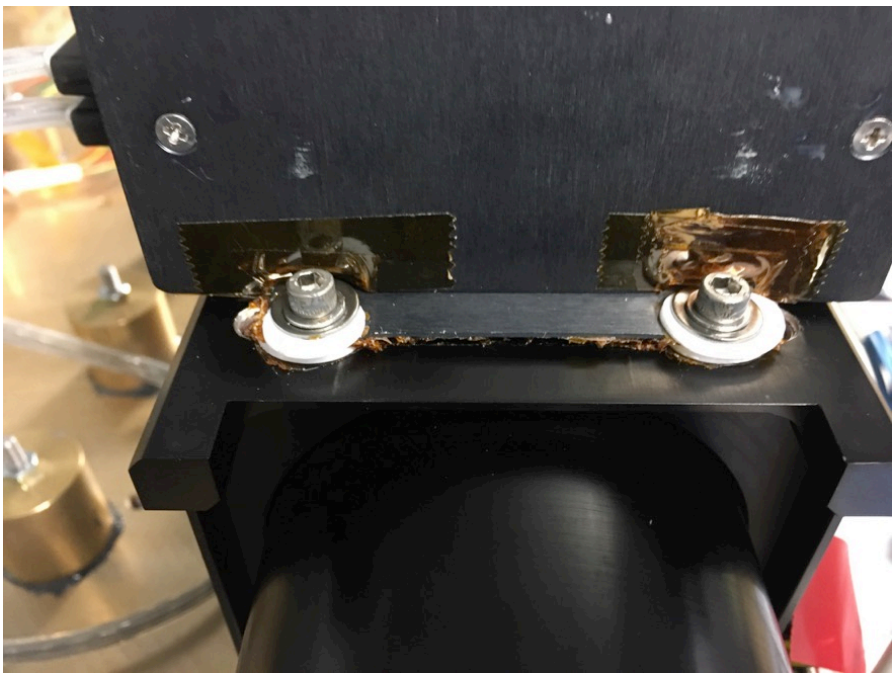

*Figure 78*. An attempt was made to isolate the infrared camera from the instrument computer. Kapton tape was used on both sides of the instrument computer flange. Teflon washer were used to prevent the torqued washer from touching the flange.

### System Boot Time

The following table describes the approximate time for booting each of the systems as well as the instrument computer shutdown time.

*Table 28. Subsystem boot times.*

| Device | Time (s) |
|---|---|
| Instrument Computer (boot) | 55 |
| Visible Camera (boot) | 3 |
| Infrared Camera (boot) | 3 |
| Instrument Computer (shutdown) | 7 |

## Space Environment

### Instrument humidity and thermal specifications.

In order to make sure that the instruments can survive the space environment, the non-operating and operating temperature limits for the instruments as well as the humidity tolerances are catalogued and specified in the appendix. The tightest non-operating temperatures are -20˚C and 60˚C for the Fujinon Lens—though the Minnowboard MAX had a non-operating temperature limit of 0˚C, this was probably conservative. Nonetheless, until tested, it should be assumed that 0˚C was the non-operating temperature limit until tested otherwise. The Point Grey camera has the tightest operating temperatures requirements at 0˚C and 45˚C. The thermal control subsystem (TCS) will maintain this operating temperature at the spacecraft level.

### Pressure specifications

The instruments must be capable of surviving in the vacuum of space. This was addressed through prohibiting materials, waiver analysis, and testing.

A prohibited practice (PP) from UNP explicitly relates to pressurized vessels.

*PP-02 Use of pressure vessels is highly discouraged. Sealed compartments are also discouraged (except where required for propulsion; see section below.) All sealed components, whether university-built or vender supplied, must have adequate documentation and verification.*

None of the materials used for the instruments are designed to be pressurized at ambient conditions. The infrared camera has a vacuum sealed detector package, but this was a negative pressure that balances in the vacuum environment of space. Electrolytic fluid capacitors are also prohibited.

The lens cavities are analyzed in order to make sure that they are sufficient for depressurization. Vent holes are drilled into the infrared camera lens housing in order to allow the pressure to drop in accordance with NASA-STD-5003.

Testing was performed on the EM in order to verify that the instruments survive in a vacuum chamber and perform nominally afterwards. Sections 0 and 0 detail these tests. The chamber was too small to capture in-focus images during the test. It was not believed that the image quality will significantly change during vacuum—though future testing in a large TVAC chamber could test this.

**Thermal Test 1**

The temperature was measured on the Minnowboard CPU in order to verify the temperature readings with a thermocouple and compared to the temperature measured accessed from the software. The conclusion was that the Tjunc was indicating a temperature that was ~20˚ C above the highest temperature measured on the board. This either indicates that Tjunc was improperly calibrated, or the Tjunc was measuring the hotter temperature of the CPU that cannot be directly measured.

Table 29.

*Temperature measurements from Test 1.*

| Measurement | Startup | Equilibrium |
|---|---|---|
| CPU0 | +53.0C | +63.0C |
| CPU2 | +54.0C. | +63.0C |
| Thermocouple | 30C. | 39.5C |
| FLIR | 33C | 42.4C |

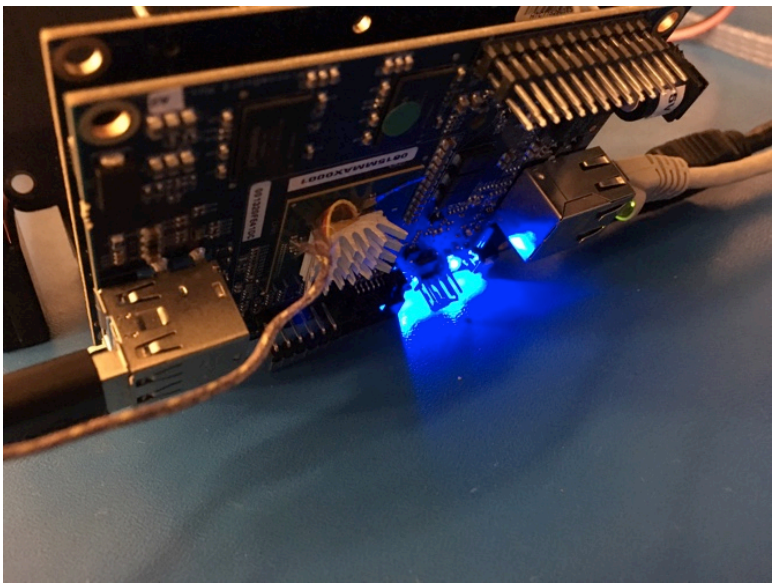

*Figure 79*. The thermocouple was attached to the CPU.

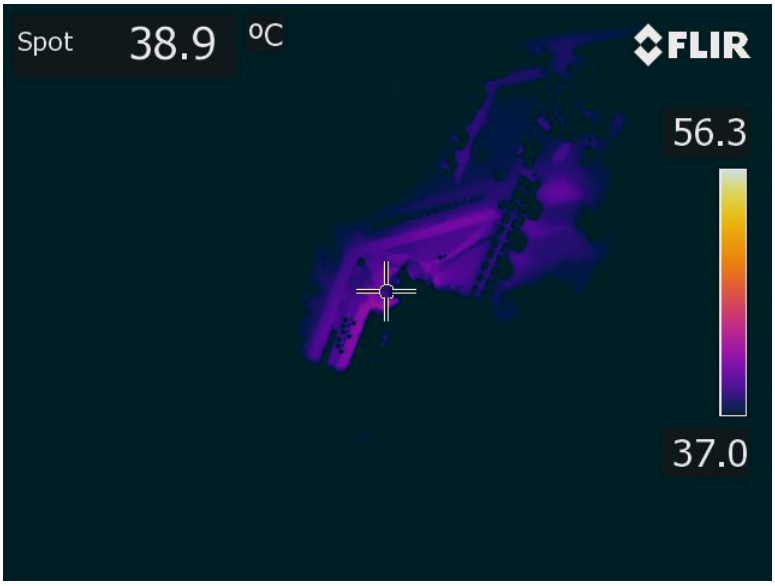


*Figure 80*. Infrared image of the board reveals the warmes part of the chip to measure the temperature. The measurement of 38.9˚C shown here was consistent with the 39.5˚C temperature measurement from a thermocouple.

**Temperature Test 2**

The temperature was measured on the Minnowboard CPU from software to determine the steady state temperature in vacuum at ambient temperature in the ASU thermophysical properties lab (*Figure 81* and *Figure 82*) after an experimental heatstrap consisting of aluminum tape was inserted in between the CPU and the case. The CPU reached a maximum of 95˚C at steady-state during idle (i.e. no imaging or image processing) at a vacuum of 9.14E-05 torr. The CPU thus appears to be ~30C warmer in vacuum during idle. The CPU may rise up ~10˚C to an absolute measurement of 105˚C during imaging. The limit of the chip was 110˚C as specified by Intel. See *Figure 83*.

As concluded in INS_Temperature_Test_1, it appeared that all additional measurements were ~20˚C cooler than what the linux command reported, so it's possible that this script was not calibrated correctly or $T_{junc}$ simply cannot be directly measured. The temperature of the CPUs in ambient conditions in the lab reached a steady-state idle was ~63˚C [see INS_Temperature_Test_1]. Temperature readings up to ~73˚C are noted during imaging and processing—an increase of 10˚C.

The maximum temperature reached during this test was ~95˚C. This was within spec per Intel of not reaching 110˚C. The instrument computer was working with 15˚C margin albeit without the load. Assuming that the load increases the temperature by 10˚C, then the loaded CPU will reach within 5˚C of its limit. This test must still be performed.

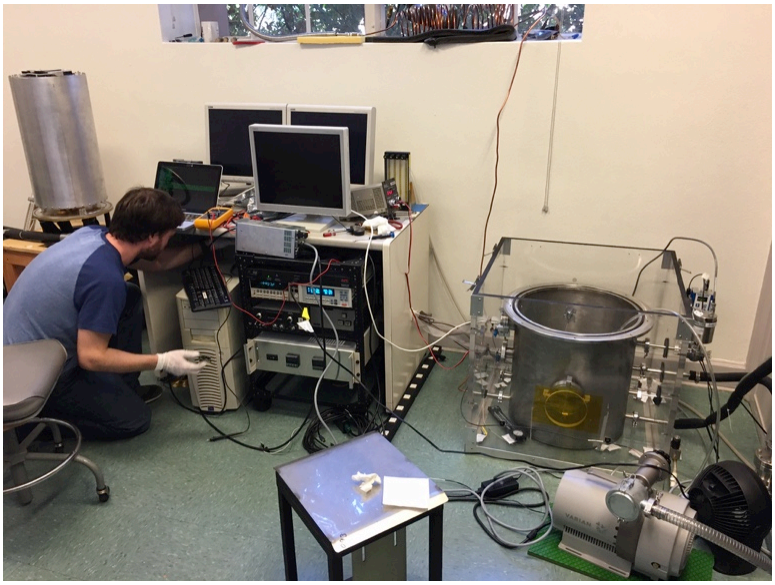

*Figure 81*. The ASU thermophysics lab thermovacuum ctest apparatus consists of a chamber, roughing pump, turbopump, supporting electronics boxes, and computer.

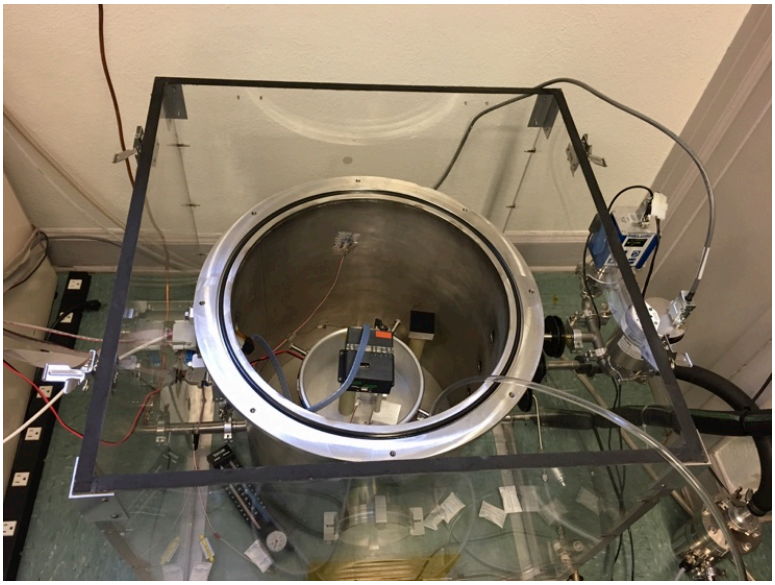

*Figure 82*. The Instrument Computer EM was installed in the chamber. Feed-throughs were assembled that allowed the harnessing to be connected outside of the chamber.

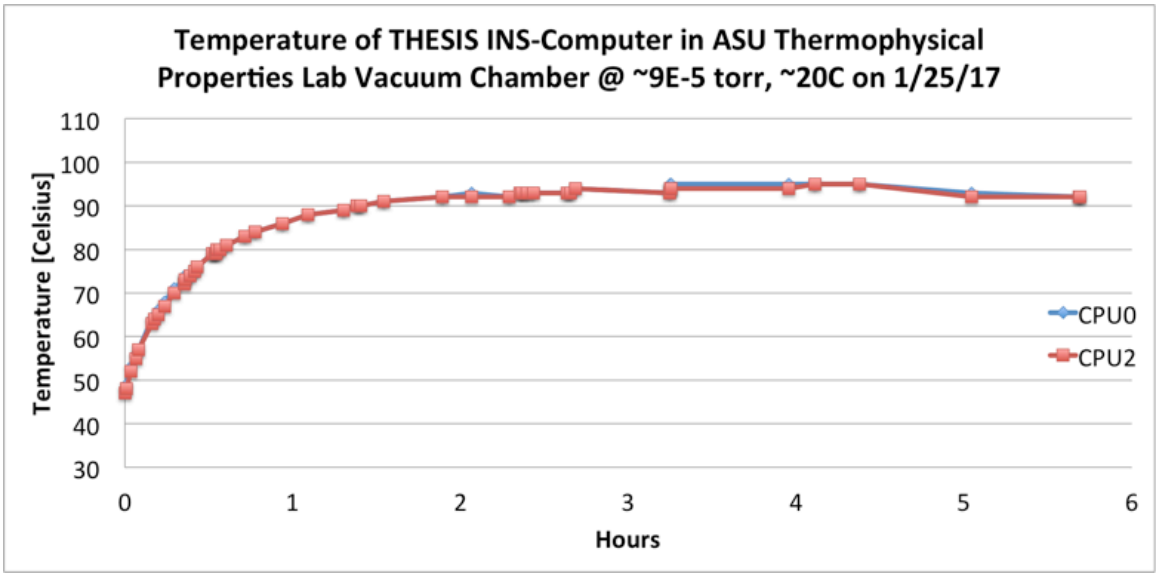


*Figure 83*. CPU0 and CPU2 reading from lm-sensors in linux. Temperature was ~20˚ C higher than in the lab. The maximum limit for Tjunc from Intel was 110˚ C. The steady state was ~15˚ C less than the limit—assuming the temperature reading was correct.

**Temperature Test 3**

The Temperature was measured on the CPU, the Infrared camera, and the Visible camera to determine the performance when the chamber was heated and a vacuum was applied. The instrument computer, the infrared camera, and the visible camera were placed into a heated chamber and a vacuum was applied. For this test, the temperatures were monitored on all of the instrument subsystems as well as imaged with an infrared camera to obtain a reference temperature in case the instruments were turned off (*Figure 84*). The plotted results are shown in *Figure 85*. The instrument computer reached a temperature of 115C in the heated vacuum chamber and continued to operate nominally, and the infrared camera operated nominally.

The visible camera recorded two temperature values before the connection to the instrument computer was lost. The temperature of the visible camera did not exceed 45˚C from the internal and remote sensing measurements. The instrument computer recorded that the camera tried to boot over 1000 times for the duration of the test. It was therefore likely that not enough current was reaching the visible camera. A combination of factors likely resulted in the failure: the added heat applied to the chamber in the vacuum likely caused the power wires to increase in resistance as they were adjacent to the heated wall which was sufficiently hot to give Mike Veto a 2$^{nd}$ degree burn, the solder joints for the feed-throughs were insufficient as they were not given adequate preparation time, and the wire length was increased beyond the USB standard.

The TVAC could be repeated for the EM to verify that the harnessing placement near the heaters caused the system to fail, however the TVAC chamber was dedicated for other investigations, so it was no longer available. The full spacecraft tests are likely to be less severe as the aluminum structures of the flight instruments will absorb heat and transfer it to the spacecraft.

As there was no path for heat to conduct from the instruments, such as the spacecraft structure, the instruments likely heated to levels well beyond what they will experience in the space environment. Furthermore, the aluminum polymer electrolytic capacitors likely are operating after this test, as the computer appears to be operating nominally—though this conclusion was not certain.

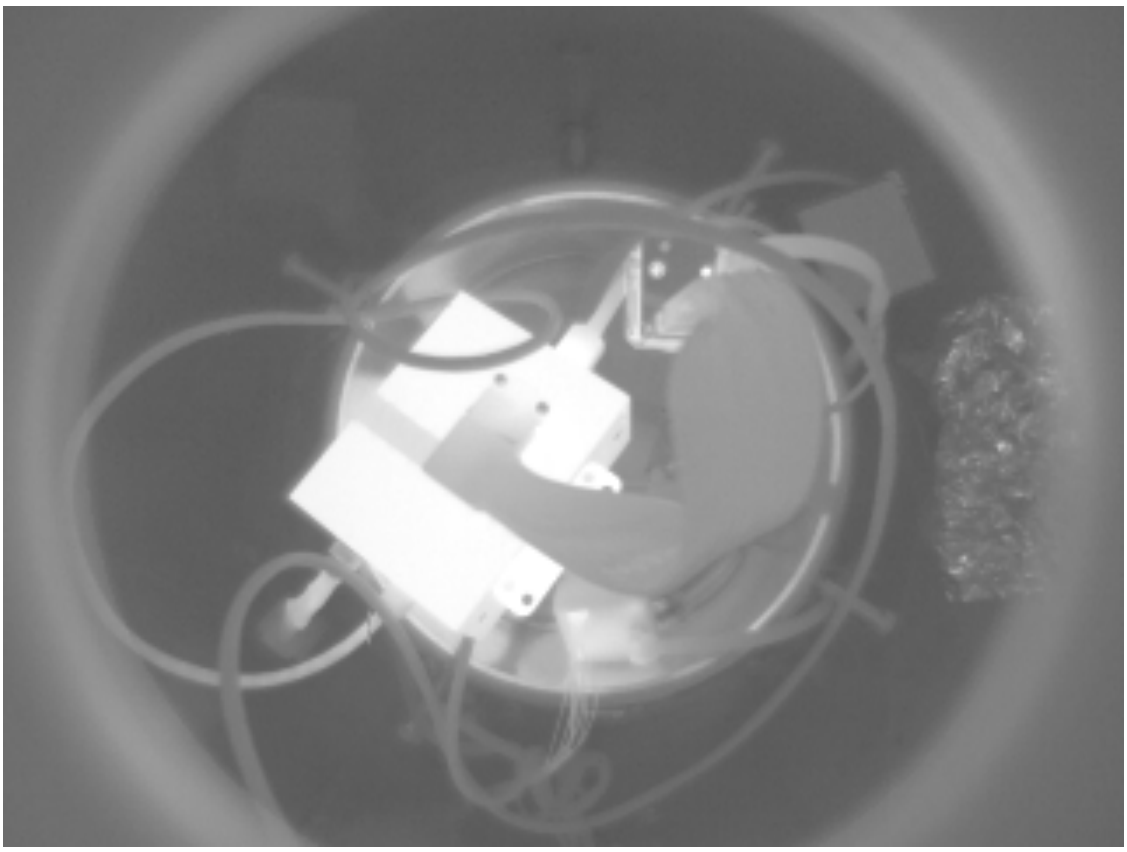

*Figure 84.* FLIR image of the instruments. The hottest object in the scene was the instrument computer. The camera link cable comes out of the top of the computer and wraps up to the one o'clock position where the infrared camera was placed. The infrared camera was facing into the page, but the back of the camera core was clearly heating up. The visible camera was in the six o'clock position. The warmest spot on the camera was the top left corner where the power was connected. The heat was being applied via heat straps on the exterior of the chamber at seven o'clock and one o'clock.

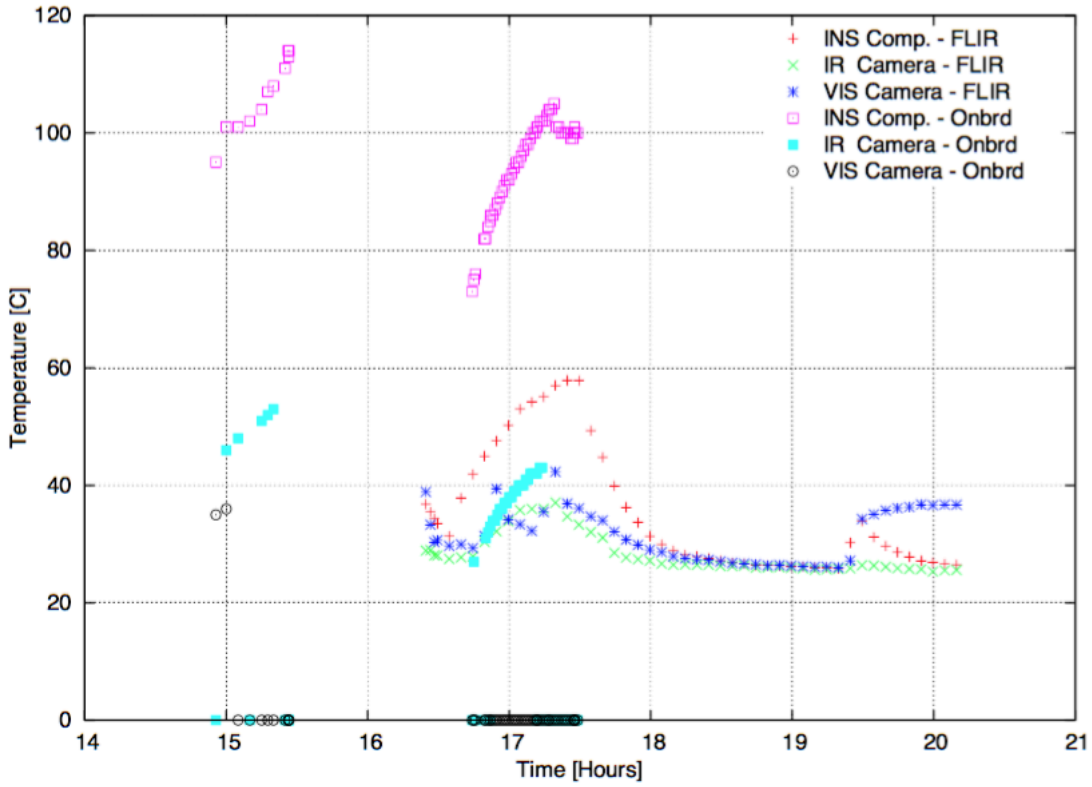


*Figure 85.* ASU-TVAC chamber results on 2/23. The visible camera appeared to stop working as data stopped being logged. The temperatures of the instrument computer and the infrared camera continued to be monitored. When the instrument computer reached 115C, it was shutoff and allowed to cool. The chamber was opened between 15.5 and 16.5 hours to verify that the visible camera was still working. The chamber FLIR was then integrated in order to capture images that could be calibrated to monitor the temperature of the instruments. After achieving vacuum, the instruments were then powered on. Because the visible camera data was not being logged, we tried to power cycle it a few times at around 17 hours. We also power cycled the IR camera a few times. It was believed that the turning off the power to the cameras may have caused the computer to cool a bit. When it was determined that the visible camera could not successfully be powered on, the instruments were all powered off at around 17.5 hours. The visible camera and the instrument computer were briefly turned on at 19.5 hours.

**Temperature Test 4**

A final thermal test in a bakeout chamber was conducted to verify the performance of the visible camera. The bakeout chamber brought the temperature of the visible camera to 78 ˚C, which was well above the recommend operating temperature of 45˚ C and well above any recorded measurements in the TVAC chamber. The performance of the camera decreased, but it did not power off. It should be noted that the power was applied via the USB cable in this test and not the GPIO. While this should not affect the camera performance, it was possible that the USB harness, shielded and encased, was more resilient to temperature induced resistance increases that may have caused the camera to fail in the previous test.

The bakeout chamber set point was set to 60˚ C. Here was measuring 59˚ C. B) The independent thermocouple for the bakeout chamber reads 52.6˚ C as the air temperature near the visible camera. The internal temperature of the visible camera noted via the software was 77.8˚ C. This was well above the operational temperature recommendation of 45˚ C. The camera still functioned, though there were some noticeable artifacts in the pixels. Eventually, the camera appeared to error out, but the temperature was not recorded.

**Radiation**

The instrument system must be radiation hardened sufficiently, so it will resist enough radiation to prevent failure. The instrument subsystems are all enclosed in the spacecraft structure, which provides an aluminum thickness of 0.3 cm (an eighth of an inch) in order to conform to the suggested radiation shielding prevention for circuit boards as described in the bulk charging mitigation approaches in SMAD(Wertz & Larson, 1999). Personal correspondence with Vincent Pisacane(Pisacane, 2008), an

expert in the space environment, confirms that COTS components will likely survive for a couple months with minimal shielding at an altitude of ~1000 km.

## Materials

### Overview

Perhaps the most difficult requirement to satisfy regards outgassing. The UNP requires that "use of non-metallic material shall be restricted to materials that have a maximum collectable volatile condensable material (CVCM) content of 0.1% or less and a total mass loss (TML) of 1.0% or less." In the following sections, we produce the tables for the bill of materials for the major subsystems, the fasteners list, and a table that details the type of plastic in each of the COTS harnessing mounts.

### Major Subsystem Components

The list of major subsystem components are found in the appendix.

### Bake out

The infrared lens and visible lenses are environmentally tested to ensure that outgassing will not affect the performance of the instrument. The infrared lens and visible lens are placed in a thermal vacuum chamber that shall bring the pressure down to 1E-4 torr and shall increase in temperature to 50C for an hour to bake out volatiles and test for structural integrity at vacuum.

***IR Lens Summary:.*** The RGA results indicated that there was residual air outgassing from the large lens (*Figure 87*). The IR Lens never got below 1.1E-03 torr in a chamber designed for 5E-04. The 1.1E-03torr was about 2E-05 psi though, which was pretty small, so we conclude that this still meets the venting requirement. Note: Do not add the partial pressures to find the total pressure. The RGA should only be used for relative values.

***Visible Lens Summary.*** With the small lens, we reached the base pressure of the TV chamber, so either the vis lens vents right away, or it was completely sealed. I believe that it's probably sealed. It doesn't seem wise to drill holes in the visible lens as they would be very small and probably damage the lens and introduce moisture. If the vacuum of space was considered as loaded under pressure then optical elements that could fracture are less than 14 grams as required in NASA-5003. If the system was considered a sealed system, then the internal pressure (14.7 psia) was less than 100 psia.

***Overall Conclusions.*** I have shown that the lenses do not fracture at a minimum pressure of 1.1E-03 (IR) and 5E-04 (VIS). The lens still require vibration testing to meet the glass requirements and this was planned to occur during full spacecraft vibration test.

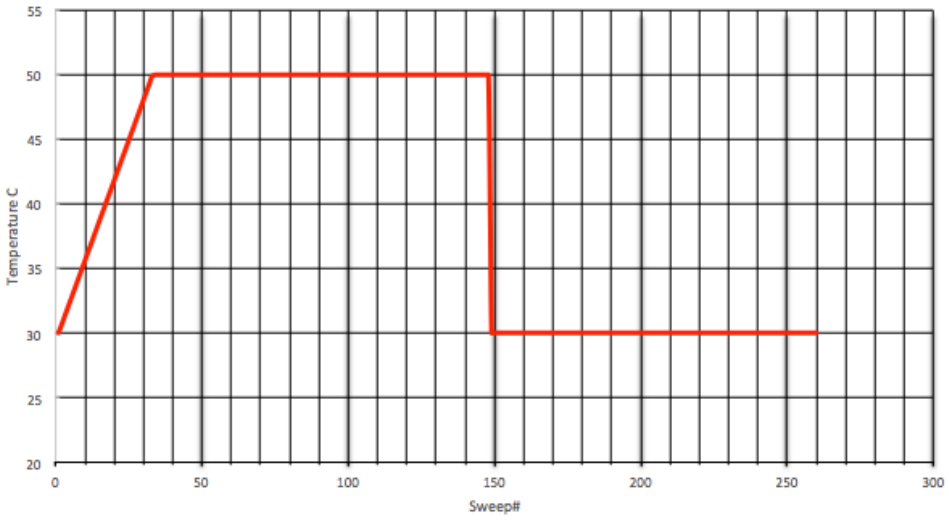


*Figure 86*. The thermal profile for bakeout consists of heating the chamber from ambient ~30˚C up to 50˚C for two hours.

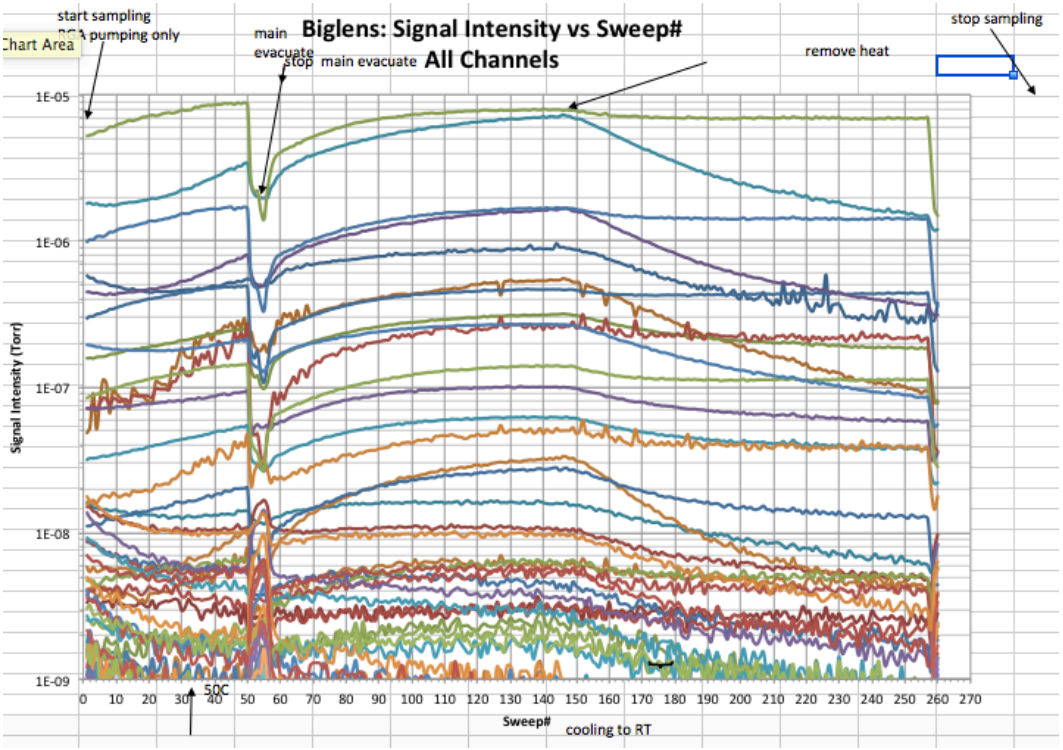


*Figure 87*. Bakeout analysis showing residual measured elements.

## Harnessing

### Harnessing Overview

As shown in the overview (*Figure 64*), the instrument subsystem as several harnesses. The harnesses had to be custom designed with the vendor in order to make sure that harnesses met outgassing requirements, had the proper connectors with jacking hardware, and were the correct length. The status and description of these harnesses was kept track in the appendix.

throughout the project and updated using the color key. All harnesses are completed and ready for integration with the spacecraft.

### Harnessing Lengths

The harnesses must be of proper length to connect the subsystems without being excessive. To determine the necessary length, physical models of each instrument subsystem were sent to Georgia Tech. The team used these physical models in their structure and used string to measure the necessary length.

The lengths of the harness are measured (Table 30). The “usable” length was the traveling length (i.e. excluding the male connector inserts) and from the center of the connecter (i.e. excluding any bulk that covers or goes beyond the connection mid-point in the opposite direction—typically ~1/2 inch.) All harness have been tested and are shown in the following figures. Images of each harness are shown in the appendix.

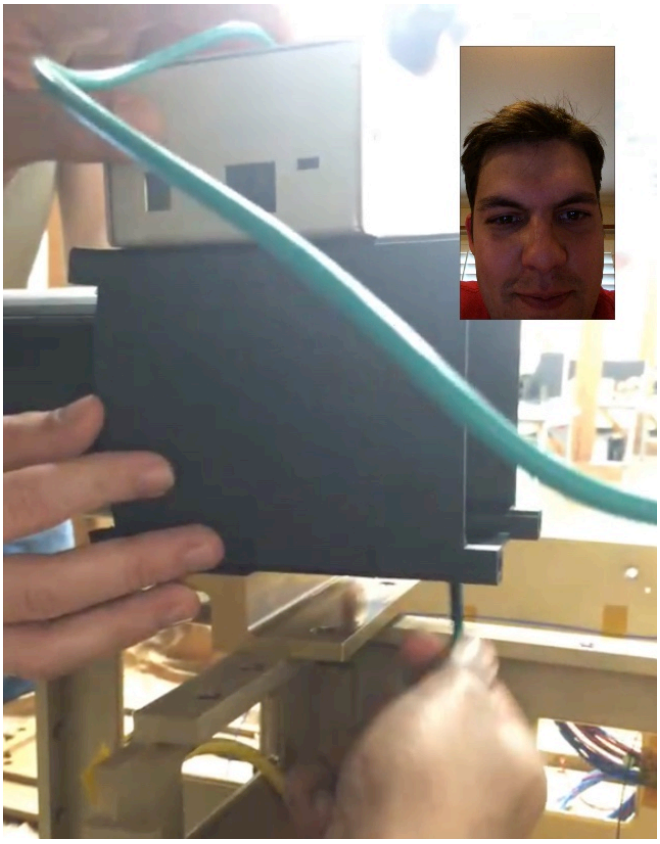

*Figure 88*. Skype session to measure the necessary lengths of the harnessing. Physical models of the instruments (spare instrument computer case and 3D printed IR camera and not-shown visible camera) were created at ASU and shipped to GT. At GT, the models are held in place with the spacecraft structure while strings are used to emulate the harness path for a measurement.

Table 30.

*Harnessing Lengths*

| Harness | Measured "usable" length in half inches. |
|---|---|
| Power (EPS-INS) | |
| Power to INS Computer | 6.5" |
| Power to Vis Camera | 6.5" |
| Power to IR Camera (Y) | 10.5” |
| Data (INS-INS) | |
| IR data to INS Computer | 10.5" |
| IR serial data to INS Computer (Y) | 23” |
| VIS data to INS Computer | 23.5" |
| Data (INS-CDH) | |
| INS Computer to S/C Computer | 47.5" |
| (Y) | This was a Y cable |

## INSTRUMENT FLIGHT SOFTWARE DESIGN

### Overview

For ease of implementation, the instrument computer was designed using Ubuntu 14.04. All of the instrument computer software was written in shell scripts. The scripts are all completely custom from scratch. The visible camera, the infrared camera, and the camera link interface board commands are all written in C and C++. These commands are all heavily modified from factory example code. The modifications allow the camera modes to be changed in-flight as well as the creation of telemetry files. All of the commands created and examples of the telemetry files are detailed in the appendix.

The threshold instrument computer software design was imaged onto a 64GB microSD card. The baseline attempted to use a PCIe card to store images apart from the operating system to minimize bit flips, however this component exceeded the allowable instrument power budget. In addition, a ruggedized 16GB Delkin hard was desired for use in both the INS that reportedly had flight heritage. However, neither the instrument subsystem nor the spacecraft flight software team, working in parallel efforts, was successful in implementing this and the ruggedized microSD was descoped.

### File structure

All commands should be executed from /home/ubuntu/FLIGHT by the spacecraft computer.

The beacon was located in /home/Ubuntu/FLIGHT/beacon

The telemetry files are located in /home/Ubuntu/FLIGHT/tlm

### Autonomous functionality of the instrument computer

Using the cron functionality of linux, a number of commands are executed (currently every 5 minutes). The commands involve capturing a visible and an infrared image that was automatically reduced to a thumbnail and saved, saving telemetry to file,

creating the instrument beacon file from the telemetry, counting the onboard visible and infrared images, and deleting the images if they reach a certain limit (currently when 700 images are reached, only the last 500 are kept). This was detailed in the appendix.

**Manual functionality of the instrument computer through spacecraft commanding**

The following tasks are executed by interaction of the spacecraft computer with the instrument computer.

**Implemented and Tested Functionality**

1. S/C computer "SSH's" into the INS-Computer over ethernet

2. S/C computer and INS computer sync clocks

3. S/C computer sends command to initialize INS serial communication of the camera link board.

4. S/C computer periodically copies the INS computer generated beacon file

5. S/C computer execute the capture commands for the Visible Camera and Infrared Camera.

5.1 INS computer automatically sends images into the IPA algorithm to create a vector.

5.2 Vector was output of imaging command that was stored on S/C computer.

6. S/C copies select images from the INS-computer for downlink.

7. S/C periodically copies the complete telemetry files from INS-computer for downlink.

**Descoped/Future desired**

8. INS records log dmesg log files that S/C copies for downlink.

**Backup Systems**

The software was backed up in a number of methods including a bitbucket account, images of the system saved to laptop and off-site storage, as well as backup SD cards.

**CPU Load Test**

The load average on the CPU was tested. The load average was queried over a two month period. This included boots, idling, and image acquisition. The purpose of this test was to determine if it would be necessary to throttle down the CPU in order to attempt to conserve power and heat dissipation. From this test, it was concluded that the CPU was not consuming enough power to warrant a throttle down.

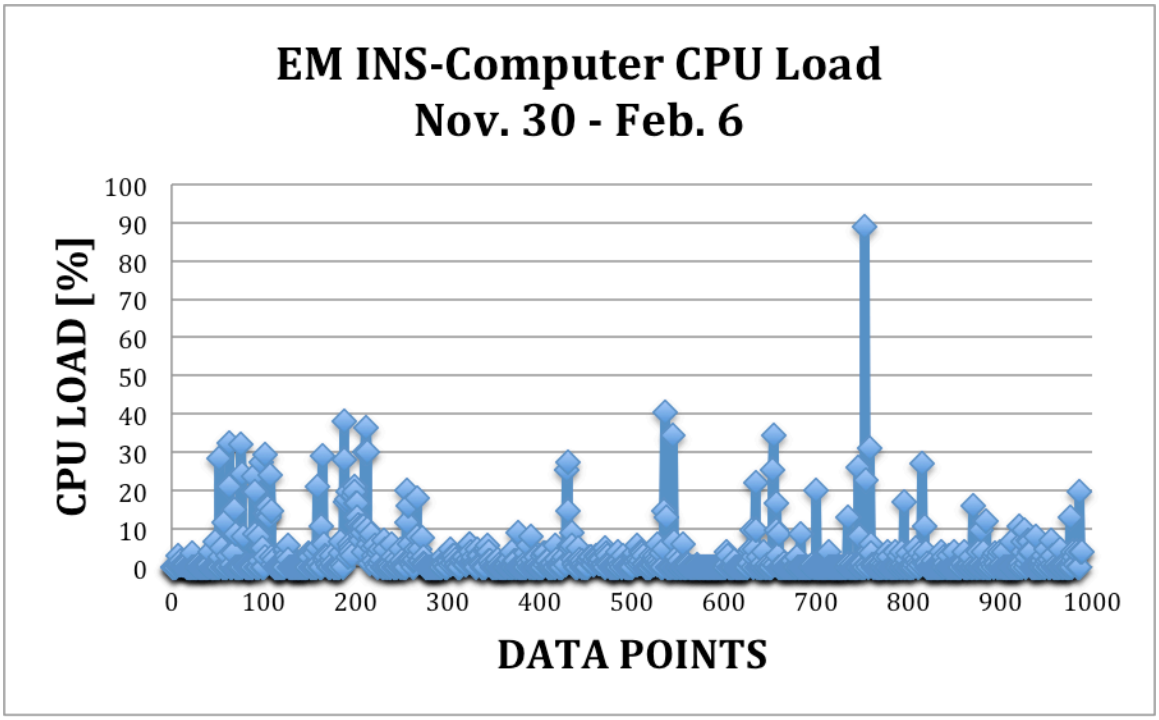


*Figure 89*. Two months of CPU one minute load average. The idle processing was less than 10% of the load. Imaging and boot of the system occasionally rose the load average to 20-40%. There was only one instance where the load rose to 90%.

## VISIBLE IMAGE DATA SUITE

### Overview

THESIS has six different modes for creating visible data products onboard to prioritize data volume, quality i.e. bit-resolution and compression, and color/monochromatic imaging. Early data was defined here as having not been only processed on the visible camera itself or having been reduced to a thumbnail in the instrument computer.

### Image Naming and Nomenclature

Images are named as follows:

<Product>-<Image Number>-<Format 7>-<Mode (0 or 1)>-<Linux Time with milliseconds>.<image format>

Example:

VEFM-257-70-1485923684.379.jpg

Table 31.

*Visible Early Image Summary*

| Visible Early Image | Description |
|---|---|
| VEFR16 | Visible Early Full Raw 16bit .pgm |
| VEFR8 | Visible Early Full Raw 8bit .pgm |
| VEFM | Visible Early Full Mono 8bit .jpg |
| VEFC | Visible Early Full Color 8bit .jpg |
| VESM | Visible Early Summed Mono 8bit .jpg |
| VETM | Visible Early Thumbnail Mono 8bit .jpg |

Table 32.

*Visible Data Suite Nomenclature*

| | |
|---|---|
| Early | A data product derived from the camera that has not been reduced (processed) on the ground. |
| RAW16 | The unprocessed DN from the CCD in 16bit format, using 12bits of data from the AD converter. |
| RAW8 | Data are binned from RAW16 to RAW8 for 8bit images. No Bayer algorithm was applied. |
| MONO8 | A monochrome, 8bit image that was created from applying the bayer algorithm to a RAW image. |
| RGB8 | A color, 8bit image this was create from applying the bayer algorithm to a RAW image. |
| gamma | A non-linear correction: OUT = 255*(IN/255)^(1/gamma) |
| Format 7 | A camera video format that allows for full or user defined partial images. |
| Mode 0 | A format 7 camera mode that allows for Full Image Resolution and user specified ROIs. |
| Mode 1 | A format 7 camera mode that performs automatic 2x,2x summing of pixels to ~640x~480 output. |

**Image specifications**

The raw voltages from the CCD are processed through the visible camera before creating an output image (*Figure 90*). Gain and Brightness are parameters applied in the A/D Converter to produce DN values from the raw voltages. These values are output into the telemetry. The gain was controlled by the Auto-Exposure, and the Brightness was typically 0. A pixel correction was always applied that accounts for various offsets on the detector determined at the factory [email with Point Grey 12/12/16]. White balance optionally tunes the Bayer algorithm output. Finally, a Gamma correction or look-up table (LUT) was applied to tune the linearity of the conversion of data from 12bit to 8bit.

Tests were performed to determine the affect of adjusting the gamma, white balance, and image format. This results in the following decisions. The gamma was set to 1.25 for VEFM, VEFC, and VETM. The white balance was set to Red: 465 and Blue: 1000. Raw images use PGM, while Mono and Color images use JPG. It was recommended that VEFC (i.e. Full Resolution 1296x968 Color Images) be used as the default image product, while VETH (86x64 Monochrome Thumbnail Images) be used as default images in a constrained downlink budget to verify instrument health. The VEFC are only slightly larger than the VEFM, however the color processing was already completed for ease of rapid use.

**Gamma: Set to 1.25**

The gamma was set to 1.25 for the nominal conversion from 12bit to 8bit. This cannot be set to auto, so the recommended gamma default gamma value from Point Grey was used i.e. 1.25. A set of test images with different gamma values seems to agree subjectively with 1.25 as a reasonable setting, while the extreme gamma values of 0.50 and 3.50 seem to have the affect of concentrating pixel values at the extreme 8 bit values of 0 and 255. Without adjusting gamma (i.e. setting gamma to 1.00), the full range of 8

bit was not utilized. The value of 1.25 was a compromise between utilizing most of the 8-bit range without saturating pixels—thus maximizing

**White Balance: Set to R:465 B:1000**

White balance was intended to correct the RGB image. It was decided that the onboard white balance will provide better 8-bit images for downlink with minimal cost. As the RGB format provides lossy data, it was decided that a best effort to clarify the image data should be performed before saving the image. These images can always be reprocessed on the ground for qualitative clarity. White Balance was ON for VEFC. The White Balance was calibrated to RED: 465 and BLUE: 1000 after tuning the histograms to match each other when staring at the all white poster in the lab.

White Balance processing was available for 8 and 16 bit RAW, so it must be programmed OFF to preserve raw, unprocessed values from the A/D converter. Using white balance without the Bayer algorithm in RAW16 and RAW8 causes pixel saturation. White Balance was OFF for VEFR8 and VEFR16. The white balance was automatically turned OFF for the summed image (i.e. Mode 1) as the Bayer algorithm was bypassed. White Balance was OFF for VESM. The effect of white balance on the MONO8 format appears to maintain the best stretch from the 12 to 8 bit conversion. White Balance was ON for VEFM, VETM.

**Image Format: PGM vs. JPG**

RAW 8 bit images were stored in both PGM and JPG format to determine how well the JPG format would preserve the RAW data without the Bayer algorithm applied. The JPG compression, as used by the camera, appears to significantly smooth out the detail of the RAW8 image. While this was acceptable for “pretty pictures”, it should not be used for RAW8 format as the data was significantly manipulated.

### Telemetry

The visible camera image telemetry was in the appendix. Notable telemetry includes the temperature of the visible camera electronics board and total number of onboard visible images. Image specific information (e.g. the auto exposure and auto shutter time) was embedded into the first few pixels of each image. The total number of onboard visible images and the temperature of the visible camera are values to add to the instruments allocation of the flight beacon as they seem to be the only pertinent diagnostics to the health of the visible camera and the disk space.

### Visible camera example data products

Examples of the visible camera data products are documented in the appendix.

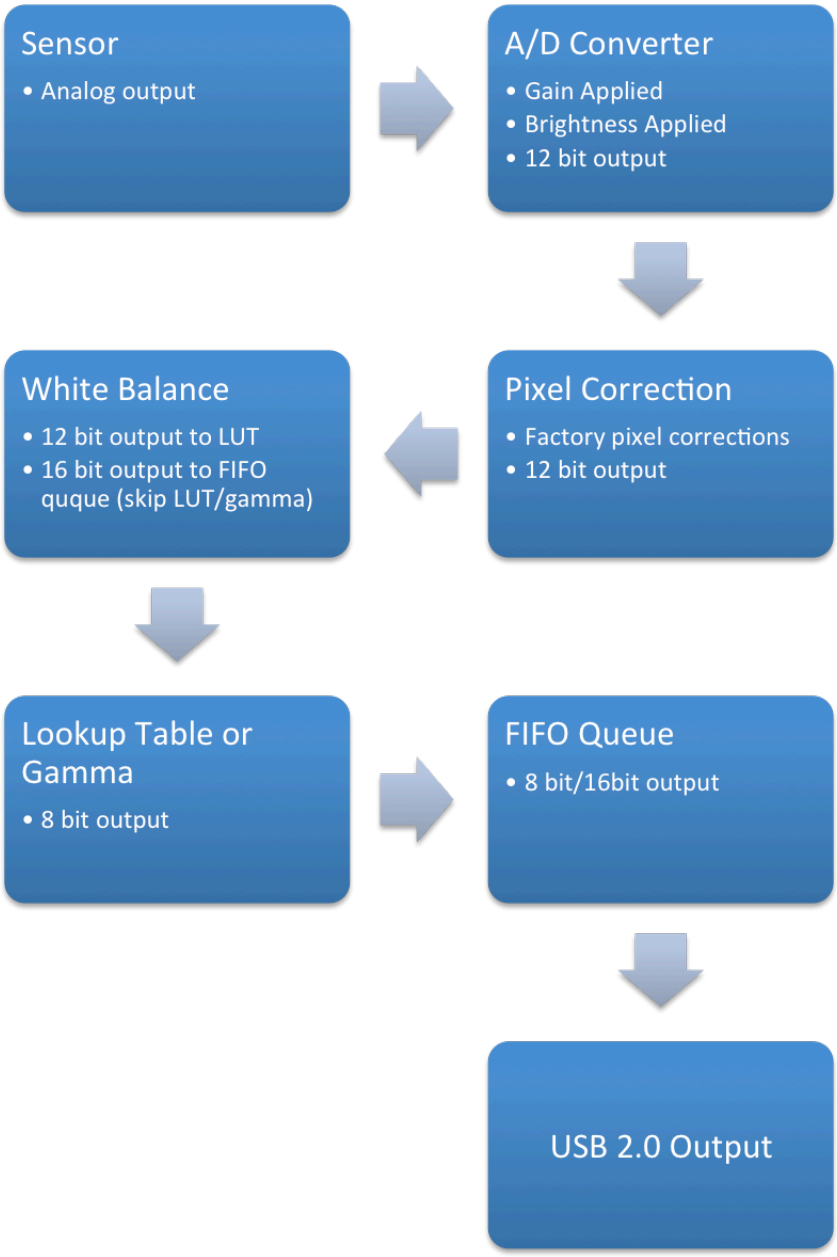


*Figure 90*. Figure reproduced from Point Grey Technical Manual.

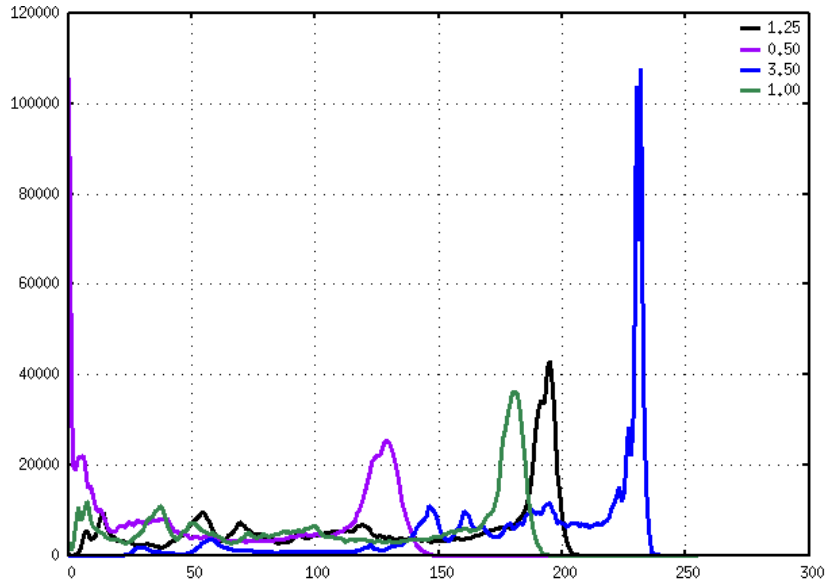


*Figure 91*. Histogram of various gamma settings of the Green filter for 0-255 bit range. Images V-44,45,46,47

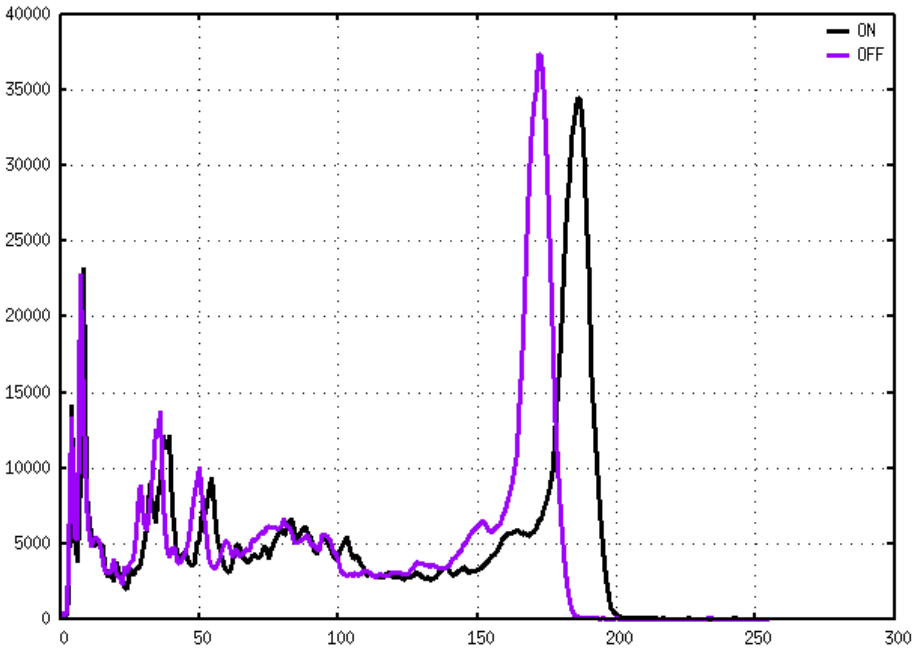


*Figure 92*. With the white balance turned ON, the data was stretched out over more of the 8 bit range of the green filter for these VEFC products. Images V-55 and V-56.

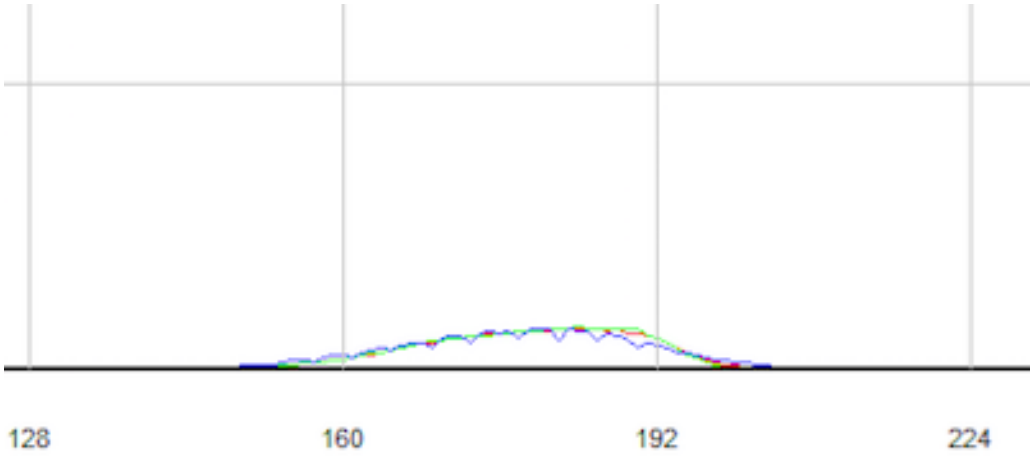


*Figure 93*. A screenshot from the Point Grey GUI showing that all RGB histograms are aligned when imaging a white target in the 100K clean lab after adjusting RED to 465 and BLUE to 1000.

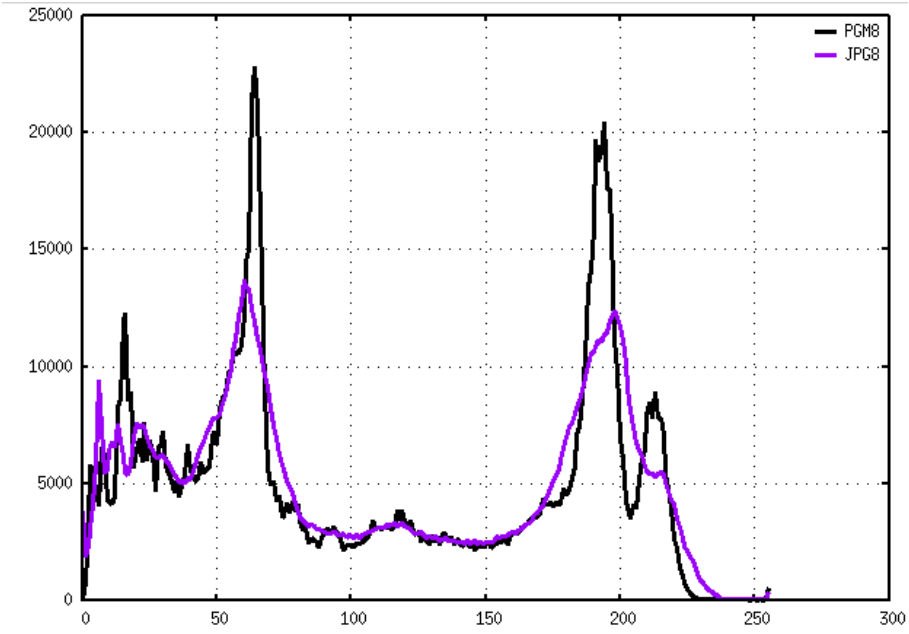


*Figure 94* . MONO8 images saved as PGM and JPG. Images V-61, 66.

Table 33.

*Visible Early Image Specifications*

| Visible Early Image | Raw Pixel Format | Saved Pixel Format | Mode | Array Size | WHITE BALANCE | GAMMA | Image Format | Data Size (Approx.) |
|---|---|---|---|---|---|---|---|---|
| VEFR16 | RAW16 | RAW16 | 0 | 1296x968 | OFF | OFF | PGM | 2.4MB |
| VEFR8 | RAW8 | RAW8 | 0 | 1296x968 | OFF | 1.25 | PGM | 1.2MB |
| VEFM | RAW8 | MONO8 | 0 | 1296x968 | R:465 B:1000 | 1.25 | JPG | 146KB |
| VEFC | RAW8 | RGB8 | 0 | 1296x968 | R:465 B:1000 | 1.25 | JPG | 172KB |
| VESM | MONO8 | MONO8 | 1 | 648x484 | OFF | 1.25 | JPG | 43KB |
| VETM | RAW8 | MONO8 | 0 | 86x64 | R:465 B:1000 | 1.25 | JPG | 2KB |

## INFRARED IMAGE DATA SUITE

### Overview

THESIS has seven different modes for creating infrared data products onboard to prioritize data volume, quality i.e. bit-resolution and compression. Early data was defined here as having not been only processed on the infrared camera itself or reduced in size for a thumbnail on the instrument computer. All of the infrared images use the T-linearization setting.

### Image Naming and Nomenclature

Images are named as follows:

<Product>-<Image Number>-< Linux Time with milliseconds>.<image format>

Example:

I16H-17443-1526525667.133.tif

Table 34.

*Infrared Image Summary*

| Infrared Early Image | Bit resolution | Gain State | T-Linearization | Image Size | Image format |
|---|---|---|---|---|---|
| I08L | 8 bit | Low | Low | 640x512 | 8 bit.tif |
| I08H | 8 bit | High | High | 640x512 | 8 bit.tif |
| I14L | 14 bit | Low | Low | 640x512 | 14 bit.tif |
| I14H | 14 bit | High | High | 640x512 | 14 bit.tif |
| I16L | 14 bit | Low | Low | 640x512 | 16 bit.tif |
| I16H | 14 bit | High | High | 640x512 | 16 bit.tif |
| I08TH | 8 bit | | | 80x64 | 8 bit.tif |

## Image specifications

### Gain State

The FLIR Tau2 was capable of two different gain states in order provide either increased range or increased sensitivity. For *Prox-1*, the high gain state will typically be used as the scene was expected to fall within -40˚C to 160˚C. In the low gain state the range expands to -40˚C to 550˚C

### T-Linearization

This feature was activated for the *Prox-1* mission. The image pixels are automatically processed such that they can easily be converted to temperature values. In the low state, the DN was multiplied by 0.4 in order to determine the temperature in Kelvin. In the high state, the DN was multiplied by 0.04 in order to determine the temperature in Kelvin.

Because flux does not vary linearly with target temperature (it varies to the power of 4), the resulting count on the detector exponentially increases at higher temperatures. An exponentially decreasing multiplier maintains a linearized temperature output. Data was collected in the lab to create *Figure 95*. This data was simply a relative relationship between the two output modes, so it was not reflect the absolute accuracy of the measured temperature versus the actual temperature.

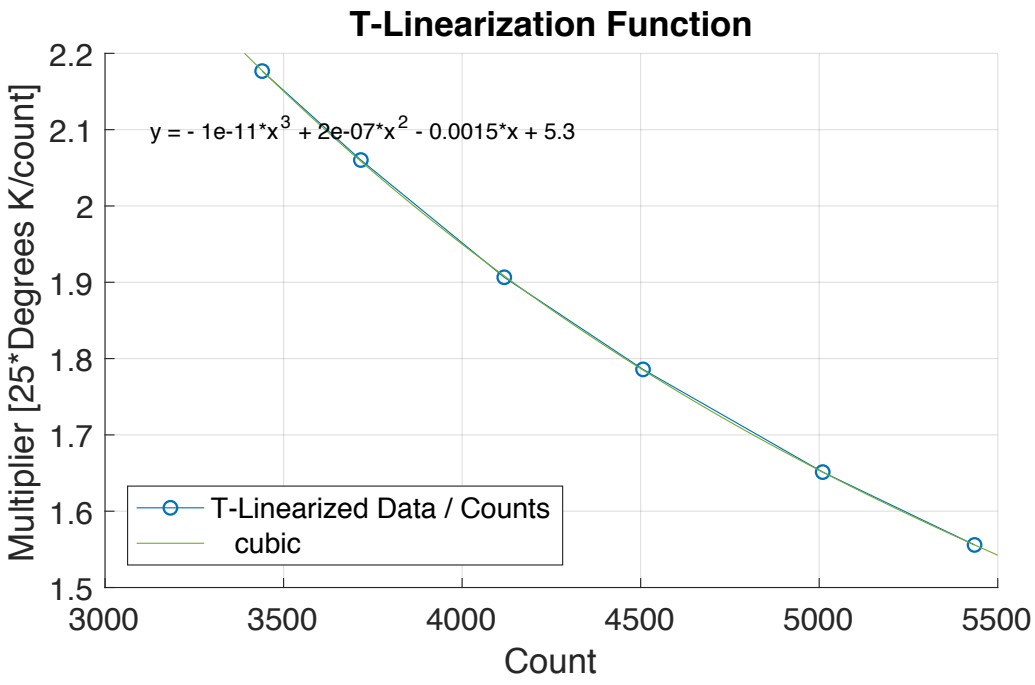


*Figure 95*. The T-Linearized data was divided by the counts to determine the multiplier. A function was fit that could be used to convert if needed. The fourth power, though may accurate, was not readily constructed from this few data points. Future analysis could capture more data and construct a fourth power fit similar to the fourth power flux equation from temperature.

### Bit-depth

Images are captured with 14-bit resolution. They can be automatically saved as 8-bit files in order reduce the data size and produce a visually appealing image.

### Image format

All images are save as tif files. The 14-bit images must be saved as a 16-bit tif in order to be processed with the image processing algorithms.

## Telemetry

The telemetry was automatically saved when an image was captured. There are three temperatures that are reported: the temperature of the FPA, the temperature of the camera housing, and a spot temperature that was calculated for a select region of interest of pixels. The gain state and the bit-depth are also output.

Table 35.

*Infrared Image Telemetry Summary*

| Parameter | Unit | Example Output | True Value |
|---|---|---|---|
| Temperature of the FPA | ˚C*10 | 222 | 22.2 |
| Temperature of House | ˚C*100 | 2512 | 25.12 |
| Spot Temperature | ˚C | 8 | 8 |
| Gain Mode | n/a | 0/1/2/3 | 0:Auto<br>1: Low<br>2: High<br>3: Manual |
| Digital Mode | n/a | 0/1 | 0:14 bit<br>1: 8 bit |

**Example Image Products**

Example image products are included in the appendix.

## SUBSYSTEM PREPARATION, INTEGRATION, AND FUNCTIONAL TESTING

### Overview

The individual components of the instrument subsystem are prepared via cleaning with isopropyl alcohol, staking, and conformal coating. The components are then assembled into the three subsystems and functional testing was performed with the flight-like engineering model harnessing.

### Staking

Upon selection of the electronics boards to be promoted to Gold level, the larger components as well as the connectors are all staked with Scotch-Weld 2216. This provides additional integrity to the parts by helping to remove the stress off of the contact points and reinforcing the connectors for loads applied from cable strain. All of the electronics boards are staked and cured in an oven overnight.

After the individual subsystems are assembled and the fasteners are torqued, any part that could become loose from the vibration of launch was also staked.

### Conformal Coating

After staking was completed, all electronics boards are conformal coated with arathane 5730 in order to seal the individual materials on the electronics boards. This exempts individual components from the materials list and protects the components from contamination and FOD. After applying a light coating and examining the work with a black light, the boards were placed in an oven for curing overnight. After curing, the boards were inspected and tested to verify that the conformal coating did not wick into the connectors.

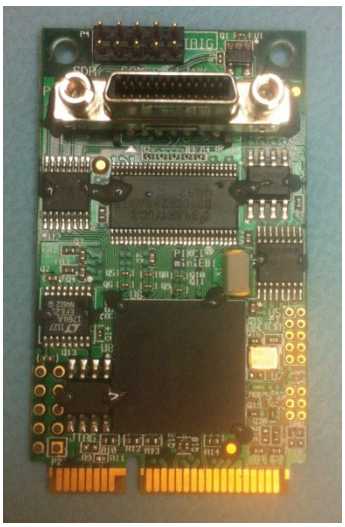

*Figure 96*. The Camera Link frame grabber board was staked as seen on the edges of the larger components. The edges of the connector are also staked to provide extra strength.

*Figure 97*. The lens focusing ring, aperture ring, and locking screws are staked to prevent alteration during launch. The assembly screws are also staked in the four corners of the housing.

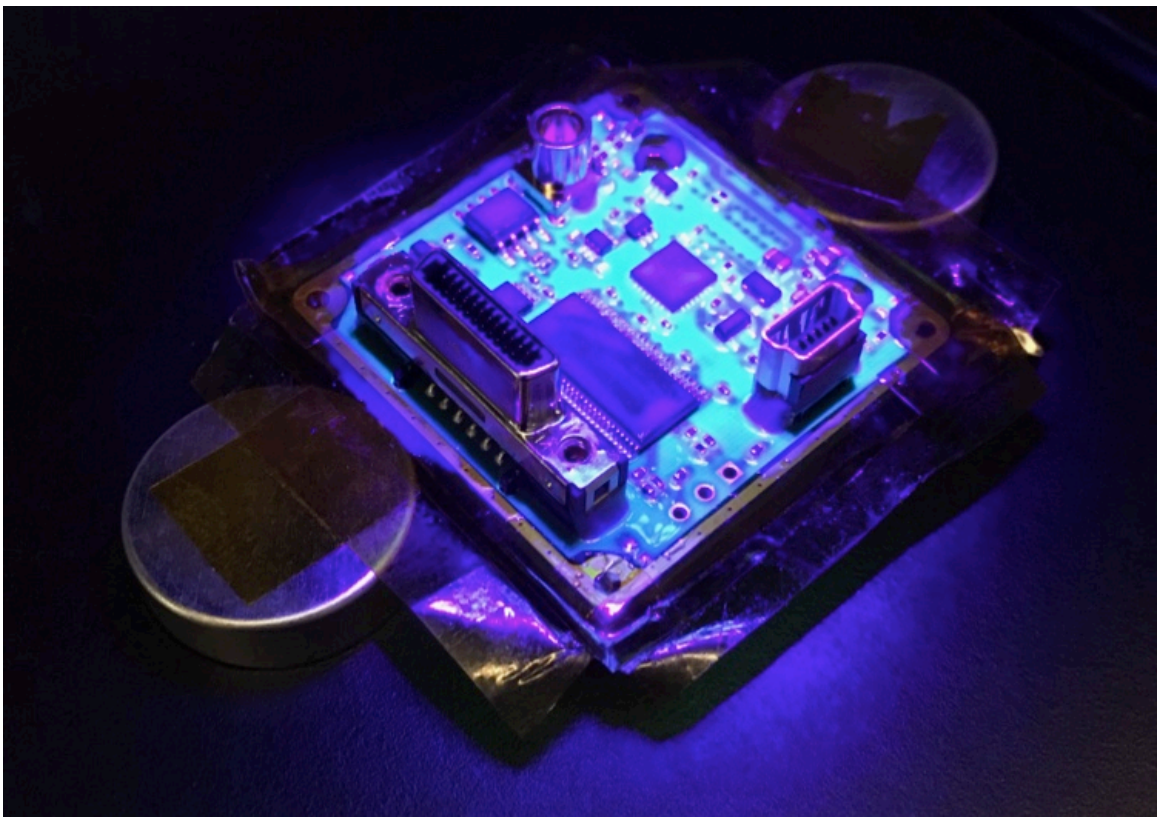

*Figure 98*. The IR camera Camera Link interface board was conformal coated. The coating fluoresces with a black light. The conductive outer edge was taped off to prevent it from being coated.

**Visible Camera Integration**

After verifying that the EM visible camera met the requirements, and after all of the visible camera housing subassemblies were completed, and after the gold boards were staked and conformal coated, the gold for-flight visible camera subsystem was integrated. The electronics boards were fit checked into the housing. Kapton tape was carefully placed on the electronics boards to isolate them from the housing as a precaution. The backplate was fitted with jack screws to attach the mini-USB. The assembly screws were carefully wrapped with Kapton and fitted through the housing. The assembly was then carefully put together and the screws were tightened with doubled nuts on the backplate. After the assembly was completed, the serial number plate was attached and the screws were staked. The completed assembly was then baked out and tested.

**Infrared Camera Integration**

The infrared camera consists of the FLIR Tau 2 camera core, the Ophir 100mm lens, the custom designed solar shade, and the mechanical structure. After the FLIR Tau 2 boards were staked and conformal coated, the assembly was reintegrated an attached to the Ophir lens. This assembly was then taken to the roof of SESE's ISTB4 and focused on A-mountain. The lens locking screw was torqued. The solar shade was installed. Finally, the camera, lens, and solar shade were collectively mounted to the infrared camera structure.

**Instrument Computer Integration**

The instrument computer stack consists of three integrated boards mounted into the instrument computer case. Prior to board integration, wires are soldered to the Minnowboard power leads to provide an additional power source. These wires are connected to a power jack with a screw lock that will provide backout protection of the

power connector. The boards are stacked with a board space in between the Minnowboard and the Silverjaw Lure. The boards are then carefully nestled into the instrument computer case and screwed into place and staked. The case cover was then attached and staked. The EM and flight computer assemblies successfully performed after integration.

Isolation of the boards from the case was attempted during spacecraft integration, however this effort inevitably was unsuccessful. This was one of the outstanding risk items, but as alternative approach, it may be possible to isolate the instrument computer case from the infrared camera case instead.

*Figure 99*. Exploded view of the visible camera. From left to right, a bracket designed by the spacecraft team was constructed from the spacecraft team's CAD file. The camera backplate housing holds the visible camera core and the lens was attached. For now, the red lens cap protects the lens. The frontplate and solar shade are one integrated component.

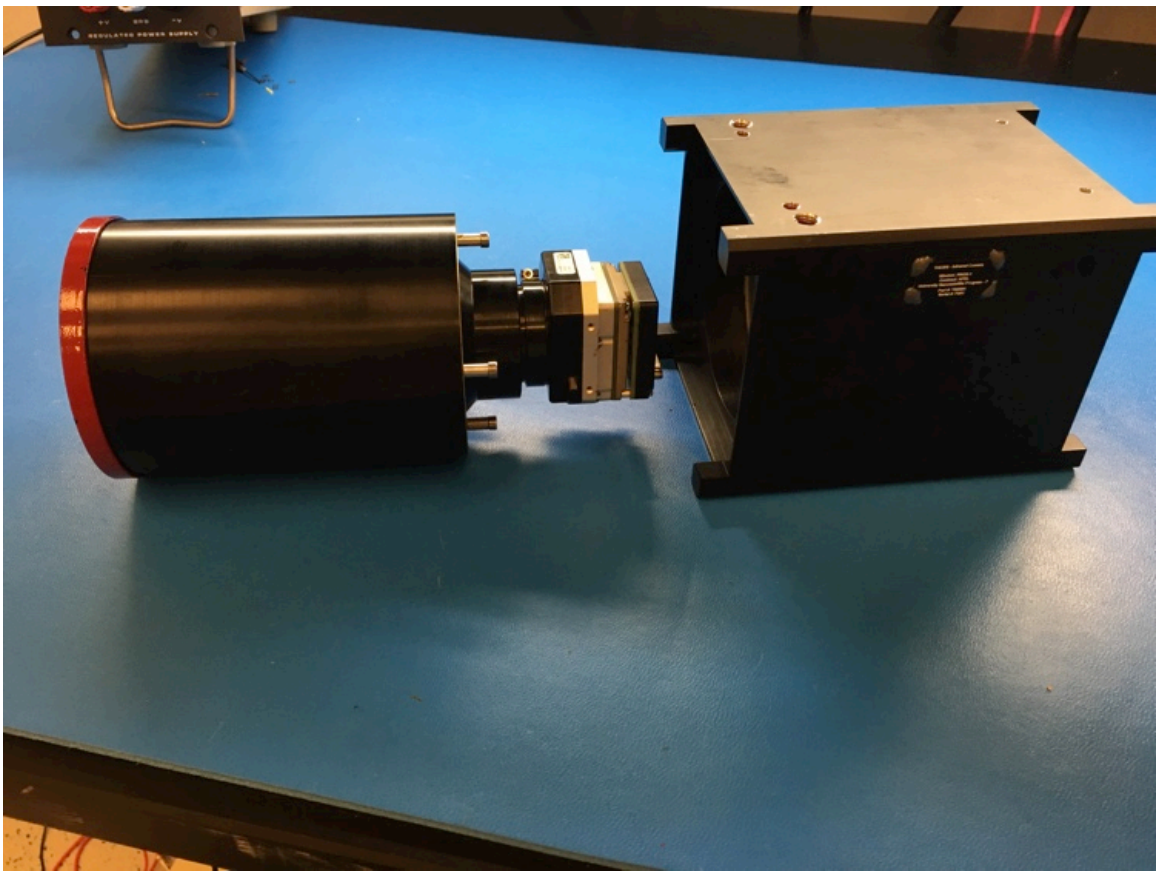

*Figure 100*. Exploded view of infrared camera. From right to left, the infrared camera structure was approximately a 1.5U structure, the Tau 2 camera core was attached to the Ophir lens with a solar shade and red lens cover.

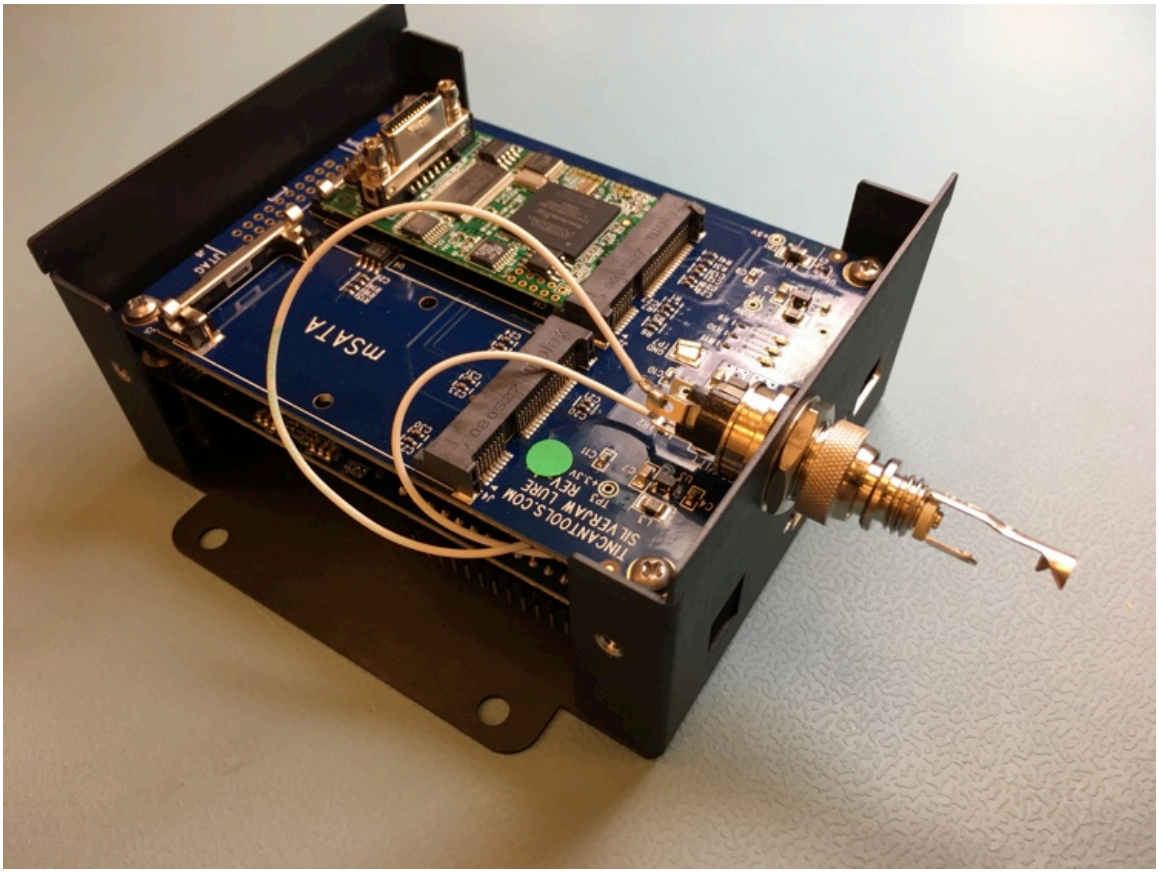


*Figure 101*. The instrument computer stack. The Minnowboard-MAX was the main computer. A SilverJaw lure was attached that provides the interface to the PIXCI EB1-Mini camera link board.

**Flight Harnessing**

The flight harnessing was initially tested at ASU on the engineering model THESIS in order to verify its performance as a fully integrated subsystem. Three sets of harnesses were ordered: EM, flight, and backup. At this time, the flight instruments had already been delivered and integrated to the spacecraft. In this integrated assembly, the communication of the instrument computer with the visible camera and the infrared camera was verified. However, power was not being supplied to the infrared camera. It was determined that the vendor mis-pinned the mini USB cable, so it had to be returned for rework. The EM proved useful for testing the harnessing and discovering this error prior to the final trip to Georgia Tech for harnessing integration.

The EM “flight-like” harnessing was extensively tested over a few months in order to verify its performance over an extended period before final integration of the for-flight harnessing at Georgia Tech.

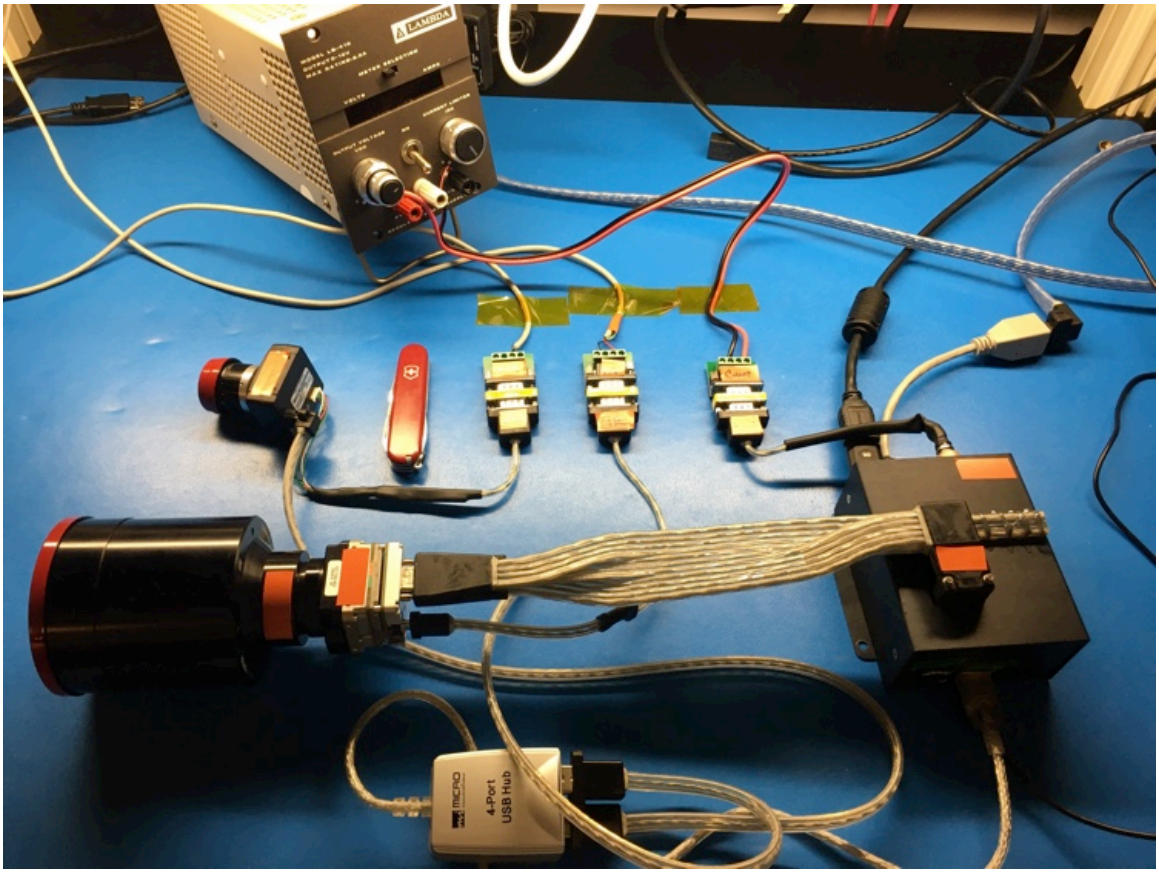


*Figure 102*. Integrated Engineering Model using EM flight-like harnessing designated for the EM.

## REQUIREMENT VERIFICATION AND VALIDATION

### Overview

The requirements are verified through analysis, inspection, and testing. Several of the requirements are verified through inspection and analysis during the design phase. Some of the requirements are first analyzed, but require subsequent testing of the completed assembly. These include the resolution testing. The radiometric testing was descoped from a baseline pre-flight test to a threshold in-flight test. Finally, the instruments were planned to undergo environmental testing with the completed spacecraft.

### Visible Camera Resolution Testing Pre-delivery

The final visible camera resolution test analysis pre-delivery was written by Amber Keske. This section was included for completeness of the project, however the work was hers and it will be included in her PhD.

The ability to accurately resolve the cubesat by the visible camera was tested. Images of a 10x10x30 $cm^3$ test blackbody were captured from distances of 50, 100, 150, and 200 m at a focal distance of infinity. For each image, a script was run to determine the average number of pixels subtended by the 10-cm side of the object. The algorithm used predicted the distance within error for 50, 100, and 150m. At 200m, the error bar exceeded the actual value by about 11 m. This was probably the result of poor contrast between the target and the background in the images.

Our expectation that the standard deviation of the distance estimates would increase with increasing distance was met. However, we expected that the true distance would fall within the range of estimates for every set of test images. That hypothesis was true for the three closer distances, but untrue for the farthest distance, which was overestimated. Therefore, we caution that counting pixels to estimate distance was

reliable only for images with high signal-to-noise ratios, which increases with shorter distances and greater contrast between the background and the target object. Our calculations were done using the 10-cm side of the object. The 30-cm side would no doubt prove to produce more accurate results for longer distances, since there will be more pixels subtending the center of the object, increasing the number of samples used in the algorithm. – Amber Keske

The results are shown in *Figure 103* and the images are included in the appendix.

**Visible camera performance**

The final visible camera performance test analysis pre-delivery was written by Amber Keske. I wrote the following paragraph to address Amber Keske's plots. This section was included for completeness of the project, however the work was hers and a more detailed description of the methods and results will be included in her PhD.

The visible camera was tested to verify performance requirements. The DN level signal vs. the noise was plotted for various images at different temperatures and exposure times (*Figure 104*). The SNR requirement of 10:1 was met for exposure times of greater than 0.5 ms (*Figure 105*). It was highly unlikely that images will be captured below this exposure time.

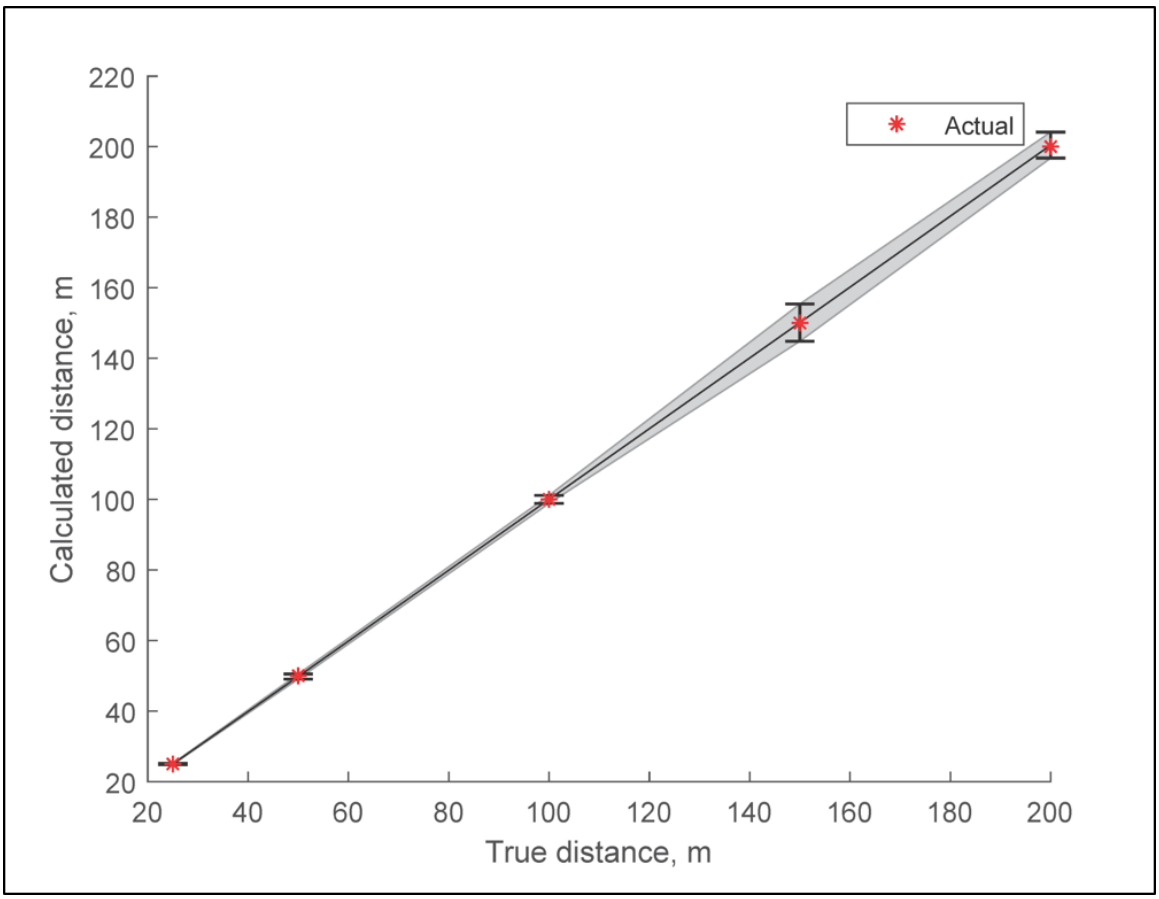


*Figure 103*. A scatter plot representation of the estimated distance data with error bars representing the standard deviation.

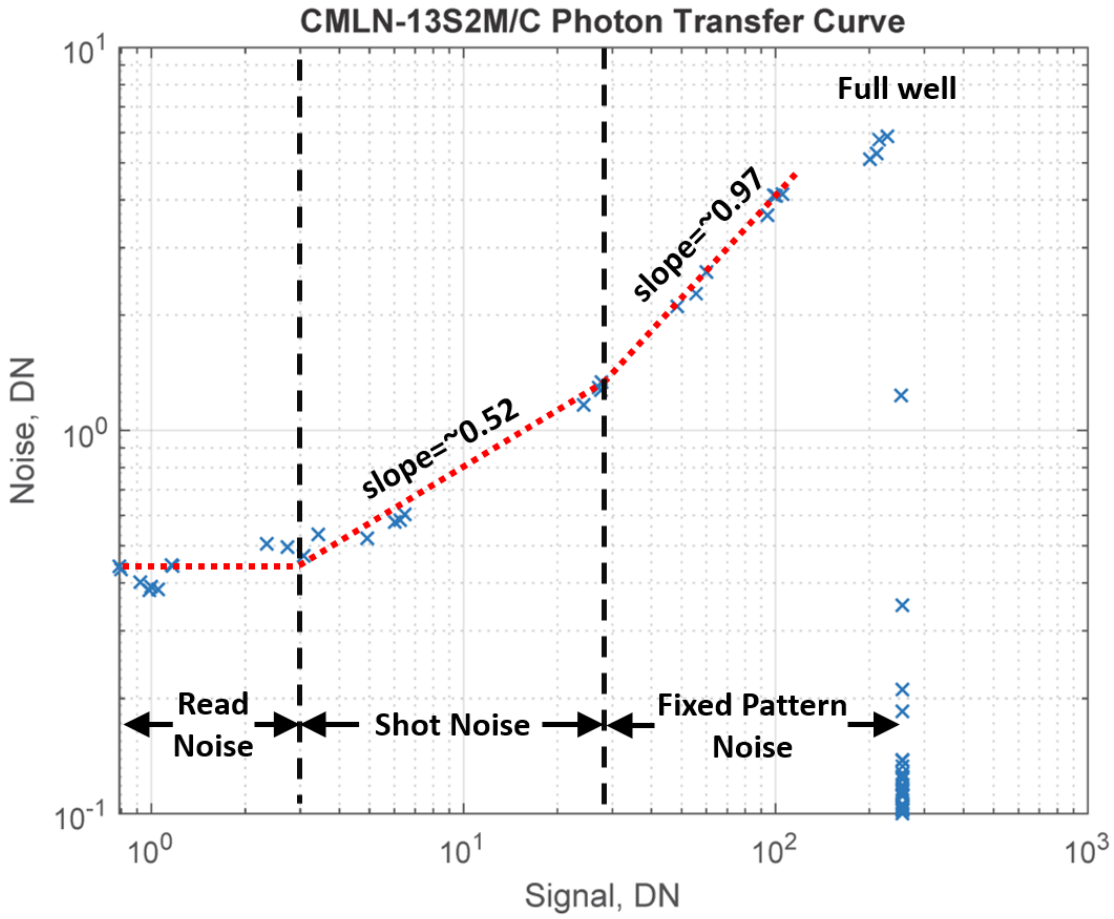


*Figure 104*. Plot of the signal vs. noise. The SNR was greater than 10:1 for various DN levels. Data includes various temperatures and exposure times.

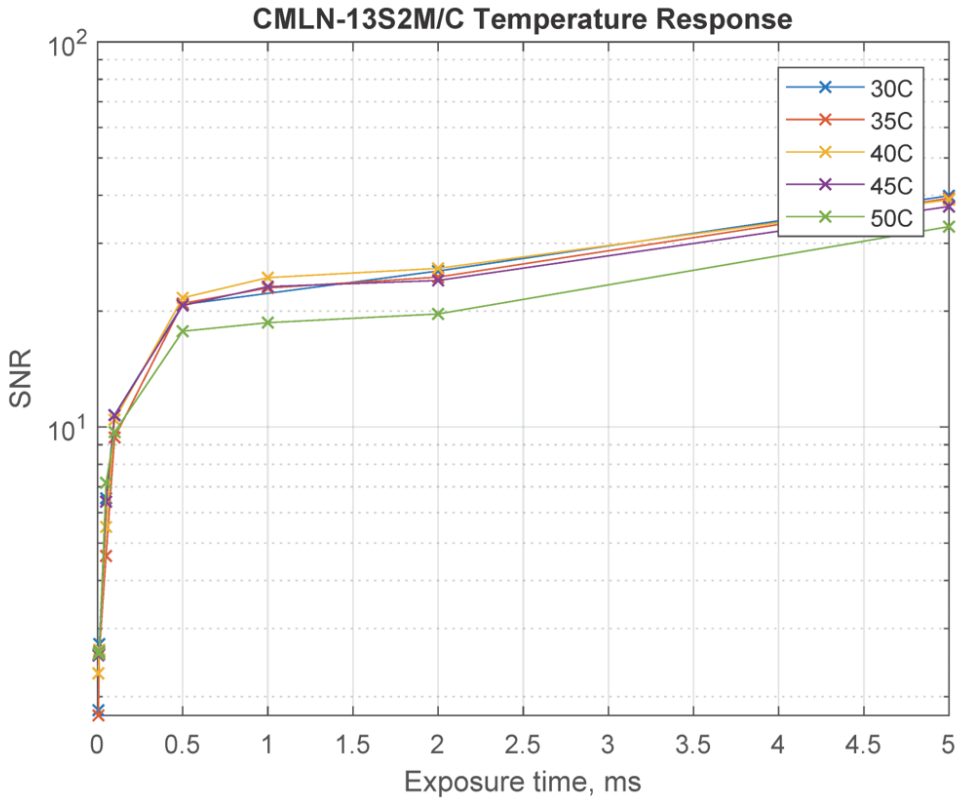


*Figure 105*. Plot of the SNR at various enumerated exposure times and temperatures. All images captured at or above 0.5 ms meet the SNR requirement of 10:1.

## Infrared camera resolution test

### Overview

Images of a 10x10x30 $cm^3$ test blackbody were captured from distances of 50, 100, 150, and 200 m at a focal distance of infinity. For each image, a representative row of pixels from the 10-cm side of the blackbody were extracted and compared with the expected signal if there were no signal rolloff at the edge of the blackbody. The final, pre-delivery infrared camera resolution test analysis was completed by Amber Keske.

### Threshold Results: Percentage of Max

We expected the maximum signal to decrease and the tail of rolloff to widen as the distance increased. Instead, the change in the rolloff curve shape as a function of distance seems to be a more complex relationship, with a transition from a rounded box shape at short distances to a more subdued Gaussian shape at longer distances. However, when the point of intersection between the measured and the expected curves was divided by the measured curve maximum (after background removal), we found they tend to cluster around an average of 87%±7%, with no distinct trend with distance. We conclude that the threshold of the 10-cm edge can be reasonably estimated by the location of full width 87% max on the signal curve up to a distance of at least 200 m. This means that, given images of an object with a width of 10 cm against a uniform background, we can estimate the distance of the object from the camera at the time of image capture using the location of full width 87% max on the rolloff curve –Amber Keske.

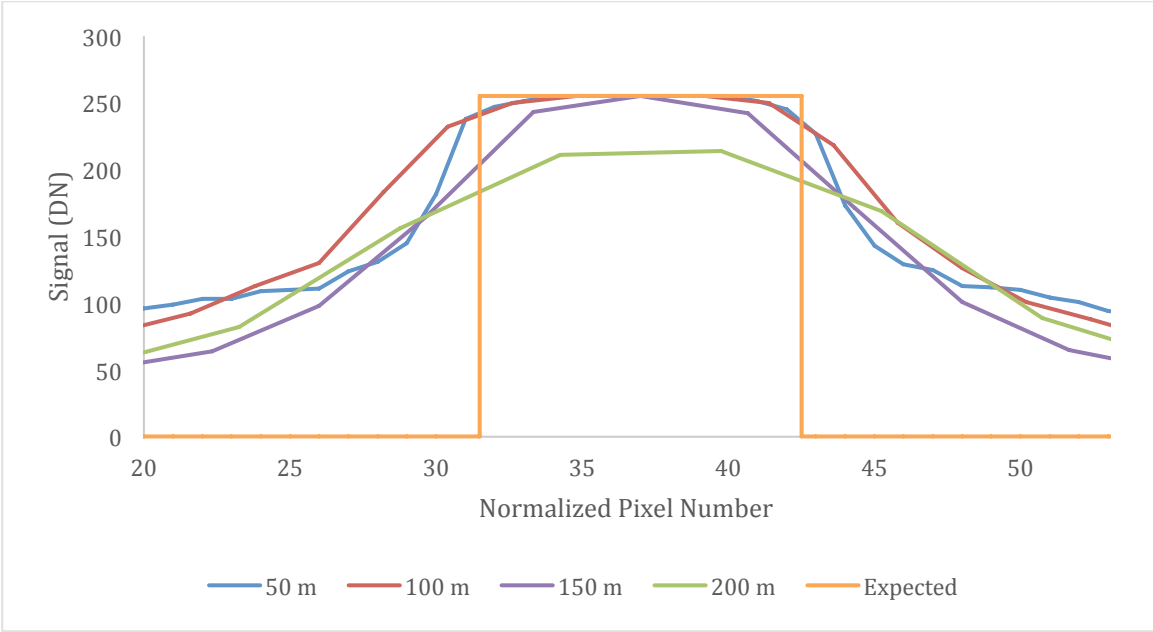


*Figure 106*. A normalized plot for comparison of the degree of rolloff for each distance (normalized to the 50 m plot):

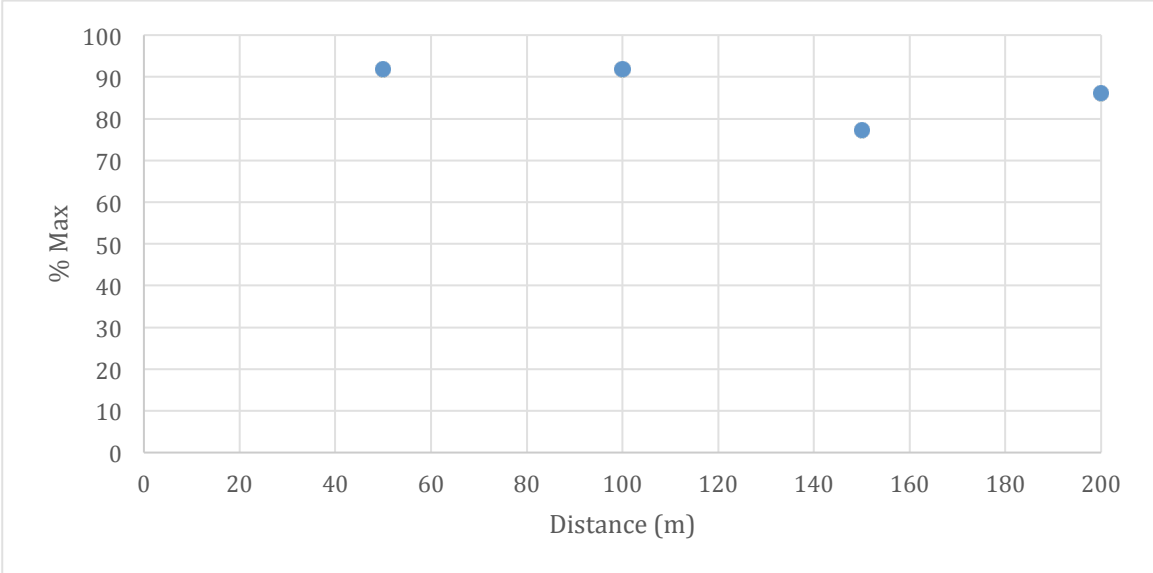


*Figure 107*. A plot of the % maximum of the average intersection point value of the expected and the measured curves (background removed). The average value was about 86.7% with a standard deviation of 6.8%.

**Baseline results: Edge-finding algorithm**

Further analysis by Amber Keske, subsequent to instrument delivery, revealed that an edge-detection algorithm was able to more accurately determine the expected value of the cubesate. Taking the 1st derivative of the data, then applying a smoothing algorithm, yields a peak and a valley that are used to determine the location of the best estimate of the edge. This algorithm works well along the entire expected imaging range of 50-200 meters. This even works well at nearer distances, e.g. 25m, that are out of focus to a greater extent. The edge-detection method produces errors at 200 meters of ~10%.

Because of these baseline results, it was suggested that the Image Processing team, reapply the edge-detection algorithm envisioned in the *R3* mission after identifying *LightSail-B* with the blobber algorithm (Védie et al., 2013). This will help the subsequent range identification algorithm to determine a more accurate distance to *LightSail-B*.

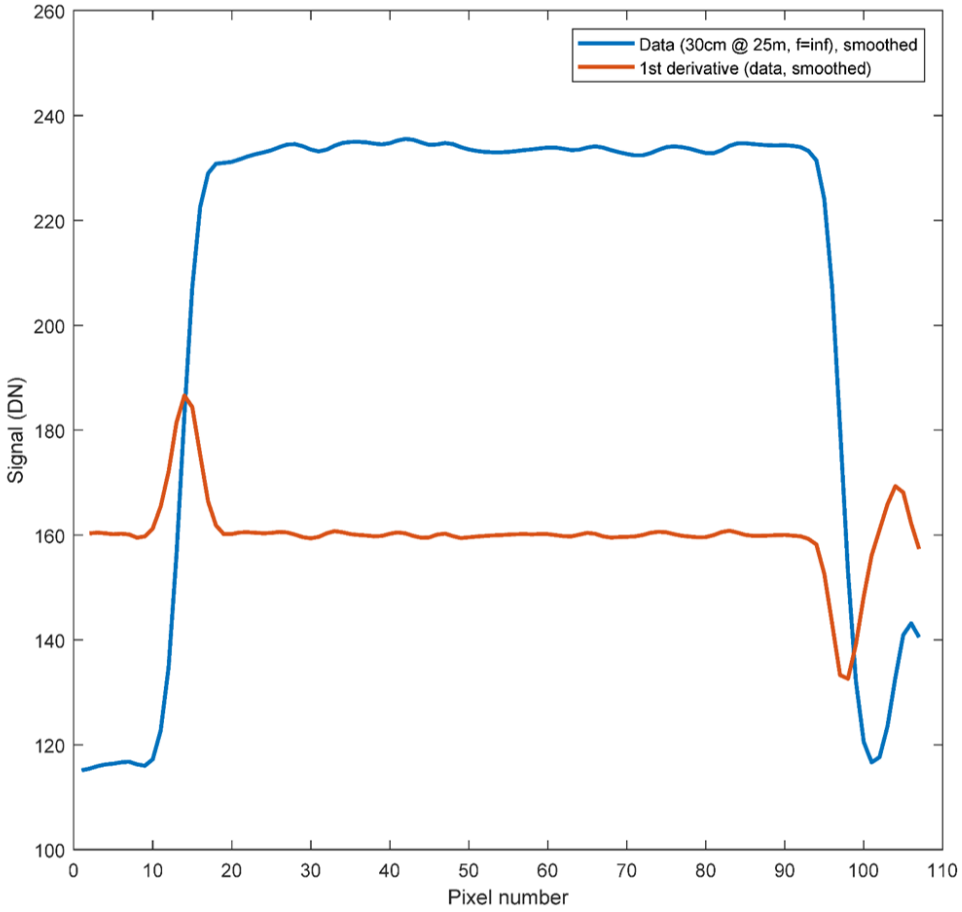


*Figure 108*. A line of data for 30cm of the cubesat at 25m from the camera was plotted. The 1st derivative was calculated and smoothed with a filter. The peak or valley predicts the true edge of the cubesat.

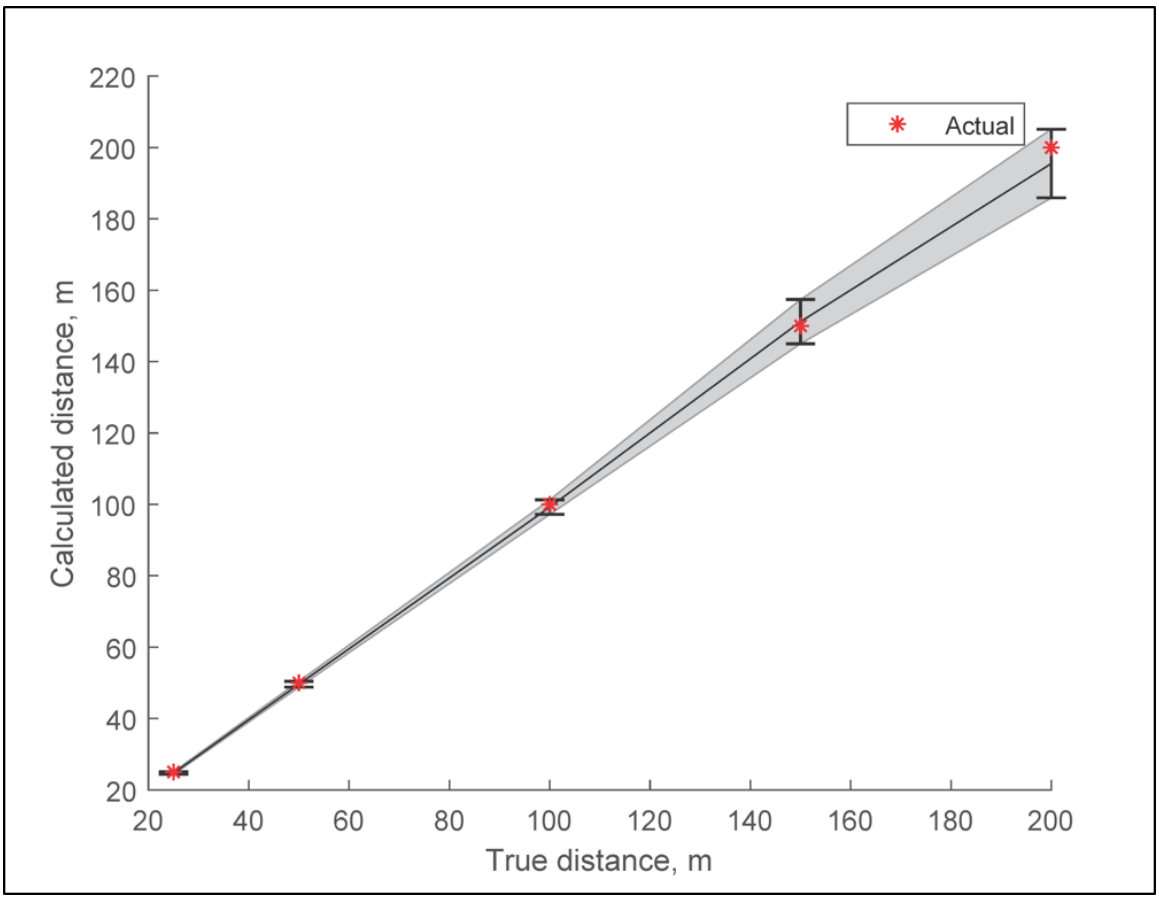


*Figure 109*. The predicted vs. true distance calculated from pixels using the derivative edge-detection method. The error at 200m was only ~10%.

**Airy diffractioxn blur of IR images**

The effects of airy diffraction were briefly investigated to show that image processing during prox-ops was fundamentally limited by focusing not diffraction.

Using 12μm for the wavelength and 62.5mm for the diameter of the aperture, the diffraction limit, using the Rayleigh criterion of ( 166 ) was 0.234 mRad. The pixel for this system have an IFOV of 0.17 mRad.

$$\sin\theta = \frac{1.22\,\lambda}{D} \qquad (166)$$

For the f/1.6 lens and 12μm wave, a diffraction blur has a diameter of 47μm for the 84% of the energy as the central disk (using equation ( 167)). The system was theoretically diffraction limited, when the airy disk was 2-3 times the pixel size. A problem with decreasing the pixel size of microbolometer focal plane arrays, in order to achieve greater resolution, was that diffraction may limit performance (Riedl, 2001).

$$B_{diff} = 2.44 * \lambda * f/\# \qquad (167)$$

In order to assess the diffraction effects, a simulation of the cubesat response with airy diffraction was completed by Amber Keske (*Figure 110*). This shows that the principal deviation in the data from the expected result was focusing, not diffraction. Furthermore, the diffraction model can be "blurred" in order to match the data. Because this would be difficult to adjust for in-flight, the 1st derivative edge-detection method was sufficient.

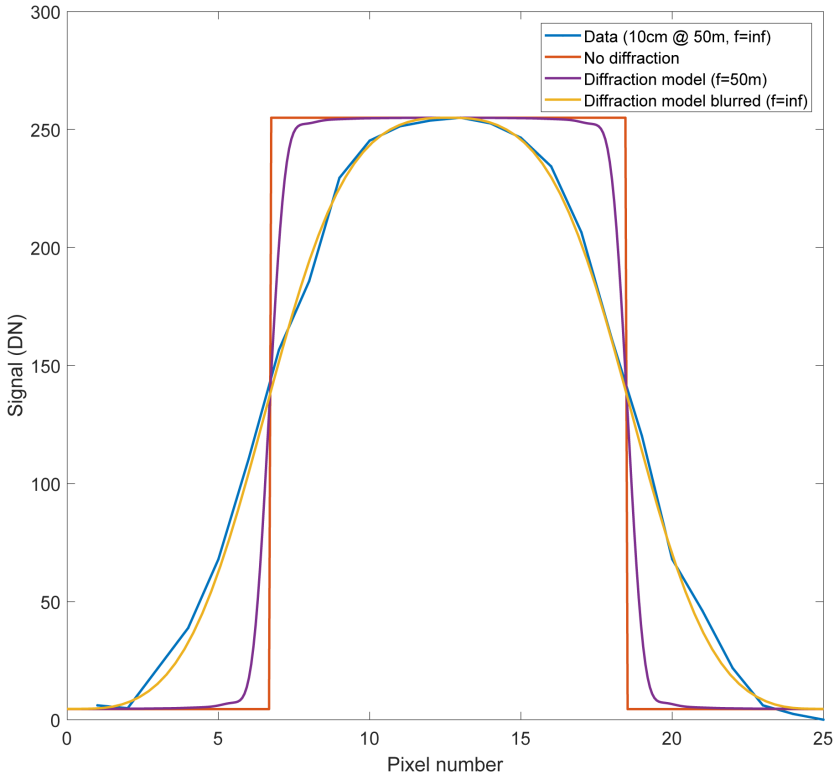


*Figure 110*. The expected cubesat model if sharp (red) was plotted with the expected values including diffraction (purple). The actual data (blue) was smoothed more than the modeled diffraction from out of focus blur. The expected diffraction (purple) requires Gaussian smoothing to simulate the blur before it approaches the data. This analysis is in Amber Keske's PhD.

## Infrared Radiometric Testing

### Background

The general equation for the counts of a detector of an infrared camera system is shown in *Figure 111*. An equation was provided that expresses each of the radiometric fluxes.

***1. Reflected Background Radiation*** The background radiation was the reflectivity or one minus the scene emissivity using Kerchov's Law, multiplied by the background thermal flux as a function of the background temperature.

$$Q_{bkg} = (1 - \epsilon) * W(T_{bkg}) \quad (168)$$

***2. Scene Radiation.*** The radiation from the scene, i.e. LightSail was equal to the emissivity of the scene multiplied by the thermal flux as a function of the scene temperature.

$$Q_{scene} = \epsilon * W(T_{scene}) \quad (169)$$

***3. Atmospheric Radiation*** The radiation from the atmosphere was equal to one minus the transmissivity of the atmosphere, equal to the emissivity of the atmosphere, multiplied by the thermal flux as a function of the temperature of the atmosphere.

$$Q_{atm} = (1 - \tau_{atm}) * W(T_{atm}) \quad (170)$$

***4. Window Radiation.*** The radiation of the window was equal to one minus the transmission and the reflection of the window, equal to the emissivity of the window, multiplied by the thermal flux as a function of the temperature of the window.

$$Q_{win} = (1 - \tau_{win} - r_{win}) * W(T_{win}) \quad (171)$$

***5. Detector Reflection.*** The radiation of the detected reflected back on itself was equal to the reflection of the window multiplied by the flux of the detector as a function of the temperature of the detector.

$$Q_{det} = (r_{win}) * W(T_{det}) \quad (172)$$

***Full Equation.*** The full equation combines these terms with the transmissivity of the atmosphere and the window multiplied as appropriate.

$$S = Q_{bkg} + Q_{scene} + Q_{atm} + Q_{win} + Q_{det} \quad (173)$$

Adding the window transmission yields the following.

$$S = \tau_{win}\left(Q_{bkg} + Q_{scene} + Q_{atm}\right) + Q_{win} + Q_{det} \quad (174)$$

Adding the atmospheric transmission yields the following.

$$S = \tau_{win}\left(\tau_{atm}\left[Q_{bkg} + Q_{scene}\right] + Q_{atm}\right) + Q_{win} + Q_{det} \quad (175)$$

Substituting the values from the previous sections yields the following.

$$S = \tau_{win}\left(\tau_{atm}\left[(1-\epsilon) * W\left(T_{bkg}\right) + \epsilon * W(T_{scene})\right] + (1-\tau_{atm}) * W(T_{atm})\right) + (1-\tau_{win}-r_{win}) * W(T_{win}) + (r_{win}) * W(T_{det}) \quad (176)$$

Because the transmission of the atmosphere was assumed to be zero (LEO looking 50-200 meters at *LightSail*) and there was no window used, the above equation simplifies to the following.

$$S = (1-\epsilon) * W\left(T_{bkg}\right) + \epsilon * W(T_{scene}) \quad (177)$$

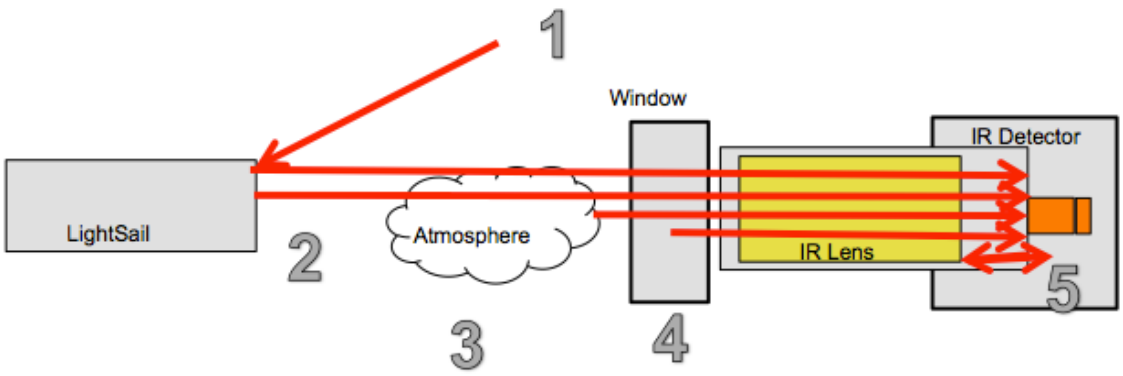


*Figure 111*. Radiometric Cartoon adapted from FLIR Advanced Radiometry note. 1) Solar radiation illuminates *LightSail*, and some of the energy was reflected. 2) *LightSail* radiates energy. 3) If there was any atmosphere between *LightSail* and the infrared camera, then part of the energy will be absorbed. For this application, the atmosphere was sufficiently thing that this was assumed to be zero. 4) If there was a window, then the window will radiate onto the detector. For this application, no window was installed in front of the infrared lens, so this was assumed to be zero. 5) The detector then reflects back onto itself if the window's transmission was less than 100%.

**Requirements Overview**

The Radiometric Test Plan will verify the performance of the onboard calibration algorithms on the Tau 2 and provide an instrument response function. It will also produce data that verify the following requirements. However, testing already and specifications seem to verify these requirements already.

INS-1.1.3 The infrared camera shall have a noise equivalent temperature difference (NETD) of 1 K.

INS-1.1.3.2 The temperature of the infrared camera environment shall be monitored to assist in calibration.

INS-1.2 The infrared camera shall produce images with a signal to noise ration of greater than 10:1 in order to ensure images of sufficient quality to assist attitude control based upon onboard processes.

The test will be performed by capturing images of blackbody targets of known temperatures to produce an instrument response function. These tests will occur prior to launch.

The imaging of *LightSail* after deployment also provides ample opportunity capture images in the space environment of an object (*LightSail*) at a known target temperature (as measured by the *LightSail*) thermocouples. We plan to use these images for calibration of the target in the space environment.

**Prior verification of requirements:**

***INS-1.1.3*** The infrared camera shall have a noise equivalent temperature difference (NETD) of 1 K.

This requirement evaluates the precision of the detector. It was explicitly verified from the FLIR Tau 2 specification sheet that lists the NETD of Industrial grade cameras to be <30 mK. In addition testing was performed at ambient conditions of 25.5˚C in the

laboratory. Twenty images were captured of a 70˚C and a 100˚C blackbody target in both count mode and t-linearized mode, for a total of 80 images. For each of the respective groups, the standard deviation was computed for each pixel. The standard deviation was <10mK. This was well within our requirement of 1K. The detector has high precision, meeting the requirement by an order of magnitude.

***INS-1.1.3.2*** The temperature of the infrared camera environment shall be monitored to assist in calibration.

This requirement was explicitly verified from the FLIR Tau 2 Software IDD, in that the temperature of the FPA and the temperature of the housing are monitored. We have also pulled this data and put it into a file.

| | | |
|---|---|---|
| Temp FPA | DgC*10 | 229 |
| Temp House | DgC*100 | 2584 |

***INS-1.2*** The infrared camera shall produce images with a signal to noise ratio of greater than 10:1 in order to ensure images of sufficient quality to assist attitude control based upon onboard processes.

For the blackbody at 100C, the average DN was 8912 and the worst case standard deviation was 12.1. This constitutes an SNR of 737. For the blackbody at 70C, the average DN was 6313 and the worst case standard deviation was 13.8. This constitutes an SNR of 457. For target temperatures of 100C and 70C in ambient conditions of 25.5C, the SNR requirement was exceeded.

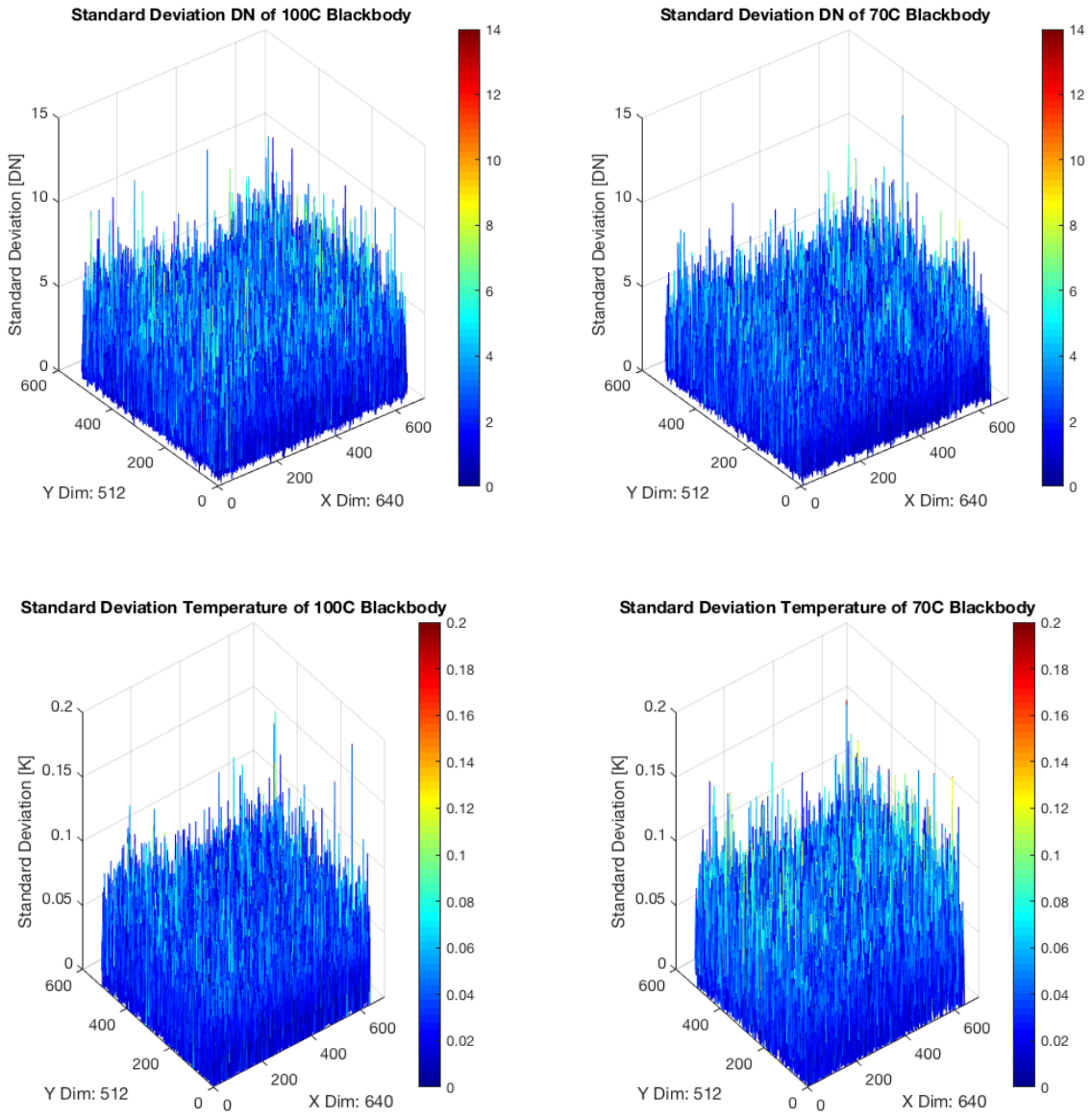


*Figure 112*. The Top figures are the standard deviation of the raw counts of each pixel in the microbolometer array. The bottom figures are the standard deviation of the resulting temperatures from the on-board T-Linearization processing. All of the T-linearized data points are <0.2K for the first standard deviation.

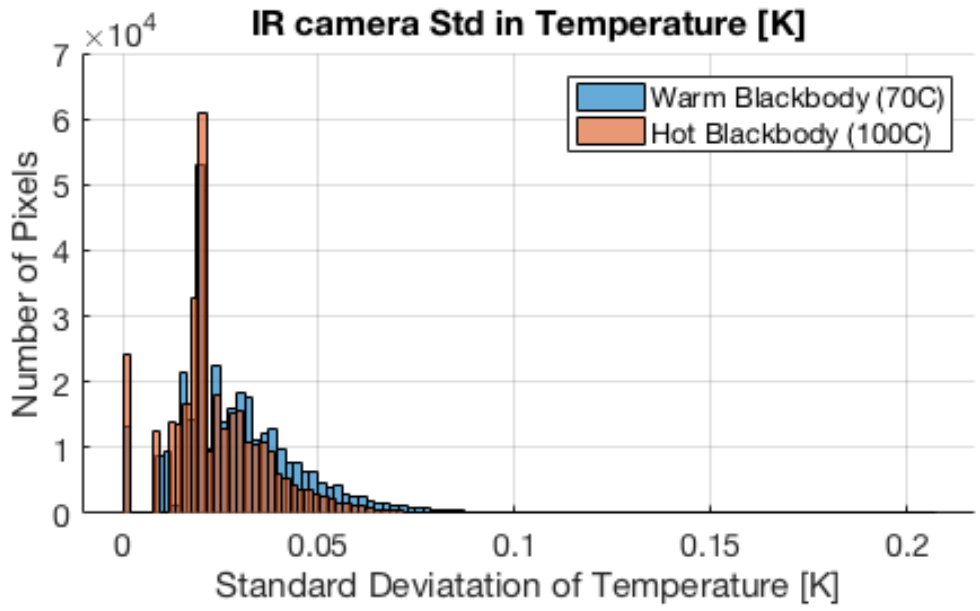


*Figure 113*. Histogram of the standard deviation of temperature for each pixel while staring at 70C and 100C targets at ambient conditions in the lab. The data meet the requirement of a NEDT of 1K by greater than an order of magnitude as nearly all of the data fall <50mK, and the peak was ~20mK.

### Absolute Radiometric Calibration Methodology

The absolute accuracy was not a requirement for THESIS. However, it was desired. As the camera does an onboard T-linearization of the data, the accuracy of this processing was tested *Figure 114*. The onboard calculated temperatures were about 114% of the recorded blackbody temperature using the internal thermocouples. When the result was multiplied by the lens transmission value (88%), then the modified calculation intersected the blackbodies temperature. The lens transmission was manually entered during original development, but it's possible that the calibration tables are factory calibrated to assume this lens already. If this was the case, then lens transmission was being applied twice, and the onboard processing was thus overcompensating.

An instrument response function was produced from a heating element that could be easily tuned as a first order approximate exercise that incorporates methods from THEMIS calibration (Christensen et al., 2004). The linear function was shown in *Figure 115*. The A future calibration would use a well-calibrated blackbody in TVAC to determine how this linear function changes with temperature of the instrument.

The absolute calibration of the system still requires future work as the 100˚C blackbody was calculated to be +15˚C and the 70˚C blackbody was calculated to be +9˚C. If the camera was simply miscalculating from the lens transmission, then the absolute error was <2K for this test.

Table 36.

*Absolute Temperature Testing*

| | 70˚C Blackbody | 100˚C Blackbody |
|---|---|---|
| Thermocouple Value ˚C | 69.5 | 99.8 |
| T-Linearization Average ˚C | 79.0 | 115.0 |
| 88% of T-Lin. ˚C | 69.5 | 101.2 |
| Absolute Error | 0.0 | 1.4 |

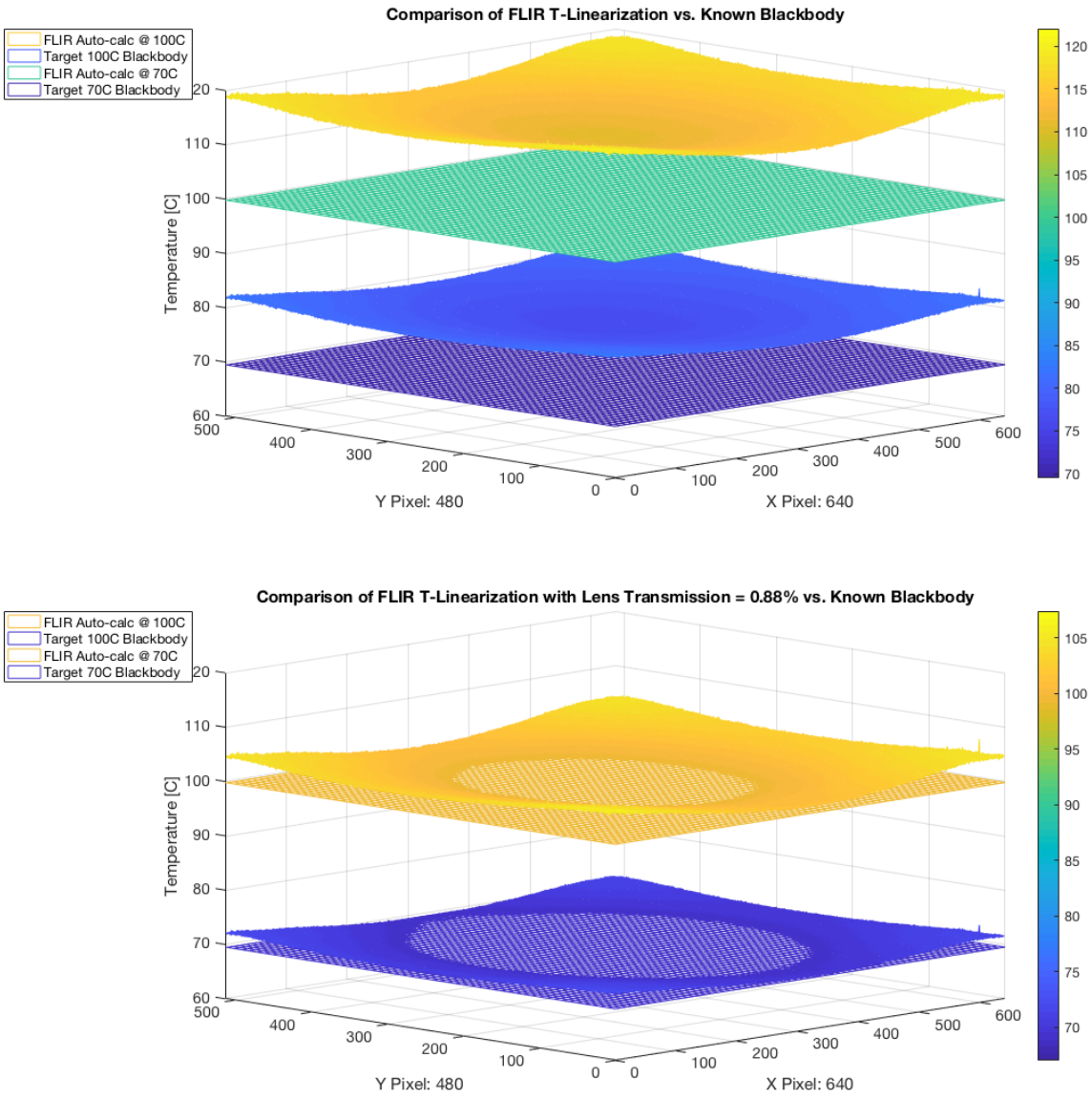


*Figure 114*. The average T-Linearized focal plane data for a 100˚C and 70˚C blackbody. The FLIR over predicts the temperature. When T-Linearized data was multiplied by the transmission of the optics (88%), then the curves intersect. The edge of the blackbody may have been hotter than the cavity itself.

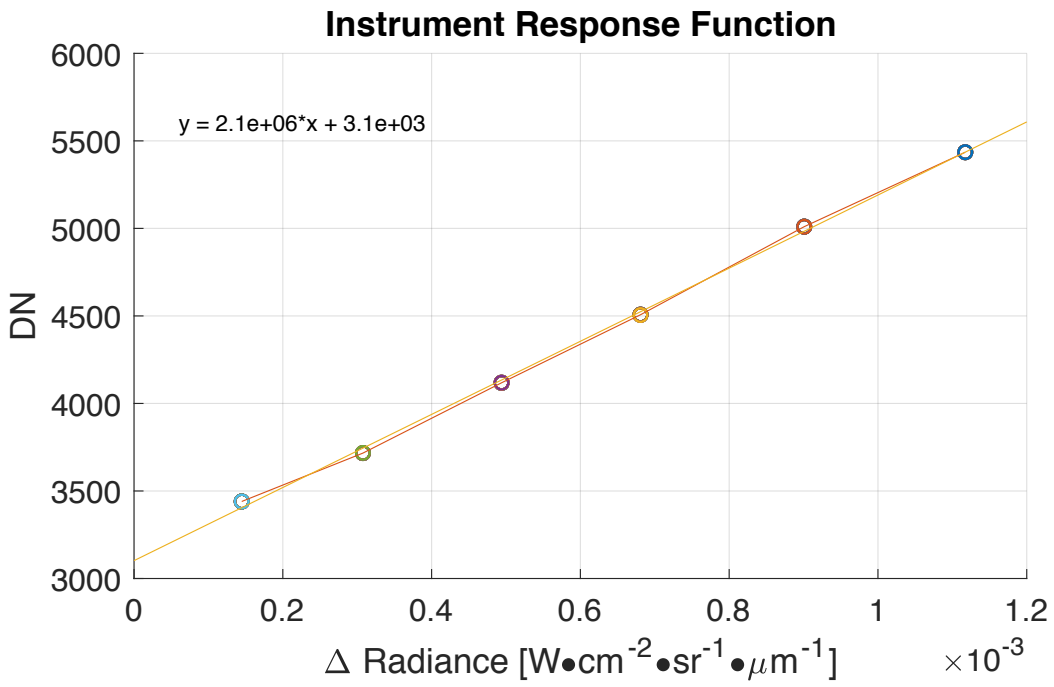


*Figure 115*. Example instrument response function using a heating element. In the ambient lab (25.5˚C) twenty images were captured of six different set points (30, 40, 50, 60, 70, and 80˚C). The delta radiance assumes the temperature of the target was blackbody and subtract the radiation of the detector using its temperature. A linear response curve fits the radiance to the DN value.

### Future laboratory calibrations

Future laboratory calibrations would produce instrument response functions similar to the above in a TVAC campaign. This would include ~10 blackbody temperatures at ~10 different instrument temperatures for a total of 100 data points. The absolute temperature anomaly must be determined as well, and this was probably a result of double-applying the lens transmission.

### In-flight calibration

There are typically two forms of in-flight calibration methods: 1-point method and 2-point method.

***1-Point Method*** The 1-point method adjusts the offset to match the temperature with a blackbody. The easiest blackbody to use would be space. If THESIS were to launch, then pointing the instruments at open space would produce a good target for calibrating to the 3K background.

***2-point method*** A 2-point method can change the slope of the instrument response function. The Earth was complicated in the infrared, because of the atmosphere. Images of the moon have been captured from the ground with our field IR camera. Commanding the spacecraft to capture images of the moon would be decent, well-constrained and modeled targets for calibration as well as a prime target for exciting public relations images.

Additionally, though probably less reliably, the exterior temperatures of *LightSail-B* would have possibly been available from the solar panels. There were some early discussion of obtaining this data.

### Mission Operations

An instrument checkout plan was completed in the Day in the Life Test for the *Prox-1* spacecraft and was provided in the appendix. The checkout plan was written by the Mission Operations Lead Terresa Spinelli (Mission Manager) with consulting from Michael Veto (Instruments) and Louis Williams (Flight Software). Verifying, through testing, that THESIS successfully completed this instrument checkout plan was required in order to pass the day-in-the-life test before delivering the spacecraft to AFRL.

## SPACECRAFT INTEGRATION AND TESTING

### Overview

Similar to NASA Discovery, New Frontiers, and Flagship missions, the *Prox-1* mission consisted of host institution responsible for the mission and spacecraft, with a partnered institution lending expertise for an instrument. For NASA missions such as, the ASU-built instrument OTES was developed and tested with a spacecraft simulator prior to delivery and an instrument simulator was provided to the spacecraft team for development. Upon completion and of instrument testing, the instrument was delivered and bolted to the spacecraft. For *Prox-1*, the instrument to spacecraft integration and testing process was a bit more iterative for three reasons. First, being a student mission, this project was primarily a learning process, many of the best practices and systems engineering were learned throughout the project lifecycle and sometimes required reevaluating previous work. Second, being a microsat mission, many of the design solutions were unique, custom, and experimental, so they required testing to validate that the solution actually worked—none of the THESIS components were purchased as flight qualified standardized components. Third, the instrument design had to respond to a number of spacecraft design changes involving the structure, power, data processing, computer interface, harnessing, and software. Fourth, we did not create an

instrument simulator, nor did GT provide a spacecraft simulator for testing. All day in the life testing required that work on the instruments be halted and the current state of the instruments be delivered to GT for DITL testing. Thus, while instrument and spacecraft are typically constructed in parallel and culminate in a single integration, we conducted a few proto-integrations on the flatsat to run day-in-the-life tests at GT. In between the major reviews, the instruments were deintegrated from the flatsat and returned to ASU for completing flight preparations.

**Integration Timeline**

The timeline for the instrument integration and testing with the spacecraft took place over a period of 20 months (*Figure 116*). While the major flight components of the instruments were still being upgraded from EM bench-top configurations to flight, day-in-the-life testing was required with the spacecraft to test the electrical, electronic, software, and mechanical interfaces. Thus, during this period, the instruments were delivered to Georgia Tech three times. After the final delivery, ruggedized harness mounts were completed and retrofitted at Georgia Tech on the integrated instruments. Finally, the EM harnessing was replaced with space rated flight harnessing before PSR.

**Initial Instrument Delivery**

The major objective of the initial instrument delivery were to validate that the instruments interfaced with all of the other subsystems. During the week long integration trip, the instruments were powered up with the spacecraft EPS. After working with the FSW lead, the CDH, or spacecraft computer, successfully connected to the instrument computer, executed the image capture commands, and finally transferred over images from the instrument computer to the spacecraft computer. Finally, the instruments were fit checked with the spacecraft structure to validate that the CAD models sufficiently designed the interfaces The instruments were left at GT in order for

the FSW, CDH, and EPS leads to continue to perform DITL testing at the direction of the Mission Manager to complete the Instrument Checkout Procedure (section 17) It was agreed upon completion of the necessary DITL testing the instruments would be shipped back to ASU for finalizing.

**Second Instrument Delivery**

The second instrument delivery consisted of shipping the instrument back to GT upon completion of electronic board staking. This was necessary to complete another DITL test. Upon completion of the test, the instruments were shipped back to ASU.

**Final Instrument Delivery**

The final delivery of the THESIS instruments consisted of hand-deliverying the visible camera, infrared camera, and instrument computer to GT and hard mounting them to the spacecraft bottom plate after completing a flatsat DITL. At this stage, the flight harnessing was not completed, so it was subsequently delivered.

**Harnessing Integration and Preparations for PSR**

A final trip to Georgia Tech was completed to finish up spacecraft integration. The primary task was to deliver and integrate the flight harnessing. Additionally, software updates completed at ASU on the EM were loaded onto the flight computer at GT. Some time was spent troubleshooting possible ground loops, and this remained an unclosed task. Finally, preparations were made for PSR, and the instrument system was presented.

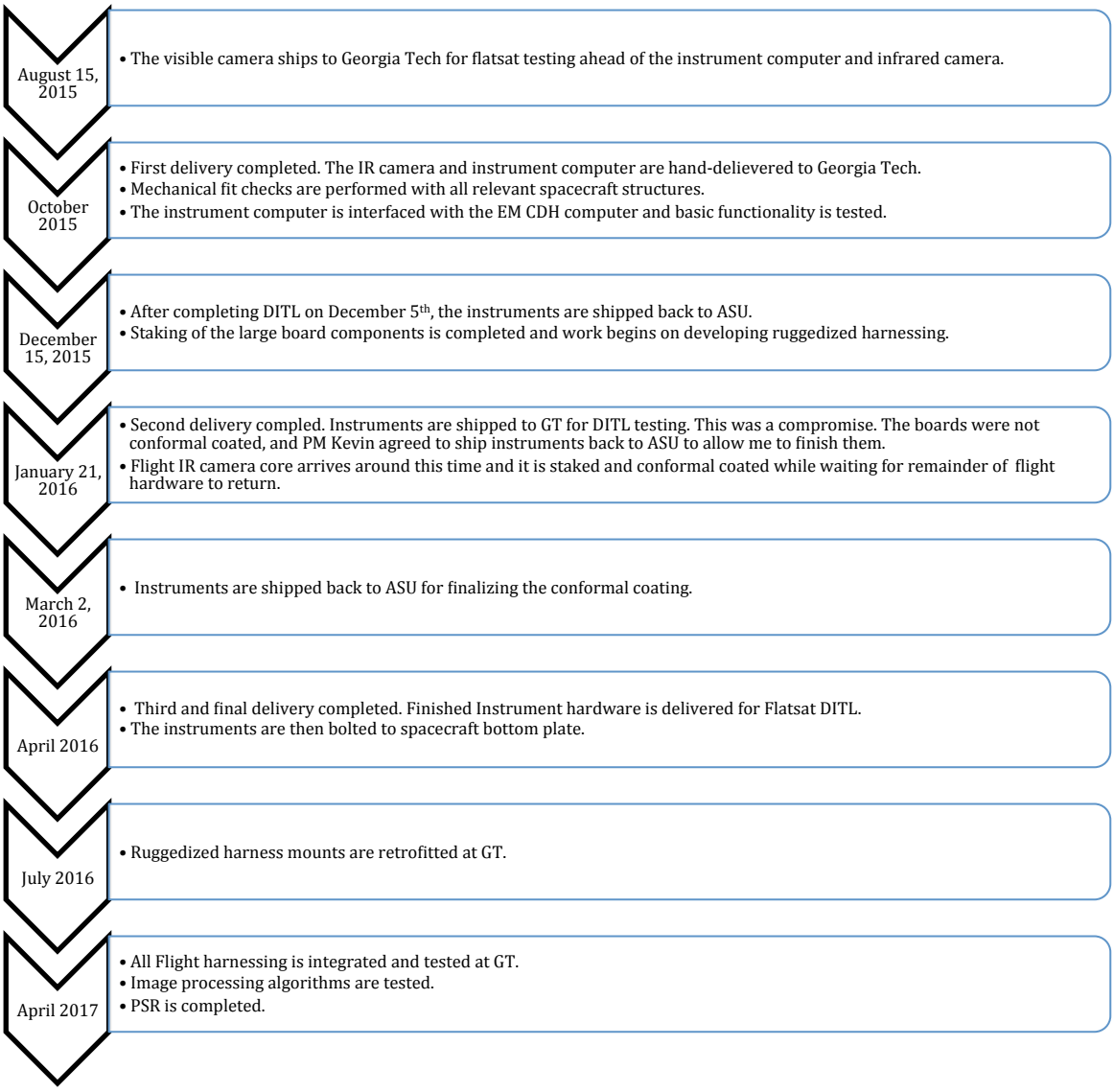


*Figure 116*. Timeline of major events during spacecraft integration and testing.

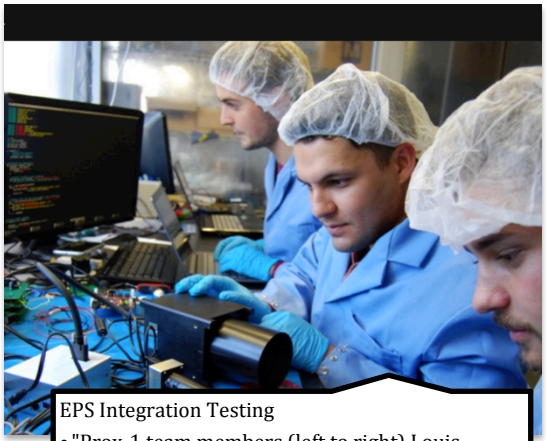

EPS Integration Testing

- "Prox-1 team members (left to right) Louis Williams, Mike Veto, and Jack Bush test out imaging instruments that will will be used for navigation during automated proximity operations relative to the LightSail spacecraft."--Planetary Society

CDH & FSW Integration Testing

- The Flight Software executes scripts to connect to the instrument computer via the CDH computer, then capture images, and copy them over from INS to CDH.

STR Inegration Testing

- Structures lead Kyle Scott leads mechanical fit check of the instruments.

*Figure 117*. Initial Instrument Delivery

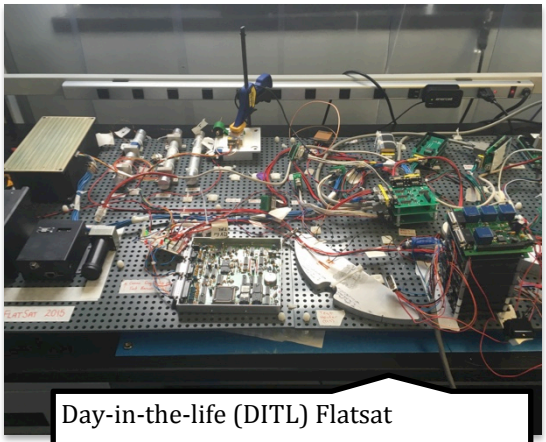

Day-in-the-life (DITL) Flatsat

- All components of the spacecraft verifiy integration of electrical and electronic systems prior to mechanical integration. The instruments passed.

Mechanical Integration Begins

- The visible camera (shown), then the infrared camera and the instrumetn computer (not shown) are handed over to Swapnil Pujari.

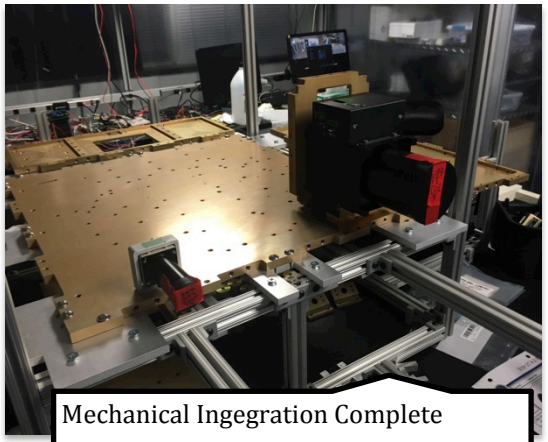

Mechanical Ingegration Complete

- All THESIS subsystems are mechanically integrated to the spacecraft bottom plate.



*Figure 118*. The final official delivery of the THESIS major hardware components.

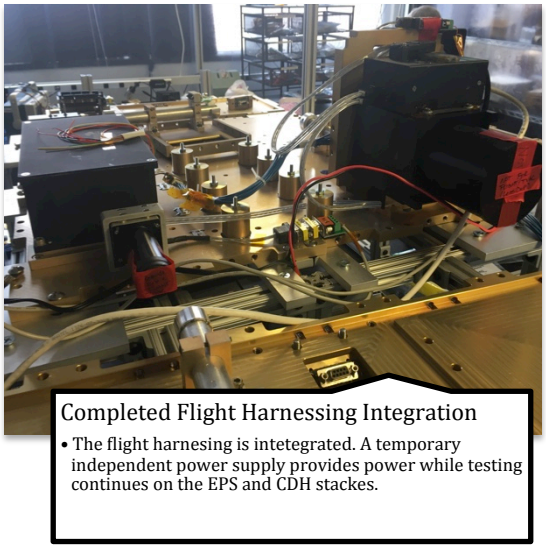

**Completed Flight Harnessing Integration**

- The flight harnesing is intetegrated. A temporary independent power supply provides power while testing continues on the EPS and CDH stackes.

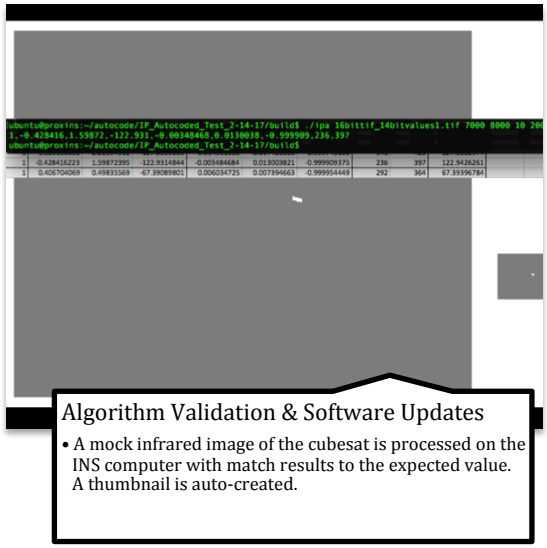

**Algorithm Validation & Software Updates**

- A mock infrared image of the cubesat is processed on the INS computer with match results to the expected value. A thumbnail is auto-created.

**Preship Review (PSR)**

- The final review with AFRL to prepare the spacecraft for shipment to Kirtland Airforce Base resulting in a conditional pass.

*Figure 119*. Final instrument preparations for PSR.

## SPACECRAFT ENVIRONMENT TESTING

### Overview

The UNP program provides a scaled mission assurance architecture to make sure that the spacecraft will be successful. The “No Harm” assurance are required to be completed prior to integration with the launch vehicle. The tests ensure that the spacecraft will not cause harm to the launch vehicle or to other spacecraft onboard. The nominal assurance consists of the previous tests and a TVAC test that simulate the space environment in order to verify that the spacecraft subsystems successfully survive and operate at their required thermal regimes. Enhanced assurance testing was performed in order to validate the performance of mission specific objectives or verify specific requirements. Finally, there was the possibility of additional tests to be required for mission assurance in special cases.

### “No Harm” Assurance

#### Bakeout

The spacecraft was baked out in order to ensure that all of the volatiles from the spacecraft are outgassed as to not interfere with other spacecraft of the launch vehicle. The spacecraft was placed in a bakeout chamber and heated to its highest survival temperature with a vacuum applied to $10^{-6}$ torr. For UNP, the spacecraft was held here until the launch vehicle requirements are met. For THESIS, as previously mention, all subsystem components are baked in a bakeout chamber am ambient pressure before subsystem integration.

#### Vibration Testing

A random vibration test was conducted in order to ensure that all of the components of the spacecraft are securely fastened to the spacecraft structure and that

the structure will not break from launch loads. Any broken parts could damage other payloads in the launch vehicle or the launch vehicle itself.

The vibration testing consists of three test phases—one for each axis. After a full functional test, a sine sweep was performed to characterize the modes of the spacecraft in a specific axis. Then the spacecraft was subjected to random vibrations. A second sine sweep was then performed to confirm that none of the modes changed during random vibration due to failures. Any amplitudes greater than 20% or frequency shifts greater than 10% indicate a failure. Failures may be audible as well during the testing. An abbreviated functional test was then performed and the spacecraft was inspected for any visible failures. The process was repeated in the remaining two axes. Then a final full functional test was performed.

**Nominal Assurance**

**Thermo-Vacuum (TVAC) testing**

This test ensures that the spacecraft will survive the temperatures and pressures of space via a chamber cooled with liquid nitrogen and pumped down to a vacuum. For UNP, the TVAC testing was done in two phases. A thermocycle in nitrogen test consists of three cycles of testing to the minimum and maximum temperatures expected with 5 degreed C of extended margin. The spacecraft was tested at these extremes with an abbreviated functional test. At the conclusion of the test, the bakeout was performed as previously detailed.

After the bakeout, the thermocycling in vacuum was performed. This test was very similar to the previous TVAC test except that a vacuum was applied.

For THESIS, the infrared camera, visible camera, and instrument computer all have internal temperature sensors on their boards that monitor their temperature. In addition, temperature control will be provided via the thermal control system (TCS) of

the spacecraft via thermocouples and heater pads. This system will keep the instruments safe in the relatively cold regime. Heat from the electronics boards was conducted to the spacecraft structure during this test. Finally, the mylar space blankets produced by the GT spacecraft team will be mounted onto the spacecraft and instrument to assist with controlling the temperature of the instruments.

Of critical importance during TVAC testing, was to verify that the optics do not collect any outgassed volatiles or condensation during the testing.

**Enhanced Assurance**

**Mission Specific Testing**

Sometimes testing specific to the mission and spacecraft are required. For *Prox-1*, the CG and MOI are required to be characterized at AFRL. This was a characterization not a test, so there was no PASS/FAIL.

For THESIS, there are two mission specific tests that are desired for during environmental testing. First, it was desired that images be acquired at long distances after vibration testing to ensure that the instruments have maintained their focus. Second, it was desired that the infrared camera undergoes a radiometric calibration during TVAC. Leading up to PSR, the feasibility of these desired tests was in doubt, so the backup plan was to verify these requirements in-flight with images conducted after the checkout phase but before proximity operations. While testing on the ground may help to identify problems, the likelihood of these problems was low, and the true performance of the instruments in orbit—combining the radiometric performance in the space environment and the resolution performance of a distant target—can only be achieved in space or highly specialized and resource intensive ground experiment.

There may be other mission specific testing required for the remainder of the Prox-1 spacecraft.

### Additional Mission Assurance

Additional testing was possible as needed in order to satisfy requirements of other customers or investors. For UNP, a lightband drop test was typically performed in order to verify that the spacecraft separation mechanism from the launch vehicle successfully operates and that the spacecraft obeys the RF silence rule. For *Prox-1*, this may involve testing the Planetary Society's *LightSail-B*.

## RISK ANALYSIS

### Overview

Several risks were identified that were either mitigated or remain outstanding. Accepting risks was inherit to a student satellite project that must carefully manage the resources of time and funding while learning the process and developing experience.

**Lens Vibrates Out of Focus**

It was possible that either of the cameras could vibrate out of focus during vibration testing or during launch. A fixed-focus infrared lens was purchased in order to simply the design. The visible camera lens has set screws that are torqued and staked in place. An in-flight resolution test of both cameras will be conducted in-orbit to check the lens focus. If the lens focus shifts, then the full mission success requirements would not be accomplished, but it may be possible to still use the image processing algorithms to conduct proximity operations with reduced accuracy.

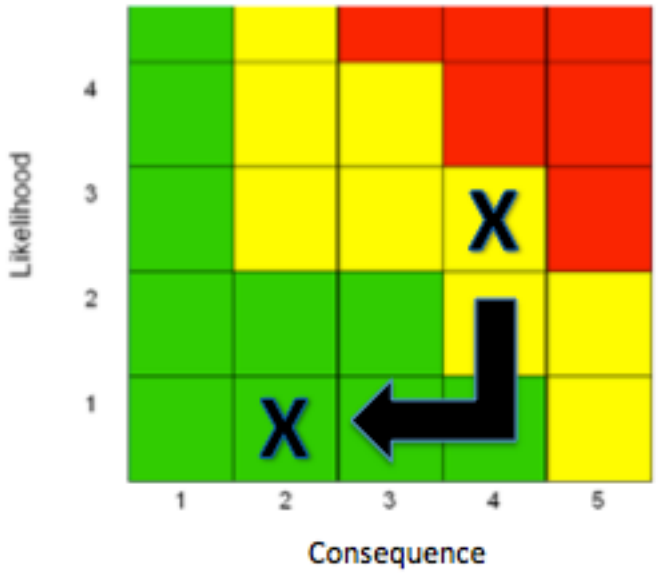


*Figure 120*. Risk of lens vibration out of focus.

**Outgassing onto Optics**

Outgassing of materials in vacuum may accumulate on the lens and cause degredation of the camera performance. In order to mitigate this risk, all materials are verified with the Goddard low outgassing website to make sure that the TML% was <1% and CVCM% was <0.1%. Additionally, all components are baked out to ensure that the volatile materials are removed prior to subsystem integration. The integrated instruments are baked out prior to spacecraft delivery. And the spacecraft was planned to bake out as well.

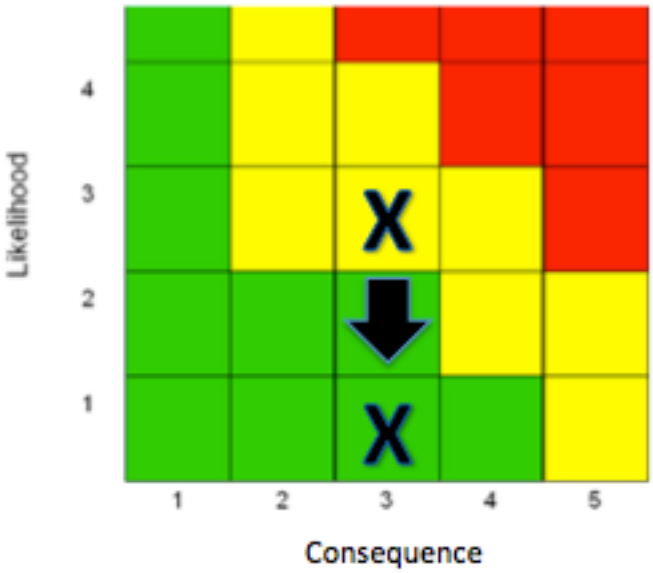


*Figure 121*. Risk of outgassing onto optics.

**Water vapor freezing on optics**

Any water vapor present in the infrared or visible camera may freeze onto the optics at low temperatures. To help mitigate this, the instruments were baked out. However, the only way to verify that the water vapor was properly evacuated was to conduct a TVAC test. This was still an open concern.

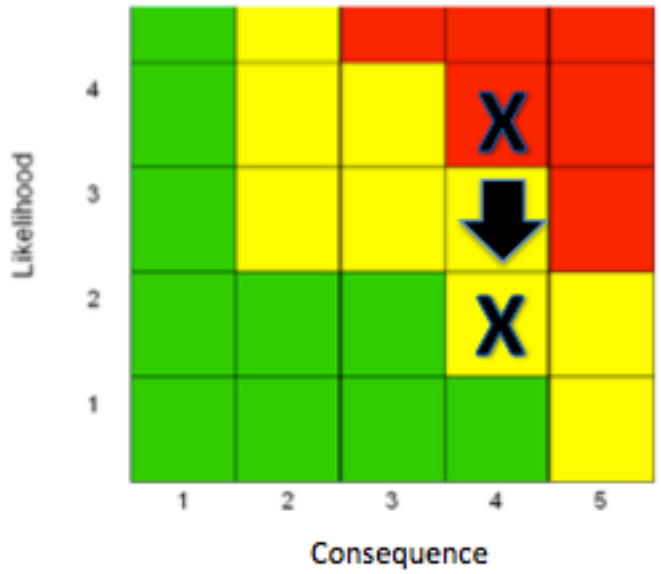


*Figure 122*. Risk of water vapor freezing onto optics.

**Ground loops**

Ground loops may interfere with proper data communication and functionality. The infrared camera and the visible camera boards were successfully isolated from their structures. However, the instrument computer was not successfully separated from the structure ground. It was currently unknown if the consequence will be significant, so this was still an open concern.

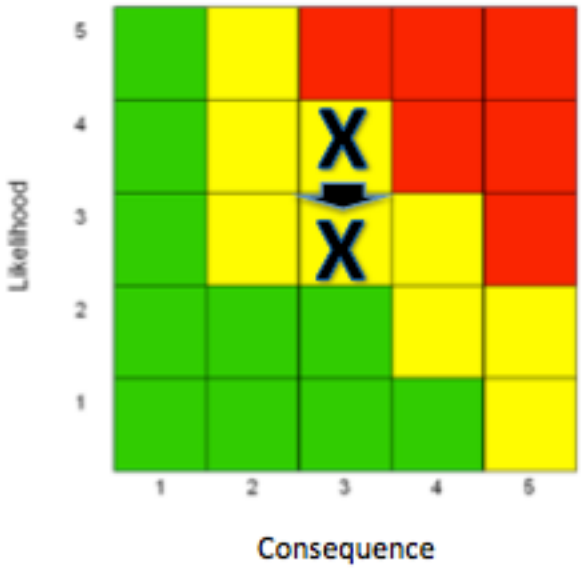


*Figure 123*. Risk of ground-loop

**Camera link driver update**

It appears that when the instrument computer automatically updated the linux kernel, the camera link driver stops working. There were many times when the driver had to be reloaded during testing. It was determined that turning off automatic updates seemed to fix this issue. A sequence of commands was created in a shell script that can be run in case of emergency to reinstall the driver. This should not occur during the mission as there will be no internet connection. Since turning off automatic updates, the issue has not occurred. Because it was possible, though unlikely, that this issue arrises from a different or additional cause, there was still some likelihood.

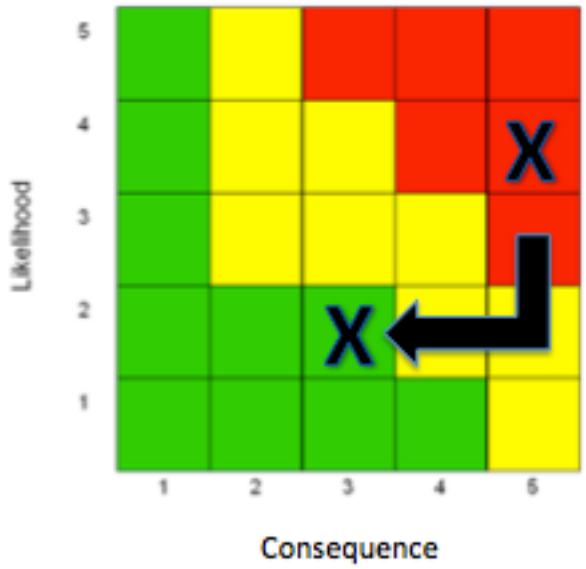


*Figure 124*. Risk of pixci driver fails.

**Images fill SD card**

It was possible that imaging could fill the SD card completely. To mitigate this, a watchdog script was created that counts deletes images.

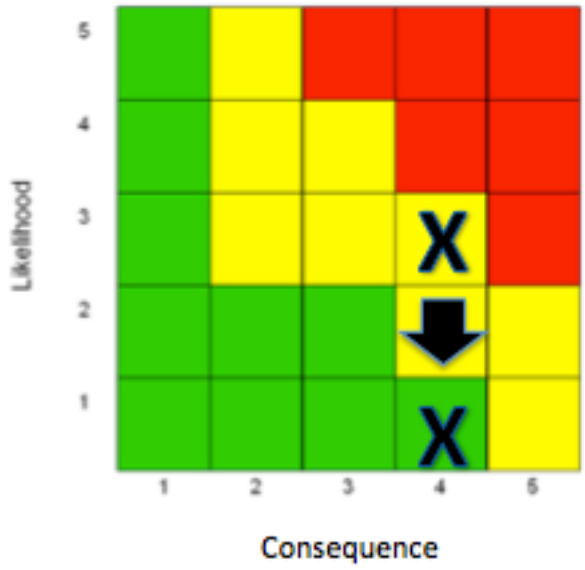


*Figure 125*. Risk of images filling SD card.

**SD card errors**

At some point, the SD card will likely start to have read/write errors. Because the operating system was on the SD card, this could prove fatal for the instrument computer. The EM has logged hundreds of hours and errors have not developed yet. Thus it was unlikely that this will be an issue during the nominal mission. It will probably happen eventually. The issue could be further mitigated by using a high performance SD card such as a Delkin. However, there was not enough resources available to accomplish this in time.

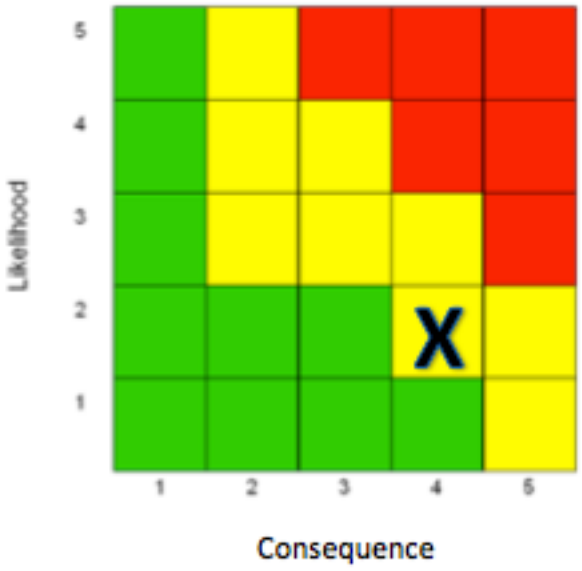


*Figure 126*. Risk of sd card errors

**Risk of manual and automatic image command overlap**

During testing, it was noticed that sometimes the manual imaging command happens to coincide with the automatic telemetry imaging. This may have adverse affects as a faulty image was generated. This risk can probably be mitigated by incorporating an image verification algorithm before sending the image into the navigation algorithms. This has not yet been done.

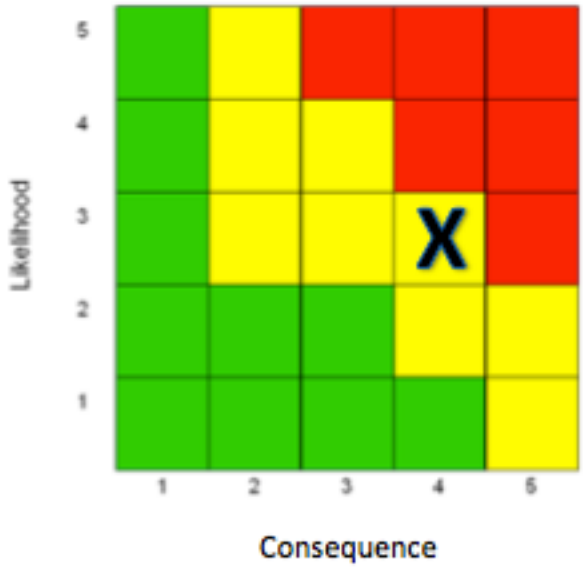


*Figure 127.* Risk of automatic and manual image overlap.

**CMOS setting turned off for IR camera**

In order to acquire T-linearized data, the CMOS setting on the IR camera must be turned ON. It was possible that this setting can be turned OFF. This requires a reboot. Attempts to create a switch for this in the software have been unsuccessful, and the only way to reactivate the CMOS setting at present was with the GUI on a lab workstation. Because of this, it was important that this feature was activated and remains activated. Furthermore, none of the imaging commands should attempt to alter this setting.

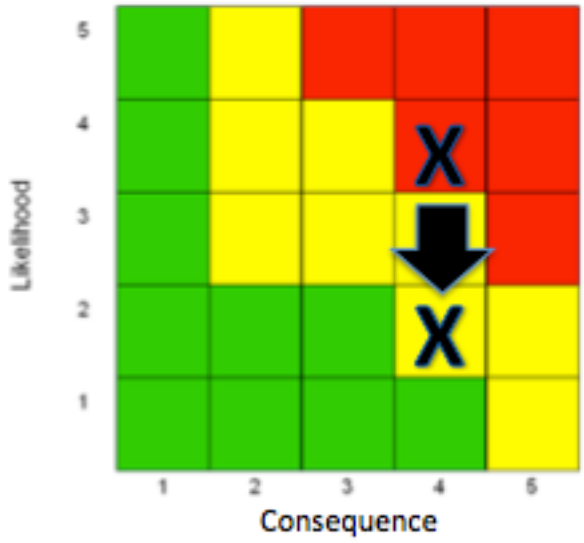


*Figure 128*. Risk of CMOS deactivation.

**Risk of Personnel**

It was difficult to accurately capture the risk associated with personnel for a student project. In order for THESIS to be successfully delivered, help from other graduate students was required and the duration of this PhD was significantly extended. For *Prox-1*, undergraduate turnover was a significant issue to combat, and THESIS development had to adjust to new personnel on the various subsystems throughout the mission development.

**Risk of Cost Growth**

THESIS was fortunate to have been funded through the Infrared Instrument Laboratory at ASU. However the original cost estimates of the instrument, because more time was required of the graduate students than expected. Cost was in-part mitigated by working side-by-side with IRIL to acquire mentorship, to share laboratory space, and to borrow tools. For student satellite programs in general, that tout low-cost, lack of funding was a significant and detrimental risk.

**Risk of Schedule**

THESIS was originally planned for launch on *Prox-1* on the Falcon Heavy in 2015. The slippage of the rocket provided two extra years of development time for THESIS to be delivered on schedule with the spacecraft. In order to further mitigate the risk of missing the delivery deadline, some of the desired baseline radiometric and environmental testing was descoped to be completed either with the spacecraft or in-flight. Furthermore, graduate students worked over-time to guarantee delivery. For the Pre-ship Review, THESIS was integrated to *Prox-1* and ready to be delivered the Air Force Research Laboratory.

## PROGRAM MANAGEMENT

Management of THESIS, by the author, consisted primarily of managing the schedule and soliciting for personnel to help as needed to maintain the schedule, maximize performance, and reduce risk. The THESIS schedule was negotiated with the project PM and the instrument schedule was maintained with a Gantt chart of all of the action items and major milestones. The chart was not included here. Funding for THESIS was secured by advisor Phil Christensen and accounts were managed by Tara Fisher. Travel and procurement was managed by Ashley Toland. Clean laboratories were managed by Bill O'Donnel and Heather Bowles. Rob Woodward assisted with risk management. Various mentors from IRIL provided expert opinions and guidance on their subject matter. Graduate students Amber Keske and Andy Ryan provided analysis and testing facilities to ensure a functional, characterized THESIS was delivered on-time.

## BUDGET

This section intentionally omitted.

## OUTSTANDING TASKS AND FUTURE WORK

### Overview

A variety of tasks are documented for future work that were either not completed at instrument integration with the spacecraft or were descoped to be completed later.

### Retrofit insulated standoffs

Insulated standoffs could be implemented to isolate the instrument computer from the instrument computer case which may cause ground loops.

### Calibration

Verification of the radiometric performance in as simulated space environment has been descoped to the threshold in-flight calibration. The resolution of the imagers

was planned to be verified in-flight after the launch event. Should funding and the opportunity arise, THESIS could undergo a dedicated environmental testing campaign.

**Environmental Testing**

All environmental testing was set to be completed at the spacecraft level. This includes the nominal TVAC and vibration. The lens should be monitored for condensation during TVAC.

**Software**

There were only a few items that could be included in the software. While, the power system can perform a hard reset of the cameras via power cycling, it could be useful to perform a soft power reset in software from the instrument computer. The

Automatic updates of the linux kernel tended to require that the pixci driver be reinstalled. After turning off automatic updates, the necessity to reinstall the driver seemed to be mitigated. Checking the driver was currently implemented in a rather brute force method of capturing an image and determining if the image capture worked. With more effort it may be possible to create a softer method of checking the driver status.

There are currently no watchdogs implemented on the instrument computer to check for errors on the cameras or the computer itself. The current plan was to simply power cycle the cameras or computer if there was an issue. A fault-protection watchdog system could be implemented.

Finally, the dmesg logs could be saved for ease of downloading to troubleshoot problems.

**Flight preparations**

The script ./SYNC_DATE must be updated to the IP address of the CDH computer and tested to make sure this works before flight.

## TECHNOLOGY READINESS LEVEL (TRL)

### Current state of TRL

The delivered THESIS instrument system was at a TRL 5. The project began at a TRL 4 with basic integration of components. Now, the components are integrated with "high-fidelity" in a clean lab, and the integrated system has logged hundreds of hours of test operations. The instruments were briefly tested in a low-fidelity TVAC chamber for functional testing in a simulated environment.

### Path to level-up

In order to reach a TRL-6, THESIS would require testing in a high-fidelity environmental testing. This was planned to take place at the AFRL. If *Prox-1* launched into the space environment, then successful demonstration would promote THESIS to a TRL-7.

## OUTREACH

Much of THESIS was built and tested in the Class 100K cleanroom on the 1st floor of ASU's Interdisciplinary Science and Technology Building 4 (ISTB4). This project was observed by thousands of children, college students, and the taxpaying public.

This project was also the subject of a TEDx: Maricopa talk entitled "Launching an Instrument into Space: Inspiration, Investigation, and Implementation" that was publicly available online.

## CONCLUSIONS

An infrared camera, visible camera, and instrument computer were designed as an instrument system called THESIS for the *Prox-1* microsat mission. THESIS has a mass of ~2kg and consumes 7W of power. Commercial components were modified and integrated into a functional system that was ready for spacecraft integration and environmental testing. Major innovations include designing a method for pulling high

speed camera link images from an infrared camera, developing custom ruggedized harnessing mounts onto standard connector receptacles, developing a mechanical instrument integration standard using the cubesat form factor, developing a distributed instrument power scheme with custom harnessing, and developing a distributed instrument computer scheme that interfaces to a flight computer over linux secure shells.

THESIS was completed as a systems engineering exercise. It was a highly iterative process that converges upon a solution. Cost, schedule, and risk are managed in an attempt to maximize performance to a baseline design. As the design matured some of the design requirements are descoped in order to deliver an instrument system on schedule that will meet the mission objectives. Unfortunately, the costs of *Prox-1* became too great and the schedule expired without completion. *Prox-1* was cancelled and THESIS was returned to ASU for safe storage. This serves a lesson that a mission must be well-defined in terms of what performance was expected within the available cost, schedule, and acceptable risk. It was common for engineering projects to become overly ambitious, and the best engineers understand what goals and objectives are good enough to attempt within the scope of available resources.

## FUNDING INFORMATION

This project was supported through the Mars Space Flight Facility at the School of Earth and Space Exploration at Arizona State University and the University Nanosat Program through the Air Force Research Lab.

# CHAPTER 6

# CONCLUSIONS AND FUTURE PLANS

Each chapter was addressed, then synthesis was drawn.

## Parabolic Thermal Inertia

A thermal inertia derivation was successfully reproduced for this project and analogies were successfully drawn that make this somewhat esoteric property easier to understand. The derivation can be sourced for students and scientists that are curious about the raw mathematics. In addition, the alternative definition, thermal effusivity, was presented as a more consistent with thermal diffusivity. Once planetary scientists are aware of thermal effusivity, the floodgates will open. Effusivity was widely studied parameter in chemistry and the textile industry. Many powders, lithics, and layered materials have been studied in these industries already, and that knowledge can be assimilated into planetary science. Finally, the diffusivity analogy framework may be extended to define other effusivity-type terms. Other fields may find this measurement useful for quantifying a process with an oscillating forcing function, conduction, and capacitance. The plan was to submit this chapter to either JGR-Planets or the Journal of Heat Transfer after my defense. A condensed paper could be submitted to science for its broad appeal.

## Hyperbolic Thermal Inertia

Using the analogies from the previous chapter and a curiosity that thermal inertia seems different than the mechanical inertia (mass), research was conducted to determine if there truly was a thermal equivalent to mass or electrical inductance. The literature was vast on hyperbolic heat conduction, but it still seems largely hypothetical as analytical derivations are inconsistently supported with experimental results. It was of chief interest that Maxwell seemed to have described this term long ago and Fourier's

Law was an empirical approximation of heat conduction. Even more interesting was the implications that heat conduction theoretically cannot be a parabolic equation, as this would imply that conduction, molecular vibration, travels infinitely faster than the speed of light. Conduction must be described by a wave equation, even if thermal inductance is almost zero. This begs the question what physically is happening during conduction. Is conductivity the efficiency of transferring heat from one molecule to the next and inductance/inertia related to the actual mass of the molecule? This may only be able to be observed in exotic circumstances that involve large distances, cold temperatures, high frequency heat sources, and gases. The heating of an exoplanet surface by a pulsar planet seems to be a reasonable candidate. Such heating may result in highly anomalous heating. Far beyond the scope of this PhD, galaxies themselves may be laboratories for testing thermal inductance and hyperbolic heat transfer. The exotic applications of this project warrant dedicated further study, but the work completed here is planned to be submitted for publication.

**The Long-Far Infrared Camera for Planetary Exploration**

An instrument response function was produced that indicated extended spectral performance for microbolometer arrays to wavelengths longer than 12μm.

Using a filter method, significant out-of-band leakage through the harmonic wings of the filters initially produced problematic results. The addition of a 30μm long pass filter helped block much of the unwanted signal, however further long pass filters are required to continue the investigation in this method.

Using an interferometer method, interferograms were captured with the microbolometer array and images of the bull's-eye pattern were captured. Interferograms were processed into spectra and an instrument response function was produced. The final instrument response function produced in this dissertation shows

peak response continues out to ~500 $cm^{-1}$/~20 μm. The response then begins to decrease to ~25% at ~285 $cm^{-1}$/~35 μm. Thermal instability of the detector was a likely source of error that inhibits the confident analysis of the IRF beyond 35 μm. This warrants further investigation. This may be the first time a diamond interferometer was interfaced with a diamond microbolometer array in order to produce an imaging interferometer at far infrared wavelengths. The characteristic proof of concept matures the PIDDP proposal from a TRL-2 to a TRL-3. These prototype results were completed for this dissertation and contributed to the E-THEMIS proposal for the *Europa Clipper*. Further refinement of higher-fidelity detectors and laboratory experiments is now being accomplished at the professional level to further refine the characterization and mature the technology to a TRL-4. When completed, it is possible that the E-THEMIS camera will detect plumes on Europa that will guide the mission to further investigate for clues life on another world.

**Thermal-camera for Exploration, Science, and Imaging Spacecraft**

The threshold design for THESIS was completed, delivered to Georgia Tech, and integrated to the *Prox*-1 spacecraft. This raised THESIS from the TRL-4 infrared camera concept developed for my undergraduate honor's thesis to a TRL-5 high-fidelity system that is ready for environmental testing. These environmental tests will promote THESIS to TRL-6. The project was an opportunity to practice systems engineering and instrument design with a separate mission team, and an oversight customer—much the way that space missions are conducted. Some of the desired baseline instrument requirements were completed as well that improve the design, but are not needed for minimum mission success. These had to be descoped in order to ensure that the instruments were completed on schedule in order to avoid cancellation. Besides the overall systems engineering exercise, significant innovations were produced. These

include a method for independent power distribution, a method for ruggedizing COTS harness receptacles, a method for interfacing a distributed computer on a smallsat, a method for using camera link on a smallsat, and the use of the cubesat standard for the payload structure.

Ultimately, the project was not completed on schedule, and the mission was cancelled. THESIS was de-integrated and was on-purge in the ASU 100K clean room awaiting to be environmental tested, which would promote the system to TRL-6. This is something that I desired to accomplish. Keeping in mind that a dissertation is somewhat of a mission, further work on THESIS is not a requirement for this PhD, and it will have to wait for the future when new resources may be available.

THESIS could also be integrated onto a spacecraft and flown if an announcement of opportunity arises. The Air Force explicitly has a vested interested in autonomous proximity operations in space. There are a variety of projects in the newspace community that are attempting to do similarly integrate infrared instruments onto smallsats. THESIS could be integrated as non-essential student payload onto a larger mission. THESIS could be proposed for aerial balloon or UAV missions. In the long run, though not stated yet, NASA may require infrared-based navigation and rendezvous of small spacecraft for the in-orbit capture of the sample canister from the surface of Mars between the Mars Ascent Vehicle (MAV) and the Mars Sample Return Orbiter (MSRO). It is useful to continue to pursue this project. One way or another I hope to get this hardware into space someday after graduating.

**Synthesis**

And so this 8 year mission comes to a close. This PhD was an attempt to study the science, to help invent new technologies, to engineer new systems, and to develop new mathematics to explore the solar system through the wavelengths of the thermal

infrared. Much of this journey is not written here. Numerous exercises, field campaigns, and half finished projects, are not included, but served to enhance the PhD experience. My oral exam projects investigating cold craters and explosive volcanism are still much a work in progress that I intend to return to when there is free time available. They were not up to standard, so they were descoped, but be on the lookout. I have included two chapters on the mathematics of thermal inertia that serve as the foundation for understanding heat transfer on a planetary surface. I intend to publish this work over the next year or so, because I truly believe it to be valuable for students to understand the fundamentals. By continuing to dive deeper and continuing to ask questions, I could only arrive at a set of hypothetical applications—though I believe they may be tantalizing if true. There is much work to be done, and I have more ideas that are formulating. Perhaps, experiments will be needed using enhanced infrared detectors to measure thermal inductance.

In this PhD I learned how to conduct experiments in the lab to investigate the performance of the long-far wavelength infrared microbolometer array. The results of this prototype will be used for detailed development of a future flagship mission to Europa. Perhaps, this project will directly influence the discovery of a life on another world someday. Future experiments can certainly refine the results I obtained in order to develop a powerful instrument. Applications that are not even thought of here may exist. Perhaps, these detectors will even be standard for future smallsat missions in space.

The experience on the THESIS instrument system was invaluable for learning how to deliver flight hardware. The experimental laboratory, at a low TRL, is much different than preparing mid to high TRL flight hardware in a clean laboratory. Now, more than ever, students are gaining hands-on experience at the universities by developing low-cost missions with COTS components. These COTS components need

only be modified for experimental space missions that can inherit risk. THESIS is part of a greater movement to develop systems that may not be as reliable or have as much performance needed for detailed investigations, but they can be used for cheap reconnaissance in plentiful. Cheap missions provide the opportunity to create networks of continuous and relatively uninterrupted reconnaissance. And maybe this will be the next paradigm: to help monitor the Earth for disasters and to continue to catalogue the exoplanets with swarms. As another example, while we need Mars Sample Return to unlock key questions about Mars and to prove that we can 'go there and back again', there are so many places on Mars that simply need cheap in-situ reconnaissance. Perhaps, the next saga of exploration will be when we can create a synthesis of hundreds of reconnaissance scouts with an even more strategically targeted heavy flagship mission: a dozen simultaneous MERs scouting ahead for a couple MSRs on the way.

Certainly, the most important part has been the people. The casual conversations, conferences, field expeditions, and happy hours are some of the most rewarding parts of doing research at ASU-SESE and the Mars Space Flight Facility. In the midst of making deadlines, troubleshooting hardware, and entertaining our egos, we must not lose track of making time to enjoy our precious little amount of time in this world with friends and family to explore the great unknown together.

The future is bright and exciting if we are willing to innovate, take risk, fail, try again, and strive for positive impact on the scientific and engineering fields, students, and our communities.

REFERENCES

Ackerman, C. C., Bertman, B., Fairbank, H. A., & Guyer, R. A. (1966). Second sound in solid helium. Physical Review Letters.

Audouard, J., Poulet, F., Vincendon, M., Bibring, J. P., Forget, F., Langevin, Y., & Gondet, B. (2014). Mars surface thermal inertia and heterogeneities from OMEGA/MEX. *Icarus*, 1–40. http://doi.org/10.1016/j.icarus.2014.01.045

Baumeister, K. J., & Hamill, T. D. (1969). Hyperbolic heat-conduction equation—a solution for the semi-infinite body problem. *Journal of Heat Transfer*, *91*(4), 543–548.

Bell, J. F., III, Joseph, J., Sohl-Dickstein, J. N., Arneson, H. M., Johnson, M. J., Lemmon, M. T., & Savransky, D. (2006). In-flight calibration and performance of the Mars Exploration Rover Panoramic Camera (Pancam) instruments. *Journal of Geophysical Research-Planets*, *111*(E2), n/a–n/a. http://doi.org/10.1029/2005JE002444

Bell, J. I. (2008). The Martian Surface - Composition, Mineralogy, and Physical Properties. *The Martian Surface - Composition, Mineralogy, and Physical Properties*, *-1*.

Bender, M. L., Callaway, P. W., Chase, S. C., Moore, G. F., & Ruiz, R. D. (1974). Infrared Radiometer for the Pioneer 10 and 11 Missions to Jupiter. *Applied Optics*, *13*(11), 2623–2628. http://doi.org/10.1364/AO.13.002623

Black, Joseph. (1786) “Lectures in Chemistry” (Unpublished)

Bosworth, R. C. L. (1946). Thermal Inductance. *Nature*, *158*(4009), 309–309. http://doi.org/10.1038/158309b0

Bouwer, H. (1967). Analyzing subsurface flow systems with electric analogs. *Water Resources Research*, *3*(3), 897–907. http://doi.org/10.1029/JZ068i020p05725

Carslaw, H. S., & Jaeger, J. C. (1959). Conduction of heat in solids. *Oxford: Clarendon Press, 1959, 2nd Ed.*, *1*.

Carslaw, H. S., & Jaeger, J. C. (1965). Conduction of Heat in Solids, By H.S. Carslaw and J.C. Jaeger.

Carslaw, H. S., & Jaeger, J. J. C. (1986). CONDUCTION OF HEAT IN SOLIDS. 2nde edition, Edition anglaise. Oxford University Press.

Cattaneo, C. (1958). A form of heat conduction equation which eliminates the paradox of instantaneous propagation. *Compte Rendus*, *247*(4), 431–433.

Chase, S. C. (1969). Infrared Radiometer for the 1969 Mariner Mission to Mars. *Applied Optics*, *8*(3), 639. http://doi.org/10.1364/AO.8.000639

Chase, S. C., & Kaplan, L. D. (1963). The Mariner 2 infrared radiometer experiment.

*Journal of Geophysical ….*

Chase, S. C., Hatzenbeler, H., Kieffer, H. H., Miner, E., Münch, G., & Neugebauer, G. (1972). Infrared Radiometry Experiment on Mariner 9. *Science*, *175*(4019), 308–309. http://doi.org/10.1126/science.175.4019.308

Chase, S. C., Miner, E. D., Morrison, D., & Münch, G. (1976). Mariner 10 infrared radiometer results: Temperatures and thermal properties of the surface of Mercury. *Icarus*.

Chase, S. C., Ruiz, R. D., Münch, G., & Neugebauer, G. (1974). Pioneer 10 infrared radiometer experiment: Preliminary results. ….

Chester, M. (1963). Second sound in solids. *Physical Review*, *131*(5), 2013.

Christensen, P. R., Anderson, D. L., Chase, S. C., Clark, R. N., Kieffer, H. H., Malin, M. C., et al. (1992). Thermal emission spectrometer experiment: Mars Observer mission. *Journal of Geophysical Research: Planets (1991–2012)*, *97*(E5), 7719–7734. http://doi.org/10.1029/92JE00453

Christensen, P. R., Bandfield, J. L., Hamilton, V. E., Ruff, S. W., Kieffer, H. H., Titus, T. N., et al. (2001). Mars Global Surveyor Thermal Emission Spectrometer experiment: Investigation description and surface science results. *Journal of Geophysical Research: Planets (1991–2012)*, *106*(E10), 23823–23871. http://doi.org/10.1029/2000JE001370

Christensen, P. R., Hamilton, V. E., Mehall, G. L., Pelham, D., O'Donnell, W., Anwar, S., et al. (2017). The OSIRIS-REx Thermal Emission Spectrometer (OTES) Instrument. *arXiv Preprint arXiv:1704.02390*.

Christensen, P. R., Jakosky, B. M., Kieffer, H. H., Malin, M. C., Jr, H. Y. M., Nealson, K., et al. (2004). 2001 Mars Odyssey. (C. T. Russell, Ed.)*2001 Mars …* (pp. 85–130). Dordrecht: Springer Netherlands. http://doi.org/10.1007/978-0-306-48600-5_3

Christensen, P. R., Mehall, G. L., Silverman, S. H., Anwar, S., Cannon, G., Gorelick, N., et al. (2003). Miniature Thermal Emission Spectrometer for the Mars Exploration Rovers. *Journal of Geophysical Research: Planets (1991–2012)*, *108*(E12). http://doi.org/10.1029/2003JE002117

de Breteuil, G.-É. L. T., & de Mairan, J.-J. D. (1744). Dissertation sur la nature et la propagation du feu.

Edwards, C. S., Nowicki, K. J., Christensen, P. R., Hill, J., Gorelick, N., & Murray, K. (2011). Mosaicking of global planetary image datasets: 1. Techniques and data processing for Thermal Emission Imaging System (THEMIS) multi-spectral data. *Journal of Geophysical Research*, *116*(E10), E10008. http://doi.org/10.1029/2010JE003755

Epstein, P. R. (1992). Cholera and the environment: an introduction to climate change. *PSR Quarterly*, *2*, 146–160.

Epstein, P. S. (1929). What is the Moon made of. *Phys. Rev*, *33*, 269.

Fergason, R. L., Christensen, P. R., & Kieffer, H. H. (2006a). High-resolution thermal inertia derived from the Thermal Emission Imaging System (THEMIS): Thermal model and applications. *Journal of Geophysical Research*, *111*(E12), E12004. http://doi.org/10.1029/2006JE002735

Fergason, R. L., Christensen, P. R., Bell, J. F., III, Golombek, M. P., Herkenhoff, K. E., & Kieffer, H. H. (2006b). Physical properties of the Mars Exploration Rover landing sites as inferred from Mini-TES–derived thermal inertia. *Journal of Geophysical Research*, *111*(E2), E02S21. http://doi.org/10.1029/2005JE002583

Fetter, C. W. (2001). Applied hydrogeology. 4th. *Supplemental Website Http://Www. Appliedhydrogeology. Info. Upper Saddle River, NJ: Prentice Hall*, 598.

Field, J. E. (1992). The Properties of Natural and Synthetic Diamond.

Formisano, V., Angrilli, F., Arnold, G., & Atreya, S. (2006). The planetary fourier spectrometer (PFS) onboard the European Venus Express mission. *Planetary and Space ….*

Formisano, V., Grassi, D., Ignatiev, N., Zasova, L., & Maturilli, A. (2002). PFS for Mars Express: A new approach to study Martian atmosphere. *Advances in Space Research*, *29*(2), 131–142. http://doi.org/10.1016/S0273-1177(01)00562-2

Formisano, V., Moroz, V. I., Hirsch, H., Orleanski, P., Michel, G., Lopez-Moreno, J., et al. (1996). Infrared spectrometer PFS for the Mars 94 orbiter. *Advances in Space Research*, *17*(12), 61–64. http://doi.org/10.1016/0273-1177(95)00759-8

Fourier Joseph, J. B. (1822). Théorie Analytique de la Chaleur (pp. 561-562). *Paris: Chez Firmin Didot, Père Et Fils.[Links]*.

Franssila, M. (1936). Mikroklimatische untersuchungen des warmehaushalts.

Fukuhara, T., Taguchi, M., Imamura, T., & Nakamura, M. (2011). LIR: Longwave infrared camera onboard the Venus orbiter Akatsuki. *Earth*.

Golombek, M. P., Arvidson, R. E., Bell, J. F., Christensen, P. R., Crisp, J. A., Crumpler, L. S., et al. (2005). Assessment of Mars Exploration Rover landing site predictions. *Nature*, *436*(7047), 44–48. http://doi.org/10.1038/nature03600

Golombek, M., Grant, J., Kipp, D., Vasavada, A., Kirk, R., Fergason, R., et al. (2012). Selection of the Mars Science Laboratory Landing Site. *Space Science Reviews*, *170*(1-4), 641–737. http://doi.org/10.1007/s11214-012-9916-y

Gomez-Elvira, J., Armiens, C., & Castañer, L. (2012). REMS: The environmental sensor suite for the Mars Science Laboratory rover. *Space Science ….*

Griffiths, P. R., & De Haseth, J. A. (2007). Fourier transform infrared spectrometry.

Gruber, T., Moore, B., Tercha, B., & Bowe, R. (2012). Next-Generation Spectroscopic

Technologies V. In M. A. Druy & R. A. Crocombe (Eds.), (Vol. 8374, p. 83740B). Presented at the SPIE Defense, Security, and Sensing, SPIE. http://doi.org/10.1117/12.919159

Hamilton, V. E., Vasavada, A. R., & Sebastián, E. (2014). Observations and preliminary science results from the first 100 sols of MSL Rover Environmental Monitoring Station ground temperature sensor measurements at Gale Crater - Hamilton - 2014 - Journal of Geophysical Research: Planets - Wiley Online Library. *Journal of ….*

Hanel, R., Crosby, D., Herath, L., Vanous, D., Collins, D., Creswick, H., et al. (1980). Infrared spectrometer for Voyager. *Applied Optics*, *19*(9), 1391–1400. http://doi.org/10.1364/AO.19.001391

Hirsch, H., Formisano, V., Moroz, V. I., & Arnold, G. (1996). The Planetary Fourier Spectrometer (PFS) for the orbiter of the spacecraft Mars 96. *Planetary and Space ….*

Hoffman, J. D., & Frankel, S. (2014). Numerical Methods for Engineers and Scientists, Third Edition. CRC PressI Llc.

Hong, B. S., Su, P. J., Chou, C. Y., & Hung, C. I. (2011). Realization of non-Fourier phenomena in heat transfer with 2D transfer function. *Applied Mathematical Modelling*.

Houstoun, R. A. (1912). An Introduction to Mathematical Physics.

Ingersoll, A. P., Münch, G., Neugebauer, G., & Diner, D. J. (1975). Pioneer 11 infrared radiometer experiment: The global heat balance of Jupiter. ….

Ingersoll, L. R., & Zobel, O. J. (1913). An introduction to the mathematical theory of heat conduction: with engineering and geological applications.

Jaeger, J. C. (1953). Cambridge Journals Online - Mathematical Proceedings of the Cambridge Philosophical Society - Abstract - Conduction of heat in a solid with periodic boundary conditions, with an application to the surface temperature of the moon. *Mathematical Proceedings of the Cambridge ….*

Jakob, M. (1967). Heat Transfer.

Jakosky, B. M. (1986). ScienceDirect.com - Icarus - On the thermal properties of Martian fines. *Icarus*.

Jakosky, B. M., Mellon, M. T., Kieffer, H. H., Christensen, P. R., Varnes, E. S., & Lee, S. W. (2000). The thermal inertia of Mars from the Mars Global Surveyor Thermal Emission Spectrometer. *Journal of Geophysical Research*, *105*(E4), 9643. http://doi.org/10.1029/1999JE001088

Joseph, D. D., & Preziosi, L. (1989). Heat waves. *Reviews of Modern Physics*, *61*(1), 41–73. http://doi.org/10.1002/cpa.3160120107

Kaminski, W. (1990). Hyperbolic Heat Conduction Equation for Materials With a

Nonhomogeneous Inner Structure. *Journal of Heat Transfer*, *112*(3), 555–560. http://doi.org/10.1115/1.2910422

Kauppinen, J., & Partanen, J. (2011). Fourier transforms in spectroscopy.

Kieffer, H. H. (2013). Thermal model for analysis of Mars infrared mapping. *Journal of Geophysical Research-Planets*, *118*(3), 451–470.

Kieffer, H. H., Chase, S. C., Jr., Miner, E., Münch, G., & Neugebauer, G. (1973). Preliminary report on infrared radiometric measurements from the Mariner 9 spacecraft. *Journal of Geophysical Research*, *78*(20), 4291. http://doi.org/10.1029/JB078i020p04291

Kieffer, H. H., Martin, T. Z., Peterfreund, A. R., Jakosky, B. M., Miner, E. D., & Palluconi, F. D. (1977). Thermal and albedo mapping of Mars during the Viking primary mission. *Journal of Geophysical Research: Planets (1991–2012)*, *82*(28), 4249–4291. http://doi.org/10.1029/JS082i028p04249

Kieffer, H. H., Neugebauer, G., Münch, G., Chase, S. C., Jr., & Miner, E. (1972). Infrared thermal mapping experiment: The Viking Mars orbiter. *Icarus*, *16*(1), 47–56. http://doi.org/10.1016/0019-1035(72)90136-4

Kranyš, M. (1967). General-relativistic thermodynamics with finite transport velocity of interaction in matter. *Il Nuovo Cimento B Series 10*.

Kreisch, C. D., O'Sullivan, J. A., Arvidson, R. E., Politte, D. V., He, L., Stein, N. T., et al. (2017). Regularization of Mars Reconnaissance Orbiter CRISM along-track oversampled hyperspectral imaging observations of Mars. *Icarus*, *282*, 136–151.

Ksanfomalfty, L. V., Moroz, V. I., Bibring, J. P., & Combes, M. (1989). Spatial variations in thermal and albedo properties of the surface of Phobos. *Nature*.

Ksanfomaliti, L. V., & Moroz, V. I. (1975). Infrared radiometry on board Mars 5. *Kosmicheskie Issledovaniia*.

Kunde, V. G., & Ade, P. (1996). Cassini infrared Fourier spectroscopic investigation. *SPIE's 1996 ….*

Kuzmin, R. O., Borozdin, V. K., & Selivanov, A. S. (1991). Thermal Inertia Mapping of Mars on the Base of VD and IR-Imaging by Termoscan Instrument. *Lunar and Planetary ….*

Langley, S. P. (1880). The bolometer and radiant energy. Presented at the Proceedings of the American Academy of Arts and ….

Lawson, S. L., Jakosky, B. M., Park, H. S., & Mellon, M. T. (2000). Brightness temperatures of the lunar surface: Calibration and global analysis of the Clementine long-wave infrared camera data. *Journal of Geophysical Research: Planets (1991–2012)*, *105*(E2), 4273–4290. http://doi.org/10.1029/1999JE001047

Lönnqvist, O. (1962). On the diurnal variation of surface temperature. *Tellus*, *14*(1), 96–

101.

Malamas, S., Davis, D. S., U.S, N. P. S., & Physics, D. O. (2006). Spectroscopic imaging with uncooled microbolometer camera and step-scan FTIR.

Maxwell, J. C. (1867). On the dynamical theory of gases. *Philosophical Transactions of the Royal Society of ...*.

McCleese, D. J., Schofield, J. T., Taylor, F. W., Calcutt, S. B., Foote, M. C., Kass, D. M., et al. (2007). Mars Climate Sounder: An investigation of thermal and water vapor structure, dust and condensate distributions in the atmosphere, and energy balance of the polar regions. *Journal of Geophysical Research: Planets (1991–2012)*, *112*(E5). http://doi.org/10.1029/2006JE002790

Mellon, M. T., Jakosky, B. M., Kieffer, H. H., & Christensen, P. R. (2000). ScienceDirect.com - Icarus - High-Resolution Thermal Inertia Mapping from the Mars Global Surveyor Thermal Emission Spectrometer. *Icarus*.

Mendell, W. W., & Low, F. J. (1974). Preliminary results of the Apollo 17 infrared scanning radiometer. *Earth, Moon, and Planets*, *9*(1-2), 97–103. http://doi.org/10.1007/BF00565396

Mendoza, E. H., Santos, J. R., Santa Rosa, A., & Silva, N. C. (2004). Land use/land cover mapping in Brazilian Amazon using neural network with aster/terra data. *Proc. Geo-Imagery Bridging Continents*, 123–126.

Minobe, S., Kuwano-Yoshida, A., Komori, N., Xie, S.-P., & Small, R. J. (2008). Influence of the Gulf Stream on the troposphere. *Nature*, *452*(7184), 206–209.

Mironer, A., & Regan, F. (1983). Venting of Space-Shuttle Payloads, 2600.

Moroz, V. I., & Ksanfomaliti, L. V. (1972). Preliminary results of astrophysical observations of Mars from Mars-3. *Icarus*.

Narasimhan, T. N. (1999). Fourier's heat conduction equation: History, influence, and connections. *Reviews of Geophysics*, *37*(1), 151–172. http://doi.org/10.1098/rspa.1953.0139

Neugebauer, G., Münch, G., Kieffer, H., Chase, S. C., Jr., & Miner, E. (1971). Mariner 1969 infrared radiometer results: Temperatures and thermal properties of the Martian surface. *The Astronomical Journal*, *76*, 719.

Newton, I. (1701). Scala graduum caloris: calorum descriptiones & signa.

Nowicki, S. A., & Christensen, P. R. (2007). Rock abundance on Mars from the Thermal Emission Spectrometer. *Journal of Geophysical Research*, *112*(E5), E05007. http://doi.org/10.1029/2006JE002798

Ohm, G. S. (1827). Die galvanische Kette, mathematisch bearbeitet.

Osterloo, M. M., Hamilton, V. E., Bandfield, J. L., Glotch, T. D., Baldridge, A. M.,

Christensen, P. R., et al. (2008). Chloride-bearing materials in the southern highlands of Mars. *Science*, *319*(5870), 1651–1654.

Paige, D. A., Foote, M. C., Greenhagen, B. T., Schofield, J. T., Calcutt, S., Vasavada, A. R., et al. (2009). The Lunar Reconnaissance Orbiter Diviner Lunar Radiometer Experiment. *Space Science Reviews*, *150*(1-4), 125–160. http://doi.org/10.1007/s11214-009-9529-2

Peshkov, V. (1944). Second Sound in Heliurn U. *J. Phys., USSR, Vol. 習*, 381.

Pettit, E., & Nicholson, S. B. (1930). Lunar radiation and temperatures. *The Astrophysical Journal*, *71*, 102–135.

Piqueux, S., & Christensen, P. R. (2009a). A model of thermal conductivity for planetary soils: 1. Theory for unconsolidated soils. *Journal of Geophysical Research*, *114*(E9), E09005. http://doi.org/10.1029/2008JE003308

Piqueux, S., & Christensen, P. R. (2009b). A model of thermal conductivity for planetary soils: 2. Theory for cemented soils. *Journal of Geophysical Research*, *114*(E9), E09006. http://doi.org/10.1029/2008JE003309

Piqueux, S., & Christensen, P. R. (2011). Temperature-dependent thermal inertia of homogeneous Martian regolith. *Journal of Geophysical Research*, *116*(E7), E07004. http://doi.org/10.1029/2011JE003805

Pisacane, V. L. (2008). The Space Environment and Its Effects on Space Systems. Amer Inst of Aeronautics &.

Presley, M. A., & Christensen, P. R. (1997a). The effect of bulk density and particle size sorting on the thermal conductivity of particulate materials under Martian atmospheric pressures. *Journal of Geophysical Research*, *102*(E4), 9221–9229. http://doi.org/10.1029/97JE00271

Presley, M. A., & Christensen, P. R. (1997b). Thermal conductivity measurements of particulate materials 2. Results. *Journal of Geophysical Research-Planets*, *102*(E3), 6551–6566. http://doi.org/10.1063/1.1728419

Price, J. C. (1977). Thermal inertia mapping: A new view of the Earth. *Journal of Geophysical Research*, *82*(18), 2582–2590. http://doi.org/10.1029/JB079i002p00317

Report on Technology Horizons: A Vision for Air Force Science and Technology During 2010-2030. (2010). Report on Technology Horizons: A Vision for Air Force Science and Technology During 2010-2030.

Riedl, M. J. (2001). Optical Design Fundamentals for Infrared Systems. SPIE Press.

Roetzel, W., Putra, N., & Das, S. K. (2003). Experiment and analysis for non-Fourier conduction in materials with non-homogeneous inner structure. *International Journal of Thermal Sciences*, *42*(6), 541–552. http://doi.org/10.1016/S1290-

0729(03)00020-6

Ruff, S. W., Christensen, P. R., & Barbera, P. W. (1997). Quantitative thermal emission spectroscopy of minerals: A laboratory technique for measurement and calibration. *Journal of ….*

Russell, E. E., Brown, F. G., Chandos, R. A., Fincher, W. C., Kubel, L. F., Lacis, A. A., & Travis, L. D. (1992). Galileo photopolarimeter/radiometer experiment, 531–563.

Saptari, V. (2004). Fourier Transform Spectroscopy Instrumentation Engineering. SPIE Press.

Schneider, P. J. (1955). Conduction heat transfer.

Schulte, P. Z., & Spencer, D. A. (2016). Development of an integrated spacecraft Guidance, Navigation, & Control subsystem for automated proximity operations. *Acta Astronautica*, *118*, 168–186.

Selivanov, A. S., Naraeva, M. K., Panfilov, A. S., Gektin, Y. M., Kharlamov, V. D., Romanov, A. V., et al. (1989). Thermal imaging of the surface of Mars. *Nature*, *341*(6243), 593–595. http://doi.org/10.1038/341593a0

Sellers, W. D. (1965). Physical climatology.

Shackelford, J. F., Han, Y. H., Kim, S., & Kwon, S. H. (2016). CRC materials science and engineering handbook.

Singh, R. P., Sarkar, S. S., & Kumar, M. (2015). Thermal Infrared Imaging Spectrometer for Mars Orbiter Mission. *Current Science ( ….*

Spencer, D. A. (2015). Automated trajectory control for proximity operations using relative orbital elements.

Stefanov, W. L., Prashad, L., Eisinger, C., Brazel, A., & Harlan, S. L. (2004). Investigation of human modifications of landscape and climate in the Phoenix Arizona Metropolitan area using MASTER data. *Pan*, *2*, 2.8.

Taylor, F. W., Beer, R., Chahine, M. T., Diner, D. J., Elson, L. S., Haskins, R. D., et al. (1980). Structure and meteorology of the middle atmosphere of Venus: Infrared remote sensing from the Pioneer Orbiter. *Journal of Geophysical Research: Planets (1991–2012)*, *85*(A13), 7963–8006. http://doi.org/10.1029/JA085iA13p07963

Touvignon, A., Durand, A., Romanens, F., Favreau, J., Gravrand, O., & Tisse, C.-L. (2014).

Spectral and angular responses of microbolometer IR FPA: a characterization method using a FTIR

, *9071*, 90710W–90710W–10. http://doi.org/10.1117/12.2053448

Vernotte, P. (1958). Les paradoxes de la théorie continue de léquation de la chaleur.

*Comptes Rendus Hebdomadaires Des Seances De L Academie Des Sciences*, *246*(22), 3154–3155.

Veto, M. (2010). Systems Design of the Thermal and Visible Imaging Systems for the Rapid, Response, and Reconnaissance (R, 1–36.

Veto, M. S., & Christensen, P. R. (2015). Mathematical Theory of Thermal Inertia Revisited: Improving our Understanding of Martian Thermophysical Properties Through Analogous Examples of. *Lunar and Planetary Science ….*

Veto, M. S., & Christensen, P. R. (2016). The Thermal-Camera for Exploration, Science, and Imaging Spacecraft (THESIS) for the Prox-1 Microsat Mission. *Lunar and Planetary ….*

Védie, N., Spencer, D. A., Walker, L., & Veto, M. S. (2013). Autonomous Ocean Current Geolocation from Orbit. *Jossonline.com*

, 1–13. Retrieved from http://www.jossonline.com/downloads/0201%20Autonomous%20Ocean%20Current%20Geolocation%20from%20Orbit.pdf

Vision and Voyages for Planetary Science in the Decade 2013-2022. (2012). Vision and Voyages for Planetary Science in the Decade 2013-2022, 1–399.

Walker, L. (2012). Automated proximity operations using image-based relative navigation.

Walker, L., & Spencer, D. (2010). R3: Thermal imaging and rapid feature detection for small satellites.

Wertz, J. R., & Larson, W. J. (1999). Space Mission Analysis and Design. Springer.

Wertz, J. R., Everett, D. F., & Puschell, J. J. (2011). Space Mission Engineering.

Wesselink, A. J. (1948). 1948BAN....10..351W Page 351. *Bulletin of the Astronomical Institutes of ….*

Wien, W. (1894). Temperatur und entropie der strahlung. *Annalen Der Physik*.

Wood, R. A. (1993). Infrared Technology XIX. In B. F. Andresen & F. D. Shepherd (Eds.), (Vol. 2020, pp. 322–329). Presented at the SPIE's 1993 International Symposium on Optics, Imaging, and Instrumentation, SPIE. http://doi.org/10.1117/12.160553

# APPENDIX A:

# TABLE OF DIFFUSION EQUATION ANALOGIES

| | *Thermal Energy* | *Molecular Concentration* | Fluid Momentum | *Linear Displacement* | *Hydraulic Discharge* | *AC Electrical Circuit* |
|---|---|---|---|---|---|---|
| Principal Quantity | Heat<br>Q [J] | Mass<br>M [mol] | Momentum<br>P [N·s] | Displacement<br>x [m] | Discharge<br>Q [$m^3$] | Charge<br>Q [C] |
| Flow | Power<br>q [$J \cdot s^{-1}$] | Mole Flow Rate<br>$\dot{M}$ [$mol \cdot s^{-1}$] | Force F [N] | Velocity v<br>[ $m \cdot s^{-1}$] | Discharge Rate<br>q [$m^3 \cdot s^{-1}$] | Current<br>I [$C \cdot s^{-1}$=A] |
| Principal Flux | Heat Flux<br>Φ [$J \cdot m^{-2} \cdot s^{-1}$] | Diffusion Flux<br>J [$mol \cdot m^{-2} \cdot s^{-1}$] | Shear Stress<br>τ[Pa = $N \cdot m^{-2}$] | Velocity Flux*<br>ϒ [$s^{-1} \cdot m^{-1}$] | Discharge Flux<br>Φ [$m \cdot s^{-1}$] | Current Density<br>j [$A \cdot m^{-2}$] |
| Potential | Temperature<br>θ [K] | Concentration<br>ϕ [$mol \cdot m^{-3}$] | Velocity<br>v [$m \cdot s^{-1}$] | Force<br>F [N] | Head<br>h [m] | Voltage<br>V [V] |
| Transport Law | $\Phi = -k\nabla\theta$<br>*Fourier's Law* | $J = -D\nabla\phi$<br>*Fick's 1st Law* | τ = −μ∇v<br>Newton's Law of Viscosity | ϒ<br>$= -(B * l)^{-1}\nabla F$<br>Modified *Dashpot Equation* | $\Phi = -K\nabla h$<br>*Darcy's Law* | $j = -\sigma_l \nabla V$<br>*Ohm's Law* |
| Conductivity/Resistivity Coefficient | Thermal Conductivity<br>k [$J \cdot m^{-1} \cdot K^{-1} \cdot s^{-1}$] | Diffusion<br>D [$m^2 \cdot s^{-1}$] | Viscosity<br>μ [Pa· s] | Damping coefficient<br>B [$N \cdot s \cdot m^{-1}$]<br>Fluidity<br>$\phi_l = \frac{1}{B * l}$<br>[ $N^{-1} \cdot s^{-1}$] | Hydraulic Conductivity<br>K=κ/μ [m· $s^{-1}$] | Electrical Conductivity<br>$\sigma_l = \frac{1}{R * l}$<br>[$\Omega^{-1} \cdot m^{-1}$] |
| Capacity Equation<br>*note *v is specific volume* | $dQ = c\rho v \frac{\partial\theta}{\partial t} dt$<br>*Newton's Law of Cooling or Joseph Black Equation** | $dM = v \frac{\partial\phi}{\partial t} dt$<br>*Diffusion Definition* | $dP = \rho v \frac{\partial v}{\partial t} dt$<br>*Newton's 2nd Law* | $dx = \frac{1}{k} \frac{\partial F}{\partial t} dt$<br>*Modified Hook's Law* | $dQ = S_s\, v \frac{\partial h}{\partial t} dt$<br>*Groundwater Flow Equation* | $dq = C \frac{\partial V}{\partial t} dt$<br>*Capacitance Equation* |
| Potential Storage Coefficient | Volumetric Heat Capacity<br>ρ c [$J \cdot K^{-1} \cdot m^{-3}$] | Unity<br>No known quantity of storage of space.<br>1 | Density<br>ρ [$kg \cdot m^{-3}$] | Spring Constant<br>k [$N \cdot m^{-1}$]<br>Compliance<br>$S \equiv k^{-1}$ [m· $N^{-1}$] | Specific Storage<br>$S_s$ [$m^{-1}$] | Capacitance<br>$C$ [$s \cdot \Omega^{-1}$] |

| | *Thermal Energy* | *Molecular Concentration* | Fluid Momentum | *Linear Displacement* | *Hydraulic Discharge* | *AC Electrical Circuit* |
|---|---|---|---|---|---|---|
| Diffusivity Coefficient [$m^2\,s^{-1}$] | $\alpha \equiv \frac{k}{\rho c}$ *Thermal Diffusivity* | $D = \frac{D}{1}$ *Diffusivity* | $\upsilon \equiv \frac{\mu}{\rho}$ *Kinematic Viscosity* | $\Lambda \equiv \frac{1}{B_l S_l} \equiv \frac{l^2}{BS}$ *Returnability** | $a \equiv \frac{K}{S_s}$ *Hydraulic Viscosity* | $a_{LRC} = \frac{1}{R_l C_l} = \frac{l^2}{RC} = \omega_{RC} * l^2$ *Electric Diffusivity** |
| Diffusion Equation | $\frac{\partial^2 \theta_x}{\partial x^2} = \frac{1}{\alpha}\frac{\partial \theta}{\partial t}$ *Heat Diffusion* | $\frac{\partial^2 \phi_x}{\partial x^2} = \frac{1}{D}\frac{\partial \phi}{\partial t}$ *Fick's 2nd Law* | $\frac{\partial^2 v_x}{\partial y^2} = \frac{1}{\upsilon}\frac{\partial v}{\partial t}$ *Simplified Navier-Stokes Equation* | $\frac{\partial^2 F}{\partial x^2} = B_l S_l \frac{\partial F}{\partial t}$ Force Diffusion* | $\frac{\partial^2 h}{\partial y^2} = \frac{1}{a}\frac{\partial h}{\partial t}$ Hydraulic Diffusion* | $\frac{\partial^2 V}{\partial x^2} = R_l C_l \frac{\partial V}{\partial t}$ Simplified Telegraph Equation |
| Periodic Flux Equation | $\phi_q = \theta_{0_1}\sqrt{k\rho c}\sqrt{\omega} \cdot \cos\left(\omega t + \frac{\pi}{4}\right)$ | $J = \phi_{0_1}\sqrt{D}\sqrt{\omega} \cdot \cos\left(\omega t + \frac{\pi}{4}\right)$ | $\tau = v_{0_1}\sqrt{\rho \cdot \mu}\sqrt{\omega} \cdot \cos\left(\omega t + \frac{\pi}{4}\right)$ | $\Upsilon = F_{0_1}\frac{\sqrt{\phi \cdot S}}{l^2}\sqrt{\omega} \cdot \cos\left(\omega t + \frac{\pi}{4}\right)$ | $\Phi = h_{0_1}\sqrt{K \cdot S_s}\sqrt{\omega} \cdot \cos\left(\omega t + \frac{\pi}{4}\right)$ | $j = V_{0_1}\frac{\sqrt{\sigma \cdot C}}{l^2}\sqrt{\omega} \cdot \cos\left(\omega t + \frac{\pi}{4}\right)$ |
| Effusivity | $\sqrt{k\rho c}$ [$J \cdot m^{-2} \cdot K^{-1} \cdot s^{-1/2}$] *Thermal Effusivity "Thermal Inertia"* | $\sqrt{D}$ [$m \cdot s^{-1/2}$] *Molecular Effusivity* | $\sqrt{\rho \cdot \mu}$ [$kg \cdot m^{-2} \cdot s^{-1/2}$] *Fluid Effusivity** | $\frac{\sqrt{\phi \cdot S}}{l^2}$ [$m \cdot N^{-1} \cdot s^{-1/2}$] *Translational Effusivity** | $\sqrt{K \cdot S_s}$ [$s^{-1/2}$] *Hydraulic Effusivity** | $\frac{\sqrt{\sigma \cdot C}}{l^2}$ [$\Omega^{-1} \cdot s^{1/2} \cdot m^{-2}$] *Electrical Effusivity** |

- Names created in this paper

# APPENDIX B

## TABLE OF HYPERBOLIC DIFFUSION EQUATION ANALOGIES

| | *Thermal Energy* | *Molecular Concentration* | *Fluid Momentum* | *Linear Displacement* | *Hydraulic Discharge* | *AC Electrical Circuit* |
|---|---|---|---|---|---|---|
| Delay Component | $L_T = \frac{\tau}{k}$<br>$[s^2 \cdot m^1 \cdot K^1 \cdot J^{-1}]$<br>Thermal Inductance | - | - | $m$<br>[kg]<br>Mass | - | $L$<br>$[\Omega \cdot s]$<br>Inductance |
| Delay Equation | $\theta = L_T \frac{\partial q}{\partial t}$<br><br>*Super-Cooled Conduction? (No Heat Storage)** | - | - | $F = m \frac{\partial v}{\partial t}$<br><br>*Newton's 2nd Law* | - | $V = L \frac{\partial I}{\partial t}$<br>*Result of Faraday's Law* |
| Modified Diffusion Equation | $\frac{\partial \theta}{\partial t} + L_T k \frac{\partial^2 \theta}{\partial t^2} = \alpha \nabla^2 \theta$<br><br>*Relativistic Heat Diffusion** | - | - | $\frac{\partial F}{\partial t} + mS \frac{\partial^2 F}{\partial t^2} = \Lambda \nabla^2 F$<br><br>*Hyperbolic Force Diffusion Equation** | - | $\frac{\partial V}{\partial t} + \frac{L_l}{R_l} \frac{\partial^2 V}{\partial t^2} = \frac{1}{R_l C_l} \nabla^2 V$<br><br>*Telegraph Equation* |
| Propagation Speed | $C = \sqrt{\frac{a}{\tau}}$<br>$[m \cdot s^{-1}]$<br><br>$\lim_{\tau \to 0} C = \infty$ | - | - | $C = \sqrt{\frac{\Lambda}{mS}}$<br>$[m \cdot s^{-1}]$<br><br>$\lim_{\tau \to 0} C = \infty$ | - | $\omega_0 = \frac{1}{\sqrt{L_l C_l}}$<br>$[m \cdot s^{-1}]$<br><br>$\lim_{L_l \to 0} \omega_0 = \infty$ |
| | | | | | | |

# APPENDIX C

## THERMOPHYSICAL PROPERTIES OF VARIOUS MATERIALS

Reproduced from Clemens J.M. Lasance in the magazine Electronics Cooling. Nov.1 2007. Note: The units are effusivity are changed to $J \cdot cm^{-2} \cdot K^{-1} \cdot s^{-0.5}$.

| material | $\rho$ | $c_p$ | $k$ | $\rho\, c_p$ | $\alpha$ | $e$ | $\delta$ (1s) |
|---|---|---|---|---|---|---|---|
| | $kg \cdot m^{-3}$ | $J \cdot kg^{-1} \cdot K^{-1}$ | $W \cdot mK^{-1}$ | $J \cdot m^{-3} \cdot K^{-1} * 10^6$ | $mm^2 \cdot s^{-1}$ | $J \cdot cm^{-2} \cdot K^{-1} \cdot s^{-0.5}$ | mm |
| air | 1.3 | 1004 | 0.03 | 0.001 | 19.2 | 0.0006 | 8.8 |
| wool | 100 | 1500 | 0.04 | 0.15 | 0.23 | 0.007 | 1.0 |
| balsa wood | 130 | 2301 | 0.05 | 0.30 | 0.17 | 0.012 | 0.8 |
| polyvinyl chloride | 1500 | 1674 | 0.17 | 2.51 | 0.07 | 0.06 | 0.5 |
| skin | 1000 | 2500 | 0.40 | 2.50 | 0.16 | 0.10 | 0.8 |
| quartz | 2200 | 745 | 1.40 | 1.64 | 0.85 | 0.15 | 1.8 |
| silicon oxide | 2200 | 745 | 1.40 | 1.64 | 0.85 | 0.15 | 1.8 |
| water | 1000 | 4184 | 0.60 | 4.18 | 0.14 | 0.16 | 0.8 |
| ice | 917 | 4217 | 2.10 | 3.87 | 0.54 | 0.28 | 1.5 |
| aluminum oxide | 2200 | 778 | 18 | 171 | 10.5 | 0.56 | 6.5 |
| stainless steel (CrNi) | 8000 | 502 | 15 | 4.02 | 3.73 | 0.78 | 3.9 |
| tin | 7310 | 226 | 61 | 165 | 36.9 | 1.00 | 12.2 |
| silicon | 2330 | 703 | 126 | 1.64 | 76.9 | 1.44 | 17.5 |
| iron | 7870 | 448 | 72 | 3.52 | 20.4 | 1.59 | 9.0 |
| aluminum alloy (7079) | 2740 | 795 | 121 | 2.18 | 55.5 | 1.62 | 14.9 |
| aluminum | 2698 | 921 | 226 | 2.48 | 91 | 2.37 | 19.1 |
| gold | 19300 | 128 | 320 | 2.47 | 129 | 2.81 | 22.8 |
| copper | 8940 | 385 | 396 | 3.44 | 115 | 3.69 | 21.5 |

# APPENDIX D:

# CHARACTERISTICS OF PARTIAL DIFFERENTIAL EQUATIONS

The heat equation is a second order, the highest derivative is to the second degree; linear, the dependent variables and their derivatives are raised to a power of one; homogenous, each term in the equation contains the dependent variable or its derivatives; partial differential equation (PDE), the derivatives of the dependent variable are taken with respect to multiple independent variables.

The heat equation is also the archetypal example of a parabolic PDE meaning that when the heat equation is expanded to be written in the form described by ( 178 ), then case described in ( 179 ) is true. Where B is zero, A is $\alpha$, and C is zero. This is analogous to the elementary quadratic formula for which the radical is equal to zero resulting in a single root. In this case, a parabolic PDE implies that within a time interval, for each spatial point, the physical information depends upon the information at each other point upstream of and each other point within the present solution (Hoffman & Frankel, 2014). In other words, the transient temperature at each point within a domain at a given time interval is influenced by the temperature at all of the points in the past and the present. In addition, the temperature at each point will influence the temperature at each point in the future.

Expansion of a 2-variable PDE:

$$au_{xx} + 2bu_{xt} + cu_{tt} + du_x + eu_t + fu = g \tag{178}$$

Condition for parabolic PDE:

$$B^2 - AC = 0 \tag{179}$$

If the system no longer varies in time, it takes on the form of ( 180 ), otherwise known as the Laplace equation, which is an archetypal elliptical PDE, satisfying equation ( 182 ). If the heat generated within the solid is added, the Poisson equation results ( 181 ); however, it is assumed that no energy is generated within the control volume for

this derivation. Elliptical equations are steady or in equilibrium. The rate of flow of the potential variable does not change, hence the 2nd derivative is zero.

Laplace's equation:

$$\nabla^2 T = 0 \; or \; \theta_{xx} = 0 \tag{180}$$

Poisson's equation:

$$k\nabla^2 T + \dot{q} = 0 \; or \; k\theta_{xx} + \dot{q} = 0 \tag{181}$$

Condition for elliptical PDE:

$$B^2 - A < 0 \tag{182}$$

Finally, the hyperbolic equation satisfies the case described by equation ( 183 ). The most archetypical example is the wave equation ( 184 ).

Condition for hyperbolic PDE:

$$B^2 - A > 0 \tag{183}$$

Wave equation:

$$\frac{\partial^2 y}{\partial x^2} = c^2 \frac{\partial^2 y}{\partial t^2} \tag{184}$$

$$\theta_{xx} = \mathrm{c}^2 * \theta_{tt} \tag{185}$$

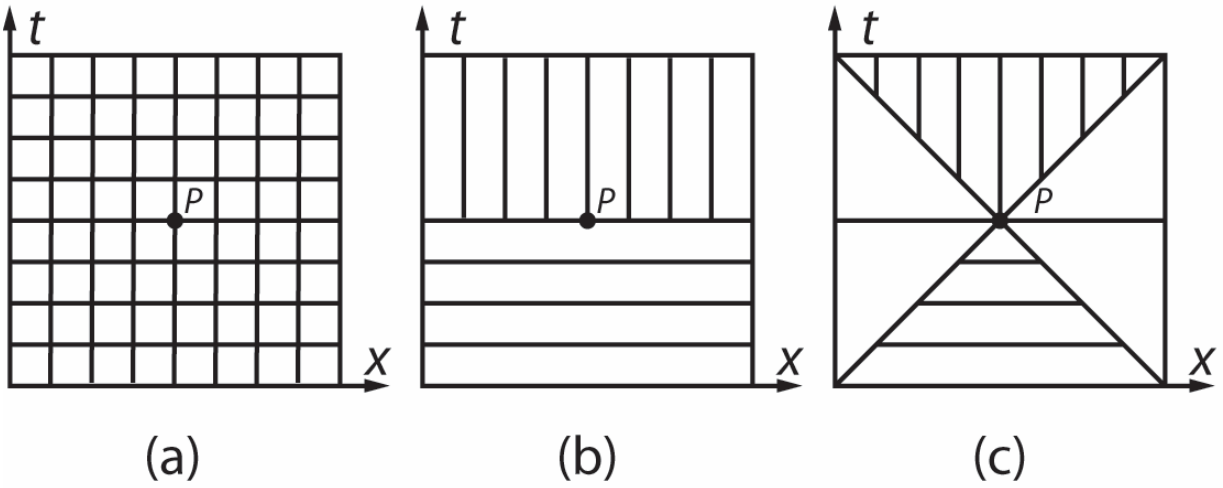


*Figure 129*. Domain of dependence (-) and the range of influence (|) for various positions (*x)* and times (*t*) for (a) elliptical PDE, (b) parabolic equation PDE, and (c) hyperbolic PDE. This figure was reproduced and modified (Hoffman & Frankel, 2014).

# APPENDIX E:

# THERMAL INFRARED REMOTE SENSING INSTRUMENTS

| Year | Planet | Mission | Instrument | PI and Reference |
|---|---|---|---|---|
| 1962 | Venus | Mariner 2 | Infrared Radiometer | G.errald Neugabauer (Chase & Kaplan, 1963) |
| 1969 | Mars | Mariner 6 | Infrared Radiometer | G.errald Neugabauer (Chase, 1969) |
| 1969 | Mars | Mariner 7 | Infrared Radiometer | G.errald Neugabauer (Chase, 1969) |
| 1971 | Mars | Mariner 9 | Infrared Interferometer Spectrometer | Gerrald Neugabauer (Chase et al., 1972) |
| 1971 | Mars | Mars 2 | Infrared Radiometer | V.I. Moroz |
| 1971 | Mars | Mars 3 | Infrared Radiometer | V.I. Moroz (Moroz & Ksanfomaliti, 1972) |
| 1972 | Moon | Apollo 17 | Infrared Scanning Radiometer | Wendell W. Mendell (Mendell & Low, 1974) |
| 1972 | Jupiter | Pioneer 10 | Infrared Radiometer | Andrew Ingersol(Chase, Ruiz, Münch, & Neugebauer, 1974), (Bender, Callaway, Chase, Moore, & Ruiz, 1974) |
| 1973 | Jupiter Saturn | Pioneer 11 | Infrared Radiometer | Andrew Ingersol (A. P. Ingersoll, Münch, Neugebauer, & Diner, 1975) |
| 1973 | Mercury | Mariner 10 | Infrared Radiometer | Stillman Chase Jr(Chase, Miner, Morrison, & Münch, 1976) |
| 1973 | Mars | Mars 5 | Infrared Radiometer | V.I. Moroz |
| 1975 | Mars | Viking 1 | Infrared Thermal Mapper | Hugh H. Kieffer (Kieffer, Neugebauer, Münch, Chase, & Miner, 1972) |

| | | | | |
|---|---|---|---|---|
| 1975 | Mars | Viking 2 | Infrared Thermal Mapper | Hugh H. Kieffer (Kieffer et al., 1972) |
| 1975 | Venus | Venera 9 | Infrared Radiometer | |
| 1975 | Venus | Venera 10 | Infrared Radiometer | |
| 1978 | Venus | Pioneer Venus | Orbiter Infrared Radiometer | F. W. Taylor(Taylor et al., 1980) |
| 1977 | Jupiter, Saturn, Titan | Voyager 1 | Infrared Interferometer Spectrometer | Rudolf Hanel(Hanel et al., 1980) |
| 1977 | Jupiter, Saturn, Uranus, Neptune | Voyager 2 | Infrared Interferometer Spectrometer | Rudolf Hanel(Hanel et al., 1980) |
| 1983 | Venus | Venera 15 | Infrared Fourier Spectrometer | |
| 1983 | Venus | Venera 16 | Infrared Fourier Spectrometer | |
| 1984 | Venus | Vega 1 | Infrared Spectrometer | |
| 1984 | Venus | Vega 2 | Infrared Spectrometer | |
| 1988 | Mars | Phobos 2 | TERMOSCAN | A.S. Selivanov |
| 1988 | MARS | Phobos 2 | Infrared Radiometer | L.V. Ksanfomalfty (Ksanfomalfty, Moroz, Bibring, & Combes, 1989) |
| 1989 | Jupiter | Galileo | Photopolarimeter-Radiometer | E.E. Russel(Russell et al., 1992) |
| 1992 | Mars | Mars Observer | Thermal Emission Spectrometer | Phil Christensen(Christensen et al., 1992) |
| 1998 | Mars | Mars Observer | Pressure Modulated Infrared Radiometer | Dan McCleese |
| 1996 | Mars | Mars Global Surveyor | Thermal Emission Spectrometer | Phil Christensen(Christensen |

| | | | | |
|---|---|---|---|---|
| | | | | et al., 2001) |
| 1996 | Mars | Mars 96 | Planetary Fourier Spectrometer | Vittorio Formisano (Formisano et al., 1996) (Hirsch, Formisano, Moroz, & Arnold, 1996) |
| 1997 | Saturn | Cassini | Composite Infrared Spectrometer | Virgil G. Kunde (Kunde & Ade, 1996) |
| 1998 | Mars | Mars Climate Orbiter | Pressure Modulated Infrared Radiometer | Dan McCleese |
| 2000 | Moon | Clementine | Long Wavelength Infrared Camera | Stefanie L. Lawson (Lawson, Jakosky, Park, & Mellon, 2000) |
| 2001 | Mars | 2001 Mars Odyssey | Thermal Emission Imaging System | Phil Christensen(Christensen et al., 2004) |
| 2003 | Mars | MER-Spirit | Miniature Thermal Emission Spectrometer | Phil Christensen(Christensen et al., 2003) |
| 2003 | Mars | MER-Opportunity | Miniature Thermal Emission Spectrometer | Phil Christensen(Christensen et al., 2003) |
| 2003 | Mars | Mars Express | Planetary Fourier Spectrometer | Vittorio Formisano (Formisano, Grassi, Ignatiev, Zasova, & Maturilli, 2002) |
| 2005 | Venus | Venus Express | Planetary Fourier Spectrometer | Vittorio Formisano (Formisano, Angrilli, Arnold, & Atreya, 2006) |
| 2005 | Mars | MRO | Mars Climate Sounder | Dan McCleese (McCleese et al., 2007) |
| 2009 | Moon | LRO | Diviner | Dave Paige (Paige et al., 2009) |
| 2010 | Venus | Akatsuki | Long Wave Infrared Camera | Tetsuya Fukuhara (Fukuhara, Taguchi, Imamura, & Nakamura, 2011) |

| | | | | |
|---|---|---|---|---|
| 2011 | Mars | MSL | Rover Environmental Monitory Station | Javier Gómez-Elvira (Gomez-Elvira, Armiens, & Castañer, 2012) |
| 2013 | Mars | Mars Orbiter Mission | Thermal Infrared Imaging Radiometer | R.P. Singh (Singh et al., 2015) |
| 2016 | Bennu | OSIRIS-Rex | OSIRIS-Rex Thermal Emission Spectrometer | Phil Christensen (Christensen et al., 2017) |
| ~2020 | Europa | Europa Clipper | E-THEMIS | Phil Christensen |

# APPENDIX F:

# NICOLET SAMPLE DERIVATION

An example derivation of the wavenumber spacing for a Nicolet Nexus 670 spectrometer is provided.

**PROBLEM**

Determine the wavenumber spacing $d\tilde{\nu}$.

**KNOWN VARIABLES AND ASSUMPTIONS**

4. The wavelength of the interferogram sampling laser is $\lambda_{HeNe}$ = 632.8 nm.
5. A desired maximum wavemuber is $\tilde{\nu}_{max}$ = 8000 cm$^{-1}$.

**ANALYSIS**

**Determine the exact maximum wavenumber.**

$$\tilde{\nu}_{max} = \frac{1}{m * \lambda_{HeNe}} = \frac{15803\ cm^{-1}}{2} = 7901\ cm^{-1}$$

Choosing m=2 will provide a maximum wavenumber of 7901 cm$^{-1}$. This is ~8000 cm$^{-1}$, so the interferogram will be sampled at every "zero crossing"—through the interferometer—or at the wavelength of the laser or at the wavelength of the laser. Again, the interferometer zero-crossing is the negative amplitude of the re-combined interfered wave. This is not the node of the raw laser.

**Verify the optical sampling displacement**

This may seem a bit circular, but for the sake of example, the following equation is used.

$$\tilde{\nu}_{max} = \frac{1}{2 * d\delta}$$

Rearranging and plugging in the maximum wavenumber yields the following.

$$d\delta = \frac{1}{2 * \tilde{\nu}_{max}} = \frac{1}{2 * 7901 cm^{-1}} = 632.8nm$$

This shows that the optical path distance for sampling the interferogram is at the wavelength of the laser or every other zero crossing.

**Determine the Spectral Resolution**

A common spectral resolution is 4cm$^{-1}$.

$$\Delta\tilde{\nu} = 4cm^{-1}$$

**Calculate the Maximum Optical Path Difference**

The maximum optical path difference is the inverse of the spectral resolution.

$$\Delta_{max} = \frac{1}{\Delta\tilde{\nu}} = \frac{1}{4cm^{-1}} = 0.25cm$$

**Calculate the Number of Samples**

$$N_s = \frac{2 * \tilde{\nu}_{max}}{\Delta\tilde{\nu}} = \frac{2 * 7901cm^{-1}}{4cm^{-1}} = 3951\ samples$$

**Validate the number of samples.**

For the FFT, the number of samples is increased to a $2^N$. The closest for this example would be $2^{12}$ or 4096 samples for a single-sided interferogram. This is 8192 samples for a double-sided interferogram.

**Calculate the wavenumber spacing**

$$d\tilde{\nu}_D = \frac{\tilde{\nu}_{max}}{N_s} = \frac{\tilde{\nu}_{max}}{N_D/2} = \frac{7901cm^{-1}}{4096} = 1.93cm^{-1}$$

$$d\tilde{\nu}_S = \frac{\tilde{\nu}_{max}}{N_s/2} = \frac{7901cm^{-1}}{2046} = 3.86cm^{-1}$$

This means that the actual spectral resolution is closer to 3.86 cm$^{-1}$ than 4 cm$^{-1}$.

# APPENDIX G:

# MICROBOLOMETER SAMPLING DERIVATIONS

## PROBLEM

1. Determine the wavenumber spacing $d\tilde{v}$.
2. Determine an equation for the $V_{pp}$.
3. Determine an equation for the wave generator frequency.

## KNOWNS AND ASSUMPTIONS

4. Microbolometer sampling frequency: $f_s = 30Hz$
5. Waveform generator frequency: $f_{wg} = 20mHz$
6. Waveform generator peak to peak voltage: $V_{PP} = 2$ volts
7. Single-sided moving mirror displacement: $\Delta X = 0.0096\ cm$

## ANALYSIS

**Calculate the Maximum Optical Path Difference:**

$$\Delta_{max} = 2 * \Delta X = 2 * 0.0096cm = 0.0193cm$$

**Calculate the Double-sided full travel displacement.**

$$\Delta X_{Double} = 2 * \Delta X_{Single} = 2 * .0096cm = 0.0193cm$$

**Calculate the Spectral Resolution**

$$\Delta\tilde{\nu} = \frac{1}{\Delta_{max}} = \frac{1}{0.0193cm} = 52.08cm^{-1}$$

**Calculate the Optical Sampling Distance**

$$d\delta = \frac{\Delta_{max}}{N_s} = \frac{0.0193cm}{311} = 0.62058\mu m$$

**Calculate the Maximum Wavenumber**

$$\tilde{\nu}_{max} = \frac{1}{2 * d\delta} = \frac{1}{2 * 0.62058\ \mu m} = 8057cm^{-1}$$

**Calculate the Spectral Sampling**

$$d\tilde{\nu} = \frac{\tilde{\nu}_{max}}{N_s} = \frac{8057cm^{-1}}{311} = 25.91cm^{-1}$$

**Derive an equation for the waveform generator frequency.**

The velocity of the moving mirror is equal to the sampling distance multiplied by the sampling frequency. It is also equal to the maximum optical path distance divided by the total sampling period for a single sided interferogram. The period for a single sided scan is also equal to a quarter of the frequency generators triangle wave. A full triangle wave starts at ZPD and travels to the maximum displacement, back to ZPD, to maximum negative displacement, and back to ZPD. Combining these three equations.

$$\vec{v} = d\delta * f_s \quad (186)$$

$$\vec{v} = \frac{\Delta_{max}}{T_{Single\ Sided}} \quad (187)$$

$$T_{Single\ Sided} = \frac{1}{4 * f_{wg}} \quad (188)$$

Combining the later two equations yields the following.

$$\vec{v} = 4 * f_{wg} * \Delta_{max} \quad (189)$$

After equating the velocities of the moving mirror, an equation for the necessary wave generator frequency follows.

$$d\delta * f_s = 4 * f_{wg} * \Delta_{max}$$

$$f_{wg} = \frac{d\delta * f_s}{4 * \Delta_{max}} = \frac{\left(\frac{1}{2 * \tilde{\nu}_{max}}\right) * f_s}{4 * \left(\frac{1}{2 * d\tilde{\nu}}\right)} = \frac{d\tilde{\nu} * f_s}{4 * \tilde{\nu}_{max}} \quad (190)$$

$$f_{wg} = \frac{f_s}{4} * \frac{d\tilde{\nu}}{\tilde{\nu}_{max}}$$

**Determine an equation for the moving mirror motor voltage.**

Combing equations for the maximum optical path difference and the moving mirror waveform response function produces an equation for the peak to peak voltage of the moving mirror as a function of the wave form response function and the desire spectral sampling.

$$\Delta_{max} = \frac{1}{2 * d\tilde{\nu}}$$

$$\Delta_{max} = 2 * \Delta X = 2 * WFR * V_{PP} \quad (191)$$

$$V_{PP} = \frac{1}{4 * WFR * d\tilde{\nu}}$$

# APPENDIX H.

# FFT NOTES

## WAVENUMBER TO WAVELENGTH CONVERSION

The wavelength-wavenumber relation for same units is as follows.

$$\lambda = \frac{1}{\nu} \tag{192}$$

$$\nu = \frac{1}{\lambda}$$

The derivatives are as follows.

$$d\lambda = -\frac{1}{\nu^2} * d\nu \tag{193}$$

$$d\nu = -\frac{1}{\lambda^2} * d\lambda$$

Equality of Radiance:

$$E_\nu * d_\nu = E_\lambda * d_\lambda \tag{194}$$

Substitute the derivatives into the equality of radiance.

$$E_\nu = E_\lambda * \lambda^2 \tag{195}$$

$$E_\lambda = E_\nu * \nu^2$$

## WAVE INTENSITY

Assuming an ideal beamsplitter, the intensity of light transmitting/reflecting to each arm of the interferometer ($I_o$) is half of the source ($I_S$).

$$\frac{I_s}{2} = I_0 \tag{196}$$

Half of the energy from the source escapes from the interferometer as transmitted/reflected light through the 2nd interaction with the beamsplitter. The intensity of light that reaches the detector is the following.

$$I(x) = 2I_0[1 + cos(2\pi\ \nu\ 2x)] \quad (197)$$

Further, using the following relation, where $I_o$ is the intensity of one arm of the energy(Kauppinen & Partanen, 2011).

$$E_\nu * d_\nu = I_0 \quad (198)$$

**MAGNITUDE DN**

The magnitude of the FFT has units of volts

$$|FFT_\nu| \quad [Volts] \quad (199)$$

**SPECTRAL DN**

The magnitude of the FFT divided by the nyquist wavenumber or multiplied by the optical sampling distance has units of Volts per wavenumber. This perhaps could be called the “spectral voltage”. There were no references found that indicate this unit, but it would be similar to how spectral power is derived. Though, it appears that if the scan velocity; the number of repetitions of an interferogram per collection, this should always be one; and the gain of the instrument are consistent, then it is probably not necessary to worry about spectral power. This seems to be more important when dealing with signals of varied length and repetition that require normalizing. In signal processing the FFT is divided by the sampling frequency to produce a power spectral density that has units of watts per hertz in the y-axis and has an x-axis of hertz. Thus the power spectrum is normalized similar to the spectral radiance plots that are normalized to wavenumber or wavelength. Remember that $d\delta$ is the optical sampling distance equal to one over two times the maximum usable wavenumber.

$$|FFT_\nu| * d\delta \qquad [V\cdot(cm^{-1})^{-1}] \quad (200)$$

## PARSEVAL'S THEOREM: MATHEMATICS

The power spectral density equation using Parseval's Theorem or the Rayleigh Energy Criterion states that the integral of the interferogram and its FFT, the spectrum, must be equal. Here, *x(n)* is the interferogram and *X(k)* is the FFT. The FFT must be divided by N, the number of samples. Only half of the FFT is used though for the radiance curve, so the output is multiplied by 2 and only half the points are summed.

( 201 )

$$\sum_{n=0}^{N-1}|x(n)|^2 = \frac{1}{N}\sum_{n=0}^{N-1}|X(k)|^2$$

$$\sum_{n=0}^{N-1}|x(n)|^2 = \frac{2}{N}\sum_{n=0}^{N/2-1}|X(k)|^2$$

## CONTINUOUS FOURIER TRANSFORM

In integral form this would be the following. Note that the integration limits probably need to be changed mathematically.

( 202 )

$$\int_{0}^{\delta(N-1)}|I(\delta)|^2 * d\delta = 2\int_{0}^{\delta(\frac{N}{2}-1)}|X(\nu) * d\delta|^2 * d\nu$$

## DISCRETE FOURIER TRANSFORM

In the discrete form, the $d\delta$ cancel. Where the differential wavaenumber is equal to one over the differential optical path distance multiplied by the number of sample points.

( 203 )

$$\sum_{n=0}^{N-1} |I(\delta)|^2 * d\delta = \frac{2 * d\delta^2}{N * d\delta} \sum_{n=0}^{\frac{N}{2}-1} |X(k)|^2$$

$$\sum_{n=0}^{N-1} |I(\delta)|^2 = \frac{2}{N} \sum_{n=0}^{\frac{N}{2}-1} |X(k)|^2$$

**SINGLE WAVE AMPLITUDE FROM DFT**

For a single wave within the interferogram, the amplitude of the wave is described here as $A_k$. This is not the amplitude of a single wave in the arms of the spectrometer or the amplitude of the electromagnetic wave. It is simply the amplitude of a specific wavelength in the output of the interferometer that reaches the detector.

As long as many waves are sampled, i.e. the time is much greater than the period of the wavelength, then the following assumption is true. This is a result of taking the integral and zeroing the resulting sine term.

( 204 )

$$\int_0^{t \gg T} |A\cos(\omega * t)|^2 * dt \cong \frac{A^2}{2} * \Delta t$$

This approximation is used on the interferogram as follows.

$$\sum_{n=0}^{N-1} |I(\delta)|^2 * d\delta = \frac{{A_k}^2}{2} * OPD$$

$$\frac{{A_k}^2}{2} * OPD = \frac{2 * d\delta}{N} * |X(k)|^2$$

$$\frac{{A_k}^2}{2} * (d\delta * N) = \frac{2 * d\delta}{N} * |X(k)|^2$$

$${A_k}^2 = \frac{4}{N^2} * |X(k)|^2$$

For any one frequency amplitude in the FFT, the absolute value of the complex result multiplied by 2 and divided by N is equal to the amplitude of a discretely sampled precursor wave. This appears to work for both single and double-sided interferograms where N is the total number of discrete samples.

$$A_k = \frac{2}{N} * |X(k)| \qquad [\text{Volts} \cdot \text{sample}^{-1}] \tag{205}$$

**NICOLET AMPLITUDE**

The Nicolet spectrometer appears to plot the following, where arbitrary unit are used for the y-axis.

$$A_{Nicolet}(k) = 2 * |X(k)| \qquad [\text{Arbitrary Units}] \tag{206}$$

**DN RADIANCE PER WAVENUMBER**

While $A_k$ seems to be a reasonable amplitude that is used in this paper, in practice, these are all scale factors that will be unimportant for the final instrument response function, because they are all "middle-man" coefficients that are calibrated out. The following seems to be the most accurate magnitude for a "spectral voltage" that is similar to the spectral radiance.

$$E_\nu(k) = |X(k) * d\delta| \quad [\text{Volts} \cdot (\text{cm}^{-1})^{-1}] \tag{207}$$

**DN RADIANCE PER WAVELENGTH**

Above the voltage from the FFT is normalized by the wavenumber bins to become a "spectral voltage". To determine a spectrum in wavelength space, this "spectral voltage" is multiplied by twice the wavenumber bin and $10^{-4}$ to change the units in the denominator from wavenumber ($\text{cm}^{-1}$) to wavelength (μm).

$$E_\lambda(k) = |X(k) * d\delta| * \nu^2 * \frac{1\ cm}{10000\ \mu m} \quad (208)$$

[Volts · μm$^{-1}$]

**DN RADIANCE PER SAMPLE (PLOTTED IN WAVELENGTH)**

The following is used in this paper, so that the IRF remains the same as is shown in a subsequent section.

$$A_\lambda(k) = \left\{\frac{2}{N} * |X(k)|\right\} * \nu^2 * \frac{1\ cm}{10000\ \mu m} \quad (209)$$

[Volts · sample$^{-1}$· $\mu m^{-1}$]

**CALIBRATED RADIANCE IN WAVELENGTH SPACE**

This produces a spectral DN in wavelength space. The wavenumber instrument response function may be used. This cancels the DN unit, however there are still units of wavenumber, so the results must be divided with the optical sampling distance. The conversions cancel in both the numerator and the denominator for the blackbody function and the result is simply plotted with a non-linear wavelength axis.

$$B_{\lambda\_scene} = \frac{V_{measured}}{IRF} + \varepsilon B_{\lambda\_ins} \quad (210)$$

$$B_{\lambda\_scene} = B_{\lambda\_measured} + \varepsilon B_{\lambda\_ins}$$

( 211 )

$$B_{\lambda\_measured} = |X(k) * d\delta| * \frac{\nu^2}{10{,}000} * \frac{(Bhot_\nu - Bwarm_\nu) * \frac{\nu^2}{10{,}000}}{(Vhot_\nu * d\delta - Vwarm_\nu * d\delta) * \frac{\nu^2}{10{,}000}}$$

$$B_{\lambda\_measured} = |X(k)| * \frac{(B6hot_\nu - Bwarm_\nu) * \frac{\nu^2}{10{,}000}}{(Vhot_\nu - Vwarm_\nu)}$$

**INSTRUMENT RESPONSE FUNCTION FOR WAVELENGTH SPECTRUM**

Assuming that the voltages here are the magnitudes from the FFT multiplied by 2 and divided by N, then multiplying the voltage by $d\delta$ equates the term to $E_\nu(k)$, and the following equation holds true.

( 212 )

$$IRF_\nu = \frac{(Vhot_\nu * d\delta - Vwarm_\nu * d\delta)}{Bhot_\nu - Bwarm_\nu}$$

The following units are used.

$$\left[\frac{DN \cdot (cm^{-1})^{-1}}{W \cdot m^{-2} \cdot sr^{-1}\,(cm^{-1})^{-1}}\right]$$

( 213 )

$$IRF_\lambda = \frac{(Vhot_\nu * d\delta - Vwarm_\nu * d\delta)}{(Bhot_\nu - Bwarm_\nu)} * \frac{\nu^2}{\nu^2} * \frac{10{,}000}{10{,}000}$$

$$\frac{DN \cdot \mu m^{-1}}{W \cdot m^{-2} \cdot sr^{-1} \cdot \mu m^{-1}}$$

Because any manipulation of the FFT of a measurement and the voltage spectrum of the blackbodies will cancel, the IRF in practice reduces to the following.

$$IRF_\nu = \frac{(Vhot_\nu - Vwarm_\nu)}{Bhot_\nu - Bwarm_\nu} \quad (214)$$

$$\left[\frac{DN}{W \cdot m^{-2} \cdot sr^{-1} \cdot (cm^{-1})^{-1}}\right]$$

For an unaltered spectrum |X(k)|, the following is used.

$$IRF_\lambda = \frac{(Vhot_\nu - Vwarm_\nu)}{(Bhot_\nu - Bwarm_\nu)} * \frac{10{,}000}{\nu^2} = \frac{(Vhot_\nu - Vwarm_\nu)}{(Bhot_\lambda - Bwarm_\lambda)} \quad (215)$$

$$\left[\frac{DN}{W \cdot m^{-2} \cdot sr^{-1} \cdot \mu m^{-1}}\right]$$

For an altered spectrum |X(k)| * $\nu^2$ / 10,000, the following alternative is used. The following was used for this analysis.

$$IRF_\lambda = \frac{(Vhot_\nu - Vwarm_\nu)}{(Bhot_\nu - Bwarm_\nu)} = IRF_\nu \quad (216)$$

$$\frac{DN}{W \cdot m^{-2} \cdot sr^{-1} \cdot (cm^{-1})^{-1}}$$

**INSTRUMENT RADIANCE CONVERTED TO WAVELENGTH UNITS**

The instrument energy however, must be converted.

( 217 )

$$\varepsilon B_{\lambda_{ins}} = \varepsilon B_{\nu_{ins}} * \frac{\nu^2}{10{,}000}$$

$$[W \cdot m^{-2} \cdot sr^{-1} \cdot (cm^{-1})^{-1}]$$

## CONCLUDING NOTES

For this paper, the FFT is altered, so the spectrum can be analyzed in wavelength space by multiplying by the wavenumber squared and dividing by 10,000. The IRF for the wavenumber spacing is thus equivalent to the IRF for the wavelength. The $d\delta$ term is ignored as it cancels out—this appears to be common practice. In this paper, the spectrum is divided by N and multiplied by 2.

# APPENDIX I:

# FILTER IMAGES

| | Wheel 1 with 30 μm | | Wheel 2 with 30 μm | | |
|---|---|---|---|---|---|
| λ (μm) | Chopped | Open | Chopped | Open | λ (μm) |
| X | 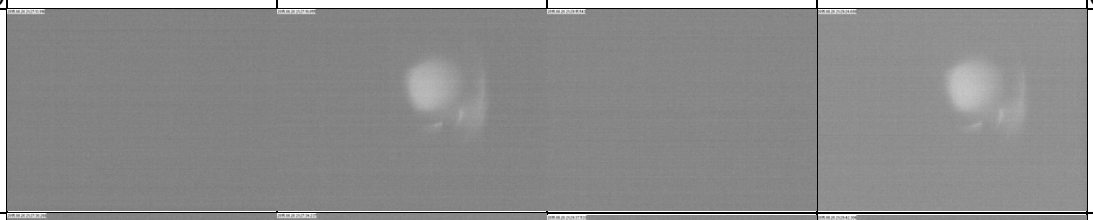 | | | | X |
| 25 | 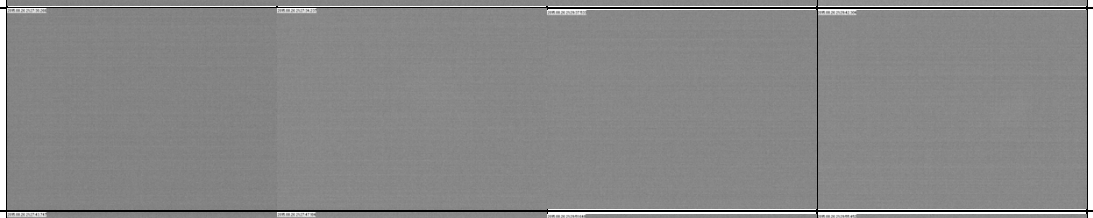 | | | | 15 |
| 30 | 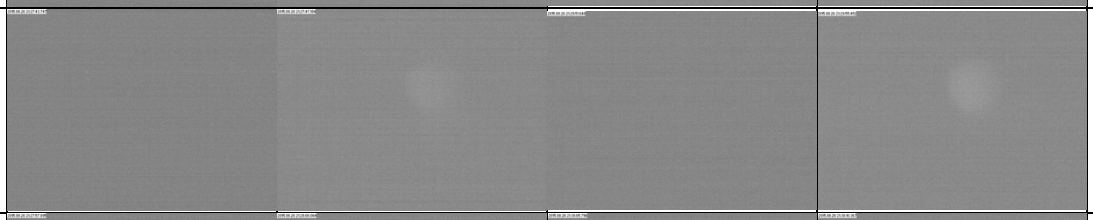 | | | | 35 |
| 45 | 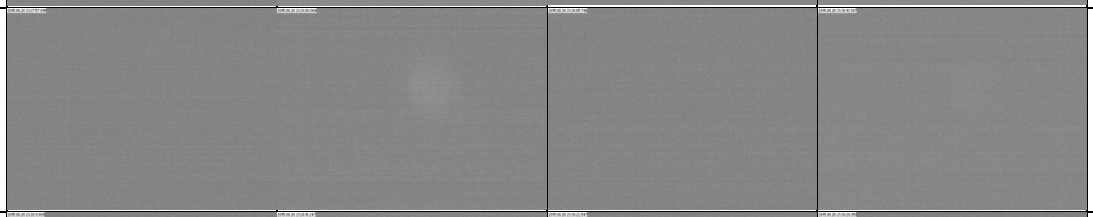 | | | | 60 |
| 70 | 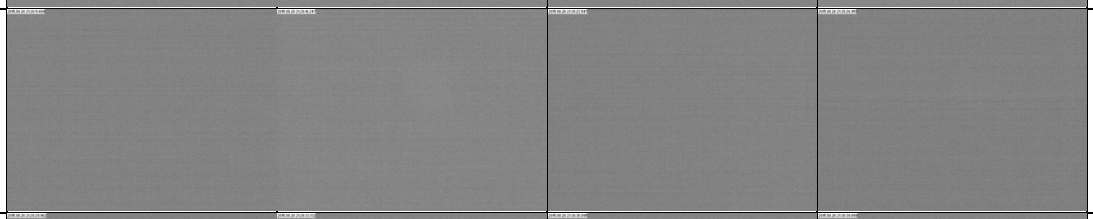 | | | | 80 |
| 90 |  | | | | 100 |

# APPENDIX J.

# BACKGROUND CALCULATIONS

The necessary calculations for remote sensing are provided.

**Specifications**

| | | |
|---|---|---|
| Detectors Specifications | | |
| Pixel Pitch | $d_{pix}$ | 25μm |
| Pixel Area | $A_p = d_{pix}^2$ | $625\mu m^2$ |
| Noise Equivalent Delta Temperature | NEdT | $< 30$mK for f/1.0 |
| Minimum wavelength | $\lambda_1$ | 8μm |
| Maximum wavelength | $\lambda_2$ | 12μm |
| Optical Specifications | | |
| Effective focal length | EFL | 100 mm |
| Enterance pupil diameter | EPD | 62.5 mm |
| F number | f/# | 1.6 |
| Optical Opacity | τ | 88% |
| Instantaneous Field of View | $\alpha_{pix}$ | 2.5 E − 4 Rad |
| Solid Angle | $\Omega_0$ | 0.2795 str |
| Mission Specifications | | |
| Target distance | | 50 – 200 m |
| Altitude | h | ~760 km |
| Target Temperature | $\theta_t$ | ~300K |
| Instrument Performance | | |

**Definitions**

Definitions of specific terms are as follows.

**Radiance or the Plank Function in wavelength**

The fundamental equation that describes the amount of radiation as a function of wavelength and temperature is the Plank function. In this equation, we use the simplified coefficients that lump the fundamental constants.

( 218 )

$$L(\lambda, T) = \frac{C_1}{\pi\lambda^5\left(e^{\frac{C_2}{\lambda T}} - 1\right)}$$

$$[W \cdot cm^{-2} \cdot str^{-1} \cdot \mu m^{-1}]$$

$$C_1 = 2\pi hc^2 = 3.74 * 10^4\ [W \cdot \mu m^4 \cdot cm^{-2}]$$

$$C_2 = \frac{ch}{k} = 1.44 * 10^4\ [\mu m^4 \cdot K]$$

**Derivative of Radiance with respect to Temperature**

The derivative of the Plank function can be taken with respect to temperature.

( 219 )

$$\frac{dL}{dT}(\lambda, T) = \frac{C_1 C_2}{\pi\lambda^6 T^2} \frac{e^{\frac{C_2}{\lambda T}}}{\left(e^{\frac{C_2}{\lambda T}} - 1\right)^2}$$

$$[W \cdot cm^{-2} \cdot str^{-1} \cdot \mu m^{-1} \cdot K^{-1}]$$

**Integrated Radiance of wavelength of derivative with respect to temperature**

The preceding derivative can then be multiplied by the wavelength band to determine an "integrated" change in radiance with respect to temperature.

( 220 )

$$\frac{dL}{dT_{\Delta\lambda}}(\lambda, T) = \frac{dL}{dT}(\lambda, T) * (\lambda_2 - \lambda_1)$$

$$[W \cdot cm^{-2} \cdot str^{-1} \cdot K^{-1}]$$

**Noise Equivalent Delta Temperature**

This is the minimum detectable temperature through the camera system that provides an SNR = 1. This is a common parameter of IR cameras. FLIR describes this as the Sensitivity. The Tau 2 has a NEdT of <30 mK for an f/1.0 system.

$$NEdT\ [K]$$

**Calculation for NEdT for different f/#**

The NEdT for an optical system changes with different optics. The following equation is used to convert the NEdT for a corresponding f/#.

( 221 )

$$NEdT_1 = NEdT_0 * \left(\frac{f\#_1}{f\#_0}\right)^2\ [K]$$

**Noise Equivalent Delta Radiance**

The radiance that produces a signal to noise ration of 1.

( 222 )

$$NEdR = NEdT * \frac{dL}{dT_{\Delta\lambda}}$$

$$[W \cdot cm^{-2} \cdot str^{-1}]$$

**Noise Equivalent Power**

This is the signal power on a pixel that produces a signal to noise ratio of 1. This is a common metric for the performance detectors. As the area of the pixel and the solid angle are factored into this equation, the units are in Watts.

( 223 )

$$NEP = NEdR * A_p * \Omega_0\ [W]$$

**Measured Power Noise**

$$P_{Noise} = \frac{V_{Noise}}{Resp_V}\ [W] \tag{224}$$

**Voltage Responsivity**

$$Resp_V = \frac{Resp_T}{\frac{dL}{dT}_{\Delta\lambda} * A_p * \Omega * 1 * K} \tag{225}$$

$$[V \cdot W^{-1}]$$

**Optical Geometry Equations**

The solid angle of a pixel is equal to the area of the pixel projected onto its emitted object over the square of the distance to the object. This is equivalent to the square of the instantaneous field of view—using the small angle approximation; the ground sample distance over the altitude is equal to the IFOV of the pixel represented here by alpha. Also note that it does not matter what the shape of a solid angle is. This is why it is the projection of square in this formula.

$$\Omega_{pix} = \frac{A_{Pixel\ on\ Object}}{r_{Object\ distance}{}^2} = \alpha_{pix}{}^2 \tag{226}$$

$$[str]$$

$$\alpha_{pix} = \frac{Ground\ Sample\ Distance}{Altitude} = \frac{d_{pix}}{EFL} \tag{227}$$

$$[Rad]$$

The ground sample distance can be determined through a proportional relationship to the equivalent relationship to the ground sample distance over the altitude.

$$Ground\ Sample\ Distance = Altitude * \frac{d_{pix}}{EFL} \quad (228)$$

$$[m]$$

The solid angle of the optical system is a function of the focal length.

$$\boldsymbol{\Omega_0 = \pi\, sin\left(tan^{-1}\left(\frac{1}{2 * f\#}\right)\right)^2} \quad (229)$$

$$[\boldsymbol{str}]$$

**Power at the Pixel**

The power received by the pixel is equal to the radiance multiplied by the transmission of the optical system, the area of the entrance pupil, and the solid angle. A numerical method can be used to integrate the radiance within the wavelength band.

$$P_P = L(\lambda_1, \lambda_2, T) * \tau * \frac{\pi}{4} EPD^2 * {\alpha_{pix}}^2 \quad (230)$$

$$[W]$$

**Area of Detector**

$$A_D = \frac{\pi}{4} EPD^2 \quad (231)$$

$$[m^2]$$

**Signal to Noise Ratio**

The theoretical signal to noise ratio is equal to the power received at the pixel over the noise equivalent power.

$$SNR = \frac{P_P}{NEP} \quad (232)$$

## Instrument Performance

### Calculation of NEdT

$$NEdT_1 = NEdT_0 * \left(\frac{f\#_1}{f\#_0}\right)^2 = 30mK * \left(\frac{1.6}{1}\right)^2 \approx 80\ mK$$

# APPENDIX K.

# ELECTROLYTIC CAPACITORS

| Subsystem Board | Company | Pass? | Verification Method | Correspondence |
|---|---|---|---|---|
| *Instrument Computer* | | | | |
| MinnowBoard-MAX | Minnowboard | Y | Testing | N/A, but the BOM revealed 4 Aluminum Polymer Electrolytic Capacitors |
| SilverJaw | TinCan | Y | Vendor Correspondence | "No the Silverjaw Lure does not use any electrolytic capacitors. Only ceramic capacitors are used." |
| PIXCI | EPIX | Y | Vendor Correspondence | "The PIXCI EB1mini uses only ceramic capacitors." |
| *Infrared Camera* | | | | |
| Tau2 | FLIR | Y | Vendor Correspondence | "We don't have access to the BOM for this board. I did a quick scan of a board for polarized passive, and found none. Large capacitors on the board appear to be stacked ceramics." |
| CameraLink Expansion | FLIR | Y | Vendor Correspondence | See above |
| *Visible Camera* | | | | |
| Chameleon | Point Grey-FLIR | Y | Vendor Correspondence | "We don't use electrolytic or wet tantalum capacitors on any of our cameras, including Chameleon." |

# APPENDIX L.

# INSTRUMENT CHECKOUT PROCEDURE

The following was co-authored with Terresa Spinelli and Louis Williams.

| Instrument and Propulsion Checkout (INS) | | Approval Initials |
|---|---|---|
| INS.1 | GS: Uplink EXECUTE INSTRUMENTS CHECKOUT (ENTER_PHASE = 2) | |
| | Notes: | |
| | **Verification:** RX counter increase is seen in beacon, see phase change in beacon | |
| INS.2 | ENTER [ACTIVE] Mode | |
| | Notes: | |
| | **Verification:** Mode change is seen in beacon | |
| INS.3 | Power on Instrument Computer<br>Power on Infrared Camera<br>Power on Visible Camera | |
| | Notes: FSW turns on switches 8, 10, and 19 | |
| | **Verification:** Increase in current draw on the 5V battery bus seen in the beacon | |
| INS.4 | Tell GNC to perform Instrument Checkout maneuver<br>GN&C commands CMG to slew to nadir (towards Earth or negative R axis)<br>GN&C returns flag to confirm NADIR pointing<br>At the time when Slew Complete = 1, log position, velocity, quaternion, and time | |
| | Notes: This flag will be preset for TRUE (1) for testing | |
| | **Verification:** See SlewComplete = 1 and see position, velocity, quaternion, and time in beacon | |
| INS.5 | FSW commands image capture from visible camera<br>If successful, set "INST_VISCAM_CHECKOUT_STATUS = 1"<br>If unsuccessful, set "INST_VISCAM_CHECKOUT_STATUS = 2" | |
| | Notes: | |
| | **Verification:** See flag change in beacon | |
| INS.6 | FSW commands image capture from infrared camera<br>If successful, set "INST_IRCAM_CHECKOUT_STATUS = 1"<br>If unsuccessful, set "INST_IRCAM_CHECKOUT_STATUS = 2" | |
| | Notes: | |
| | **Verification:** See flag change in beacon | |
| INS.7 | ENTER [SAFE] mode | |
| | Notes: | |
| | **Verification:** See mode change in beacon | |
| INS.8 | GS: Upon beacon update, Uplink request for images<br>Downlink images (see Command Execution Test file transfer) | |
| | Notes: This completes the instruments checkout. | |

| | | |
|---|---|---|
| | **Verification:** See RX counter increase in beacon, and see images transferred to ground station | |
| INS.9 | GS Uplink: EXECUTE PROPULSION CHECKOUT (ENTER_PHASE = 3) | |
| | Notes: | |
| | **Verification:** See RX counter increase, see phase change in beacon | |
| INS.10 | ENTER [ACTIVE] Mode | |
| | Notes: | |
| | **Verification:** See mode change in beacon | |
| INS.11 | GN&C points thruster along cross track (W) direction using Microsat CMG and commands a 132 sec thruster firing<br>During firing: collect current data from the thruster 5V line | |
| | Notes: At the time when Slew Complete = 1, log position, velocity, quaternion, and time<br>This flag will be preset for TRUE (1) for testing | |
| | **Verification:** See increase of current on 5V battery bus during firing | |
| INS.12 | Log all sensor data and all state information (13x1 vector) | |
| | Notes: | |
| | **Verification:** See sensor data and state information in beacon | |
| INS.13 | Set “PROPULSION_CHECKOUT_STATUS = 1”<br>Set “CHECKOUT_PHASE = 1” | |
| | Notes: | |
| | **Verification:** See flag change in beacon | |
| INS.14 | Enter [SAFE] Mode | |
| | Notes: | |
| | **Verification:** See mode change in beacon | |
| INS.15 | GS: Uplink request for propulsion sensor data (TELEM_PROP, include previously logged current data from INS.12)<br>Downlink data | |
| | Notes: | |
| | **Verification:** See RX counter increase and receive requested telemetry | |

# APPENDIX M

# THERMAL AND HUMIDITY LIMITS FOR ELECTRONIC COMPONENTS

| | Non-Operating Temperature ˚C | | Operating Temperature ˚C | | Humidity | Source |
|---|---|---|---|---|---|---|
| Component | Min | Max | Min | Max | | |
| Instrument Computer | | | | | | |
| MinnowBoard | 0* | 70* | 0 | 70 | Unknown** | Vendor email |
| SilverJaw | -65 | 125 | -40 | 85 | Unknown** | Vendor email |
| EB1mini | -50 | 125 | 0 | 70 | Unknown** | Vendor email |
| Visible Computer | | | | | | |
| Point Grey | -30 | 60 | 0 | 45 | 20 to 95% (no condensation) | Spec sheet |
| Fujinon | -20 | 60 | N/A | N/A | 0 to 90% (no condensation) | Vendor phone conversation |
| Infrared Computer | | | | | | |
| FLIR Tau 2 | -55 | 95 | -40 | 80 | 5% to 95% non-condensing | Spec sheet |
| Ophir Lens | -50 | 85 | N/A | N/A | 0 to 95% (no condensation) | Spec Sheet |
| Descoped components | | | | | | |
| SwissBit - I | -50 | 100 | -40 | 85 | 0 to 85% (no condensing) | Spec sheet |
| Delkin | -50 | 100 | -40 | 85 | 20 to 95% (no condensation) | Spec sheet |

* The non-operating temperature limits for the Minnowboard were reported to be equal to the operating temperature limits by the vendor, however this is probably a conservative response derived from a lack of testing.

** The vendors did not explicitly test the componetnts for humidity. The requirement is assumed to be the most stringent from the other components.

# APPENDIX N:

# INSTRUMENT SUBSYSTEM BILL OF MATERIALS

| Assembly / Part | Material | Specification or Manufacturer's Part # | PPL (Y/N) | TML (%) | CVCM (%) |
|---|---|---|---|---|---|
| Infrared Camera | - | - | - | - | - |
| Infrared Camera Core Assembly | | FLIR Tau 2 (Proprietary, but REACH/RoHS certified) | - | - | - |
| Base, Ceramic | Assembly with solder | | N | 0.02 | 0.01 |
| Lid, Stamped | Kovar, Nickel, gold, plating solutions | | N | 0.34 | 0.01 |
| Silicon Window, Autocam | Float zone silicon coating nickel, gold, titanium | | N | 0.63 | 0.11 |
| Solder Preform, Window/Lid | 97 Indium/3 Gold | | N | 0.23 | 0.08 |
| Getter | Nicrofer® 6025 HT (Ni, Cr, Fe, C) | | N | 0.30 | 0.00 |
| Getter Sheet | Nicrofer® 6025 HT (Ni, Cr, Fe, C) | | N | 0.30 | 0.00 |
| Camera Frame, Cast | Mg Alloy, AZ91D (RoHS-Conversion Coat) | | N | N/D | N/D |
| Retainer Clip | Zytel | | N | 0.81 | 0.03 |

| | | | | | |
|---|---|---|---|---|---|
| Shutter ASSY | | Sub-assembly-declare RoHS | N | N/A | N/A |
| UV Curable | Loctite | | N | 4.23* | 1.08* |
| Primer | Loctite | | N | 1.21* | 0.14* |
| Housing | Calibre 300/301 | | N | 0.12 | 0.00 |
| Motor/Harness Assembly | | RoHs; Sub-contractor specified | N | N/A | N/A |
| Pinion Gear | Zytel | | N | 0.81 | 0.03 |
| Bevel Gear/Shaft | Zytel | | N | 0.81 | 0.03 |
| Return Spring | Stainless Steel 302 | | N | 0.02 | 0.00 |
| Cap | Calibre 300/301 | | N | 0.12 | 0.00 |
| Paddle-Shutter | Al 1100, 5052, 1145 | | N | 0.09 | 0.05 |
| Shutter Grease | Nye 8512S | Nye Lubricants UniFlor 8512S Synthetic Oil | N | 0.21 | 0.05 |
| Lends Holder Machined | Aluminum 6061-T6 | | N | 0.09 | 0.05 |
| Core | PCB | | N | 0.18 | 0.01 |
| Cover | Mg ALLOY, AZ91D (RoHS conversion coat) | | N | N/D | N/D |
| Infrared Lens Assembly | - | Ophir 680026 | - | - | - |

| | | | | | |
|---|---|---|---|---|---|
| Lenses | Germanium (Ge) (Hard Carbon) | Ophir | N | 0.24 | 0.01 |
| Housing and Structural Components | Aluminum 6061 (Anodize) | Ophir | N | 0.09 | 0.05 |
| | | | | | |
| Wave Spring | Steel 17-7 PH | Ophir | N | 0.02 | 0.00 |
| O-rings | Nitrile (BUNA N) | Ophir N103-70 | N | 2.58* | 0.22* |
| Silicon Comp | RTV 560 | Ophir | N | 0.63 | 0.11 |
| Grease | Molykote Grease | Ophir Molykote Lite 33 | N | 3.20* | 1.25* |
| Glue | Loctite-270 | Ophir Loctite-270 | N | 6.10* | 1.23* |
| Structure | Aluminum 6061 (Alodine, Anodize) | Arizona State University | N | 0.09 | 0.05 |
| Solar Shade | Aluminum 6061 (Alodine, Anodize, Aeroglaze) | Arizona State University | N | 0.09 | 0.05 |
| Alodine | Alodine | ChemResearch IAW MIL-DTL-5541 | N | 0.51 | 0.00 |
| Anodize | Anodize | ChemResearch IAW MIL-A-8625, TII, CL 2 BLACK. | N | 0.75 | 0.02 |
| Aeroglaze Paint | Aeroglaze Z306 Flat Black Absorptive Polyurethane | STP Performance Coating (painted) | N | 1.00 | 0.02 |

| | | | | | |
|---|---|---|---|---|---|
| Epoxy | 2216 a/b gray | 3M Scotchweld 2216 a/b gray | N | 0.78 | 0.05 |
| Camera Link Cable | PTFE Non-Stick Coating insulation | | N | 0.02 | 0.00 |
| USB Power Cable | PTFE Non-Stick Coating insulation | | N | 0.02 | 0.00 |
| Socket Head Screws for Camera Fastening | Stainless Steel 44316 | McMaster-Carr M3 × Pitch: 0.5, 16mm; Part# 92290A120 | N | 0.02 | 0.00 |
| Visible Computer | - | - | - | - | - |
| Visible Camera Core Assembly | PCB | Point Grey Chameleon CMLN-13S2C | N | 0.18 | 0.01 |
| Visible Camera Lens Assembly | - | Fujinon HF25HA-1B | - | - | - |
| Housing and Structural Components | Aluminum 6061 (Anodize) | Fujinon | N | 0.09 | 0.05 |
| Housing Fasteners | Aluminum/Steel | Fujinon | N | 0.09 | 0.05 |
| Lenses | Glass (SiO2 Assumed) | Fujinon $SiO_2$ | N | 0.44 | 0.17 |
| Lubricant | Fluorocarbon Grease | Fujinon | N | 5.72* | 3.00* |
| Lubricant | Oil | Fujinon | N | * | |
| Lens Adjustment Knobs | Aluminum/Steel | Fujinon | N | 0.09 | 0.05 |

| | | | | | |
|---|---|---|---|---|---|
| Structure | Aluminum 6061 (Alodine, Anodize, Aeroglaze) | Arizona State University | N | 0.09 | 0.05 |
| Alodine | Alodine | ChemResearch IAW MIL-DTL-5541 | N | 0.51 | 0.00 |
| Anodize | Anodize | ChemResearch IAW MIL-A-8625, TII, CL 2 BLACK. | N | 0.75 | 0.02 |
| Aeroglaze Paint | Aeroglaze Z306 Flat Black Absorptive Polyurethane | STP Performance Coating (painted) | N | 1.00 | 0.02 |
| Epoxy | 2216 a/b gray | 3M Scotchweld 2216 a/b gray | N | 0.78 | 0.05 |
| USB Data Cable | PTFE Non-Stick Coating insulation | | N | 0.02 | 0.00 |
| USB Power Cable | PTFE Non-Stick Coating insulation | | N | 0.02 | 0.00 |
| M2x30mm Structure Fastening Screws | Stainless Steel 18-8 | McMaster-Carr M2 × Pitch: 0.4, 30mm; Part# 91292A034 | N | 0.02 | 0.00 |
| M2x30mm Structure Fastening Hex Nuts | Stainless Steel 316 | McMaster-Carr M2 × Pitch: 0.4, 1.6mm Part# 94150A305 | N | 0.02 | 0.00 |
| Shim for Bearings, 0.003" Thick | Stainless Steel 18-8 | McMaster-Carr 0.003 "Thick, 0.088" ID, 0.153" OD, Part# | N | 0.02 | 0.00 |

| | | | | | |
|---|---|---|---|---|---|
| | | 93574A155 | | | |
| M2x8mm Screws for spacecraft mounting (either 8/10 or 10/12 used) | Stainless Steel 316 | McMaster-Carr M2 Thread, 8mm Length, .4mm Pitch, Part# 92290A015 | N | 0.02 | 0.00 |
| M2x10mm Screws for spacecraft mounting | Stainless Steel 316 | McMaster-Carr M2 Thread, 10mm Length, .4mm Pitch, Part# 92290A017 | N | 0.02 | 0.00 |
| M2x12mm Screws for spacecraft mounting (either 8/10 or 10/12 used) | Stainless Steel 316 | McMaster-Carr M2 Thread, 12mm Length, .4mm Pitch, Part# 92290A019 | N | 0.02 | 0.00 |
| Instrument Computer | - | - | - | - | - |
| Computer | PCB (Conformal Coating) | Intel (spinoff) Minnowboard-MAX | N | 0.18 | 0.01 |
| Computer Expansion | PCB (Conformal Coating) | Tin Can Tools Silverjaw Lure | N | 0.18 | 0.01 |
| Camera Link Framegrabber | PCB (Conformal Coating) | EPIX PIXCI | N | 0.18 | 0.01 |
| microSD Card | PCB | Samsung | N | 0.18 | 0.01 |
| Expansion mSATA drive | PCB (Conformal Coating) | | N | 0.18 | 0.01 |
| Structure | Aluminum 6061 | Protocase | N | 0.09 | 0.05 |

| | | | | | |
|---|---|---|---|---|---|
| (Anodized) | | | | | |
| Anodize | Anodize | ChemResearch IAW MIL-A-8625, TII, CL 2 BLACK. | N | 0.75 | 0.02 |
| Power Cable | PTFE Non-Stick Coating insulation | | N | 0.02 | 0.00 |
| Ethernet Cable | PTFE Non-Stick Coating insulation | | N | 0.02 | 0.00 |
| Epoxy | PCB (Conformal Coating) | | N | 0.18 | 0.01 |

# APPENDIX O.

# INSTRUMENT SUBSYSTEM FASTENERS LIST

| Assembly / Part | Type | Thread | Length | Material | High Strength, Load Bearing (>100g) | Specification or Manufacturer's Part # | Qty. | Torque | Staked |
|---|---|---|---|---|---|---|---|---|---|
| Infrared Camera | | | | | | | | | |
| Socket Head Screws for Camera Fastening | Socket | M3x0.5 | 16 mm | Steel A286 | Yes | NA0069A030016 | 4 | 140 in-oz | Yes |
| FLIR Camera Core | Socket | M1.6 | 6 mm | | No | Stock | 2 | 18 in-oz | Yes |
| FLIR Camera Core | Socket | M1.6 | 8 mm | | No | Stock | 6 | 18 in-oz | Yes |
| FLIR Camera Core | Socket | M1.6 | 16 mm | | No | Stock | 2 | 18 in-oz | Yes |
| FLIR Camera Core to Lens | Socket | | | | No | Stock | 1 | 18 in-oz | Yes |
| Visible Camera | | | | | | | | | |
| M2x30mm Structure Fastening | | M2x0.4 | 30 mm | Stainless Steel 18- | No | McMaster-Carr; Part# 91292A034 | 4 | 30 in-oz | Yes |

| | | | | | | | | | |
|---|---|---|---|---|---|---|---|---|---|
| Screws | | | | 8 | | | | | |
| M2x30mm Structure Fastening Hex Nuts | | M2x0.4 | 1.6 mm | Stainless Steel 316 | No | McMaster-Carr; Part# 94150A305 | 8 | N/A | Yes |
| Shim for Bearings, 0.003" Thick (USED AS A SPACER and A WASHER) | | 0.088" ID, 0.153" OD | 0.003 Thick | Stainless Steel 18-8 | No | McMaster-Carr; Part# 93574A155 | 4/8 | N/A | N/A |
| Screws for spacecraft mounting (either 8/10 or 10/12 used) | | M2x0.4 | 8 mm | Stainless Steel 316 | No | McMaster-Carr Part# 92290A015 | 0/2/4 | Spacecraft Team Owns | Yes |
| Screws for spacecraft mounting | | M2x0.4 | 10 mm | Stainless Steel 316 | No | McMaster-Carr; Part# 92290A017 | 0/2/4 | Spacecraft Team Owns | Yes |
| Screws for spacecraft mounting | | M2x0.4 | 12 mm | Stainless Steel 316 | No | McMaster-Carr; Part# 92290A019 | 0/2/4 | Spacecraft Team Owns | Yes |
| Instrument Computer | | | | | | | | | |
| Electronics | Socket | 4-40 | 0.625” | A286 | Yes | NAS1352N04-10 | 4 | 64 in-oz | Yes |

| | | | | | | | | |
|---|---|---|---|---|---|---|---|---|
| Board Fasteners | | | | | | | | |
| Case Fasteners | Countersink | 4-40 | 0.250” | No | MS 24693-C2 | | 64 in-oz | Yes |
| 8-32 x 0.375” for mounting IR Computer to IR Camera | Socket | | | Yes | | 4 | Spacecraft Team Owns | Yes |
| 8-32 Locking Nuts for mounting IR Computer to IR Camera | Socket | | | Yes | | 2 | Spacecraft Team Owns | Yes |

# APPENDIX P.

# PLASTIC IN CONNECTORS

| Cables | Plastic | NASA Outgas? | TML | CVCM |
|---|---|---|---|---|
| USB Type A | pbt ul94v-0 | Similar PBT found | ~0.6 | ~0.08 |
| USB Mini | pbt ul94v-0 | Similar PBT found | ~0.6 | ~0.08 |
| DB9 | 1757820-6 | MIL SPEC | MIL | MIL |
| Visible, JST | pbt ul94v-0 | Similar PBT found | ~0.6 | ~0.08 |
| Ethernet | ul94v-0 | Similar PBT found | ~0.6 | ~0.08 |

# APPENDIX Q.

## HARNESSING STATUS

| Harness | Designed Length \| Actual "Usable" Length | Connector on INS (ASU) | INS-INS Harness (ASU) | INS-sc Harness (ASU) | Sc-INS Connection (ASU Deliver to GT) | Cable Type (GT) | Connector s/c (GT) | EM Status |
|---|---|---|---|---|---|---|---|---|
| Power (EPS-INS) | | | | | | | | |
| Power to INS Computer | 34" (Joe) \| (6.5" usable dongle) | Sealed Power Jack | | Power Jack-->Cicoil-->Female DB9 w/ screws (6.5") | Male DB9 w/ threads | GTRI spacecraft wire? (GT) | Georgia Tech EPS (Molex ?) | DC Power Jack |
| Power to Vis Camera | 48" (Joe) \| (6.5" usable dongle) | GPIO | | PGGPIO-->Cicoil-->Female DB9 w/ screws (6.5") | Male DB9 w/ threads | GTRI spacecraft wire? (GT) | Georgia Tech EPS (Molex ?) | GPIO |
| Power to IR Camera (Y) | 32.5" (Joe) \| ? | USB-mini w/ screw (1.8 in-lbs) | | USB2 (split)-->Cicoil-->Female DB9 w/ screws | Male DB9 w/ threads | GTRI spacecraft wire? (GT) | Georgia Tech EPS (Molex ?) | USB2 |

| | | | | | | | | |
|---|---|---|---|---|---|---|---|---|
| Data (INS-INS) | | | | | | | | |
| IR data to INS Computer | 14.5" for side wrap/ 10" for back wrap \| (~10.5" usable) | Camera Link w/ threads (PHILLIPS - not measured) | CL SDR w/ screws--> Cicoil Camera Link --> CL SDR w/ screws | | | | | Camera Link |
| IR serial data to INS Computer (Y) | 24" (Veto) 20+4 slack \| ? | USB-mini w/ threads (1.8 in-lbs) | USBmini w/ screws --> Cicoil USB2 (split)-->USB TypeA w/ screws | | | | | N/A |
| VIS data to INS Computer | 24" (Swapnil and Team) \| (~23.5" usable-MSV) | USB-mini w/ threads (1.8 in-lbs) | USBmini w/ screws --> Cicoil USB --> USB Type A w/ screws | | | | | USB2 w/ splice |
| Data (INS-CDH) | | | | | | | | |
| INS Computer to S/C Computer | 48" (Swapnil and Team) \| (47.5" MSV) | RJ45 w/ screws. (Polycarbonate and Cu-Ni) | | | | | RJ45 must add jack screws (Swapnil) | Ethernet cable |


COMPLETE
PROCURED.
Must Integrate
ORDERED
QUOTED.
Must Order
DESIGNED.
Must Quote
NOT
DESIGNED

# APPENDIX R.

## ALL IMAGE MODE OUTPUT FOR VISIBLE IMAGES

****CAPTURE ALL MODES*******

VEFR16: Visible Early Full RAW 16 bit in PGM

FlyCapture2 library version: 2.9.3.43

Application build date: Jan 31 2017 20:53:54

Number of cameras detected: 1

*** CAMERA INFORMATION ***

Serial number -15032296

Camera model - Chameleon CMLN-13S2C

Camera vendor - Point Grey Research

Sensor - Sony ICX445AQ (1/3" 1296x964 CCD)

Resolution - 1296x964

Firmware version - 1.17.3.0

Firmware build time - Fri Jul 12 16:14:39 2013

*** CAMERA SETUP ***

Max image pixels: (1296, 964)

Image Unit size: (8, 2)

Offset Unit size: (2, 2)

Pixel format bitfield: 0x6291456

EMBEDDED STATUS CODE 2147484671

HARD CODE ALL EMB ON 2147484671

CHECK EMBEDDED CODE 2147484671

IMAGE FORMAT 3758096384

IMAGE MODE 0

IMAGE MODE ABS. [#] 0

IMAGE FORMAT ABS[#] 7

N onbrd images [n] 0

Frame rate is 12.00 fps

Grabbing 1 images

*** CAPTURE STATS ***

TEMPERATURE [.K] 3244

TIME > INIT. [s] 1814

TIME > RESET [s] 1814

XMIT ERROR [n] 366

REG READ FAIL [n] 0

REG WRITE FAIL [n] 0

IMAGE ENDIANNESS 2147483648

PIXEL CLCK 754 [MHz] 1273291200

HOREZ LINE 754 [Hz] 1178353856

FRAME_RATE [fps] 12.00

[On/Off] [A/M] [Abs] 110

BRIGHTNESS [%] 0.00

[On/Off] [A/M] [Abs] 100

AUTO_EXPOSURE [EV] 1.00

[On/Off] [A/M] [Abs] 110

WHITE_BALANCE_R [NA] 465

WHITE_BALANCE_B [NA] 1000

[On/Off] [A/M] [Abs] 000

SHUTTER [ms] 10.81

[On/Off] [A/M] [Abs] 110

GAIN [dB] 0.00

[On/Off] [A/M] [Abs] 110

GAMMA [N/A] 1.25

[On/Off] [A/M] [Abs] 001

*** RAW IMAGE META DATA ***

ImageTimeStamp 796272563

ImageGain 2197815456

ImageShutter 2147483842

ImageBrightness 2181038080

ImageExposure 2197815553

ImageWhiteBalance 2151580113

ImageFrameCounter 22731

ImageStrobePattern 2147483904

ImageGPIOPinState 2952790016

ImageROIPosition 0

*** RAW PIXEL INFORMATION ***

ROWS [n] 964

COLS [n] 1296

RAW PIX FORMAT 2097152

Pixel Format [Str] RAW16

*** CONVERTED PIX INFORMATION ***

ROWS [n] 964

COLS [n] 1296

CONVERTED PIX FORMAT 2097152

Pixel Format [Str] RAW16

CAP image sclk [s] 1485923678.025

FILE FORMAT .pgm

Last Image No. [#] 255

*** FINISHED ***

N onbrd images [n] 1

VEFR8:Visible Early Full RAW 8 bit in PGM

FlyCapture2 library version: 2.9.3.43

Application build date: Jan 31 2017 20:52:31

Number of cameras detected: 1

*** CAMERA INFORMATION ***

Serial number -15032296

Camera model - Chameleon CMLN-13S2C

Camera vendor - Point Grey Research

Sensor - Sony ICX445AQ (1/3" 1296x964 CCD)

Resolution - 1296x964

Firmware version - 1.17.3.0

Firmware build time - Fri Jul 12 16:14:39 2013

*** CAMERA SETUP ***

Max image pixels: (1296, 964)

Image Unit size: (8, 2)

Offset Unit size: (2, 2)

Pixel format bitfield: 0x6291456

EMBEDDED STATUS CODE 2147484671

HARD CODE ALL EMB ON 2147484671

CHECK EMBEDDED CODE 2147484671

IMAGE FORMAT 3758096384

IMAGE MODE 0

IMAGE MODE ABS. [#] 0

IMAGE FORMAT ABS[#] 7

N onbrd images [n] 1

Frame rate is 18.00 fps

Grabbing 1 images

*** CAPTURE STATS ***

TEMPERATURE [.K] 3244

TIME > INIT. [s] 1817

TIME > RESET [s] 1817

XMIT ERROR [n] 366

REG READ FAIL [n] 0

REG WRITE FAIL [n] 0

IMAGE ENDIANNESS 2147483648

PIXEL CLCK 754 [MHz] 1273291200

HOREZ LINE 754 [Hz] 1183658136

FRAME_RATE [fps] 18.00

[On/Off] [A/M] [Abs] 110

BRIGHTNESS [%] 0.00

[On/Off] [A/M] [Abs] 100

AUTO_EXPOSURE [EV] 1.00

[On/Off] [A/M] [Abs] 110

WHITE_BALANCE_R [NA] 465

WHITE_BALANCE_B [NA] 1000

[On/Off] [A/M] [Abs] 000

SHUTTER [ms] 10.81

[On/Off] [A/M] [Abs] 110

GAIN [dB] 0.00

[On/Off] [A/M] [Abs] 110

GAMMA [N/A] 1.25

[On/Off] [A/M] [Abs] 101

*** RAW IMAGE META DATA ***

ImageTimeStamp 905156738

ImageGain 2197815456

ImageShutter 2147483907

ImageBrightness 2181038080

ImageExposure 2197815844

ImageWhiteBalance 2151580113

ImageFrameCounter 22770

ImageStrobePattern 2147483904

ImageGPIOPinState 2952790016

ImageROIPosition 0

*** RAW PIXEL INFORMATION ***

ROWS [n] 964

COLS [n] 1296

RAW PIX FORMAT 4194304

Pixel Format [Str] RAW8

*** CONVERTED PIX INFORMATION ***

ROWS [n] 964

COLS [n] 1296

CONVERTED PIX FORMAT 4194304

Pixel Format [Str] RAW8

CAP image sclk [s] 1485923681.239

FILE FORMAT .pgm

Last Image No. [#] 256

*** FINSIHED ***

N onbrd images [n] 2

VEFM: Visible Early Full MONO 8 bit in JPG

FlyCapture2 library version: 2.9.3.43

Application build date: Jan 31 2017 20:43:56

Number of cameras detected: 1

*** CAMERA INFORMATION ***

Serial number -15032296

Camera model - Chameleon CMLN-13S2C

Camera vendor - Point Grey Research

Sensor - Sony ICX445AQ (1/3" 1296x964 CCD)

Resolution - 1296x964

Firmware version - 1.17.3.0

Firmware build time - Fri Jul 12 16:14:39 2013

*** CAMERA SETUP ***

Max image pixels: (1296, 964)

Image Unit size: (8, 2)

Offset Unit size: (2, 2)

Pixel format bitfield: 0x6291456

EMBEDDED STATUS CODE 2147484671

HARD CODE ALL EMB ON 2147484671

CHECK EMBEDDED CODE 2147484671

IMAGE FORMAT 3758096384

IMAGE MODE 0

IMAGE MODE ABS. [#] 0

IMAGE FORMAT ABS[#] 7

N onbrd images [n] 2

Frame rate is 18.00 fps

Grabbing 1 images

*** CAPTURE STATS ***

TEMPERATURE [.K] 3244

TIME > INIT. [s] 1820

TIME > RESET [s] 1820

XMIT ERROR [n] 366

REG READ FAIL [n] 0

REG WRITE FAIL [n] 0

IMAGE ENDIANNESS 2147483648

PIXEL CLCK 754 [MHz] 1273291200

HOREZ LINE 754 [Hz] 1183658136

FRAME_RATE [fps] 18.00

[On/Off] [A/M] [Abs] 110

BRIGHTNESS [%] 0.00

[On/Off] [A/M] [Abs] 100

AUTO_EXPOSURE [EV] 1.01

[On/Off] [A/M] [Abs] 110

WHITE_BALANCE_R [NA] 465

WHITE_BALANCE_B [NA] 1000

[On/Off] [A/M] [Abs] 100

SHUTTER [ms] 10.81

[On/Off] [A/M] [Abs] 110

GAIN [dB] 0.00

[On/Off] [A/M] [Abs] 110

GAMMA [N/A] 1.25

[On/Off] [A/M] [Abs] 101

*** RAW IMAGE META DATA ***

ImageTimeStamp 1010272938

ImageGain 2197815456

ImageShutter 2147483907

ImageBrightness 2181038080

ImageExposure 2197815681

ImageWhiteBalance 2185134545

ImageFrameCounter 22826

ImageStrobePattern 2147483904

ImageGPIOPinState 2952790016

ImageROIPosition 0

*** RAW PIXEL INFORMATION ***

ROWS [n] 964

COLS [n] 1296

RAW PIX FORMAT 4194304

Pixel Format [Str] RAW8

*** CONVERTED PIX INFORMATION ***

ROWS [n] 964

COLS [n] 1296

CONVERTED PIX FORMAT 2147483648

Pixel Format [Str] MONO8

CAP image sclk [s] 1485923684.379

FILE FORMAT .jpg

Last Image No. [#] 257

*** FINSIHED ***

N onbrd images [n] 3

VEFC: Visible Early Full RGB 8 bit in JPG

FlyCapture2 library version: 2.9.3.43

Application build date: Jan 31 2017 20:59:37

Number of cameras detected: 1

*** CAMERA INFORMATION ***

Serial number -15032296

Camera model - Chameleon CMLN-13S2C

Camera vendor - Point Grey Research

Sensor - Sony ICX445AQ (1/3" 1296x964 CCD)

Resolution - 1296x964

Firmware version - 1.17.3.0

Firmware build time - Fri Jul 12 16:14:39 2013

*** CAMERA SETUP ***

Max image pixels: (1296, 964)

Image Unit size: (8, 2)

Offset Unit size: (2, 2)

Pixel format bitfield: 0x6291456

EMBEDDED STATUS CODE 2147484671

HARD CODE ALL EMB ON 2147484671

CHECK EMBEDDED CODE 2147484671

IMAGE FORMAT 3758096384

IMAGE MODE 0

IMAGE MODE ABS. [#] 0

IMAGE FORMAT ABS[#] 7

N onbrd images [n] 3

Frame rate is 18.00 fps

Grabbing 1 images

*** CAPTURE STATS ***

TEMPERATURE [.K] 3243

TIME > INIT. [s] 1823

TIME > RESET [s] 1823

XMIT ERROR [n] 366

REG READ FAIL [n] 0

REG WRITE FAIL [n] 0

IMAGE ENDIANNESS 2147483648

PIXEL CLCK 754 [MHz] 1273291200

HOREZ LINE 754 [Hz] 1183658136

FRAME_RATE [fps] 18.00

[On/Off] [A/M] [Abs] 110

BRIGHTNESS [%] 0.00

[On/Off] [A/M] [Abs] 100

AUTO_EXPOSURE [EV] 1.01

[On/Off] [A/M] [Abs] 110

WHITE_BALANCE_R [NA] 465

WHITE_BALANCE_B [NA] 1000

[On/Off] [A/M] [Abs] 100

SHUTTER [ms] 10.81

[On/Off] [A/M] [Abs] 110

GAIN [dB] 0.00

[On/Off] [A/M] [Abs] 110

GAMMA [N/A] 1.25

[On/Off] [A/M] [Abs] 101

*** RAW IMAGE META DATA ***

ImageTimeStamp 1114577237

ImageGain 2197815456

ImageShutter 2147483907

ImageBrightness 2181038080

ImageExposure 2197815680

ImageWhiteBalance 2185134545

ImageFrameCounter 22882

ImageStrobePattern 2147483904

ImageGPIOPinState 2952790016

ImageROIPosition 0

*** RAW PIXEL INFORMATION ***

ROWS [n] 964

COLS [n] 1296

RAW PIX FORMAT 4194304

Pixel Format [Str] RAW8

*** CONVERTED PIX INFORMATION ***

ROWS [n] 964

COLS [n] 1296

CONVERTED PIX FORMAT 134217728

Pixel Format [Str] RGB8

CAP image sclk [s] 1485923687.464

FILE FORMAT .jpg

Last Image No. [#] 258

*** FINSIHED ***

N onbrd images [n] 4

VESM: Visible Early Summed (aka VGA) MONO 8 bit in JPG

FlyCapture2 library version: 2.9.3.43

Application build date: Jan 31 2017 20:58:08

Number of cameras detected: 1

*** CAMERA INFORMATION ***

Serial number -15032296

Camera model - Chameleon CMLN-13S2C

Camera vendor - Point Grey Research

Sensor - Sony ICX445AQ (1/3" 1296x964 CCD)

Resolution - 1296x964

Firmware version - 1.17.3.0

Firmware build time - Fri Jul 12 16:14:39 2013

*** CAMERA SETUP ***

Max image pixels: (648, 482)

Image Unit size: (4, 2)

Offset Unit size: (2, 2)

Pixel format bitfield: 0x2214592512

EMBEDDED STATUS CODE 2147484671

HARD CODE ALL EMB ON 2147484671

CHECK EMBEDDED CODE 2147484671

IMAGE FORMAT 3758096384

IMAGE MODE 536870912

IMAGE MODE ABS. [#] 1

IMAGE FORMAT ABS[#] 7

N onbrd images [n] 4

Frame rate is 30.00 fps

Grabbing 1 images

*** CAPTURE STATS ***

TEMPERATURE [.K] 3244

TIME > INIT. [s] 1826

TIME > RESET [s] 1826

XMIT ERROR [n] 366

REG READ FAIL [n] 0

REG WRITE FAIL [n] 0

IMAGE ENDIANNESS 2147483648

PIXEL CLCK 754 [MHz] 1273291200

HOREZ LINE 754 [Hz] 1181697984

FRAME_RATE [fps] 30.00

[On/Off] [A/M] [Abs] 110

BRIGHTNESS [%] 0.00

[On/Off] [A/M] [Abs] 100

AUTO_EXPOSURE [EV] 1.07

[On/Off] [A/M] [Abs] 110

WHITE_BALANCE_R [NA] 0

WHITE_BALANCE_B [NA] 0

[On/Off] [A/M] [Abs] 000

SHUTTER [ms] 10.79

[On/Off] [A/M] [Abs] 110

GAIN [dB] 0.00

[On/Off] [A/M] [Abs] 110

GAMMA [N/A] 1.25

[On/Off] [A/M] [Abs] 101

*** RAW IMAGE META DATA ***

ImageTimeStamp 1222149818

ImageGain 2197815456

ImageShutter 2147483863

ImageBrightness 2181038080

ImageExposure 2197815626

ImageWhiteBalance 0

ImageFrameCounter 22940

ImageStrobePattern 2147483904

ImageGPIOPinState 2952790016

ImageROIPosition 0

*** RAW PIXEL INFORMATION ***

ROWS [n] 482

COLS [n] 648

RAW PIX FORMAT 2147483648

Pixel Format [Str] MONO8

*** CONVERTED PIX INFORMATION ***

ROWS [n] 482

COLS [n] 648

CONVERTED PIX FORMAT 2147483648

Pixel Format [Str] MONO8

CAP image sclk [s] 1485923690.641

FILE FORMAT .jpg

Last Image No. [#] 259

*** FINSIHED ***

N onbrd images [n] 5

VETM: Visible Early Thumbnail (86x64) MONO 8 bit in JPG

FlyCapture2 library version: 2.9.3.43

Application build date: Jan 31 2017 20:51:44

Number of cameras detected: 1

*** CAMERA INFORMATION ***

Serial number -15032296

Camera model - Chameleon CMLN-13S2C

Camera vendor - Point Grey Research

Sensor - Sony ICX445AQ (1/3" 1296x964 CCD)

Resolution - 1296x964

Firmware version - 1.17.3.0

Firmware build time - Fri Jul 12 16:14:39 2013

*** CAMERA SETUP ***

Max image pixels: (1296, 964)

Image Unit size: (8, 2)

Offset Unit size: (2, 2)

Pixel format bitfield: 0x6291456

EMBEDDED STATUS CODE 2147484671

HARD CODE ALL EMB ON 2147484671

CHECK EMBEDDED CODE 2147484671

IMAGE FORMAT 3758096384

IMAGE MODE 0

IMAGE MODE ABS. [#] 0

IMAGE FORMAT ABS[#] 7

N onbrd images [n] 5

Frame rate is 18.00 fps

Grabbing 1 images

*** CAPTURE STATS ***

TEMPERATURE [.K] 3244

TIME > INIT. [s] 1829

TIME > RESET [s] 1829

XMIT ERROR [n] 366

REG READ FAIL [n] 0

REG WRITE FAIL [n] 0

IMAGE ENDIANNESS 2147483648

PIXEL CLCK 754 [MHz] 1273291200

HOREZ LINE 754 [Hz] 1183658136

FRAME_RATE [fps] 18.00

[On/Off] [A/M] [Abs] 110

BRIGHTNESS [%] 0.00

[On/Off] [A/M] [Abs] 100

AUTO_EXPOSURE [EV] 1.43

[On/Off] [A/M] [Abs] 110

WHITE_BALANCE_R [NA] 465

WHITE_BALANCE_B [NA] 1000

[On/Off] [A/M] [Abs] 000

SHUTTER [ms] 12.30

[On/Off] [A/M] [Abs] 110

GAIN [dB] 0.00

[On/Off] [A/M] [Abs] 110

GAMMA [N/A] 1.25

[On/Off] [A/M] [Abs] 101

*** RAW IMAGE META DATA ***

ImageTimeStamp 1321730123

ImageGain 2197815456

ImageShutter 2147483934

ImageBrightness 2181038080

ImageExposure 2197815756

ImageWhiteBalance 2151580113

ImageFrameCounter 23029

ImageStrobePattern 2147483904

ImageGPIOPinState 2952790016

ImageROIPosition 0

*** RAW PIXEL INFORMATION ***

ROWS [n] 964

COLS [n] 1296

RAW PIX FORMAT 4194304

Pixel Format [Str] RAW8

*** CONVERTED PIX INFORMATION ***

ROWS [n] 964

COLS [n] 1296

CONVERTED PIX FORMAT 2147483648

Pixel Format [Str] MONO8

CAP image sclk [s] 1485923693.657

FILE FORMAT .jpg

Last Image No. [#] 260

*** FINSIHED ***

N onbrd images [n] 6

Converting VETH-260-70-1485923693.657.jpg to a 86x64 Thumbnail

****FINISHED**********

***

# APPENDIX S.

# VISIBLE CAMERA EXAMPLE DATA PRODUCTS

**VEFR16 – Visible Early Full Raw 16 bit**

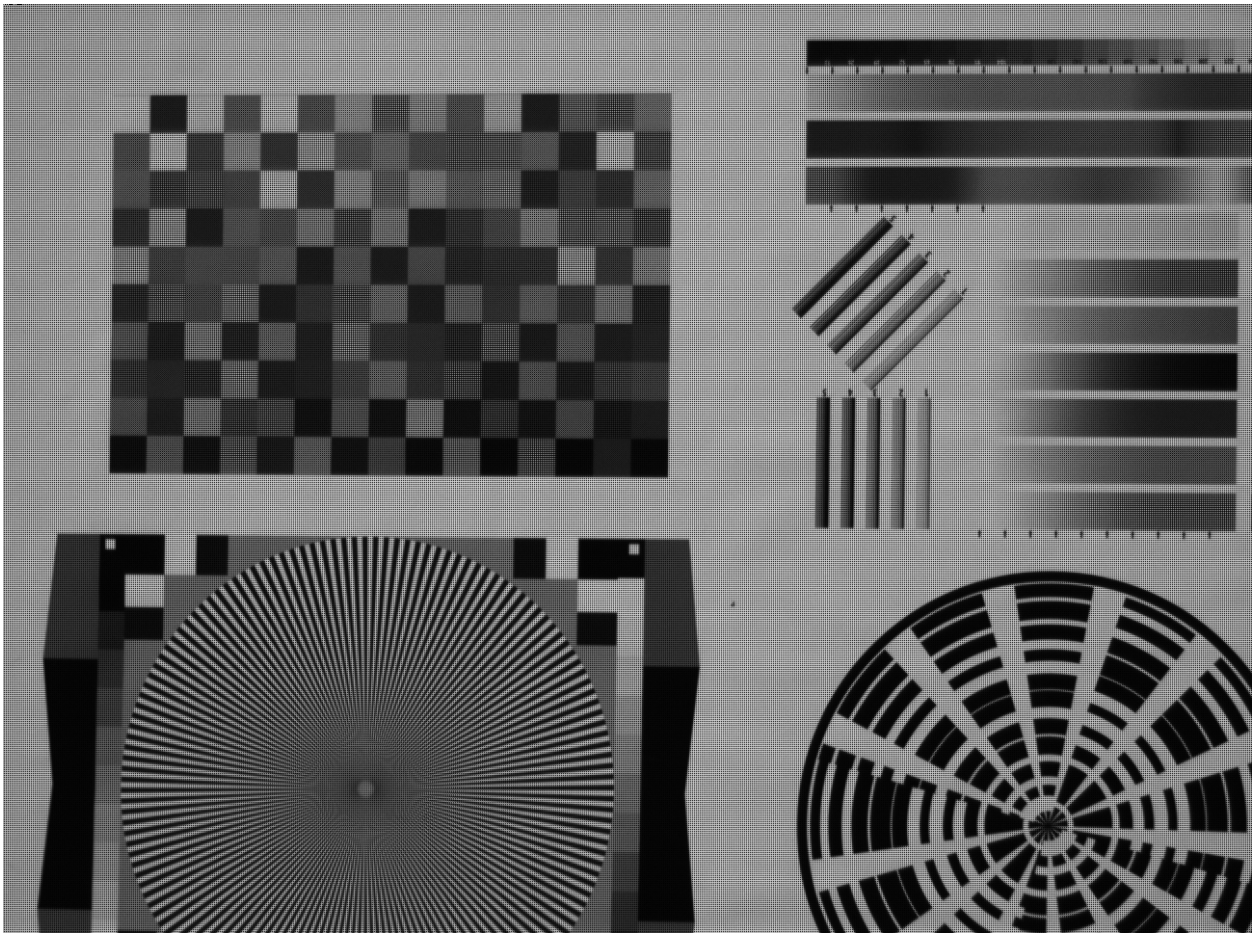

*Figure 130*. VEFR16 was a visible early full Image in "16" (really 12 bits of data fit into a 16 bit package) without Bayer algorithm. This was rawest data as it has not been binned to a lower bit depth, it does not have the bayer algorithm applied, there was no processing such as white balance processing, and a PGM format was used to prevent lossy image compression (see section 4). The figure below shows a VEFR16 image. The Bayer pattern can be seen at high zoom levels. Because this format was data intensive, it was unlikely that this format will be used. Bell notes that 73% of Pancam images for Mars are sent as 8 bit, and Christensen notes that all of the THEMIS Visible images are 8-bit (J. F. Bell III et al., 2006; Christensen et al., 2004).

**VEFR8: Visible Early Full Raw 8 bit**

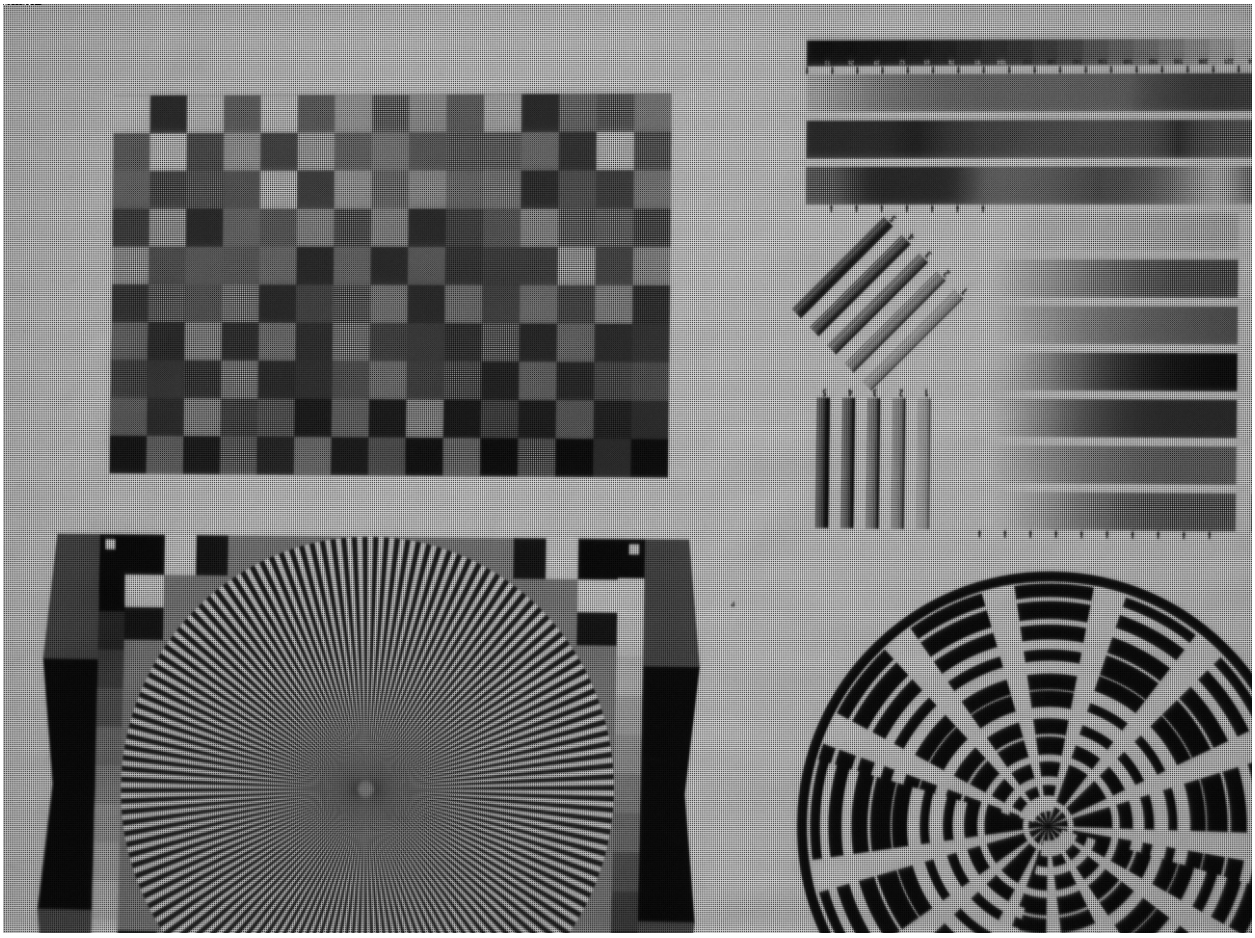

*Figure 131*. VEFR8 was a visible early full Image in 8 bit with 1.25 gamma conversion to perform the best 12 to 8 bit conversion (see section 3) without performing the Bayer algorithm. White Balance was turned OFF. The image format it PGM. The image below shows a VEFR8 image. The Bayer pattern can be seen at high zoom levels as was shown in the subsequent image. Because this format was data intensive, it was unlikely that this format will be used.

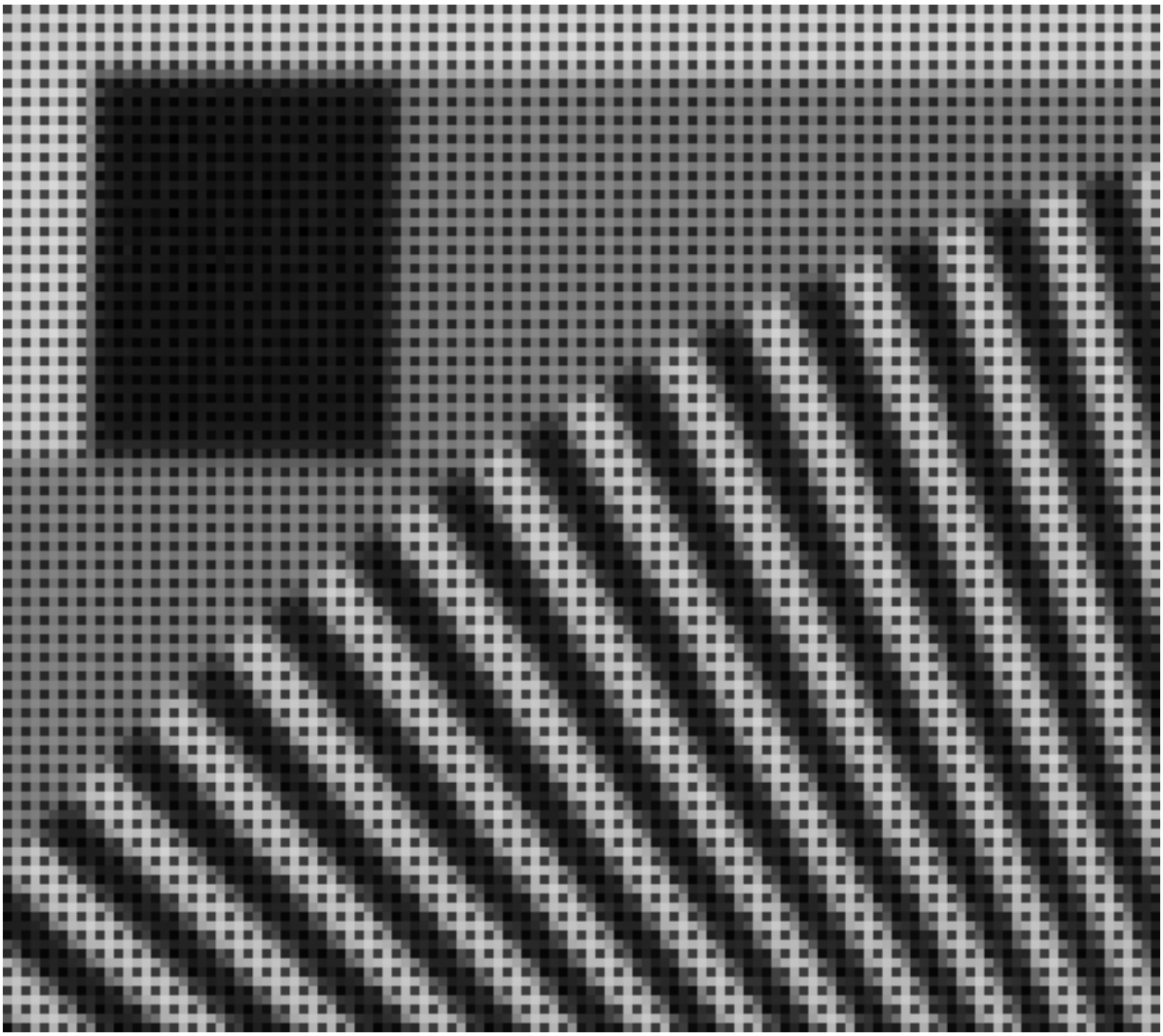

*Figure 132*. The VEFR8 close up shows that the bayer processing was not performed.

**VEFM: Visible Early Full Mono (8 bit) in JPG**

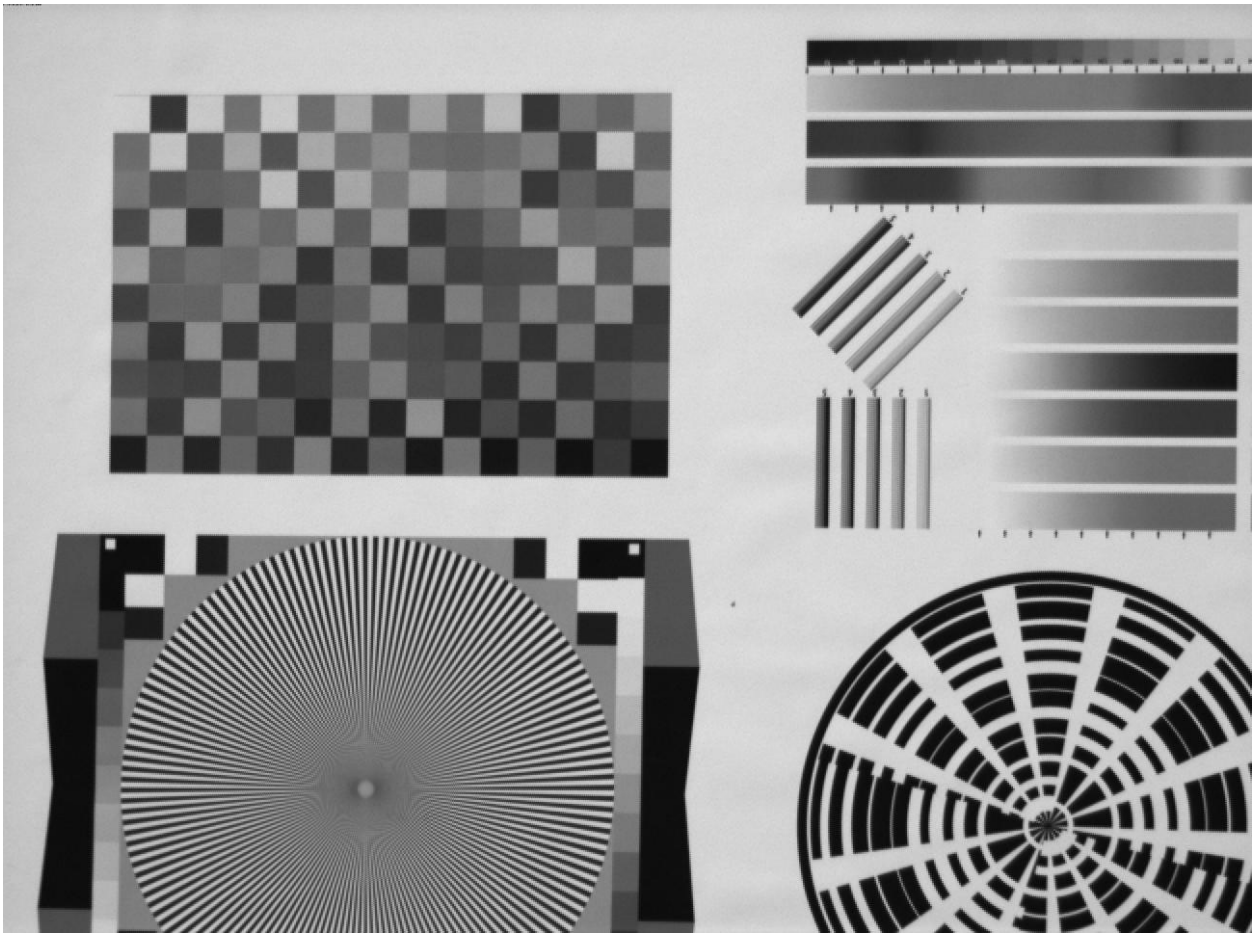

*Figure 133*. VEFM was a visibel early full Image in 8 bit with 1.25 gamma conversion for best conversion to monochromatic format. This image product was used as a full resolution image with Bayer processing and JPG image format in order to sufficiently compress the data volume. The image was white balanced using 465 for Red and 1000 for Blue (see section 3), before the Bayer processing algorithm. This was the smallest image file that preserves the full resolution. The image saves ~15% of the data of the VEFC format (see section 8), so it was unlikely that his format should be often used. The image below was an example of VEFM, and a zoomed image was followed that shows how the Bayer algorithm and JPG compression manipulate the raw data.

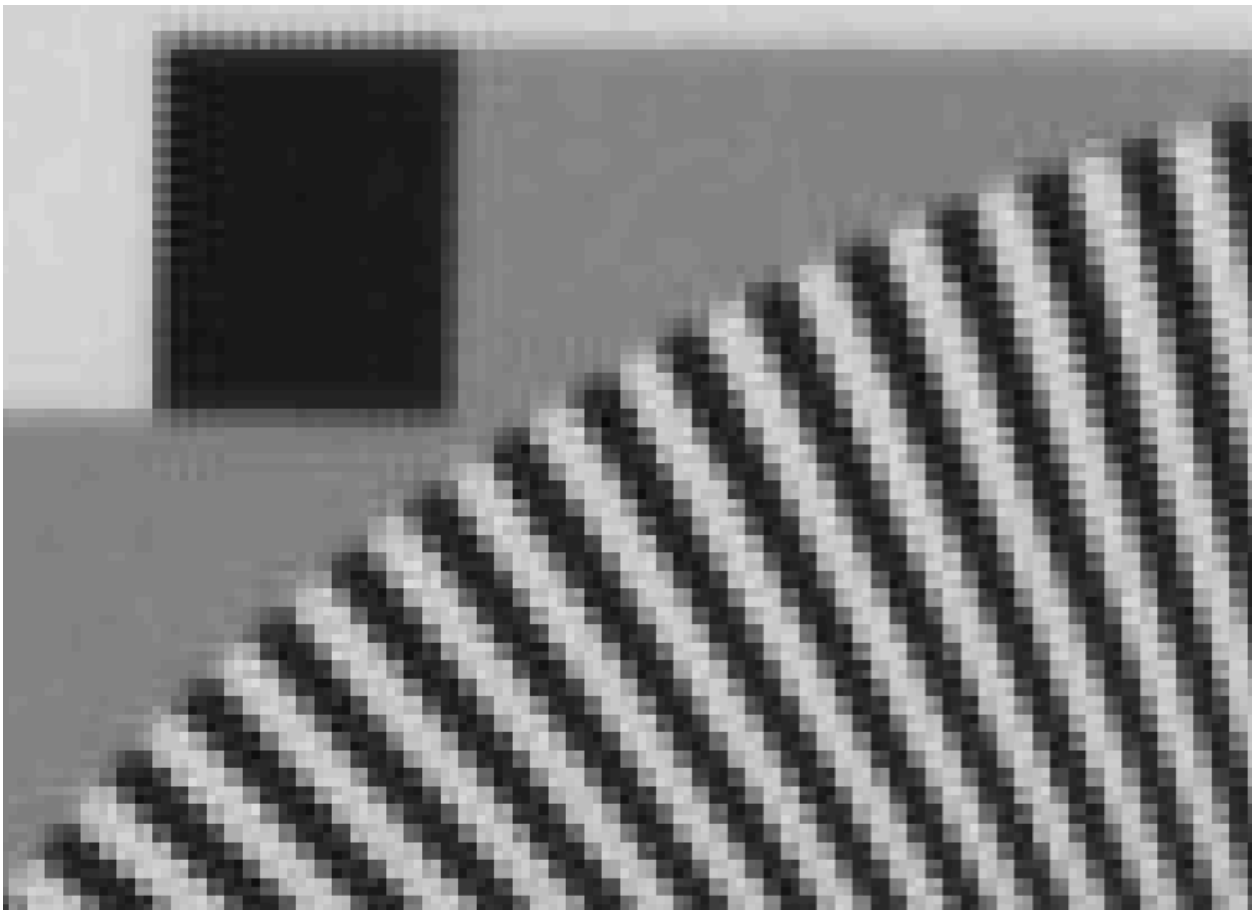

*Figure 134*. The VEFM close up shows that the bayer processing has been performed.

**VEFC: Visible Early Full Color (8 bit) in JPG**

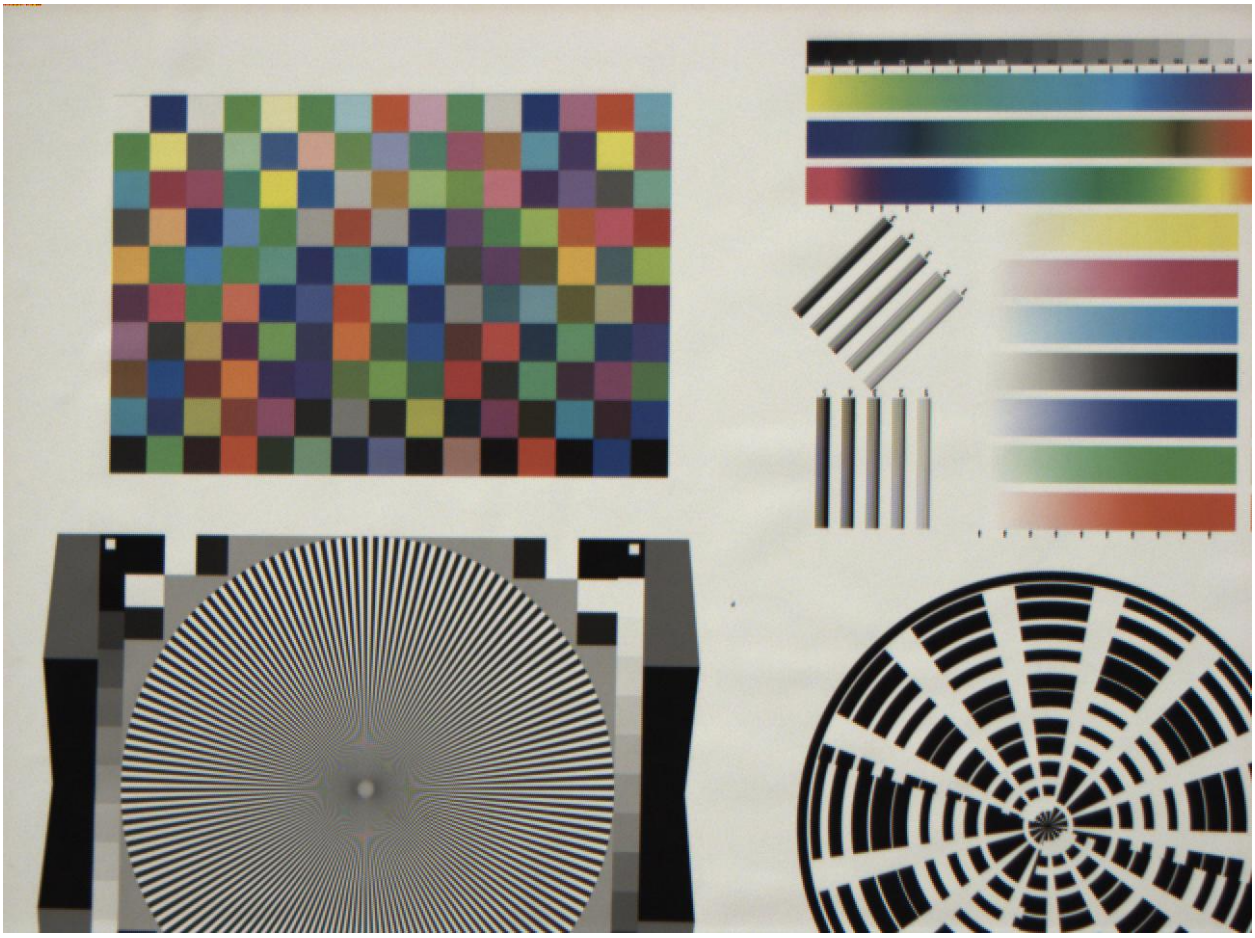

*Figure 135*. VEFC was a visible early full image in 8 bit color with 1.25 gamma conversion for conversion to RGB color format. This image product was used as a full resolution color image with on-board Bayer processing algorithm and JPG image format in order to sufficiently compress the data volume. The image was white balanced using 465 for Red and 1000 for Blue (see section 3), before the Bayer processing algorithm. VEFC was the preferred image product**.** Only when the true value of a single pixel was required should VEFR8 or VEFR16 be used. VEFM reduces the image size by only ~15% for this test image. The image below was an example of VEFC.

**VESM: Visible Early Summed Mono (8 bit) in JPG**

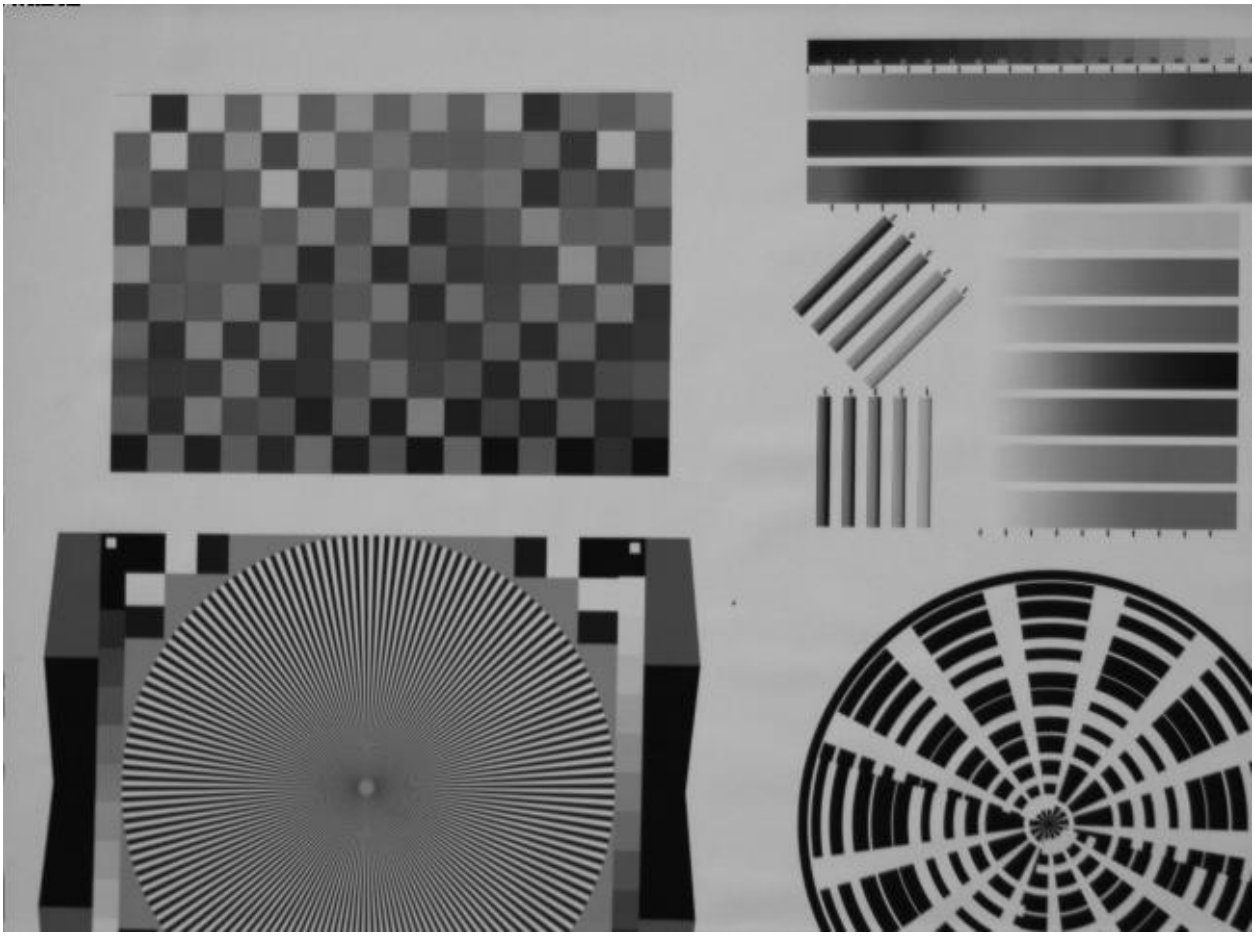

*Figure 136*. VESM was a visible early summed monochromatic image (2x in horizontal and 2x in vertical i.e. 4x reduction) that provides a moderate amount of 25% of the resolution at ~25% of the image data size. The gamma processing value of 1.25 was used to convert to 8 bit. White Balance was turned OFF in this format for summing. This product should only be used when the data budget was significantly limited.

**VETM: Visible Early Thumbnail Mono (8 bit) in JPG**

*Figure 137*. VETM was a visible early thumbnail in monochromatic 8 bit. VETM was a small image (86x64 pixels) that has very poor resolution, but takes up a very small amount of data. This format uses JPG compression to minimize the data consumption. This format was ~1% of the VEFC product and ~0.1% of the VEFR16 product. These images should be routinely used for verifying instrument health on as many downlinks as possible, and VETM can be used for capturing multiple low data products in a sequence to create a time-lapse that can be downlinked.

# APPENDIX T.

# INFRARED CAMERA TELEMETRY

**********FLIR SERIAL TELEMETRY**********

| | | | | | |
|---|---|---|---|---|---|
| COM Port: | 1 | | Digital Mode? 0:14,1:8 | | 1 |
| Device: | /dev/com1 | | Set LVDS to ON | | |
| Connect Ret.: | 3 | | FFC Period | frms | 7200 |
| COM1 | Opened | | FFC Period LG | frms | 1800 |
| SW ver. | 15.0.13.6 | | FFC Temp Delta | DegC*10 | 5 |
| FW ver. | 15.2.12.12 | | FFC Mode 0M1A | 1 | |
| S/N | | | Shutter Pos. | 0-O 1-C | 0 |
| 92228981817030290 00 | | | Gain Mode. | 0A1L2H3M | 2 |
| P/N | | | Gain Mode.??? | 0A1L2H3M | 2 |
| 46640001X-FPNLX^46640001X | | | PhotonSetDigitalOutputMode Failed. | | |
| Temp FPA DgC*10 | 222 | | Error code-263 | | |
| Temp House | DgC*100 | 2512 | Set CMOS to ON | | |
| Spot Temp.??? | DgC | 8 | THE DIGITAL OUT IS.... | | 1 |
| Gain Mode.??? | 0A1L2H3M | 2 | COM1 | | Closed |

# APPENDIX U.

# INFRARED IMAGES

**IR16H: Infrared High Gain 14 bit image in 16 bit tif**

*Figure 138*. IR16H: This was the default data product for the infrared camera. Pixel values are multiplied by 0.04 in order to determine the on-board calibrated temperature in Kelvin.

**IR8H: Infrared High Gain 8 bit image in 8 bit tif**

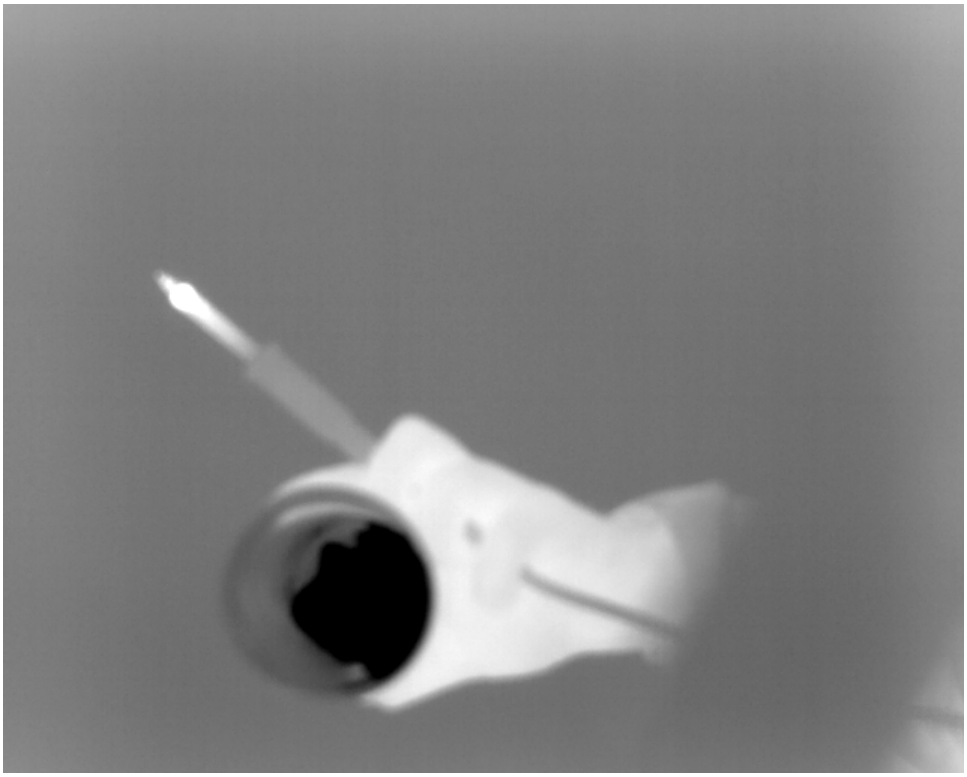

*Figure 139*. IR8H: The above image was captured in 8 bit mode. This uses the automatic gain control to create the best possible image for visualization. As compared to the 14 bit image, the variation in temperature between the cup of ice, skin, and a soldering iron was readily seen.

**IR16TH: Infrared High Gain 14 bit thumbnail image in 16 bit tif**

*Figure 140*. IR16TH: A thumbnail was produced for a 14 bit image in the 16 bit tif file. This was the default thumbnail file.

**IR8TH: Infrared High Gain 8 bit thumbnail image in 8 bit tif**

*Figure 141*. IR8TH: Thumbnails can also be produced in 8-bit mode in order to reduce the size of the image.

# APPENDIX V.

# INSTRUMENT COMPUTER TELEMETRY

PARAM UNITS VALUE UNIX TIME [sec]

CPU0TEMP C +71.0 1485836905.968

CPU2TEMP C +70.0 1485836906.022

Mem-Use %-Used 5.432 1485836906.055

Mem-Max MB 1956 1485836906.080

Disk-Use %-Used 13.76 1485836906.099

Disk-Max MB 57538 1485836906.120

LoadAvg 2=100% 0.03 1485836906.139

Epix-Det 1Y|0N 1 1485836906.185

^driver 1Y|0N 1 1485836908.266

IRsr-Det 1Y|0N 0 1485836908.718

VIS-Det 1Y|0N 0 1485836909.126

Uptime Min. 00111 1485836909.172

Cron No. 0000204 1485836701.220

PC--Boot No. 00060 1422489632.199

VIS-Boot No. 00042 1485836688.831

IR--Boot No. 00062 1485836645.282

# APPENDIX W.

# INSTRUMENT HARNESSING


*Figure 142*. The Camera Link cable was 11” long. Jack screws are not shown in this image, but they have been integrated with the EM flight-like test harness and work. The distance from the center of the 90 degree bend to the edge of the harness was closer to 10.5”.

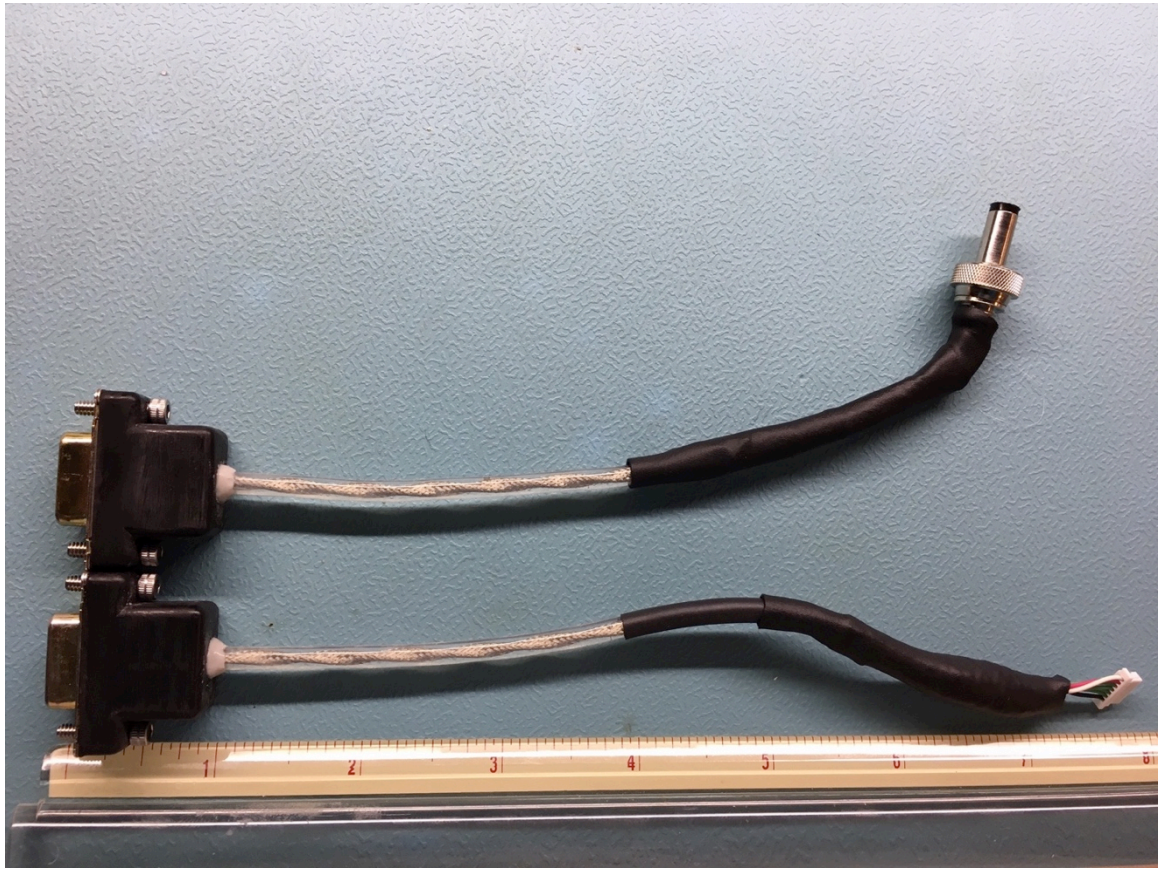

*Figure 143*. Instrument Power Dongles for EPS harness. Top) The INS-Computer plug with mounting ring to 6.5” length cable terminating in a female DB9 with male harnessing screws. Bottom) the INS-Visible plug with GPIO plug to 6.5” length cable terminating in a female DB9 with male harnessing screws. The GPIO will be staked to the Visible camera. Note: the holes in the DB9 were opened a bit at ASU, so the 4-40 screws could pass through.


*Figure 144*. The visible camera data harness was about 24” from the tip of the USB to the tip of the USB mini. The effective length from the non-inserted point of the USB to the mid point of the extruded insert on the USB mini was about 23.5”.

*Figure 145*. Ethernet Harness. The total length of the Ethernet harness was 48”. There was a combined total of about 0.5” of non-usable length from the midpoint of the connector to the edge of the harness.

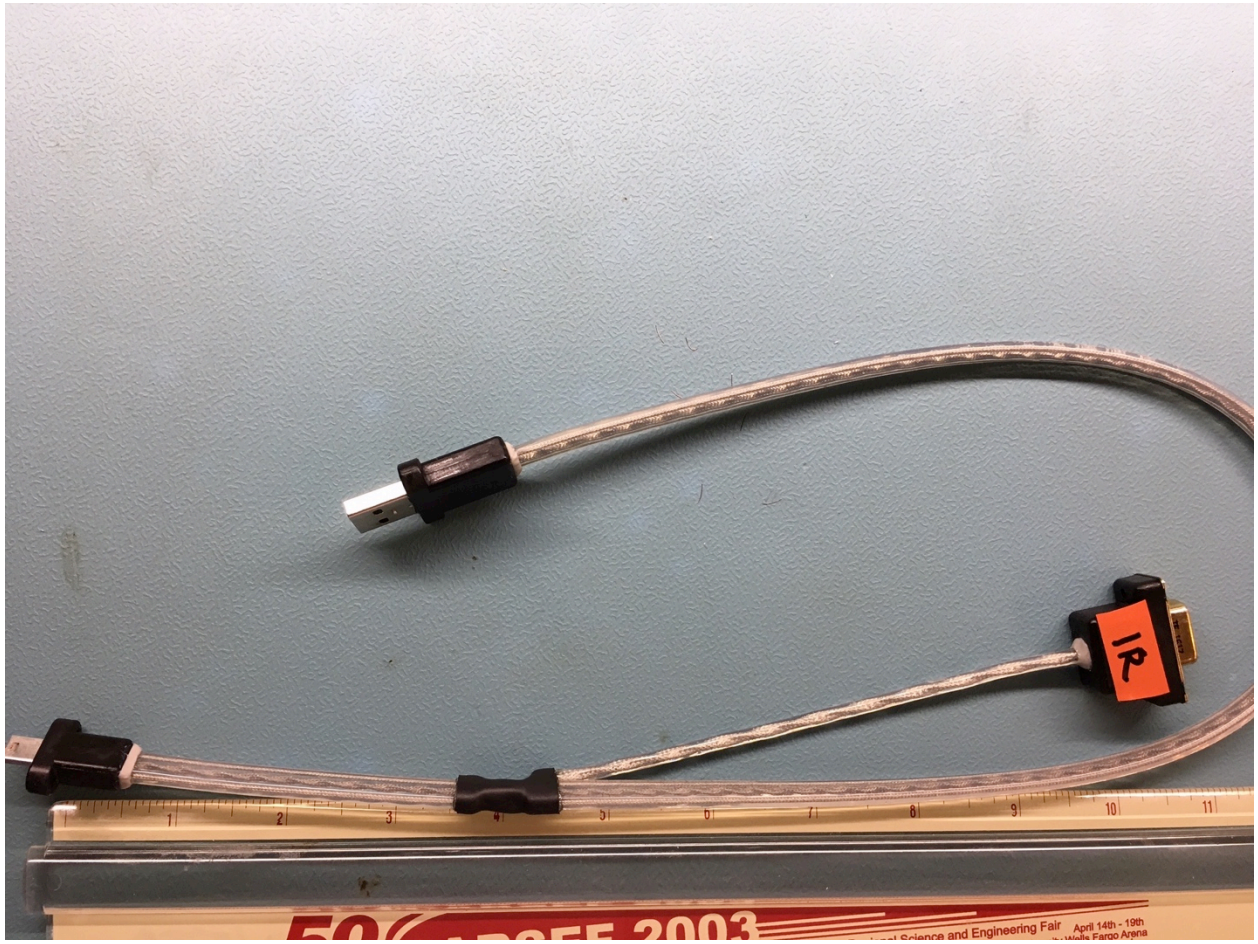


*Figure 146*. IR Power-Serial Harness. The total length of the USB-mini to DB9 for Power side was 10.5” and the total length of the USB-mini to USB Type A for serial communication was 23”. Note: the holes in the DB9 were opened a bit at ASU, so the 4-40 screws could pass through.

# APPENDIX X.

# VISIBLE RESOLUTION TEST DATA

*Figure 147.* Visible resolution test image of the CubeSat at 50 meters.

*Figure 148*. Visible resolution test image of the CubeSat at 100 meters.

*Figure 149*. Visible resolution test image of the CubeSat at 150 meters.

*Figure 150*. Visible resolution test image of the CubeSat at 200 meters.

APPENDIX Y.

INFRARED CAMERA RESOLUTION TEST DATA

*Figure 151*. Infrared resolution test image of the CubeSat at 50 meters.

*Figure 152*. Infrared resolution test image of the CubeSat at 100 meters.

*Figure 153*. Infrared resolution test image of the CubeSat at 150 meters.

*Figure 154*. Infrared resolution test image of the CubeSat at 200 meters.

# APPENDIX Z.

# INSTRUMENT COMPUTER COMMAND DICTIONARY

## Automatic Instrument Computer boot scripts

### Overview

The instrument computer automatically performs three scripts every time it boots.

### Boot Increment

The boot increment command runs to automatically increment the instrument computer boot counter for telemetry.

### Create a soft link for the IR serial interface

A soft link was created that was used for the serial communication of the infrared camera.

ln –s /dev/ttyUSB0 /dev/com1

### Establish serial connection to IR camera

The serial setup command was run. It was currently recommended that the spacecraft computer run this command to be safe. The command was described below.

## Required Setup Scripts for the spacecraft computer

### Steps

1. Make sure the CDH was in the /home/ubuntu/FLIGHT

2. Execute ./SYNC_DATE.sh

3. Execute ./SERIAL_SETUP.sh

### ./SYNC_DATE.sh

NOTE! This command syncs the date of the INS computer with the CDH computer. This command must be updated with the IP address of the spacecraft computer prior to flight.

**./SERIAL_SETUP.sh**

Must run this once after

This command will configure the IR camera for serial commanding. It should be executed after ssh-ing into the Instrument Computer. The command runs the following to setup the serial communication.

screen –d –m /dev/ttyUSB0

screen –r -X kill

**Beacon**

**Overview**

The beacon was located in /home/ubuntu/FLIGHT/beacon/ins-beacon.txt

It was a text file with currently 9 lines of characters that represent values.

The beacon was currently generated every 5 minutes.

**Example Beacon**

70: CPU Temp: 1 unsigned byte

32: VIS Temp: 1 unsigned byte

26: IR FPA Temp: 1 unsigned byte

29: IR Housing Temp: 1 unsigned byte

20: IR Spot Temp: 1 signed 16-bit (short) integer

9 : % Disk Space Used: 1 unsigned byte

107: Visible Images Onboard: 1 unsigned 16-bit (short) integer

22: Infrared Images Onboard: 1 unsigned 16-bit (short) integer

15: Status byte: 1 unsigned byte

Currently: 13 bytes (maybe a little more, but 20 bytes are allocated by the flight software team)

## Image Files

All images are stored in either of the following:

/home/ubuntu/FLIGHT/IR

/home/ubuntu/FLIGHT/VIS

## Infrared Capture Scripts

### Overview

The three most common imaging scripts are the following:

./IR16H_CAP.sh – This was the 14-bit high gain image in a 16-bit tif.

./IR8H_CAP.sh – This was the 8-bit high gain image tif.

./IR8TH_CAP.sh – This was the 8-bit thumbnail in 80x64 pixels tif.

### ./IR16H_CAP.sh

Primary IR Capture Command!

This function should be used for capturing images in Prox-Ops.

This was a wrapper script that should be used by the SC in order to capture a 16 bit image with 14 bits of values in high gain mode with high temperature resolution. This command configures the camera first, just in case a different mode was used previous. Then it executes the 16bit capture command—which was really the 14bit command followed by the convert command and the rename command. Finally, the output of ./IR16 was renamed with an H for this configuration and echoes the final name.

Calls:

./SER_HG_14B.exe

./IR16

./IR14

**./IR16L_CAP.sh**

This was a wrapper script that should be used by the SC in order to capture a 16 bit image with 14 bits of values in low gain mode with low temperature resolution. The command could be used for looking at temperatures greater than 140C, but this was not likely for this mission. This command configures the camera first, just in case a different mode was used previous. Then it executes the 14bit capture command. Finally, it renames the image with an L for this configuration and echoes the final name.

Calls:

./SER_LG_14B.exe

./IR16

./IR14

**./IR14H_CAP.sh**

This was a wrapper script that should be used by the SC in order to capture a 14 bit image in high gain mode with high temperature resolution. This command configures the camera first, just in case a different mode was used previous. Then it executes the 14bit capture command. Finally, it renames the image with an H for this configuration and echoes the final name.

Calls:

./SER_HG_14B.exe

./IR14

**./IR14L_CAP.sh**

This was a wrapper script that should be used by the SC in order to capture a 14 bit image in low gain mode with low temperature resolution. The command could be used for looking at temperatures greater than 140˚C, but this was not likely for this mission. This command configures the camera first, just in case a different mode was

used previous. Then it executes the 14bit capture command. Finally, it renames the image with an L for this configuration and echoes the final name.

Calls:

./SER_LG_14B.exe

./IR14

**./IR8H_CAP.sh**

Secondary IR Capture command for data reduction of ~50%

This was a wrapper script that should be used by the SC in order to capture a 8 bit image in high gain mode with high temperature resolution. This command configures the camera first, just in case a different mode was used previous. Then it executes the 8bit capture command. Finally, it renames the image with an H for this configuration and echoes the final name.

Calls:

./SER_HG_8B.exe

./IR8

**./IR8L_CAP.sh**

This was a wrapper script that should be used by the SC in order to capture a 8 bit image in high gain mode with high temperature resolution. The command could be used for looking at temperatures greater than 140C, but this was not likely for this mission. This command configures the camera first, just in case a different mode was used previous. Then it executes the 8 bit capture command. Finally, it renames the image with an L for this configuration and echoes the final name.

Calls:

./SER_LG_8B.exe

./IR8

**./IR8TH_CAP.sh**

Infrared Thumbnail Image for data reduction of ~99%

This was a wrapper script that should be used by the SC in order to capture an 8-bit thumbnail images in high gain mode with high temperature resolution. This command uses the IR8H_CAP command first (see above), then it coverts the image to an 80x64 image.

Calls:

./IR8H_CAP.sh

./SER_HG_8B.exe

./IR8

**Visible Capture Scripts**

**Overview**

The default visible image should be the color image **./VEFC_CAP.sh** and the thumbnail **./VETM_CAP.sh**. All of the following scripts use the corresponding compiled code and output the text to the log file.

**./VEFR16_CAP.sh**

Visible Early Full Raw 16 bit

VEFR16 was a visible early full Image in “16” (really 12 bits of data fit into a 16 bit package) without Bayer algorithm. This was rawest data as it has not been binned to a lower bit depth, it does not have the bayer algorithm applied, there was no processing such as white balance processing, and a PGM format was used to prevent lossy image compression (see section 4). The figure below shows a VEFR16 image. The Bayer pattern can be seen at high zoom levels. Because this format was data intensive, it was unlikely that this format will be used. Bell notes that 73% of Pancam images for Mars are sent as

8 bit, and Christensen notes that all of the THEMIS Visible images are 8-bit (J. F. Bell III et al., 2006; Christensen et al., 2004).

**./VEFR8_CAP.sh**

Visible Early Full Raw 8 bit

VEFR8 was a visible early full Image in 8 bit with 1.25 gamma conversion to perform the best 12 to 8 bit conversion (see section 3) without performing the Bayer algorithm. White Balance was turned OFF. The image format it PGM. The image below shows a VEFR8 image. The Bayer pattern can be seen at high zoom levels as was shown in the subsequent image. Because this format was data intensive, it was unlikely that this format will be used.

**./VEFM_CAP.sh:**

Visible Early Full Mono (8 bit) in JPG

VEFM was a visible early full Image in 8 bit with 1.25 gamma conversion for best conversion to monochromatic format. This image product was used as a full resolution image with Bayer processing and JPG image format in order to sufficiently compress the data volume. The image was white balanced using 465 for Red and 1000 for Blue (see section 3), before the Bayer processing algorithm. This was the smallest image file that preserves the full resolution. The image saves ~15% of the data of the VEFC format (see section 8), so it was unlikely that his format should be often used. The image below was an example of VEFM, and a zoomed image was followed that shows how the Bayer algorithm and JPG compression manipulate the raw data.

**./VEFC_CAP.sh**

Visible Early Full Color (8 bit) in JPG

VEFC was a visible early full image in 8 bit color with 1.25 gamma conversion for conversion to RGB color format. This image product was used as a full resolution color

image with on-board Bayer processing algorithm and JPG image format in order to sufficiently compress the data volume. The image was white balanced using 465 for Red and 1000 for Blue (see section 3), before the Bayer processing algorithm. VEFC was the preferred image product. Only when the true value of a single pixel was required should VEFR8 or VEFR16 be used. VEFM reduces the image size by only ~15% for this test image. The image below was an example of VEFC.

**./VESM_CAP.sh**

Visible Early Summed Mono (8 bit) in JPG

VESM was a visible early summed monochromatic image (2x in horizontal and 2x in vertical i.e. 4x reduction) that provides a moderate amount of 25% of the resolution at ~25% of the image data size. The gamma processing value of 1.25 was used to convert to 8 bit. White Balance was turned OFF in this format for summing. This product should only be used when the data budget was significantly limited.

**./VETM_CAP**

Visible Early Thumbnail Mono (8 bit) in JPG

VETM was a visible early thumbnail in monochromatic 8 bit. VETM was a small image (86x64 pixels) that has very poor resolution, but takes up a very small amount of data. This format uses JPG compression to minimize the data consumption. This format was ~1% of the VEFC product and ~0.1% of the VEFR16 product. These images should be routinely used for verifying instrument health on as many downlinks as possible, and VETM can be used for capturing multiple low data products in a sequence to create a time-lapse that can be downlinked.

**Image Processing Algorithm**

The following was copied from Matt Krumwiede's README file for reference.

./ipa <image name> <x1> <x2> <x3> <x4>

This was the Image Processing Algorithm

The image processing algorithm was executed in the flight directory.

The image should be images/IR/<desired image>

x1: minimum intensity

x2: maximum intensity

x3: minimum blob area

x4: maximum blob area

**Telemetry Scripts**

**Overview**

These scripts run automatically with cron every 5 minutes. They are proceeded by the image count cleanup scripts. They are detailed in <crontab –e>.

**./IR_TLM.sh**

This command runs the Serial IR script to acquire data from the IR camera without changing any settings. This command then writes the output into ins-ir_tlm.txt. It also stores the infrared camera temperature and infrared image count data into the ins-ir_beacon.txt

**./VIS_TLM.sh**

This command captures a thumbnail and saves the telemetry into ins-vis_tlm.txt. It also stores the visible camera temperature and visible image count data into the ins-vis_beacon.txt

**./tlm/pc_tlm/get_pc_tlm.sh**

This command gets all of the pc_tlm and compiles it into the ins-pc_tlm.log.

**./beacon/make_beacon.sh**

This command was used in cron the beacon.

**./tlm/pc_tlm/crons/crons_increment.sh**

This command iterates the cron count.

**./CLEANUP_IR.sh**

The script was an if-statement that will check the images/IR folder and if there are more images 700 images it will delete 200.

**./CLEANUP_VIS.sh**

The script was an if-statement that will check the images/VIS folder and if there are more images 700 images it will delete 200.

**IN-CASE-of-EMERGENCY SCRIPTS:**

**Overview**

Emergency commands are located in /home/ubuntu/FLIGHT/ICE

**./ICE/pixci_kernal_recompile.sh**

This script will recompile the pixci driver should there be an error. The error that has been detected thus far, has been attributed to the automatic updates. The automatic updates will be turned off when the system was no longer connected to the internet for security reasons.

**Commands Made to be Sourced from Above**

**./home/ubuntu/sync_date.sh**

Currently this works with Mike Veto's Laptop in the home directory to set the clock.

**./IR14**

This was the direct command to capture a 14 bit image.

**./IR8**

This was the direct command to capture an 8 bit image.

**./IR_SER_TLM**

This was the direct command to acquire IR telemetry.

**./SER_HG_14B.exe**

The serial command to set the IR camera into high gain mode with 14 bit data.

**./SER_HG_8B.exe**

The serial command to set the IR camera into high gain mode with 8 bit data.

**./SER_LG_14B.exe**

The serial command to set the IR camera into low gain mode with 14 bit data.

**./SER_LG_8B.exe**

The serial command to set the IR camera into low gain mode with 8 bit data.

**./VEFR16**

This was the direct command for a Visible Early Full Raw 16 bit image.

**./VEFR8**

This was the direct command for a Visible Early Full Raw 8 bit image.

**./VEFM**

This was the direct command for a Visible Early Full Mono 8 bit image.

**./VESM**

This was the direct command for a Visible Early Subframe Mono 8 bit image.

**./VEFC**

This was the direct command for a Visible Early Full Color 8 bit image.

**./VETH**

This was the direct command for the 8-bit full resolution image that was used to make the Visible Early Thumbnail 8 bit image.

**./VET2.sh**

This command takes the out output of VETH and converts it into a 86x64 thumbnail.

**./tlm/pc_tlm/make_pc_beacon.sh**

This command creates the ins-pc_beacon.txt

**./tlm/pc_tlm/make_status_byte.sh**

This command pulls the status_bits.txt and converts them into status_byte.txt

**./tlm/pc_tlm/make_pc_beacon**

This command creates the pc_beacon

**./tlm/pc_tlm/boot_counter/boot_increment.sh**

This command iterates the boot counter

**./tlm/pc_tlm/boot_counter/log_boot.sh**

This command logs the boot count with the date.

**./tlm/pc_tlm/current_uptime/get_uptime.sh**

This command gets the current uptime.

**./tlm/pc_tlm/current_uptime/log_uptime.sh**

This command logs the current uptime.

**./tlm/pc_tlm/disk/get_diskmax.sh**

This command gets the maximum disk space.

**./tlm/pc_tlm/disk/get_disk.sh**

This command logs the disk space.

**./tlm/pc_tlm/disk/log_disk.sh**

This command logs the disk space with the date.

**./tlm/pc_tlm/driver_status/log_driver_status.sh**

This command checks the output of the IR_TLM and searches for 640 to see if the driver was working successfully. This command needs to be revised once the driver fails again during automatic updates.

**./tlm/pc_tlm/ir_counter/ir_boot_increment.sh**

This function was called whenever the computer detects that the IR camera has been detected using /etc/udev/rules.d/IR-usb.rules

**./tlm/pc_tlm/ir_counter/log_ir_count.sh**

This function logs the IR count with the date.

**./tlm/pc_tlm/loadavg/get_load.sh**

Checks for the current load over the past minute.

**./tlm/pc_tlm/loadavg/log_load.sh**

This function logs the load with the date.

**./tlm/pc_tlm/mem/get_mem.sh**

Checks for the % of memory in use.

**./tlm/pc_tlm/mem/log_mem.sh**

This function logs the % of memory in use with the date.

**./tlm/pc_tlm/pcie/get_pcie.sh**

Checks for detection of the EPIX card.

**./tlm/pc_tlm/pcie/log_pcie.sh**

Logs the detection of the EPIX card with the date.

**./tlm/pc_tlm/tempo/get_temp.sh**

Checks for temperature of COREo using lm-sensors.

**./tlm/pc_tlm/tempo/log_tempo.sh**

Logs the temperature of COREo.

**./tlm/pc_tlm/temp2/get_temp.sh**

Checks for temperature of CORE2 using lm-sensors.

**./tlm/pc_tlm/temp2/log_temp.sh**

Logs the temperature of CORE2.

**./tlm/pc_tlm/vis_counter/vis_boot_increment.sh**

This function was called whenever the computer detects that the IR camera has been detected using /etc/udev/rules.d/VIS-usb.rules

**./tlm/pc_tlm/vis_counter/log_vis_count.sh**

This function logs the VIS count with the date.